DEVELOPMENT OF GOLD AND COPPER CATALYSTS FOR SUSTAINABLE CHEMICAL PROCESSING

MAOSHUAI LI

A dissertation submitted for the degree of Doctor of Philosophy

Heriot-Watt University

School of Engineering and Physical Sciences

<February> 2016

Abstract

Supported Au and Cu catalysts have been developed for clean/sustainable production of value fine chemicals (including alcohols, ketone, amines and imines) from selective reduction (of benzaldehyde, nitrobenzene and furfural) and coupled (dehydrogenation-hydrogenation) reaction in the continuous gas phase operation. Critical catalyst physicochemical properties are characterised by applying a range of techniques and correlated to the catalytic response.

The role of support, Au particle size and electronic character in determining catalytic activity and selectivity in the hydrogenation of benzaldehyde and nitrobenzene over oxide supported nano-scale (2-8 nm) Au has been established. Hydrogenation (turnover frequency) *TOF* increases with decreasing Au size (from 8 to 4 nm) with measurably lower *TOF* over Au < 3 nm. Repulsion of –C=O and $–NO_2$ functionalities with respect to $Au^{\delta+}$ and strong binding to surface oxygen vacancies have been found to lower hydrogenation rates. Promotional effect of water *via* catalytic dissociation has been found to enhance the selective benzaldehyde hydrogenation rate.

Two catalytic routes for imine (*N*-benzylideneimine) synthesis in continuous gas phase operation have been established. Reductive coupling of benzaldehyde with nitrobenzene (using external hydrogen) over supported Au generated up to 99% selectivity to the target imine. Coupling of benzyl alcohol dehydrogenation with nitrobenzene hydrogenation (in the absence of external hydrogen supply) over Au/TiO_2 + Cu/SiO_2 mixture produced imine with full hydrogen utilisation. Incorporation of Au/TiO_2 to Cu/SiO_2 created a synergy between Cu and Au and enhanced catalyst stability. A tandem dehydrogenation/amination/reduction process has been developed for high throughout production of benzylamine in continuous gas phase operation over Cu/SiO_2 and Au/TiO_2. A synergy between Cu/SiO_2 and Au/TiO_2 serves to promote benzylamine formation with 81% yield achieved through an optimization of process parameters.

Coupling of 2-butanol dehydrogenation with nitrobenzene hydrogenation over Cu/SiO_2 in the absence of an external H_2 supply delivered exclusive production of both 2-butanone and aniline at full conversion. Hydrogen utilisation efficiency was

appreciably greater (by a factor of up to 50) in the coupled system relative to conventional stand-alone hydrogenation using pressurised hydrogen.

Selective conversion of biomass-derived furfural to furfuryl alcohol over supported Au catalysts has been established. A series of approaches (*e.g.* promotional effect of water *via* catalytic dissociation, increased spillover hydrogen with addition of oxide support and coupling strategy) directed at increasing the surface availability of reactive hydrogen were adopted to enhance furfuryl alcohol production and hydrogen utilisation.

Continuous production of γ-butyrolactone has been established in both stand-alone hydrogenation of succinic acid (using external H_2) and reaction coupling with formic acid decomposition (as a source of H_2) over Cu/SiO_2. Pd/SiO_2 and Ni/SiO_2 promoted propanoic acid formation at higher reaction rates.

The results presented in this thesis establish feasible catalytic routes to high value alcohols, imines and amines where critical process optimisation is demonstrated in terms of catalyst composition/surface structure and reaction conditions.

Acknowledgements

Foremost, I would like to thank my PhD supervisor, Professor Mark A. Keane, for supporting me during the past four years. He has been actively interested in my work and has always been available to advise me. I am grateful for his guidance, suggestion and patience that make this doctoral thesis a reality. His rich professional knowledge, enthusiasm to science and responsibility to students always inspire me.

Many thanks to the staffs at the Chemical Engineering Department in Heriot-Watt University whose support ensures my research work conducted smoothingly. I would especially like to thank Marian K. Millar and Dr. Georgina Rosair (Chemistry Department) for their assistance with XRD scanning and Dr. Koenraad Collart (Chemistry Department) for his help with element analysis. I would also appreciate technical help from Cameron Smith, Curtis L. Abbott, Richard Kinsella and Ronald Millar with acquisition, ordering goods and maintenance of the lab facilities. Also thanks to Dr. Fernando Cárdenas-Lizana for the cooperation on catalyst characterisation (STEM and XPS) and comments on data analysis/interpretation and to Jose at Newcastle University for his assistance in XPS analysis.

I want to thank my colleagues and friends: Dr. Noemie Perret, Dr. Xiaodong Wang, Dr. Yufen Hao and Dr. Gregor Sneddon for teaching me the lab skills required for my projects and sharing their knowledge and experience. Also thanks to the people who have ever helped me with my experimental work: Dr. Craig Callahan, Kamil Mustafin and Pedro Benavente Donayre.

This research was possible by the financial support from Overseas Research Student Awards Scheme (ORSAS), James-Watt Scholarship and Great Britain-China Education Trust.

Finally, I am forever grateful to my parents for their education, endless love and unconditional support over the past years and to my sisters for their advice whenever I need help. Without their continuous support and encouragement, the completion of this thesis would not have been possible.

ACADEMIC REGISTRY
Research Thesis Submission

Name*:*	MAOSHUAI LI		
School/PGI:	Engineering and Physical Sciences		
Version: *(i.e. First, Resubmission, Final)*	Final	Degree Sought (Award **and** Subject area)	Doctor of Philosophy

Declaration

In accordance with the appropriate regulations I hereby submit my thesis and I declare that:

1) the thesis embodies the results of my own work and has been composed by myself
2) where appropriate, I have made acknowledgement of the work of others and have made reference to work carried out in collaboration with other persons
3) the thesis is the correct version of the thesis for submission and is the same version as any electronic versions submitted*.
4) my thesis for the award referred to, deposited in the Heriot-Watt University Library, should be made available for loan or photocopying and be available via the Institutional Repository, subject to such conditions as the Librarian may require
5) I understand that as a student of the University I am required to abide by the Regulations of the University and to conform to its discipline.

* *Please note that it is the responsibility of the candidate to ensure that the correct version of the thesis is submitted.*

Signature of Candidate*:*		Date:	

Submission

Submitted By *(name in capitals):*	
Signature of Individual Submitting:	
Date Submitted:	

For Completion in the Student Service Centre (SSC)

Received in the SSC by *(name in capitals):*			
Method of Submission *(Handed in to SSC; posted through internal/external mail):*			
E-thesis Submitted (mandatory for final theses)			
Signature:		Date:	

Table of Contents

List of Tables

List of Figures

Glossary

Acronyms

AAS	Atomic Absorption Spectroscopy
BET	S. Brunauer, P. H. Emmett and E. Teller theory; Measurements of surface area
BJH	Barret-Joyner-Halenda
DP	Deposition-Precipitation
FTIR	Fourier Transform Infrared Spectroscopy
FID	Flame Ionisation Detector
GHSV	Gas Hourly Space Velocity
IMP	Impregnation
ICP-OES	Inductively Coupled Plasma-Optical Emission Spectrometry
IUPAC	International Union of Pure and Applied Chemsitry
JCPDS-ICDD	Joint Committee on Powder Diffraction Standards-International Centre for Diffraction Data
MvK	Mars and van Krevelen
(S)TEM	(Scanning) Transmission Electron Microscopy
TCD	Thermal Conductivity Detector
TPR	Temperature Programmed Reduction
TPD	Temperature Programmed Desorption
TGA-DSC	Thermogravimetric Analysis-Differential Scanning Calorie
TOF	Turnover Frequency
XRD	X-ray Diffraction
XPS	X-ray Photoelectron Spectroscopy

Symbols

A_{metal}	Metal atom surface area (m^{-2} $atom^{-1}$)
BE	Binding energy (eV)
d	Metal particle size (nm)
D	Metal dispersion
E_{redox}	Redox potential
ΔE_a	Activation energy (kJ mol^{-1})
F	Molar flow rate (mol h^{-1})
i.d.	Internal diameter (mm)
k	Pseudo first-order rate constant (h^{-1})
M_{metal}	Metal atomic mass (g mol^{-1})
$N_{Avogadro}$	Avogadro number
n	Number of moles (mol)
P	Pressure (atm)
pH_{pzc}	pH at the point of zero charge
R (R_0)	(Initial) Reaction rate (h^{-1})
S	Selectivity
S_{metal}	Metal surface area per gram (m^{-2} g_{metal}^{-1})
SSA	Specific surface area (m^2 g^{-1})
t	Time on-stream (h)
T (T_{max})	(Maximum) Temperature (K)
V	Catalyst bed volume (cm^3)
W	Catalyst weight (g)
X (X_0)	(Initial) Conversion
Y	Yield
β	Time scale fitting parameter
τ	Contact time (s)
ρ_{metal}	Metal density (g cm^{-3})

Chapter 1

Introduction and Scope of the Thesis

This chapter presents a short overview of sustainability in industrial catalytic processes and briefly introduces the materials and approaches employed in this thesis work. The motivation and objectives of this PhD study are also identified.

1.1 Industrial Sustainability

The global chemical manufacture is stepping into an age of industrial sustainability where green chemistry and green engineering are advocated and developed as a response to the demand for environmentally friendly and economically competitive chemical processes. Industrial sustainability is defined as the continuous innovation, application of clean technologies to minimise pollution and consumption of resources [1.1]. In addition to the 12 principles of green chemistry, industrial sustainability also addresses utilisation of renewable resources and sustainable energy, reduction of greenhouse gases emissions and development of inherently safer processes. Catalytic processes can be designed to fulfill these guidelines. Development of continuous processes, reduction or elimination of waste products, use of renewable feedstock and atom efficiency are the cornerstones of progressing chemical processes.

Catalytic hydrogenation is essential in the manufacture of functionalised alcohols, imines and amines that are employed as precursors for the synthesis of herbicides and insecticides, pharmaceuticals, agrochemicals, cosmetics, corrosion inhibitor and pigments [1.2-1.5]. Industrial processes to date have focused on batch liquid phase operation at elevated hydrogen pressure [1.6]. Selectivity in terms of targeted –C=O and/or $–NO_2$ reduction in the presence of other reactive functional groups (*e.g.* C=C) is challenging. Non-selective reactions lead to low product yield, toxic by-products and energy inefficiency [1.7]. Further improvements are required in order to achieve continuous clean production. Moreover traditional hydrogenation is conducted using (pressurised) hydrogen that is far in excess of stoichiometric requirements. Hydrogen is not a naturally occurring resource and is produced in fossil fuel based technologies [1.8-1.10]. Sustainable catalytic hydrogenation must tackle issues associated with hydrogen

sourcing and utilisation. Energy and chemical manufacture still rely on fossil fuel and petrochemicals. The quest for sustainable resources is now the driver to develop efficient routes to commodity chemicals from renewable feedstock. Use of biomass and/or biomass-derived feedstock as a renewable source of fuels and chemicals is a first step in ensuring global sustainability.

1.2 Scope and Organisation of the Thesis

The objective of this PhD study is to develop continuous selective catalytic systems for high throughout production of high value fine chemicals (*e.g.* alcohols, imines and amines). The work addresses selectivity, productivity and sustainability issues in catalytic hydrogenation processes. A schematic diagram that outlines the scope and organisation of the PhD research is presented in **Fig. 1.1**. The selective hydrogenation of benzaldehyde (***Chapters* 2** and **3**), nitrobenzene (***Chapter* 3**) and benzaldehyde + nitrobenzene mixtures (***Chapter* 4**) to benzyl alcohol, aniline and imine (*N*-benzylideneaniline) is examined. An alternative route for the production of imine (*N*-benzylideneaniline) from coupling of benzyl alcohol dehydrogenation with nitrobenzene reduction (without using external hydrogen) is considered in ***Chapter* 5**. Simultaneous production of 2-butanone (from 2-butanol dehydrogenation) and aniline (from nitrobenzene hydrogenation) in one unit *via* reaction coupling (in N_2) is evaluated in ***Chapter* 6**. Transformation of benzyl alcohol to benzylamine *via* a tandem dehydrogenation/amination/reduction route is the focus of ***Chapter* 7**. Sustainable production of furfuryl alcohol from the hydrogenation of biomass-derived furfural is presented in ***Chapters* 8 and 9** with an investigation of a series of approaches to enhance furfuryl alcohol generation in ***Chapter* 10**. The thesis ends (***Chapter* 11**) with an evaluation of renewable succinic acid and formic acid to produce γ-butyrolactone *via* reaction coupling (in N_2).

Interest in Au catalysts for hydrogenation has been driven by the high chemoselectivity achieved in the reduction of targeted functional groups while preserving other, often more reactive, functionalities [1.11,1.12]. There are a number of instances where supported Au has generated enhanced selectivity relative to conventional transition metal (*e.g.* Pd, Pt and Ni) catalysts, notably in batch liquid phase operation [1.13]. Gold catalysts, however, deliver significantly lower hydrogenation rates, which can be attributed to a lesser capacity for hydrogen activation/dissociation [1.14-1.16]. A specific objective of this PhD work has been to enhance selective

hydrogenation rate of supported Au through an understanding of the fundamental relationships between catalyst structure and catalytic response. A systematic approach to increase surface reactive hydrogen *via* (i) catalytic dissociation of water, (ii) spillover hydrogen by incorporation of oxide supports and (iii) coupling with dehydrogenation with hydrogen release (over Cu catalyst) is presented in ***Chapters* 2** and **10**. The role of Au particle size and support properties in terms of redox character, surface deficient sites and metal interaction will be illustrated for the hydrogenation of benzaldehyde, nitrobenzene (***Chapter* 3**), benzaldehyde + nitrobenzene mixtures (***Chapter* 4**) and furfural (***Chapters* 8** and **9**). An exploration of the promotional effect of supported Au in benzylamine synthesis *via* tandem dehydrogenation/amination/reduction route is the topic of ***Chapter* 7**.

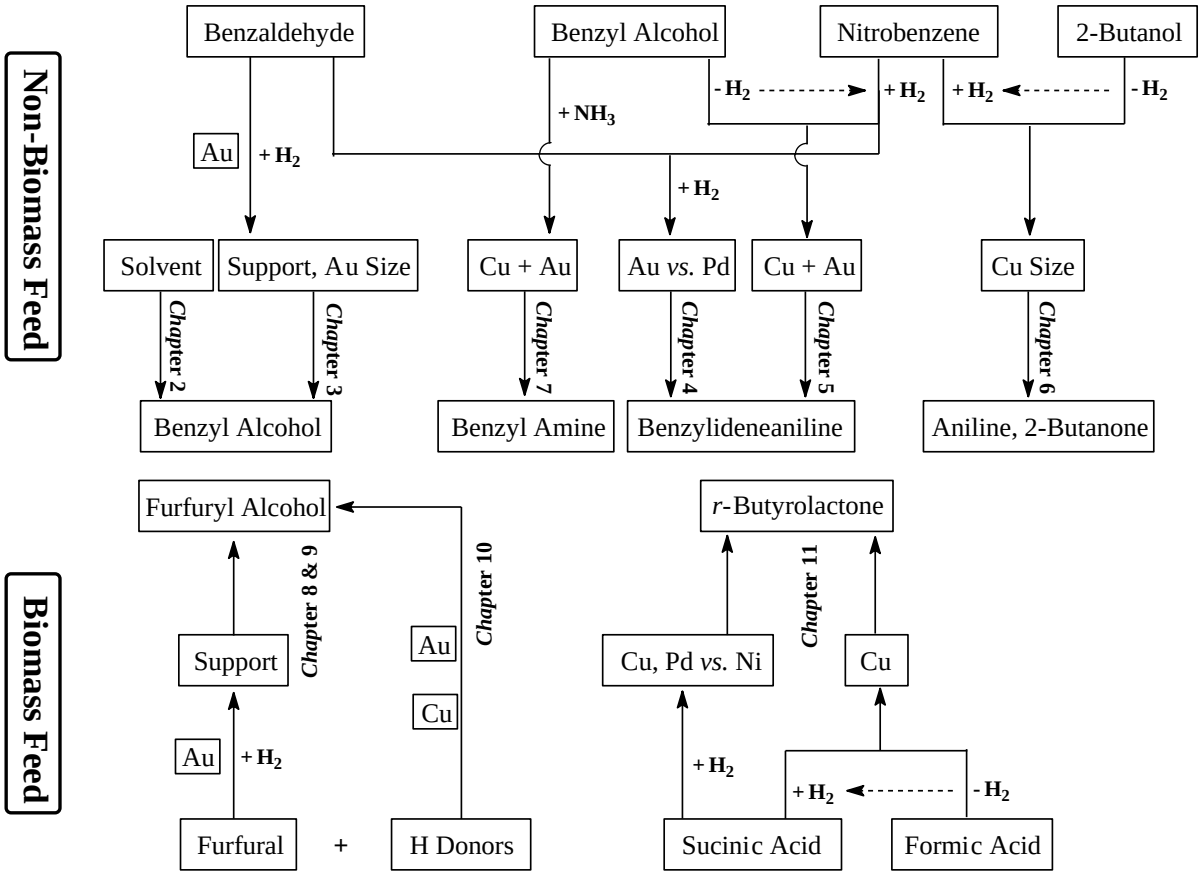

Fig. 1.1: Scope of studies undertaken in this thesis

Hydrogen utilisation is a critical issue in hydrogenation application and is tackled in this thesis. A continuous heterogeneous catalytic system that combines dehydrogenation with hydrogen release that is utilised in hydrogenation is presented as an alternative approach that circumvents the requirement for an external hydrogen supply. This offers clear advantages over conventional (stand-alone) reaction processes. The feasibility of

alcohols (benzyl alcohol and 2-butanol) and formic acid as hydrogen donors to replace (pressurised) hydrogen gas in the conversion of nitrobenzene to imine (***Chapter* 5**), aniline (***Chapter* 6**) and in the reduction of furfural to furfuryl alcohol (***Chapter* 10**) and succinic acid to γ-butyrolactone (***Chapter* 11**) is fully assessed. Hydrogen utilisation efficiency is used as the metric to compare the performance of the coupled reaction systems against traditional hydrogenation process.

Use of biomass based feedstock is attracting increasing attention as a renewable, non-petroleum based raw material for the sustainable production of a diversity of high value products [1.17-1.19]. Furfural and succinic acid are derived from lignocellulosic biomass and have been identified as promising platform reactants for the production of commodity and specialty chemicals [1.20-1.23]. Selective hydrogenation of furfural to furfuryl alcohol over supported Au is presented and discussed in ***Chapters* 8** and **10**. Preliminary results for utilisation of renewable formic acid as hydrogen donors in succinic hydrogenation to γ-butyrolactone (over Cu/SiO_2) are also presented in ***Chapter* 11**.

The primary contributions of this thesis are summarised in ***Chapter* 12** with suggestions for future directions in sustainable chemical manufacturing.

1.3 References

[1.1] J.F. Jenck, F. Agterberg, M.J. Droescher, *Products and processes for a sustainable chemical industry: A review of achievements and prospects*, Green Chem. 6 (2004) 544-556.

[1.2] J. Scognamiglio, L. Jones, D. Vitale, C.S. Letizia, A.M. Api, *Fragrance material review on benzyl alcohol*, Food Chem. Toxicol. 50 (2012) S140-S160.

[1.3] L. Pranger, R. Tannenbaum, *Biobased nanocomposites prepared by in situ polymerization of furfuryl alcohol with cellulose whiskers or montmorillonite clay*, Macromol. 41 (2008) 8682-8687.

[1.4] W.J. Cui, Q. Xiao, S. Sarina, W.L. Ao, M.X. Xie, H.Y. Zhu, Z. Bao, *Au-Pd alloy nanoparticle catalyzed selective oxidation of benzyl alcohol and tandem synthesis of imines at ambient conditions*, Catal. Today 235 (2014) 152-159.

[1.5] R.K. Marella, K.S. Koppadi, Y. Jyothi, K.S.R. Rao, D.R. Burri, *Selective gas-phase hydrogenation of benzonitrile into benzylamine over Cu-MgO catalysts without using any additives*, New J. Chem. 37 (2013) 3229-3235.

[1.6] R.A. Sheldon, R.S. Downing, *Heterogeneous catalytic transformations for environmentally friendly production*, Appl. Catal. A: Gen. 189 (1999) 163-183.

[1.7] T. Mitsudome, K. Kaneda, *Gold nanoparticle catalysts for selective hydrogenations*, Green Chem. 15 (2013) 2636-2654.

[1.8] R.M. Navarro, M.A. Pena, J.L.G. Fierro, *Hydrogen production reactions from carbon feedstocks: Fossils fuels and biomass*, Chem. Rev. 107 (2007) 3952-3991.

[1.9] R. Kothari, D. Buddhi, R.L. Sawhney, *Comparison of environmental and economic aspects of various hydrogen production methods*, Renew. Sust. Energ. Rev. 12 (2008) 553-563.

[1.10] E. Cetinkaya, I. Dincer, G.F. Naterer, *Life cycle assessment of various hydrogen production methods*, Int. J. Hydrogen Energ. 37 (2012) 2071-2080.

[1.11] A. Corma, P. Serna, H. Garcia, *Gold catalysts open a new general chemoselective route to synthesize oximes by hydrogenation of α, β-unsaturated nitrocompounds with H_2*, J. Am. Chem. Soc. 129 (2007) 6358-6359.

[1.12] M. Pan, A.J. Brush, Z.D. Pozun, H.C. Ham, W.Y. Yu, G. Henkelman, G.S. Hwang, C.B. Mullins, *Model studies of heterogeneous catalytic hydrogenation reactions with gold*, Chem. Soc. Rev. 42 (2013) 5002-5013.

[1.13] A. Corma, P. Serna, *Chemoselective hydrogenation of nitro compounds with supported gold catalysts*, Science 313 (2006) 332-334.

[1.14] C. Kartusch, J.A. van Bokhoven, *Hydrogenation over gold catalysts: The interaction of gold with hydrogen*, Gold Bull. 42 (2009) 343-347.

[1.15] G.C. Bond, *Chemisorption and reactions of small molecules on small gold particles*, Molecules 17 (2012) 1716-1743.

[1.16] M. Manzoli, A. Chiorino, F. Vindigni, F. Boccuzzi, *Hydrogen interaction with gold nanoparticles and clusters supported on different oxides: A FTIR study*, Catal. Today 181 (2012) 62-67.

[1.17] D.M. Alonso, J.Q. Bond, J.A. Dumesic, *Catalytic conversion of biomass to biofuels*, Green Chem. 12 (2010) 1493-1513.

[1.18] B. Gabrielle, L. Bamiere, N. Caldes, S. De-Cara, G. Decocq, F. Ferchaud, C. Loyce, E. Pelzer, Y. Perez, J. Wohlfahrt, G. Richard, *Paving the way for sustainable bioenergy in Europe: Technological options and research avenues for large-scale biomass feedstock supply*, Renew. Sust. Energ. Rev. 33 (2014) 11-25.

[1.19] R.A. Sheldon, J.P.M. Sanders, *Toward concise metrics for the production of chemicals from renewable biomass*, Catal. Today 239 (2015) 3-6.

[1.20] E.S. Kim, S. Liu, M.M. Abu-Omar, N.S. Mosier, *Selective conversion of biomass hemicellulose to furfural using maleic acid with microwave heating*, Energ. Fuel 26 (2012) 1298-1304.

[1.21] J. Akhtar, A. Idris, R.A. Aziz, *Recent advances in production of succinic acid from lignocellulosic biomass*, Appl. Microbiol. Biotechol. 98 (2014) 987-1000.

[1.22] J.-P. Lange, E. van der Heide, J. van Buijtenen, R. Price, *Furfural: A promising platform for lignocellulosic biofuels*, ChemSusChem 5 (2012) 150-166.

[1.23] I. Bechthold, K. Bretz, S. Kabasci, R. Kopitzky, A. Springer, *Succinic acid: A new platform chemical for biobased polymers from renewable resources*, Chem. Eng. Technol. 31 (2008) 647-654.

Chapter 2

Enhanced Production of Benzyl Alcohol in Benzaldehyde Hydrogenation over Au/Al_2O_3

This chapter investigates catalyst (Au/Al_2O_3) preparation (deposition-precipitation *vs*. impregnation) in modifying Au properties and catalytic action in the continuous gas phase hydrogenation of benzaldehyde. The effect of reactant carrier (ethanol *vs*. water) on enhancing the selective hydrogenation rate is also considered.

2.1 Introduction

Benzyl alcohol finds wide utilisation as a solvent for inks, paints and lacquers and as precursor to a variety of esters in the production of cosmetics and flavors [2.1]. Industrial benzyl alcohol production involves hydrolysis of benzyl chloride (using NaOH) or toluene oxidation [2.2,2.3]. The hydrolysis route suffers severe drawbacks in terms of chlorine release and significant by-product (benzyl ether and NaCl) formation, which necessitates downstream separation/purification. The latter exhibits a sustainability gap with respect to the quantities of solvent used and the inclusion of toxic bromides to enhance the alcohol yield [2.3]. The selective hydrogenation of benzaldehyde, as an alternative, has been promoted using Rh and Ru complexes where alcohols (methanol, ethanol, glycerol and methoxy ethanol) and organic acids (formic acid) have served as hydrogen donors [2.4,2.5]. Product separation and catalyst reuse impact on efficiency but this can be circumvented by a switch to heterogeneous catalysis. The use of solid catalysts has focused on liquid phase reaction using transition metals (Ni, Ru, Pt and Pd) on a range of supports (monolith, Al_2O_3, activated carbon and SiO_2) [2.6-2.9]; pertinent conversion/selectivity and associated reaction conditions are compiled in **Table 2.1**. Okamoto. *et al* [2.9] achieved full selectivity to benzyl alcohol at a conversion up to 84% over polyethylene glycol (PEG) modified Pd/SiO_2. Zhao and co-workers [2.10] recorded near complete benzaldehyde conversion (> 97%) and 100% selectivity to the alcohol over Pt/C at 323 K and elevated H_2 pressure (4 MPa). Gas phase continuous operation has employed a series of metal oxides (ZnO, Fe_2O_3, Al_2O_3, ZrO_2, CeO_2 and TiO_2) [2.11] and oxide supported Pt, Cu and Ni catalysts [2.12-2.14]. Supported Pt showed superior performance with 100% selectivity to benzyl

alcohol at a partial conversion (80%) over Pt/TiO_2 (**Table 2.1**), which was attributed to –C=O activation at the metal-support interface that enhanced reactivity [2.12]. Reaction over Cu generated a product distribution that was dependent on the support and reaction temperature where Cu/SiO_2 delivered selectivities up to 83% (at 373 K) but there was no detectable benzyl alcohol formation over Cu supported on Al_2O_3, TiO_2, CeO_2 or ZrO_2, regardless of temperature [2.13]. Exclusive gas phase carbonyl group reduction at high conversions remains a challenge as hydrogenolysis and phenyl ring reduction predominate to generate benzene, toluene and methylcyclohexane [2.14].

Table 2.1: Catalytic results (conversion (*X*) and selectivity (*S*)) with associated reaction temperatures and pressures reported in the literature for benzaldehyde hydrogenation.

Catalyst	Phase	*T* (K)	P_{H_2} (MPa)	*X* (%)	*S* (%)	Ref.
PEG-Pd/SiO_2	liquid	453	3	84	100	[2.9]
Pt/C	liquid	323	4	98	100	[2.10]
Pt/TiO_2	gas	453	0.1	80	100	[2.12]
Cu/SiO_2	gas	373	0.1	68	83	[2.13]
Au/Al_2O_3	gas	393	0.1	15	100	[2.17]

Oxide supported gold has exhibited enhanced chemoselectivity in the hydrogenation of aldehydes and ketones relative to standard transition metal catalysts [2.15,2.16]. This is offset somewhat by the lower reaction rates due to the lesser capacity of Au for H_2 activation [2.16]. We previously reported complete selectivity to benzyl alcohol in the hydrogenation of benzaldehyde over Au/Al_2O_3 (prepared by impregnation) under reaction conditions where Al_2O_3 supported Ni and Pd were non-selective, generating toluene as principal product [2.17]. However, exclusive production of benzyl alcohol over Au/Al_2O_3 was obtained at low reaction rates (feed conversion ≤ 15%). As an extension to that work, we have evaluated the catalytic action of Au/Al_2O_3 prepared by deposition-precipitation to generate smaller Au size and have established enhanced performance relative to the impregnated system. The existing studies on benzaldehyde hydrogenation use toxic dedecane [2.9] and supercritical CO_2 [2.10] as solvent. We demonstrate for the first time the use of water as an environmentally benign aldehyde carrier to elevate catalytic productivity in continuous gas phase operation (at 1 am). We have also assessed the catalytic performance of Au/TiO_2 and Au/ZrO_2 to validate the promotional effect of water.

2.2 Experimental

2.2.1 Catalyst Preparation and Activation

The γ-Al_2O_3 (Puralox, Condea Vista) and TiO_2 (P25, Degussa) supports were used as received. The ZrO_2 carrier was synthesised by precipitation of $ZrOCl_2$ (0.1 M) with aqueous NH_3 (2.5 M) under vigorous stirring (600 rpm) at pH 9.4-11.8. The resultant hydrogel was washed thoroughly with deionised water and dried at 373 K for 24 h with subsequent calcination (1 K min^{-1}) in flowing air (60 cm^3 min^{-1}) at 673 K for 5 h. Alumina supported Au prepared by impregnation (denoted as Au/Al_2O_3-IMP) has been described in detail previously [2.17]. Catalyst synthesis by deposition-precipitation (Au/Al_2O_3-DP, Au/ZrO_2 and Au/TiO_2) employed urea as basification agent. An aqueous solution of urea (100 fold excess) and $HAuCl_4$ (5×10^{-3} M) was added to the support, the suspension was heated to 353 K (2 K min^{-1}) under vigorous stirring and maintained at this temperature for 3 h. The pH progressively increased to *ca.* 7 as a result of thermal decomposition of urea. The resultant solid was separated by filtration, washed with distilled water until chlorine free and dried in He (45 cm^3 min^{-1}) at 373 K (2 K min^{-1}) for 5 h. The catalyst precursors were sieved (ATM fine test sieves) into a batch of 75 μm average diameter and activated at 2 K min^{-1} to 473-603 K in 60 cm^3 min^{-1} H_2.

2.2.2 Catalyst Characterisation

The Au content was determined by atomic absorption spectroscopy using a Shimadzu AA-6650 spectrometer with an air-acetylene flame from the diluted extract in aqua regia (25% v/v HNO_3/HCl). Temperature programmed reduction (TPR) and H_2 chemisorption measurements were recorded on the commercial CHEM-BET 3000 (Quantachrome) unit with data acquisition/manipulation using the TPR Win™ software. Samples were loaded into a U-shaped Pyrex glass cell (100 mm × 3.76 mm i.d.) and heated in 17 cm^3 min^{-1} (Brooks mass flow controlled) 5% v/v H_2/N_2 to 473-603 K at 2 K min^{-1}. The effluent gas passed through a liquid N_2 trap and H_2 consumption was monitored by thermal conductivity detector (TCD). The activated samples were swept with 65 cm^3 min^{-1} N_2 for 1.5 h, cooled to reaction temperature (413 K) and subjected to H_2 chemisorption by pulse (10 μl) titration. In blank tests, there was no measurable H_2 uptake on the supports alone. Nitrogen adsorption-desorption isotherms were obtained using the commercial Micromeritics Gemini 2390 system with sample outgassing at 423 K for 1 h prior to analysis; specific surface area was determined using the standard BET method. Cumulative pore volumes were obtained by BJH analysis from the desorption

isotherms. Powder X-ray diffractograms (XRD) were recorded on a Bruker/Siemens D500 incident X-ray diffractometer using Cu Kα radiation. Samples were scanned at 0.02º per step over the range 20º ≤ 2θ ≤ 80º and the diffractograms identified using JCPDS-ICDD reference standards, *i.e.* Au (Card No. 04-0784) and γ-Al_2O_3 (Card No. 10-0425). Gold particle size and morphology were determined by transmission (TEM, JEOL JEM 2011) and scanning transmission (STEM, JEOL 2200FS) electron microscopy, employing Gatan Digital Micrograph 1.82 for data acquisition/ manipulation. Samples for analysis were prepared by dispersion in acetone and deposited on a holey carbon/Cu grid (300 Mesh). Surface area weighted mean Au size (*d*) was obtained from a count of at least 300 particles according to

$$d = \frac{\sum_i n_i d_i^3}{\sum_i n_i d_i^2} \qquad \textbf{(2.1)}$$

where n_i is the number of particles of diameter d_i.

2.2.3 Catalytic Procedure

Catalyst testing was carried out at atmospheric pressure and 393-423 K, *in situ* after activation in a continuous flow fixed-bed tubular reactor (i.d. = 15 mm). A layer of borosilicate glass beads served as preheating zone, ensuring that the benzaldehyde reactant was vaporised and reached reaction temperature before contacting the catalyst. Isothermal conditions (± 1 K) were maintained by diluting the catalyst with ground glass (75 μm); the ground glass was mixed thoroughly with catalyst before insertion into the reactor. Reaction temperature was continuously monitored by a thermocouple inserted in a thermowell within the catalyst bed. The benzaldehyde reactant was delivered as ethanolic or aqueous solutions to the reactor *via* a glass/teflon air-tight syringe and teflon line using a microprocessor controlled infusion pump (Model 100 kd Scientific) at a fixed calibrated flow rate. A co-current flow of benzaldehyde and H_2 was maintained at $GHSV = 2 \times 10^4$ h^{-1} with an inlet benzaldehyde flow (F) of 4.8×10^{-5} mol h^{-1}. The molar Au to benzaldehyde feed rate (n/F) spanned the range 1.2×10^{-2} - 9×10^{-2} h. In a series of blank tests, passage of benzaldehyde in a stream of H_2 through the empty reactor or over the supports alone did not result in any detectable conversion. The reactor effluent was condensed in a liquid nitrogen trap for subsequent analysis using a Perkin-Elmer Auto System XL gas chromatograph equipped with a programmed split/splitless injector and a flame ionisation detector (FID), employing a DB-1 (50 m × 0.33 mm i.d., 0.20 μm

film thickness) capillary column (J&W Scientific). Benzaldehyde (Fluka, ≥98%), benzyl alcohol (Riedel-de Haën, ≥99%) and ethanol (Sigma Aldrich, ≥99%) were used without further purification. Benzaldehyde conversion (X) is defined by

$$X = \frac{[benzaldehyde]_{\text{in}} - [benzaldehyde]_{\text{out}}}{[benzaldehyde]_{\text{in}}} \times 100 \quad \textbf{(2.2)}$$

where the subscripts "in" and "out" refer to the inlet and outlet gas streams, respectively. Selectivity in terms of benzyl alcohol as the target product is given by

$$S = \frac{[benzyl\ alcohol]_{\text{out}}}{[benzaldehyde]_{\text{in}} - [benzaldehyde]_{\text{out}}} \times 100 \quad \textbf{(2.3)}$$

Repeated reaction with different samples from the same batch of catalyst delivered reproducibility that was better than ± 5% with a carbon mass balance ≥ 95%. Turnover frequency (*TOF*, rate per active site) was obtained from

$$TOF\ (\text{h}^{-1}) = \frac{R}{D} \quad \textbf{(2.4)}$$

where D is the metal dispersion (surface metal per total metal atoms) and R (h^{-1}) represents the reactant consumption rate. Metal dispersion was obtained from

$$D = \frac{S_{surface} \times M_{metal}}{A_{metal} \times N_{Avogadro}} = \frac{(6/d \times \rho_{metal}) \times M_{metal}}{A_{metal} \times N_{Avogadro}} \quad \textbf{(2.5)}$$

where d resulted from STEM measurements, $S_{surface}$ is the metal atom surface area, ρ_{metal} metal density, M_{metal} metal atomic mass, A_{metal} metal atom surface area and $N_{Avogadro}$ the Avogadro number. Reactant consumption rate (R) was obtained from

$$R\ (\text{h}^{-1}) = \frac{X_0 \times F}{n} \quad \textbf{(2.6)}$$

where initial fractional conversion (X_0) was extracted from time on-stream measurements.

2.3 Results and Discussion

2.3.1 Catalyst Characteristics

Table 2.2: Physicochemical characteristics of the supported Au catalysts.

Catalyst	Au/Al_2O_3-DP	Au/Al_2O_3-IMP	Au/TiO_2	Au/ZrO_2
Au loading (% w/w)	1.1	1.1	1.2	0.8
Specific surface area ($m^2\ g^{-1}$)	166	161	48	93
Pore volume ($cm^3\ g^{-1}$)	0.36	0.36	0.12	0.13
TPR T_{max} (K)	450	415	364	452
Measured TPR H_2 consumption ($\mu mol\ g^{-1}$)	87	79	126	56
Theoretical[a] TPR H_2 consumption ($\mu mol\ g^{-1}$)	84	80	91	61
H_2 chemisorption ($\mu mol\ g_{Au}^{-1}$) at 413 K	318	45	162	137
Au particle size range (nm)	1-8	1-21	1-9	3-12
d (nm)	4.3	7.9	4.5	7.0

[a] amount required for Au precursor reduction

The textural characteristics (Au loading, specific surface area and pore volume) of the four catalysts considered in this study are given in **Table 2.2**. Temperature programmed reduction (TPR) of Au/Al_2O_3-DP and Au/Al_2O_3-IMP generated the profiles shown in **Fig. 2.1**, characterised by H_2 consumption with temperature related maxima (T_{max}) at 450 K and 415 K, respectively. A single TPR peak over the 434-490 K range has been reported elsewhere for Au/Al_2O_3 and ascribed to the reduction of Au^{3+} species to Au^0 [2.18]. The H_2 consumed during TPR coincided with that required for precursor reduction (theoretical values recorded in **Table 2.2**). The reduction profile for Au/Al_2O_3-IMP spanned a lower temperature range than Au/Al_2O_3-DP, suggesting weaker precursor-support interactions that result in a more facile reduction. Activation of Au/ZrO_2 was accompanied by H_2 consumption with similar T_{max} (452 K) to Au/Al_2O_3-DP and matched the requirement for $Au^{3+} \rightarrow Au^0$ (**Table 2.2**). The T_{max} recorded for Au/TiO_2 (prepared by DP) reduction was lower than that for Au/Al_2O_3-DP. Excess H_2 consumption during the TPR of Au/TiO_2 can be attributed to a partial reduction of the support with oxygen vacancies formation, as reported elsewhere [2.19]. Delannoy *et al.* [2.20] considered the possible role of the carrier to modify reducibility of supported Au^{3+} species and proposed an order of decreasing reducibility (TiO_2 > CeO_2 > Al_2O_3) that is consistent with our results. The higher reduction temperature for Au/Al_2O_3-DP and Au/ZrO_2 relative to Au/TiO_2 can be linked to non-reducibility of the support that generates stronger metal-support interactions [2.21].

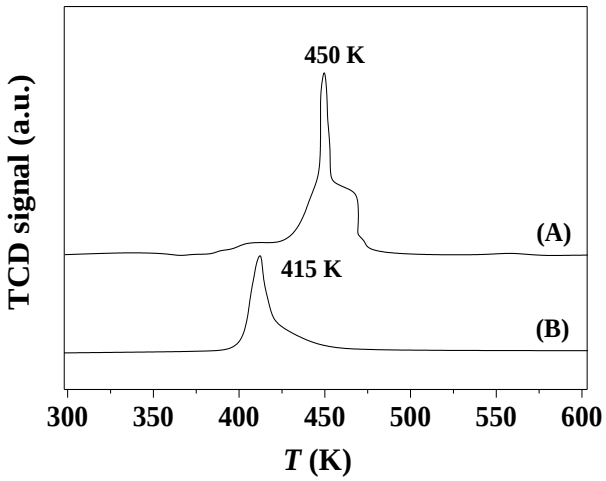

Fig. 2.1: TPR profiles for (A) Au/Al_2O_3-DP and (B) Au/Al_2O_3-IMP.

Catalyst structural analysis by XRD generated the diffractograms presented in **Fig. 2.2**. In the case of Au/Al_2O_3-DP, diffraction peaks at 2θ = 37.6°, 39.5°, 45.9° and 67.0° correspond to (311), (222), (400) and (440) planes of γ-Al_2O_3 (JCPDS-ICDD 10-0425, profile **(C)** in **Fig. 2.2**), respectively. The diffraction peak due to metallic Au is masked by stronger signals due to the support. Au/Al_2O_3-IMP exhibits, in addition to γ-Al_2O_3 signals, peaks at 38.1°, 44.3°, 64.6° and 77.5° that can be assigned to the (111), (200), (220) and (311) planes of Au (JCPDS-ICDD 04-0784, profile **(D)** in **Fig. 2.2**), diagnostic of larger Au particles. This was confirmed by TEM/STEM analysis and representative images are given in **Fig. 2.3** for Au/Al_2O_3-DP **(A)** and Au/Al_2O_3-IMP **(B)**. The Au particles exhibited a quasi-spherical morphology with a narrower distribution of smaller Au particles on Au/Al_2O_3-DP (1-8 nm, mean = 4.3 nm) relative to Au/Al_2O_3-IMP (1-21 nm, mean size = 7.9 nm). This agrees with the literature where

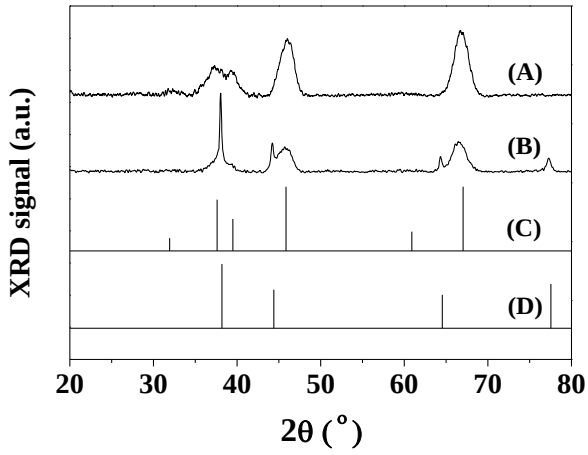

Fig. 2.2: XRD patterns for (A) Au/Al_2O_3-DP, (B) Au/Al_2O_3-IMP and JCPDS-ICDD reference for (C) γ-Al_2O_3 (10-0425) and (D) Au (04-0784).

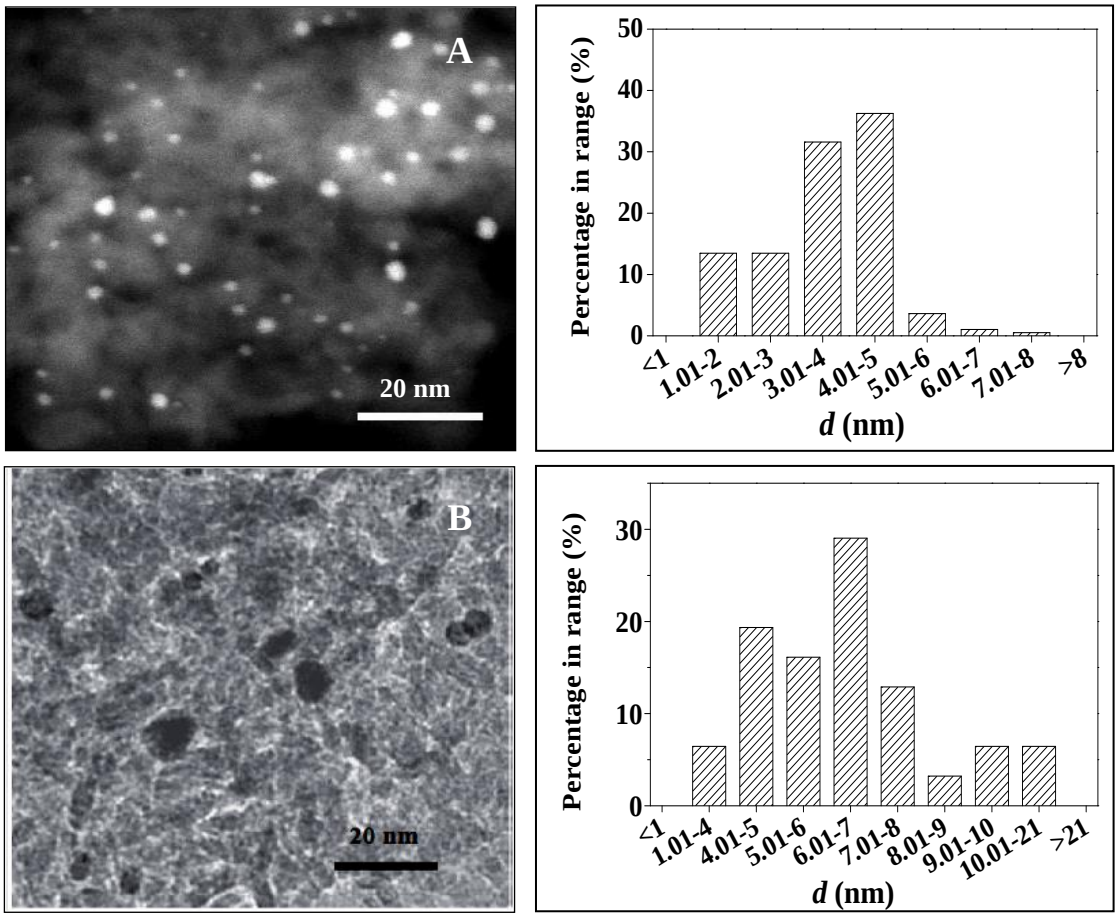

Fig. 2.3: Representative STEM and TEM images for (A) Au/Al_2O_3-DP and (B) Au/Al_2O_3-IMP with associated Au size distribution histograms.

catalyst preparation by DP generates smaller Au particles than IMP synthesis where the weak metal-support interaction associated with IMP preparations results in mobility and agglomeration of Au species during thermal treatment [2.21]. Gold particle size distribution (1-9 nm, mean = 4.5 nm) on TiO_2 was close to that determined for Au/Al_2O_3-DP which can be attributed to surface oxygen vacaies stabilise Au partices; whereas Au/ZrO_2 exhibited larger Au particles (3-12 nm, mean = 7.0 nm) that can be linked to lower surface area relative to Au/Al_2O_3-DP (**Table 2.2**). Hydrogen uptake/activation is a critical catalyst property in hydrogenation applications. We have noted previously [2.17] that H_2 chemisorption on Au/Al_2O_3-IMP at ambient temperature (<1 μmol g^{-1}) was appreciably lower than that reported for oxide supported transition metals, *e.g.* Ni/Al_2O_3 (4 μmol g^{-1}) and Pd/Al_2O_3 (24 μmol g^{-1}). This follows from the lower capacity of supported Au to chemisorb H_2, as reported for a range of Au systems [2.22]. Hydrogen chemisorption on supported Au is an activated process with increased uptake under reaction conditions (45-318 μmol g_{Au}^{-1} at 413 K, **Table 2.2**). Bus *et al.*

[2.23] have shown that H_2 chemisorption is favoured on smaller Au particles (supported on Al_2O_3) that possess a higher fraction of low coordinated Au atoms at corners and edge sites. This agrees with the higher uptake that we have recorded for Au/Al_2O_3-DP relative to Au/Al_2O_3-IMP. We should, however, note that Nakamura *et al.* [2.24] have proposed that $Au^{\delta+}$-$O^{\delta-}$-Ti sites at the Au-TiO_2 interface are active for H_2 dissociation where reactivity showed no apparent correlation with Au site coordination.

2.3.2 Catalyst Activity and Selectivity

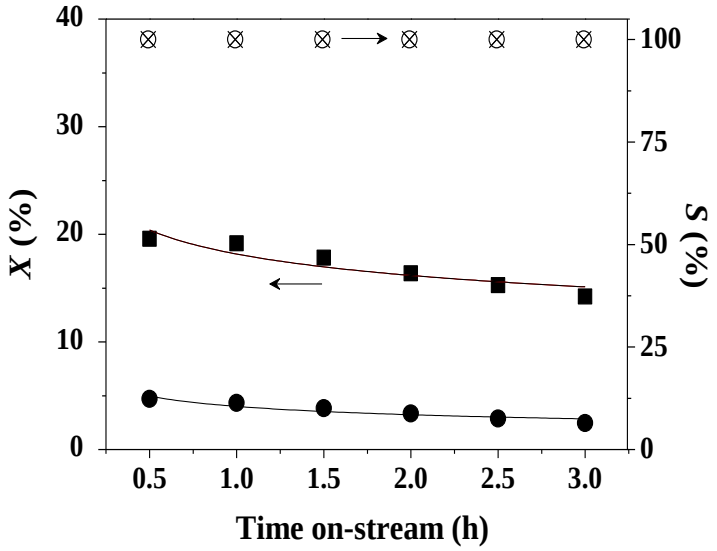

Fig. 2.4: Variation of conversion (*X*) and benzyl alcohol selectivity (*S*) with time on-stream over Au/Al_2O_3-DP (■ and ×) and Au/Al_2O_3-IMP (● and ○): *T* = 413 K; *n*/*F* = 1.2×10^{-2} h.

Time on-stream conversion (X) and benzyl alcohol selectivity (S) over Au/Al_2O_3-DP and Au/Al_2O_3-IMP (under representative common reaction conditions) are presented in **Fig. 2.4**, where a temporal decline in activity was observed. Initial conversion (X_0) can be extracted from fitting the data to the empirical relationship

$$\frac{(X - X_0)}{(X_{3h} - X_0)} = \frac{\Delta t}{(\beta + \Delta t)} \qquad \textbf{(2.7)}$$

where β is a time scale fitting parameter and X_{3h} is the conversion after 3 h on-stream. Initial conversion data were used to determine turnover frequency (*TOF*) where Au/Al_2O_3-DP delivered a significantly higher value (86 h^{-1}) relative to Au/Al_2O_3-IMP (30 h^{-1}). We attribute this to the occurrence of smaller Au particles at the nano-scale on Au/Al_2O_3-DP with a greater preponderance of defect (edge and corner) sites that enhances H_2 uptake/activation (**Table 2.2**) and reaction. We can flag the work of Mohr *et al.* [2.25] who demonstrated structure sensitivity in the hydrogenation of acrolein

over Au/ZrO_2 where *TOF* increased with decreasing particle diameter (from 8 to 4 nm). However, there is insufficient published data to establish any real consensus regarding Au size effects in carbonyl group reduction.

Both Au/Al_2O_3 catalysts generated benzyl alcohol as sole product, *i.e.*, 100% selectivity in promoting –C=O reduction. The influence of reaction temperature on the catalytic response of Au/Al_2O_3-DP with ethanol as carrier can be assessed from the entries in **Table 2.3** where conversion was elevated at higher temperatures (393→423 K)

Table 2.3: Initial conversion (X_0) and selectivity (S_0) for benzaldehyde hydrogenation over Au/Al_2O_3-DP as a function of contact time, reaction temperature and carrier.

T (K)	Carrier	$n/F \times 10^2$ (h)	X_0 (%)	S_0 (%) benzyl alcohol	S_0 (%) toluene
393	ethanol	1.2	19	100	-
413	ethanol	1.2	27	100	-
423	ethanol	1.2	53	92	8
413	water	1.2	58	100	-
413	water	9	100	100	-

with the formation of toluene as by-product (at 423 K). We note that Saadi *et al.* [2.13] have reported preferential production of benzyl alcohol over supported Ni and Cu at low reaction temperature (<373 K) with the occurrence of toluene at temperatures in excess of 383 K. Exclusivity to the alcohol is challenging as illustrated by the reaction pathways shown in **Fig. 2.5**, where toluene formation can occur *via* consecutive hydrogenolysis of benzyl alcohol or direct conversion of benzaldehyde. Benzene results from scission of the aldehydic C–H bond [2.26]; there was no detectable benzene formation in this study. The nature of the solvent can influence activity and selectivity in heterogeneous catalysis, particularly in batch liquid phase reactions. Solvent effects in the hydrogenation of unsaturated aldehydes/ketones are associated with polarity, H_2 solubility and surface interactions [2.27,2.28]. In gas phase applications, the solvent serves as a carrier and possible contributions to catalyst performance have not been studied. Green chemistry principles highlight use of innocuous (or non-toxic) solvents where water utilisation as a cleaner, inexpensive and benign polar carrier is an important sustainability consideration. In this study, use of water as carrier resulted in a dramatic increase in conversion (relative to ethanol), while retaining full selectivity to

benzyl alcohol (**Table 2.3**). Moreover, an increase in the *n*/*F* parameter, which equates to contact time, resulted in the complete conversion of the inlet benzaldehyde feed and 100% selectivity to the alcohol. This represents unprecedented selective hydrogenation efficiency with respect to the existing literature (**Table 2.1**) for both liquid and gas phase operations.

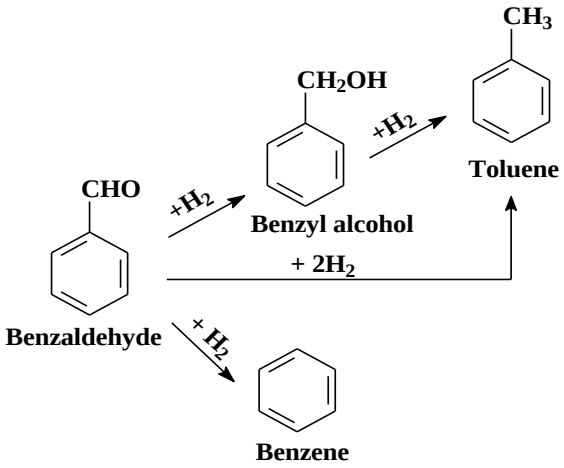

Fig. 2.5: Reaction pathways in the hydrogenation of benzaldehyde.

The beneficial effect of water as carrier in terms of elevated selective hydrogenation rate extended to Au/TiO_2 and Au/ZrO_2, as demonstrated in **Table 2.4**. The promotional role of water on the selective –C=O reduction in the liquid phase hydrogenation of crotonaldehyde over Au/CeO_2 was attributed to a facilitated interaction of the hydrophilic –C=O moiety with surface catalytic sites [2.29]. In gas phase hydrogenation over supported Au the rate is limited by the available surface reactive hydrogen. Any additional hydrogen supply should elevate rate, as demonstrated

Table 2.4: Initial turnover frequency (*TOF*) for benzaldehyde hydrogenation using ethanol and water as carrier; *Reaction conditions*: *T* = 413 K, *n*/*F* = 1.2×10^{-2} h.

Carrier	*TOF* (h^{-1})		
	Au/Al_2O_3-DP	Au/TiO_2	Au/ZrO_2
ethanol	86	52	37
water	188	98	46

in the case of Au/Al_2O_3-DP that delivered higher rate relative to Au/Al_2O_3-IMP as a consequence of greater H_2 uptake. Alcohol chemisorption on metal oxides can proceed

via interaction between the oxygen electron lone pair and a Lewis acid site on the oxide with H abstraction and alcoxide formation that is enhanced with increasing alcohol chain length [2.30]. The ethanol carrier can serve as a source of surface hydrogen but competitive adsorption may also result in rate inhibition due to an occlusion of active sites [2.27]. Possible hydrogen release *via* ethanol dehydrogenation can be discounted given Au inactivity in catalytic dehydrogenation [2.31]. Creation of surface hydrogen (protons) from water dissociation is promoted by Lewis acid sites on Al_2O_3 [2.32] and oxygen vacancies on TiO_2 [2.33]. The abstracted protons can bond with two-coordinate O^{2-} sites on the support to form bridging hydroxyl groups. Buchanan and Web [2.34] have demonstrated that surface hydroxyl groups on Al_2O_3 act as a source of atomic 'hydrogen' where dehydroxylated Au/Al_2O_3 was inactive in butadiene hydrogenation. Moreover, activity of Au/ZrO_2 in the hydrogenation of 1,3-butadiene has been correlated with surface hydroxyl group density where dehydroxylated Au/ZrO_2 was inactive and activity was partially recovered by water treatment [2.35]. We therefore attribute the beneficial effect of water as carrier to a facilitated surface dissociation that generates reactive hydrogen.

2.4 Conclusion

Gas phase hydrogenation of benzaldehyde over Au supported on Al_2O_3, ZrO_2 and TiO_2 was fully selective to benzyl alcohol as the target product. Increased benzaldehyde *TOF* over Au/Al_2O_3-DP can be associated with increased H_2 uptake on well dispersed Au (mean = 4.3 nm) relative to synthesis by impregnation (mean = 7.9 nm), as confirmed by H_2 chemisorption, XRD and TEM/STEM analyses. Use of an aqueous rather than ethanolic benzaldehyde feed delivered appreciably higher chemoselective rates with 100% benzyl alcohol yield. This is attributed to water dissociation on the catalyst, generating surface reactive hydrogen that compensates for the limited capability of Au to dissociate H_2, with an overall increased hydrogenation rate. This promotional effect extends to benzaldehyde conversion over Au/ZrO_2 and Au/TiO_2. Our results represent a significant advancement over reported batch liquid and continuous gas phase catalytic systems for the cleaner (exclusive) sustainable high throughput production of benzyl alcohol.

2.5 References

[2.1] J. Scognamiglio, L. Jones, D. Vitale, C.S. Letizia, A.M. Api, *Fragrance material review on benzyl alcohol*, Food Chem. Toxicol. 50 (2012) S140-S160.

[2.2] G.D. Yadav, P.H. Mehta, *Theoretical and experimental analysis of capsule membrane phase transfer catalysis: Selective alkaline hydrolysis of benzyl chloride to benzyl alcohol*, Catal. Lett. 21 (1993) 391-403.

[2.3] C.C. Guo, Q. Liu, X.T. Wang, H.Y. Hu, *Selective liquid phase oxidation of toluene with air*, Appl. Catal. A: Gen. 282 (2005) 55-59.

[2.4] B.R. Cho, R.M. Laine, *Homogeneous rhodium catalyzed hydrogenation of benzaldehyde: Kinetic evidence in favor of cluster catalysis*, J. Mol. Catal. 15 (1982) 383-389.

[2.5] D. Tavor, O. Sheviev, C. Dlugy, A. Wolfson, *Transfer hydrogenations of benzaldehyde using glycerol as solvent and hydrogen source*, Can. J. Chem. 88 (2010) 305-308.

[2.6] X.D. Xu, H. Vonk, A. vande Riet, A. Cybulski, A. Stankiewicz, J.A. Moulijn, *Monolithic catalysts for selective hydrogenation of benzaldehyde*, Catal. Today 30 (1996) 91-97.

[2.7] M. Arai, A. Obata, Y. Nishiyama, *The influence of reduction methods and conditions on the activity of alumina-supported platinum catalysts for the liquid phase hydrogenation of benzaldehyde in ethanol*, J. Catal. 166 (1997) 115-117.

[2.8] M. Baidossi, A.V. Joshi, S. Mukhopadhyay, Y. Sasson, *Pd/C-catalyzed transfer-hydrogenation of benzaldehydes to benzyl alcohols using potassium formate as the selective hydrogen donor*, Synthetic. Commun. 34 (2004) 643-650.

[2.9] M. Okamoto, T. Hirao, T. Yamaai, *Polymers as novel modifiers for supported metal catalyst in hydrogenation of benzaldehydes*, J. Catal. 276 (2010) 423-428.

[2.10] F.Y. Zhao, S. Fujita, S. Akihara, M. Arai, *Hydrogenation of benzaldehyde and cinnamaldehyde in compressed CO_2 medium with a Pt/C catalyst: A study on molecular interactions and pressure effects*, J. Phys. Chem. A 109 (2005) 4419-4424.

[2.11] D. Haffad, U. Kameswari, M.M. Bettahar, A. Chambellan, J.C. Lavalley, *Reduction of benzaldehyde on metal oxides*, J. Catal. 172 (1997) 85-92.

[2.12] M.A. Vannice, D. Poondi, *The effect of metal-support interactions on the hydrogenation of benzaldehyde and benzyl alcohol*, J. Catal. 169 (1997) 166-175.

[2.13] A. Saadi, Z. Rassoul, M.M. Bettahar, *Gas phase hydrogenation of benzaldehyde over supported copper catalysts*, J. Mol. Catal. A: Chem. 164 (2000) 205-216.

[2.14] A. Saadi, R. Merabiti, Z. Rassoul, M.M. Bettahar, *Benzaldehyde hydrogenation over supported nickel catalysts*, J. Mol. Catal. A: Chem. 253 (2006) 79-85.

[2.15] P. Claus, *Heterogeneously catalysed hydrogenation using gold catalysts*, Appl. Catal. A: Gen. 291 (2005) 222-229.

[2.16] L. McEwan, M. Julius, S. Roberts, J.C.Q. Fletcher, *A review of the use of gold catalysts in selective hydrogenation reactions*, Gold Bull. 43 (2010) 298-306.

[2.17] N. Perret, F. Cárdenas-Lizana, M.A. Keane, *Selective hydrogenation of benzaldehyde to benzyl alcohol over Au/Al_2O_3*, Catal. Commun. 16 (2011) 159-164.

[2.18] F. Cárdenas-Lizana, S. Gómez-Quero, M.A. Keane, *Gas phase hydrogenation of m-dinitrobenzene over alumina supported Au and Au-Ni alloy*, Catal. Lett. 127 (2009) 25-32.

[2.19] X.D. Jiang, Y.P. Zhang, J. Jiang, Y.S. Rong, Y.C. Wang, Y.C. Wu, C.X. Pan, *Characterization of oxygen vacancy associates within hydrogenated TiO_2: A positron annihilation study*, J. Phys. Chem. C 116 (2012) 22619-22624.

[2.20] L. Delannoy, N. Weiher, N. Tsapatsaris, A.M. Beesley, L. Nchari, S.L.M. Schroeder, C. Louis, *Reducibility of supported gold (III) precursors: Influence of the metal oxide support and consequences for CO oxidation activity*, Top. Catal. 44 (2007) 263-273.

[2.21] G.C. Bond, D.T. Thompson, *Catalysis by gold*, Catal. Rev. 41 (1999) 319-388.

[2.22] G.C. Bond, C. Louis, D.T. Thompson, *Catalysis by gold*, Imperial College Press, London, 2006.

[2.23] E. Bus, J.T. Miller, J.A. van Bokhoven, *Hydrogen chemisorption on Al_2O_3-supported gold catalysts*, J. Phys. Chem. B 109 (2005) 14581-14587.

[2.24] I. Nakamura, H. Mantoku, T. Furukawa, T. Fujitani, *Active sites for hydrogen dissociation over TiO_x/Au(111) surfaces*, J. Phys. Chem. C 115 (2011) 16074-16080.

[2.25] C. Mohr, H. Hofmeister, P. Claus, *The influence of real structure of gold catalysts in the partial hydrogenation of acrolein*, J. Catal. 213 (2003) 86-94.

[2.26] M.A. Keane, *Gas phase hydrogenation/hydrogenolysis of benzaldehyde and o-tolualdehyde over Ni/SiO_2*, J. Mol. Catal. A: Chem. 118 (1997) 261-269.

[2.27] U.K. Singh, M.A. Vannice, *Kinetics of liquid-phase hydrogenation reactions over supported metal catalysts: A review*, Appl. Catal. A: Gen. 213 (2001) 1-24.

[2.28] N.M. Bertero, A.F. Trasarti, C.R. Apesteguia, A.J. Marchi, *Solvent effect in the liquid-phase hydrogenation of acetophenone over Ni/SiO_2: A comprehensive study of the phenomenon*, Appl. Catal. A: Gen. 394 (2011) 228-238.

[2.29] M.-M. Wang, L. He, Y.-M. Liu, Y. Cao, H.-Y. He, K.-N. Fan, *Gold supported on mesostructured ceria as an efficient catalyst for the chemoselective hydrogenation of carbonyl compounds in neat water*, Green Chemistry 13 (2011) 602-607.

[2.30] S. Gómez-Quero, F. Cárdenas-Lizana, M.A. Keane, *Unique selectivity in the hydrodechlorination of 2,4-dichlorophenol over hematite-supported Au*, J. Catal. 303 (2013) 41-49.

[2.31] Y. Guan, E.J.M. Hensen, *Ethanol dehydrogenation by gold catalysts: The effect of the gold particle size and the presence of oxygen*, Appl. Catal. A: Gen. 361 (2009) 49-56.

[2.32] K.C. Hass, W.F. Schneider, A. Curioni, W. Andreoni, *The chemistry of water on alumina surfaces: Reaction dynamics from first principles*, Science 282 (1998) 265-268.

[2.33] J. Oviedo, R. Sanchez-de-Armas, M.A. San-Miguel, J.F. Sanz, *Methanol and water dissociation on TiO_2 (110): The role of surface oxygen*, J. Phys. Chem. C 112 (2008) 17737-17740.

[2.34] D.A. Buchanan, G. Webb, *Catalysts by Group IB Metals: 1. Reaction of buta-1,3-diene with hydrogen and with deuterium catalyzed by alumina supported gold*, J. Chem. Soc.-Faraday Trans. 71 (1975) 134-144.

[2.35] X. Zhang, H. Shi, B.-Q. Xu, *Vital roles of hydroxyl groups and gold oxidation states in Au/ZrO_2 catalysts for 1,3-butadiene hydrogenation*, J. Catal. 279 (2011) 75-87.

Chapter 3

Role of Support Redox Character on Catalytic Performance in Gas Phase Hydrogenation of Benzaldehyde and Nitrobenzene over Supported Gold Catalyst

The previous chapter has established selective hydrogenation of benzaldehyde to benzyl alcohol with enhanced reaction rate using water as carrier over (Al_2O_3, TiO_2 and ZrO_2) supported Au catalysts. In this chapter the role of support redox property in determining the catalytic response for the hydrogenation of benzaldehyde and nitrobenzene are examined.

3.1 Introduction

The work of Haruta *et al.* [3.1] demonstrating CO oxidation activity for supported Au *nano*-particles at *sub*-ambient temperatures is widely credited for the current interest in gold catalysis. Research is now focused on factors that control activity/selectivity in terms of new Au catalyst formulations (*e.g.* Au clusters and bimetallic) [3.2-3.4], extending the range of applications beyond oxidation (of hydrocarbons [3.5-3.7], alcohols [3.8,3.9] and amines [3.10,3.11]) and into hydrogenation [3.12]. Selective hydrogenation of benzaldehyde to benzyl alcohol and nitrobenzene to aniline are important in the production of herbicides, dyes, pigments and fine chemicals [3.13, 3.14]. Conventional processes, drawing on batch liquid phase, suffer low product yields, energy inefficiency and waste production [3.15]. Supported Au at the nano-scale (<10 nm) exhibits unique selectivity in the hydrogenation of multi-functional reactants, although activity is significantly lower than conventional transition metals (Pt, Ru, Pd and Ni) [3.16] due to the limited capacity to chemisorb/activate H_2 [3.17]. Catalytic performance of supported Au in hydrogenation of carbonyl (acrolein, benzalacetone, cinnamaldehyde and crotonaldehyde) [3.18] and nitro (chloronitrobenzene, nitrostyrene and nitrobenzaldehyde) [3.19] compounds has shown a dependence on Au particle size, electronic and geometric properties, which are influenced by the support. Oxides are used as Au carriers, where support reducibility and acidity-basicity can influence catalytic action. Taking crotonaldehyde hydrogenation, Okumura *et al*. [3.20] found that

Au on a reducible oxide (TiO_2) delivered enhanced selectivity to the alcohol relative to Au/Al_2O_3 and Au/SiO_2 but the authors did not identify the source of the distinct selectivity. Milone and co-workers [3.21] proposed that a reduced support (iron oxides) favours –C=O reduction due to the generation of electron-rich Au species *via* metal-support electron transfer. Rojas *et al.* [3.22] concluded negatively charged Au species (on non-reducible SiO_2) bind the electrophilic carbon in –C=O, facilitating hydrogenation of cinnamaldehyde and benzalacetone. In nitro reduction, the high selectivity exhibited by Au/TiO_2 in the reduction of the $–NO_2$ group has been attributed to metal-support synergy that serves to enhance $–NO_2$ activation [3.23]. Shimizu *et al.* [3.24] considered the role of Al_2O_3 acidity/basicity in tandem with coordinatively unsaturated Au to dissociate H_2 to H^+/H^- at the metal/support interface and selectively reduce $–NO_2$ in the presence of other reactive functionalities. In the hydrogenation of *p*-chloronitrobenzene unwanted hydrodechlorination was reported for $Au/Ce_{0.62}Zr_{0.38}O_2$ and ascribed to C–Cl scission at vacancy sites [3.25]. Although Au catalysts have now been widely applied in selective hydrogenation, the role of support in modifying Au structure, reactant activation and surface reaction mechanism is far from being resolved.

In previous work, we demonstrated higher specific benzaldehyde hydrogenation rate over Au/Al_2O_3 bearing smaller Au nano-particles (mean size from 8 to 4 nm) with exclusivity to benzyl alcohol [3.26]. There is, however, no real consensus regarding the effect of Au size on –C=O hydrogenation rate. Turnover frequency (*TOF*) in the hydrogenation of acrolein has been found to decrease with increasing metal size for Au diameters > 4 nm on ZrO_2 [3.27] but also to increase with increasing size (1-5 nm) for Au/ZrO_2 and Au/TiO_2 [3.28]. In this study, we compare the catalytic action of Au nanoparticles on oxides (γ-Al_2O_3, ZrO_2, TiO_2, CeO_2, α-Fe_2O_3 and Fe_3O_4) with distinct redox character in the hydrogenation of –C=O (benzaldehyde) and $–NO_2$ (nitrobenzene) and correlate performance with catalyst structural properties. We propose surface reaction mechanisms to account for the role of support reducibility in governing –C=O and $–NO_2$ activation and product selectivity.

3.2 Experimental

3.2.1 Catalyst Preparation

The supports employed in this study were obtained from commercial sources (γ-Al_2O_3 (Puralox, Condea Vista), TiO_2 (P25, Degussa) and CeO_2 (Grace Davison)) or

synthesised (α-Fe_2O_3, Fe_3O_4 and ZrO_2) as described elsewhere [3.29,3.30]. The supported Au catalysts were prepared by deposition-precipitation using urea as basification agent. An aqueous solution of urea (100-fold excess) and $HAuCl_4$ ($3\text{-}7 \times 10^{-3}$ M, 400 cm^3) was added to the support (10-30 g). The suspension was stirred and heated (2 K min^{-1}) to 353 K, where the pH progressively increased (to 6.5-8.0) as a result of urea decomposition:

$$NH_2\text{-}CO\text{-}NH_2 + 3H_2O \xrightarrow{T=353K} 2NH_4^+ + 2OH^- + CO_2 \qquad \textbf{(3.1)}$$

The solid obtained was separated by filtration, washed with distilled water until Cl free (based on the $AgNO_3$ test) and dried (2 K min^{-1}) in 45 cm^3 min^{-1} He at 373 K for 5 h. The catalyst precursors were sieved (ATM fine test sieves) to a mean particle diameter = 75 μm and activated at 2 K min^{-1} to 423-673 K in 60 cm^3 min^{-1} H_2. The catalysts were cooled to ambient temperature and passivated in 1% v/v O_2/He for off-line characterisation.

3.2.2 Catalyst Characterisation

The Au content was measured by atomic absorption spectroscopy (Shimadzu AA-6650 spectrometer with an air-acetylene flame) from the diluted extract in aqua regia (25% v/v HNO_3/HCl). The pH associated with the point of zero charge (pH_{pzc}) of the support was determined using the potentiometric mass titration technique. Three masses (25, 50 and 75 mg) of sample were immersed in 0.1 M NaCl (50 cm^3) to which a known volume of NaOH (0.1 M) was added to adjust initial pH to 11. Titration was performed under continuous agitation in a He atmosphere with HCl (0.1 M) as titrant with on-line pH measurement (Pico Technology Ltd.). Temperature programmed reduction (TPR), H_2 temperature programmed desorption (TPD), H_2/O_2 chemisorption and specific surface area (SSA) measurements were conducted using the CHEM-BET 3000 (Quantachrome Instrument) unit; data acquisition/manipulation employed the TPR Win™ software. Samples were loaded into a U-shaped Pyrex quartz cell (3.76 mm i.d.) and heated in 17 cm^3 min^{-1} (Brooks mass flow controlled) 5% v/v H_2/N_2 at 2 K min^{-1} to 423-673 K. The effluent gas passed through a liquid N_2 trap and H_2 consumption was monitored by a thermal conductivity detector (TCD). The activated samples were swept with 65 cm^3 min^{-1} N_2 for 1.5 h, cooled to ambient (or reaction (413 K)) temperature and subjected to H_2 (10 μl) chemisorption by pulse titration with subsequent TPD at 50 K min^{-1} to 873-1173 K. In blank tests, there was no measurable H_2 uptake on the supports alone. Oxygen pulse (50 μl) titration at 413 K post-TPR was employed to determine the

extent of support reduction, where a contribution from Au to the total O_2 adsorption is negligible [3.31]. SSA (reproducible to ±8%) was recorded in 30% v/v N_2/He using N_2 as internal standard. At least three cycles of N_2 adsorption-desorption were employed using the standard single point BET method. Pore volume measurement was conducted using the Micromeritics Gemini VII 2390p system. Prior to analysis, samples were outgassed at 423 K for 1 h in N_2. Total pore volume was obtained at a relative N_2 pressure of P/P_0 = 0.95. X-ray diffractograms (XRD) were recorded on a Bruker/Siemens D500 incident X-ray diffractometer using Cu Kα radiation. Samples were scanned at 0.02º step^{-1} over the range 20º ≤ 2θ ≤ 80º and the diffractograms identified against the JCPDS-ICDD reference standards, *i.e.* Au (04-0784), γ-Al_2O_3 (10-0425), anatase-TiO_2 (A-TiO_2, 21-1272), rutile-TiO_2 (R-TiO_2, 21-1276), monoclinic-ZrO_2 (M-ZrO_2, 37-1784), tetragonal-ZrO_2 (T-ZrO_2, 50-1089), CeO_2 (43-1002), α-Fe_2O_3 (hematite, 33-0664) and Fe_3O_4 (magnetite, 19-0629). X-ray photoelectron spectroscopic (XPS) analysis was performed on a VG ESCA spectrometer equipped with monochromatised Al Kα radiation (1486 eV). Sample was adhered to conducting carbon tape, mounted in the sample holder and subjected to ultra-high vacuum conditions (<10^{-8} Torr). Full range surveys (Au 4$f_{5/2}$ and 4$f_{7/2}$ spectra) were collected where the binding energies (BE) were calibrated with respect to the C 1*s* peak (284.5 eV). The Au 4*f* spectra were fitted with abstraction of the Shirley background using the Gaussian-Lorentzian function in XPSPEAK 41. Gold particle morphology (size and shape) was examined by transmission (TEM, JEOL JEM 2011) and scanning transmission (STEM, JEOL 2200FS field emission gun-equipped unit) electron microscopy, employing Gatan Digital Micrograph 1.82 for data acquisition/ manipulation. Samples for analysis were dispersed in acetone and deposited on a holey carbon/Cu grid (300 Mesh). The surface area weighted mean Au size (d) was based on a count of at least 300 particles according to

$$d = \frac{\sum_i n_i d_i^3}{\sum_i n_i d_i^2} \qquad \textbf{(3.2)}$$

where n_i is the number of particles of diameter d_i.

3.2.3 Catalytic Procedure

Catalyst testing was carried out at atmospheric pressure, *in situ* after activation, in a continuous flow fixed bed tubular reactor (i.d. = 15 mm) at 413-573 K under operating

conditions of negligible heat/mass transport limitations. A layer of borosilicate glass beads served as preheating zone, ensuring the organic reactant was vaporised and reached reaction temperature before contacting the catalyst. Isothermal conditions (±1 K) were maintained by diluting the catalyst bed with ground glass (75 μm). Reaction temperature was continuously monitored by a thermocouple inserted in a thermowell within the catalyst bed. Reactants (benzaldehyde (Fluka, ≥98%), nitrobenzene (Riedel-de Haën, ≥99%) or benzyl alcohol (Riedel-de Haën, ≥99%)) were delivered as an ethanolic (Sigma Aldrich, ≥99%) solution to the reactor *via* a glass/teflon air-tight syringe and teflon line using a microprocessor controlled infusion pump (Model 100 kd Scientific) at a fixed calibrated flow rate. The reaction was conducted in a co-current flow of reactant with H_2 (BOC, >99.98%) at $GHSV = 2 \times 10^4$ h^{-1}. The molar Au to inlet organic molar feed rate (n/F) spanned the range 1.2×10^{-3} - 3.7×10^{-3} h. In blank tests, passage of each reactant in a stream of H_2 through the empty reactor or over the support did not result in any detectable conversion. The reactor effluent was condensed in a liquid nitrogen trap for subsequent analysis using a Perkin-Elmer Auto System XL gas chromatograph equipped with a programmed split/splitless injector and a flame ionization detector (FID), employing a DB-1 (50 m × 0.33 mm i.d., 0.20 μm film thickness) capillary column (J&W Scientific). Data acquisition and manipulation were performed using the TurboChrom Workstation Version 6.3.2 (for Windows) chromatography data system. Reactant (i) conversion (X) is defined by

$$X_{\mathrm{i}} = \frac{[reactant]_{\mathrm{i,\ in}} - [reactant]_{\mathrm{i,\ out}}}{[reactant]_{\mathrm{i,\ in}}} \qquad \textbf{(3.3)}$$

and selectivity (S) to product (j) is given by

$$S_{\mathrm{j}}(\%) = \frac{[product]_{\mathrm{j,\ out}}}{[reactant]_{\mathrm{i,\ in}} - [reactant]_{\mathrm{i,\ out}}} \times 100 \qquad \textbf{(3.4)}$$

where the subscripts "in" and "out" refer to the inlet and outlet gas streams. Catalytic activity is also quantified in terms of initial conversion obtained from the time on-stream measurements [3.26] and turnover frequency (*TOF*, rate per active site) calculated using Au dispersion obtained from TEM/STEM analysis [3.26]. Repeated reactions with different samples from the same batch of catalyst delivered raw data reproducibility and mass balances within ±5 %.

3.3 Results and Discussion

3.3.1 Catalyst Characterisation

3.3.1.1 *Structural Characteristics and Temperature Programmed Reduction (TPR)*

Catalyst characteristics are presented in **Table 3.1**. Total surface areas range from 11 $m^2\ g^{-1}$ (Au/Fe_3O_4) to 166 $m^2\ g^{-1}$ ($Au/\gamma\text{-}Al_2O_3$) with a corresponding increase in pore volume (0.02-0.36 $cm^3\ g^{-1}$). The values obtained for each catalyst fall within the range reported in the literature for comparable systems [3.32-3.35]. The TPR profiles of the supported Au catalyst precursors and the corresponding supports are given in **Fig. 3.1**. TPR of $Au/\gamma\text{-}Al_2O_3$ **(AI)** and Au/ZrO_2 **(CI)** generated positive signals with associated temperature maxima (T_{max}) at 451 and 476 K, where H_2 consumption matched the requirement for Au^{3+} reduction to Au^0 (**Table 3.1**). The profiles generated for $\gamma\text{-}Al_2O_3$ and ZrO_2 over the same temperature range were featureless with no evidence of H_2 uptake or release, as noted elsewhere [3.33]. Activation of Au/TiO_2 **(BI)** and Au/CeO_2 **(DI)** presented H_2 consumption peaks at lower temperatures, *i.e.* T_{max} = 364 and 420 K, respectively. This is consistent with the work of Delannoy *et al.* [3.36] who examined

Table 3.1: Gold loading, specific surface area (SSA), pore volume, Au particle size from TEM/STEM analysis (*d*), H_2 consumption during temperature programmed reduction (TPR) and requirements for reduction of the Au precursor, H_2 released during temperature programmed desorption (TPD), O_2 chemisorption, support point of zero charge (pH_{pzc}), Au $4f_{7/2}$ binding energy (BE) and standard redox potential (E_{redox}) of support.

Catalyst	$Au/\gamma\text{-}Al_2O_3$	Au/TiO_2	Au/ZrO_2	Au/CeO_2	$Au/\alpha\text{-}Fe_2O_3$	Au/Fe_3O_4
Au loading (% w/w)	1.1	1.3	1.0	3.0	1.2	0.9
SSA ($m^2\ g^{-1}$)	166	44	93	108	57	11
Pore volume ($cm^3\ g^{-1}$)	0.36	0.12	0.13	0.15	0.16	0.02
d (nm)	4.3	4.5	7.0	2.0	2.6	7.6
TPR H_2 consumption ($\mu mol\ g^{-1}$)	87[a]/84[b]	126[a]/91[b]	56[a]/61[b]	553[a]/231[b]	750[a]/93[b]	500[a]/90[b]
H_2 desorbed ($mmol\ g_{Au}^{-1}$)	51	9	28	6	4	<1
O_2 uptake ($\mu mol\ g^{-1}$)	1	5	3	132	168	58
pH_{pzc}	7.1	6.7	7.4	6.8	8.1	5.8
Au $4f_{7/2}$ BE (eV)	83.3	83.5	83.6	84.7	84.2	84.1
E_{redox} (V)	-1.7	-0.6	-1.5	1.6	0.8	0.1

[a]value obtained from TPR analysis
[b]calculated value for $Au^{3+} \rightarrow Au^0$

the effect of support redox character on Au reducibility and reported more facile reduction on TiO_2 and CeO_2 relative to Al_2O_3. Hydrogen consumed during TPR of Au/TiO_2 exceeded the amount required for the $Au^{3+} \rightarrow Au^0$ (**Table 3.1**) and can be attributed to a combined Au reduction with Ti^{4+} conversion to Ti^{3+} at the metal/support

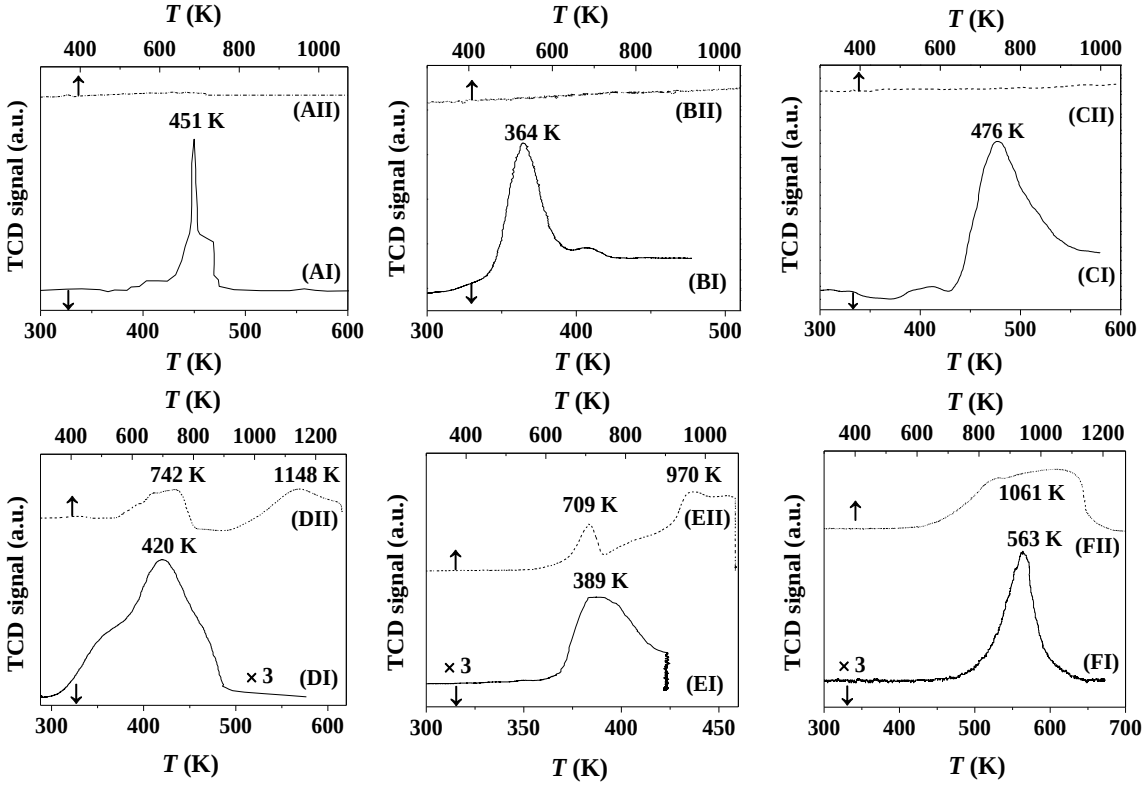

Fig. 3.1: Temperature programmed reduction (TPR) profiles for (I) supported Au samples (solid lines) and (II) the corresponding supports (dotted lines): (A) γ-Al_2O_3, (B) TiO_2, (C) ZrO_2, (D) CeO_2, (E) α-Fe_2O_3 and (F) Fe_3O_4.

interface [3.37]. The bare TiO_2 support did not exhibit a detectable TPR response **(BII)**. In contrast, the same treatment of CeO_2 generated two broad signals at 742 K and 1148 K **(DII)** that can be ascribed to surface (523-848 K [3.38]) and bulk (>1073 K [3.38]) reduction. Hydrogen consumed during the activation of Au/CeO_2 far exceeded the requirements for Au precursor reduction (**Table 3.1**) but was significantly lower than that needed for full reduction of the CeO_2 carrier (3300 μmol g^{-1}), suggesting partial support reduction where the incorporation of Au on CeO_2 lowered the requisite temperature [3.39]. TPR of Au/Fe_2O_3 **(EI)** resulted in H_2 consumption at T_{max} = 389 K that exceeded Au^{3+} reduction but was less than the requirement for reduction of Fe_2O_3 to Fe_3O_4 (2100 μmol g^{-1}). The TPR profile of α-Fe_2O_3 **(EII)** is characterised by a positive signal at 709 K with a broader consumption at T >800 K, suggesting a two-stage reduction of hematite, *i.e.* α-$Fe_2O_3 \rightarrow Fe_3O_4 \rightarrow$ Fe. The TPR response for

Au/Fe_3O_4 **(FI)** reveals a shift in T_{max} relative to the support **(FII)**. The excess H_2 consumed (**Table 3.1**) fell below that for conversion of Fe_3O_4 to Fe (17000 μmol g^{-1}), indicating partial support reduction. Our results demonstrate that Au incorporation facilitates reduction of ceria and iron oxide supports. Jacobs *et al.* [3.40] have established partial CeO_2 reduction by spillover hydrogen generated by dissociative adsorption (373 K) on supported Au (0.1-5% w/w) that spills onto support. Furthermore, Scire and co-workers [3.41] proposed that Au can weaken the Fe-O bond in iron oxide substrates (413 K) resulting in greater lattice oxygen mobility and enhanced reducibility.

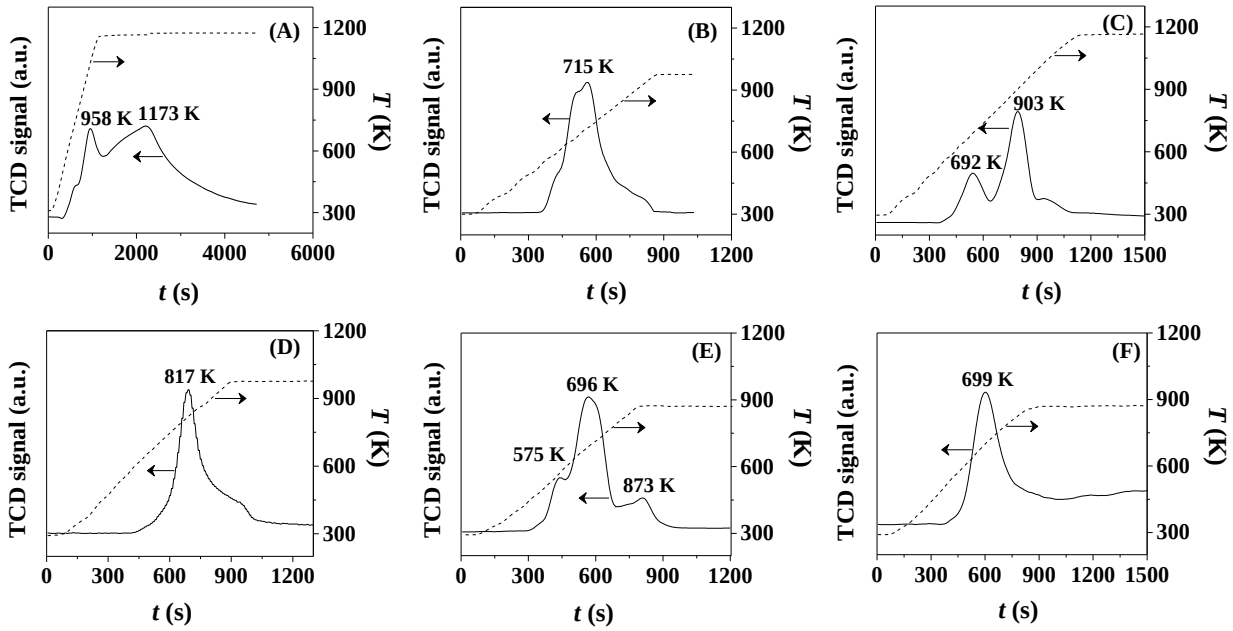

Fig. 3.2: Hydrogen temperature programmed desorption (TPD) profiles: (A) Au/γ-Al_2O_3, (B) Au/TiO_2, (C) Au/ZrO_2, (D) Au/CeO_2, (E) Au/α-Fe_2O_3, (F) Au/Fe_3O_4.

3.3.1.2 *H_2 Temperature Programmed Desorption (TPD) and O_2 Chemisorption*

We have applied temperature programmed desorption as a measure of surface hydrogen that can allow a differentiation between chemisorbed and spillover species where both can serve as reactive hydrogen for hydrogenation. The TPD profiles generated for all the catalysts are shown in **Fig. 3.2**. The available literature suggests a lower temperature requirement for H_2 desorption from metal sites (<473 K) compared to release of the spillover (>503 K) [3.42]. A predominant H_2 desorption at T >575 K was observed for all the catalysts in this work, suggesting the main contribution is due to spillover. Hydrogen desorption (up to 51 mmol g_{Au}^{-1}, **Table 3.1**) was at least two orders of magnitude greater than that measured (<60 μmol g_{Au}^{-1}) in pulse chemisorption, suggesting that the surface hydrogen was generated during TPR. As a

general observation, H_2 release from Au supported on non-reducible supports (28-51 mmol g_{Au}^{-1}) was significantly greater than that recorded for Au on reducible carriers (≤9 mmol g_{Au}^{-1}). The greater H_2 desorption from Au/Al_2O_3 relative to Au/ZrO_2 can be attributed (at least in part) to the higher SSA of Al_2O_3 which can accommodate more spillover. Moreover, surface oxygen groups (terminal hydroxyls) and Lewis acid sites on Al_2O_3 are known to facilitate spillover hydrogen [3.30]. There is compelling evidence in the literature for hydrogen spillover onto Al_2O_3 from supported metals (Ru, Pt, Pd and Ni) [3.42-3.45]. The extent of spillover is influenced by such factors as concentration of initiating and acceptor sites, catalyst activation and metal-support interaction(s) [3.42]. Consumption of spillover hydrogen in partial reduction of titania, ceria and iron oxide can account for the observed lower levels of H_2 desorption.

We employed O_2 chemisorption post-TPR as a measure of support reduction [3.31]. Gold on CeO_2, α-Fe_2O_3 and Fe_3O_4 exhibited greater O_2 uptake (**Table 3.1**) than that measured for Au on TiO_2, γ-Al_2O_3 and ZrO_2. The difference in O_2 adsorption can be correlated with support redox capacity, where the former group shows higher redox potentials (E_{redox}) (**Table 3.1**). Increasing O_2 chemisorption coincided with a greater excess H_2 consumption during TPR due to partial support reduction with the formation of oxygen vacancies. Oxygen deficient sites can be generated by the loss of lattice oxygen from reducible metal oxides during thermal treatment in H_2 or CO [3.46]. Boccuzzi *et al.* [3.47,3.48], using FTIR spectroscopy, demonstrated H_2 dissociation on Au supported on Fe_2O_3, TiO_2 and CeO_2 with spillover that resulted in surface reduction and the occurrence of oxygen vacancies. Formation of Ce^{3+} defects and surface oxygen vacancies in Au/CeO_2-Fe_2O_3 has also been linked to the action of reactive spillover hydrogen [3.49].

3.3.1.3 *X-ray Diffraction (XRD) and Electron Microscopy Analysis*

Structural analysis by XRD generated the diffractograms presented in **Fig. 3.3**. A weak signal due to metallic Au was observed at $2\theta = 38.1 \pm 0.1°$ for Au/ZrO_2 and Au/Fe_3O_4 (see inset). This diffraction peak is masked by stronger signals due to the support for Au/γ-Al_2O_3 and Au/TiO_2. There was no detectable signal due to Au associated in Au/CeO_2 and Au/Fe_2O_3 suggesting formation of Au particles at the nano-scale below detection limit (<5 nm) [3.50]. The XRD pattern of Au/γ-Al_2O_3 is characterised by peaks at 2θ = 37.6°, 39.5°, 45.9° and 67.0° due to γ-Al_2O_3. XRD analysis of Au/TiO_2 revealed a mixture of tetragonal anatase (2θ = 25.3°, 37.8°, 48.1°

and 62.8°) and tetragonal rutile (2θ = 27.4°, 36.1°, 41.2°, 54.3°, 56.6°, 69.0° and 69.8°) phases, where the anatase : rutile ratio (5:1) matches the reported Degussa P25 composition [3.51]. Au/ZrO_2 shows a mixed monoclinic (2θ = 28.2°, 31.5°, 34.2°, 34.4°, 35.3°, 40.8°, 49.3°, 50.2°, 50.6° and 55.6°) and tetragonal (2θ = 30.3°, 35.3°, 50.4°, 50.7°, 59.6° and 60.2°) phase with monoclinic/tetragonal ≈ 2. Zirconia phase composition is sensitive to synthesis route and calcination temperature with ratios in the range (1.2-3.2) reported for comparable ZrO_2 preparation and pre-treatment [3.33]. The XRD patterns of Au on CeO_2, α-Fe_2O_3 and Fe_3O_4 (**Fig. 3.3(D-F)**) matched those of the supports and we can discount bulk reduction, *i.e.* $CeO_2 \rightarrow Ce_2O_3$, $Fe_2O_3 \rightarrow Fe_3O_4$ and/or $Fe_3O_4 \rightarrow FeO$.

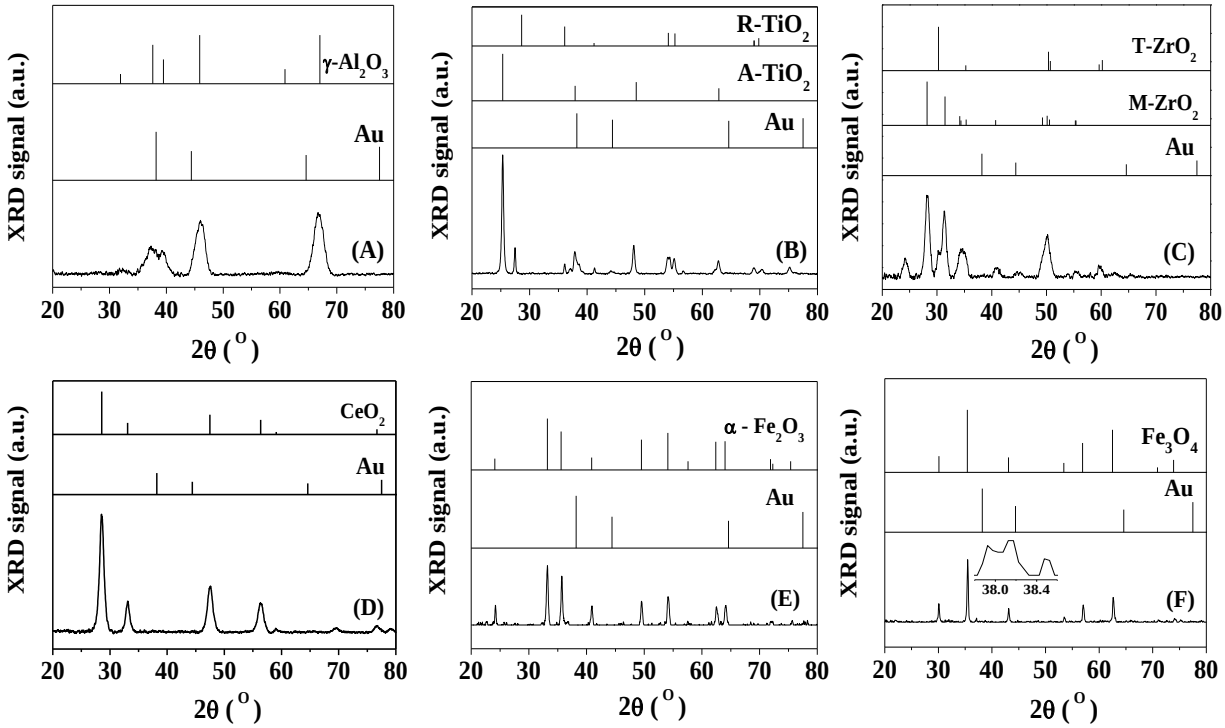

Fig. 3.3: XRD patterns for activated/passivated (A) Au/γ-Al_2O_3, (B) Au/TiO_2, (C) Au/ZrO_2, (D) Au/CeO_2, (E) Au/α-Fe_2O_3 and (F) Au/Fe_3O_4; reference JCPDS-ICDD patterns (see card No in section 2.2) are included for Au, γ-Al_2O_3, rutile (R-TiO_2), anatase (A-TiO_2), tetragonal ZrO_2 (T-ZrO_2), monoclinic ZrO_2 (M-ZrO_2), α-Fe_2O_3 (hematite), Fe_3O_4 (magnetite).

Gold particle morphology was probed by TEM/STEM and the representative images in **Fig. 3.4** reveal quasi-spherical particles at the nano-scale. Surface area weighted mean Au size was obtained from the size distribution histograms and are recorded in **Table 3.1**. Gold on γ-Al_2O_3 and TiO_2 exhibits similar mean size (4.3-4.5 nm) with size distributions in 1-8 and 1-9 nm, respectively. Appreciably larger Au particles (3-12 nm, mean = 7.0 nm) are observed on ZrO_2, consistent with that reported

by Mohr *et al*. [3.27] for the preparation of Au/ZrO_2 by deposition-precipitation. The CeO_2 and Fe_2O_3 redox supports show much narrower Au size distributions (≤5 nm) and smaller mean diameters (2.0-2.6 nm). A wider Au size range was measured for Au/Fe_3O_4 with a mean = 7.6 nm but the majority of Au particles are <10 nm, which has

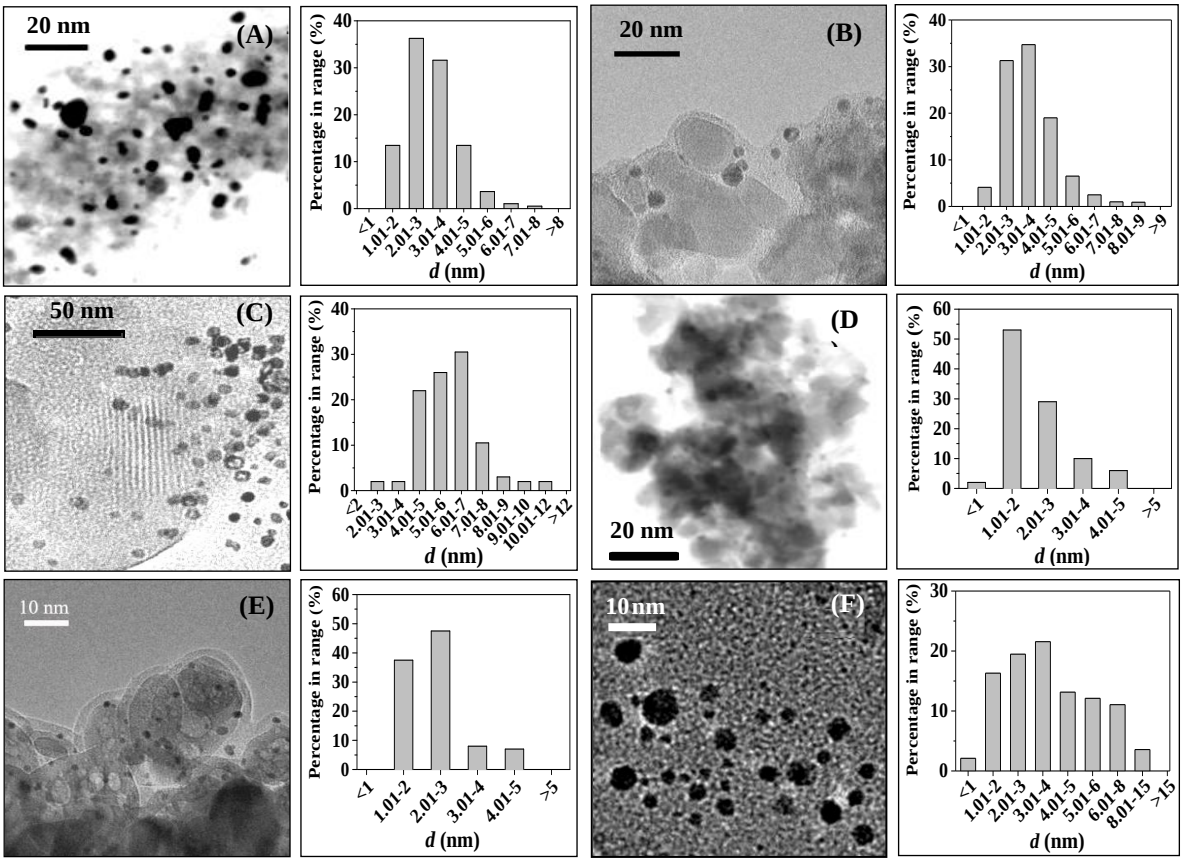

Fig. 3.4: Representative TEM/STEM images for (A) Au/γ-Al_2O_3, (B) Au/TiO_2, (C) Au/ZrO_2, (D) Au/CeO_2, (E) Au/α-Fe_2O_3 and (F) Au/Fe_3O_4 with associated Au size distribution histograms.

been demonstrated critical for hydrogenation activity [3.50]. Support charge density, which is reflected in the pH point of zero charge (pH_{pzc}), determines precursor-support interaction in synthesis by deposition-precipitation and can govern ultimate Au size post-TPR. Where solution pH < pH_{pzc}, the support bears a positive charge favouring interaction with anionic Au species ($AuCl_4^-$ and/or $Au(OH)Cl_3^-$). Conversely, where solution pH > pH_{pzc}, the Au precursor and support experience repulsive effects due to the negative surface charge, resulting in weaker Au-support interaction that can lead to Au agglomeration during activation [3.52]. Solution pH controls $AuCl_4^-$ hydrolysis rate *via* substitution of Cl^- by OH^- where $Au(OH)_4^-$ predominates at the final pH (6.5-8.0) [3.53]. Support pH_{pzc} values are given in **Table 3.1** where the appreciably lower value for Fe_3O_4 (5.8) does not favour interaction with (anionic) Au precursor species and can

account for the lower Au loading and larger particle size **(Table 3.1)**. Support oxygen vacancies stabilise transition metal nanoparticles and inhibit sintering [3.54], which may result in the formation of smaller Au particles on α-Fe_2O_3 and CeO_2.

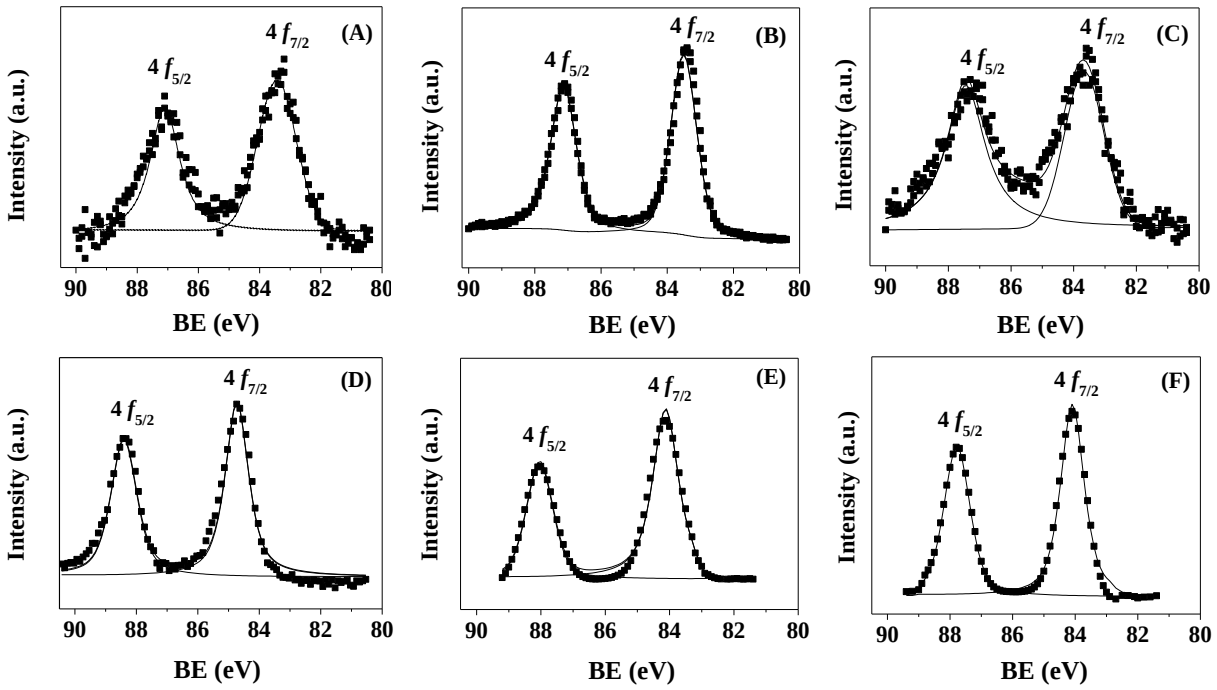

Fig. 3.5: XPS profiles for (A) Au/γ-Al_2O_3, (B) Au/TiO_2, (C) Au/ZrO_2, (D) Au/CeO_2, (E) Au/α-Fe_2O_3 and (F) Au/Fe_3O_4; experimental data are given by ■ where lines represent the fits with peak deconvolution.

3.3.1.4 *X-ray Photoelectron Spectroscopy (XPS) Analysis*

XPS measurements were conducted to probe support effects in modifying Au electronic character. The XPS profiles over the Au 4*f* binding energy (BE) region are presented in **Fig. 3.5**. The signals with BE in the 83.7-84.0 eV and 87.8-88.2 eV ranges can be attributed to Au $4f_{7/2}$ and $4f_{5/2}$ levels, respectively [3.55]. The Au $4f_{7/2}$ BE for Au/γ-Al_2O_3 (83.3 eV), Au/TiO_2 (83.5 eV) and Au/ZrO_2 (83.6 eV) agrees with values reported for Au/Al_2O_3 (83.1 eV) [3.56] and Au/TiO_2 (83.0 eV) [3.57] but fall below the reference metallic Au (84.0 eV) [3.56], suggesting electron donation from the support [3.58]. Gold on reducible CeO_2, α-Fe_2O_3 and Fe_3O_4 ($E_{redox} > 0$, **Table 3.1**) exhibits measurably higher Au $4f_{7/2}$ BE consistent with values published for Au/CeO_2 (84.5 eV) [3.59], Au/Fe_2O_3 (84.4 eV) [3.60] and Au/$Ce_{0.62}Zr_{0.38}O_2$ (84.5 eV) [3.25] but lower than Au^+ (85.8-86.0 eV) [3.55]. This response suggests a partial positive charge ($Au^{\delta+}$) for Au/CeO_2 where electron transfer ($Au^0 + Ce^{4+} \rightarrow Au^+ + Ce^{3+}$) [3.61] modifies Au electronic structure. The data presented in **Fig. 3.6** suggests a direct dependence of Au

$4f_{7/2}$ BE on support redox potential, where electron transfer from Au is facilitated by carriers with higher potential. This is the first reported correlation of Au $4f_{7/2}$ BE shift to support redox properties. Gold electronic structure is also dependent on Au cluster size where the BE shift is more pronounced with decreasing coordination number [3.62]. The occurrence of small particles on Au/CeO_2 and Au/Fe_2O_3 can also contribute to a BE shift to higher values.

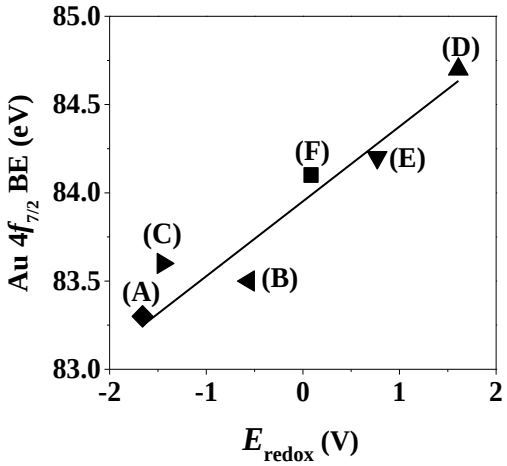

Fig. 3.6: Dependence of Au $4f_{7/2}$ binding energy (BE) on the standard redox potential (E_{redox}) of the oxide supports: (A) ◆ $Au/\gamma\text{-}Al_2O_3$, (B) ◄ Au/TiO_2, (C) ► Au/ZrO_2, (D) ▲ Au/CeO_2, (E) ▼ $Au/\alpha\text{-}Fe_2O_3$, (F) ■ Au/Fe_3O_4.

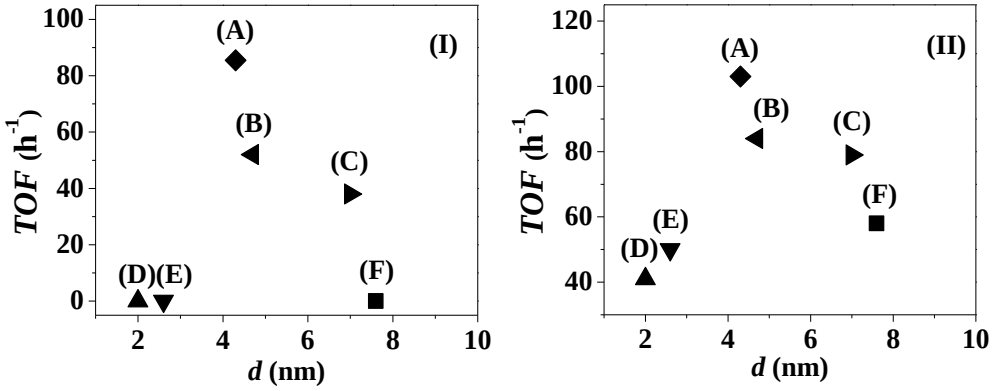

Fig. 3.7: (I) Benzaldehyde (T = 413 K, $n/F = 1.2 \times 10^{-3}$ h) and (II) nitrobenzene (T = 413 K, $n/F = 3.7 \times 10^{-3}$ h) turnover frequency (TOF) as a function of Au particle size (d): (A) ◆ $Au/\gamma\text{-}Al_2O_3$, (B) ◄ Au/TiO_2, (C) ► Au/ZrO_2, (D) ▲ Au/CeO_2, (E) ▼ $Au/\alpha\text{-}Fe_2O_3$, (F) ■ Au/Fe_3O_4.

3.3.2 Catalytic Activity/Selectivity

Benzyl alcohol was the sole product detected in the hydrogenation of benzaldehyde, demonstrating exclusive reduction of the carbonyl function with no hydrogenolytic reaction or phenyl ring reduction [3.63]. In contrast, benzaldehyde conversion over Cu

and Ni (on SiO_2, Al_2O_3, TiO_2, CeO_2 and ZrO_2) has resulted in –C=O hydrogenolysis (to toluene) and/or C–C scission (to benzene) in continuous gas phase operation under similar reaction conditions (373-623 K) [3.63,3.64]. The relationship between Au particle size (*d*) and benzaldehyde turnover frequency (*TOF*) is shown in **Fig. 3.7(I)** for reaction at 413 K. An increase in *TOF* is evident with decreasing Au particle size over the 4-8 nm range which can be linked to increased H_2 uptake at under reaction conditions (<1→ 318 μmol g_{Au}^{-1}). The highest specific rate was recorded for Au/γ-Al_2O_3 with no detectable activity for catalysts bearing the smallest Au sizes (Au/α-Fe_2O_3 and Au/CeO_2). It has been established that Au exhibits a metal to insulator transition for particles ≤2 nm and decreasing hydrogenation activity over smaller Au particles (5→1 nm) has been ascribed to a critical loss of metallic character [3.28]. Although there is insufficient published data to arrive at any reliable trends regarding Au size effects in –C=O hydrogenation, we can note the reported decrease in acrolein *TOF* over Au/ZrO_2 for Au diameters >4 nm [3.27] and increase with increasing Au size (1-5 nm) over Au/ZrO_2 and Au/TiO_2 [3.28]. In contrast to the benzaldehyde reaction, each catalyst was active in nitrobenzene hydrogenation (**Fig. 3.7(II)**) with a *TOF* maximum at *ca.* 4 nm (Au/γ-Al_2O_3). The greater reactivity of the nitro-reactant agrees with the results of Arai *et al*. [3.65] where a six-fold higher rate was recorded for nitrobenzene hydrogenation (over Pt/Al_2O_3) relative to benzaldehyde which can be linked to reaction thermodynamics where nitrobenzene to aniline ($\Delta G_{413\,K}$ = -436 ± 1 kJ mol^{-1}) is more thermodynamically favourable than benzaldehyde hydrogenation to benzyl alcohol ($\Delta G_{413\,K}$ = -24 ± 2 kJ mol^{-1}).

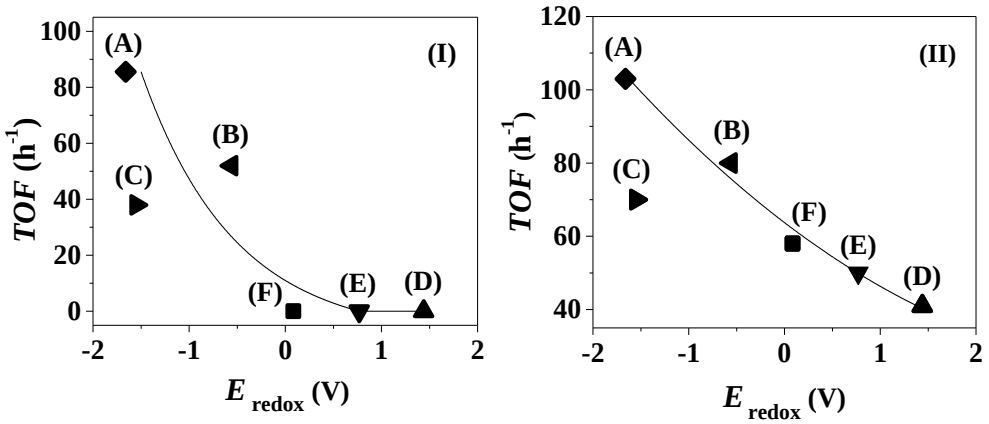

Fig. 3.8: Dependence of turnover frequency (*TOF*) on the standard redox potential of the oxide supports in (I) benzaldehyde and (II) nitrobenzene hydrogenation; (A) ◆ Au/γ-Al_2O_3, (B) ◄ Au/TiO_2, (C) ► Au/ZrO_2, (D) ▲ Au/CeO_2, (E) ▼ Au/α-Fe_2O_3, (F) ■ Au/Fe_3O_4.

The possible role of support reducibility was probed where *TOF* increased at lower redox potential (**Fig. 3.8**). Au/ZrO_2 deviates somewhat from the general trend, which we tentatively attribute to the occurrence of larger Au particles (>10 nm, see **Fig. 3.4(C)**) on ZrO_2 that show little activity in hydrogenation. Lower *TOF* at higher redox potential suggests that enhanced support reducibility with associated oxygen vacancy formation does not favour –C=O or $–NO_2$ activation for reaction. Oxygen vacancies can strongly bind adsorbed oxygenated species [3.66]. The higher relative density of oxygen vacancies (see O_2 uptake in **Table 3.1**) on ceria and iron oxides supported Au can suppress –C=O and $–NO_2$ activation/conversion and lower reactivity. In contrast, less oxygen vacancies on γ-Al_2O_3, TiO_2 and ZrO_2 supported Au results in enhanced reactivity and higher *TOF*. Correlation of Au charge (from Au $4f_{7/2}$ BE) with catalytic response suggests that negatively charged ($Au^{\delta-}$) species on Al_2O_3, TiO_2 and ZrO_2 exhibit higher activity. This is consistent with published studies [3.22,3.67] that have shown –C=O activation/reduction to the alcohol is facilitated on negatively charged Au. Lower activity for $Au^{\delta+}$ (on α-Fe_2O_3, Fe_3O_4 and CeO_2) must result from a partial repulsion with –C=O and binding to surface oxygen vacancies that suppresses reactivity.

Table 3.2: Effect of reaction temperature on turnover frequency (*TOF*) and product selectivity ($S_{product}$, %) for the reaction of benzaldehyde over $Au/\gamma\text{-}Al_2O_3$, Au/Fe_3O_4 and Au/CeO_2.

Catalyst	*T* (K)	*TOF* (h^{-1})	$S_{benzene}$ (%)	$S_{toluene}$ (%)	$S_{benzyl\ alcohol}$ (%)
$Au/\gamma\text{-}Al_2O_3$	413	82	0	0	100
	473	126	0	70	30
	573	258	71	21	8
Au/Fe_3O_4	413[a]	-	-	-	-
	473	192	10	90	0
	573	378	21	79	0
Au/CeO_2	413[a]	-	-	-	-
	473	8	0	100	0
	573	49	20	80	0

[a]no detectable activity

Given the negligible benzaldehyde hydrogenation activity exhibited by catalysts bearing smaller (<4 nm) and larger (>7 nm) Au particles at 413 K, we evaluated the effect of reaction temperature on rate and selectivity delivered by Au/CeO_2 and Au/Fe_3O_4, which are compared with $Au/\gamma\text{-}Al_2O_3$ in **Table 3.2**. An increase in *TOF* was

observed at higher temperature. A switch from exclusive –C=O hydrogenation (to benzyl alcohol) at 413 K to hydrogenolysis (to toluene) at 473 K and a predominant aryl-carbonyl C–C hydrogenolysis (to benzene) at 573 K over Au/γ-Al_2O_3 suggest increased temperature (473-573 K) facilitates activation/scission of –C=O and C–C for hydrogenolytic cleavage. Higher temperature (to 498 K) has been shown to favour benzaldehyde hydrogenolysis to toluene and benzene over Cu/Al_2O_3 [3.64] and Ni/SiO_2 [3.68] in gas phase reaction. Benzaldehyde hydrogenation to benzyl alcohol was not observed over Au/Fe_3O_4 and Au/CeO_2 at any reaction temperature (**Table 3.2**). Increased reaction temperature generated toluene as principal product with enhanced selectivity to benzene at 573 K (**Table 3.2**). This response suggests that Au on redox supports exhibits dominant hydrogenolytic character. Reaction of benzyl alcohol as feedstock (at 573 K) generated toluene as principal product and benzaldehyde (with no detectable benzene) over Au/Fe_3O_4 at a similar *TOF* to that recorded for the benzaldehyde reaction (**Table 3.3**). This suggests that production of toluene from benzaldehyde can result from direct hydrogenolysis or consecutive conversion of benzyl alcohol, whereas benzene is generated from aldehyde hydrogenolysis. Au/CeO_2 delivered an appreciably lower benzyl alcohol *TOF* relative to benzaldehyde, suggesting a limited contribution from stepwise conversion of the aldehyde *via* the alcohol. The occurrence of benzaldehyde as product may be attributed to oxidative dehydrogenation, as proposed by Vannice and Poondi for reaction over Pt/TiO_2 [3.69]. This step can involve the catalytic action of surface or lattice oxygens associated with the support and the higher aldehyde selectivity exhibited by Au/CeO_2 (**Table 3.3)** can be due to greater oxygen mobility relative to Fe_3O_4, as inferred from TPR measurements in tandem with O_2 chemisorption.

Table 3.3: Benzyl alcohol turnover frequency (*TOF*) and product selectivity ($S_{product}$, %) for reaction over Au/Fe_3O_4 and Au/CeO_2: *T* = 573 K.

Catalyst	*TOF* (h^{-1})	$S_{benzene}$ (%)	$S_{toluene}$ (%)	$S_{benzaldehyde}$ (%)
Au/Fe_3O_4	364	0	95	5
Au/CeO_2	17	8	17	75

Surface oxygen vacancies have been proposed as active sites in a range of applications from automobile exhaust treatment [3.70], water-gas shift [3.71] to steam reforming of oxygenates [3.72]. There is ample evidence that oxygen vacancies can act

to stimulate a Mars and van Krevelen (MvK) catalytic mechanism with catalyst surface reduction (oxygen depletion) and re-oxidation (oxygen generation) [3.73]. We propose the involvement of oxygen vacancies in catalytic hydrogenation following a reversible MvK reaction mechanism, as illustrated in **Fig. 3.9**. Oxygen vacancies act as strong anchoring sites for the carbonyl group [3.74], inhibiting reactivity (step C, **Fig. 3.9(I)**). The stabilised carbonyl function at oxygen vacancies can be activated at elevated temperature (473 K) with hydrogen scission of the –C=O bond generating toluene *via* hydrogenolysis (step **D** and **E**, **Fig. 3.9(I)**). Higher temperature facilitates C–C activation with hydrogen cleavage to give benzene (step **F**). In contrast, the mode of adsorption on

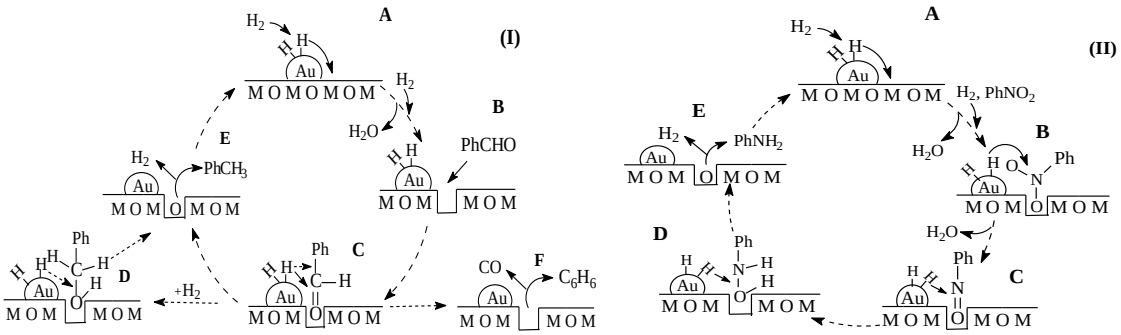

Fig. 3.9: Proposed reaction mechanism for (I) benzaldehyde and (II) nitrobenzene hydrogenation over Au on reducible supports; M = Ce or Fe.

non-reducible surfaces (*e.g.* Al_2O_3) *via* the carbonyl function (step **A** and **B**, **Fig. 3.10**) results in low temperature (413 K) hydrogenation to the alcohol. DFT calculations have shown that the perpendicular adsorption mode is the most stable configuration with –C=O

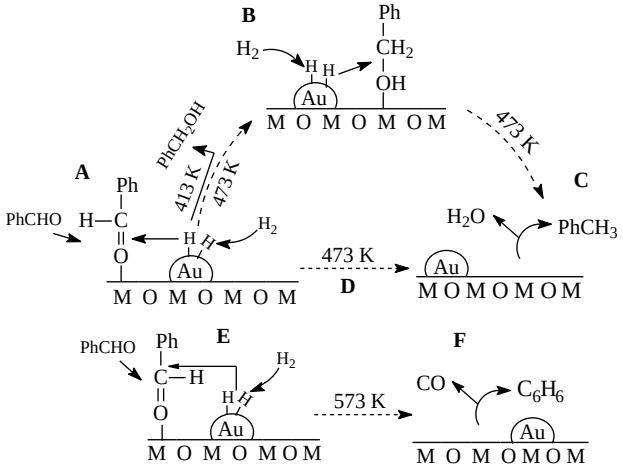

Fig. 3.10: Proposed reaction mechanisms for benzaldehyde hydrogenation over Au/γ-Al_2O_3 (M = Al) at different reaction temperatures.

bonded to the metal oxide surface *via* the O lone pair that acts as Lewis base [3.75]. FTIR analysis has demonstrated that strong surface Lewis acid sites on Al_2O_3 promote –C=O activation in the hydrogenation of nitrobenzaldehyde [3.76]. Activation and scission of –C–OH (step **C**, **Fig. 3.10**), –C=O (step **D**) and aryl-carbonyl C–C (step **E** and **F**) was again promoted at elevated temperature (473-573 K). In the nitrobenzene reaction, nitro group interaction with oxygen vacancies *via* the oxygen lone pair (**Fig. 3.9(II)**) has been proposed [3.77]. Attachment to oxygen vacancies also serves to stabilise the nitro group with resultant lower reaction rates but the higher reactivity of the $–NO_2$ function (relative to –C=O) results in measurable activity for each catalyst at 413 K. Interaction of $–NO_2$ with oxygen vacancy results in N–O bond dissociation to nitrosobenzene (step **C**, **Fig. 9(II)**) with subsequent reduction to a phenylhydroxylamine intermediate (step **D**) and aniline formation (step **E**) [3.73]. As in the case of carbonyl group activation, weak adsorption of $–NO_2$ on a non-reducible surface generated higher rates.

3.4 Conclusion

We have demonstrated that oxide support redox property governs catalytic performance of nano-scale (2-8 nm) supported Au in the reduction of –C=O (benzaldehyde) and $–NO_2$ (nitrobenzene). Temperature programmed reduction (TPR) coupled with oxygen chemisorption has established partial support (TiO_2, CeO_2, α-Fe_2O_3 and Fe_3O_4) reduction due to the action of spillover hydrogen generated by H_2 dissociation on Au. XPS analysis provided evidence of electron interaction between Au and the oxide carriers. Increasing reaction rates were observed with decreasing Au size (from 8 to 4 nm) with measurably lower rates over Au <3 nm. Gold on reducible supports (CeO_2, α-Fe_2O_3 and Fe_3O_4 where $E_{redox} > 0$) exhibited lower benzaldehyde and nitrobenzene *TOF* relative to Au/γ-Al_2O_3, Au/ZrO_2 and Au/TiO_2 ($E_{redox} <0$) which we attribute to inhibition due to the action of surface oxygen vacancies. Moreover, repulsion of –C=O and $–NO_2$ functions at $Au^{\delta+}$ sites served to lower hydrogenation rate. There was no measurable benzaldehyde hydrogenation activity over Au/CeO_2, Au/α-Fe_2O_3 and Au/Fe_3O_4 at 413 K. Reaction at higher temperatures generated toluene as principal product with secondary benzene formation and no detectable alcohol product. In contrast, reaction over Au/γ-Al_2O_3 resulted in exclusive benzyl alcohol formation at 413 K with a progressive shift in hydrogenolysis selectivity (to toluene and benzene) at higher temperatures.

3.5 References

[3.1] M. Haruta, S. Tsubota, T. Kobayashi, H. Kageyama, M.J. Genet, B. Delmon, *Low-temperature oxidation of CO over gold supported on TiO_2, α-Fe_2O_3, and Co_3O_4*. J. Catal. 144 (1993) 175-192.

[3.2] A. Taketoshi, M. Haruta, *Size- and structure-specificity in catalysis by gold clusters*. Chem. Lett. 43 (2014) 380-387.

[3.3] A. Corma, P. Concepción, M. Boronat, M.J. Sabater, J. Navas, M.J. Yacaman, E. Larios, A. Posadas, M.A. Lopez-Quintela, D. Buceta, E. Mendoza, G. Guilera, A. Mayoral, *Exceptional oxidation activity with size-controlled supported gold clusters of low atomicity*. Nature Chem. 5 (2013) 775-781.

[3.4] Z.X. Fan, Y.H. Zhu, X. Huang, Y. Han, Q.X. Wang, Q. Liu, Y. Huang, C.L. Gan, H. Zhang, *Synthesis of ultrathin face-centered-cubic Au@Pt and Au@Pd core-shell nanoplates from hexagonal-close-packed Au square sheets*. Angew. Chem. Int. Edit. 54 (2015) 5672-5676.

[3.5] B.E. Solsona, T. Garcia, C. Jones, S.H. Taylor, A.F. Carley, G.J. Hutchings, *Supported gold catalysts for the total oxidation of alkanes and carbon monoxide*. Appl. Catal. A: Gen. 312 (2006) 67-76.

[3.6] Y. Liu, H. Tsunoyama, T. Akita, S. Xie, T. Tsukuda, *Aerobic oxidation of cyclohexane catalyzed by size-controlled Au clusters on hydroxyapatite: Size effect in the sub- 2 nm regime*. ACS Catal. 1 (2011) 2-6.

[3.7] S. Scire, L.F. Liotta, *Supported gold catalysts for the total oxidation of volatile organic compounds*. Appl. Catal. B: Environ. 125 (2012) 222-246.

[3.8] C.D. Pina, E. Falletta, M. Rossi, *Update on selective oxidation using gold*. Chem. Soc. Rev. 41 (2012) 350-369.

[3.9] V.V. Costa, M. Estrada, Y. Demidova, I. Prosvirin, V. Kriventsov, R.F. Cotta, S. Fuentes, A. Simakov, E.V. Gusevskaya, *Gold nanoparticles supported on magnesium oxide as catalysts for the aerobic oxidation of alcohols under alkali-free conditions*. J. Catal. 292 (2012) 148-156.

[3.10] L. Aschwanden, T. Mallat, M. Maciejewski, F. Krumeich, A. Baiker, *Development of a new generation of gold catalysts for amine oxidation*. ChemCatChem 2 (2010) 666-673.

[3.11] M.T. Schuemperli, C. Hammond, I. Hermans, *Developments in the aerobic oxidation of amines*. ACS Catal. 2 (2012) 1108-1117.

[3.12] M. Pan, J.L. Gong, G.B. Dong, C.B. Mullins, *Model studies with gold: A versatile oxidation and hydrogenation catalyst*. Acc. Chem. Res. 47 (2014) 750-760.

[3.13] D. Divakar, D. Manikandan, G. Kalidoss, T. Sivakumar, *Hydrogenation of benzaldehyde over palladium intercalated bentonite catalysts: Kinetic studies*. Catal. Lett. 125 (2008) 277-282.

[3.14] J. Relvas, R. Andrade, F.G. Freire, F. Lemos, P. Araujo, M.J. Pinho, C.P. Nunes, F.R. Ribeiro, *Liquid Phase hydrogenation of nitrobenzene over an industrial Ni/SiO_2 supported catalyst*. Catal. Today 133 (2008) 828-835.

[3.15] V. van Brunt, J.S. Kanel, *Reactive separation processes*, S. Kulprathipanja (Ed.) Taylor & Francis, London, 2002.

[3.16] T. Mitsudome, K. Kaneda, *Gold nanoparticle catalysts for selective hydrogenations*. Green Chem. 15 (2013) 2636-2654.

[3.17] E. Bus, J.T. Miller, J.A. van Bokhoven, *Hydrogen chemisorption on Al_2O_3-supported gold catalysts*. J. Phys. Chem. B 109 (2005) 14581-14587.

[3.18] P. Claus, *Heterogeneously catalysed hydrogenation using gold catalysts*. Appl. Catal. A: Gen. 291 (2005) 222-229.

[3.19] A. Corma, P. Serna, H. Garcia, *Gold catalysts open a new general chemoselective route to synthesize oximes by hydrogenation of α, β-unsaturated nitrocompounds with H_2*. J. Am. Chem. Soc. 129 (2007) 6358-6359.

[3.20] M. Okumura, T. Akita, M. Haruta, *Hydrogenation of 1,3-butadiene and of crotonaldehyde over highly dispersed Au catalysts*. Catal. Today 74 (2002) 265-269.

[3.21] C. Milone, R. Ingoglia, L. Schipilliti, C. Crisafulli, G. Neri, S. Galvagno, *Selective hydrogenation of α, β-unsaturated ketone to α, β-unsaturated alcohol on gold-supported iron oxide catalysts: Role of the support*. J. Catal. 236 (2005) 80-90.

[3.22] H. Rojas, G. Díaz, J.J. Martínez, C. Castañeda, A. Gómez-Cortés, J. Arenas-Alatorre, *Hydrogenation of α, β-unsaturated carbonyl compounds over Au and Ir supported on SiO_2*. J. Mol. Catal. A: Chem. 363 (2012) 122-128.

[3.23] M. Boronat, P. Concepción, A. Corma, S. González, F. Illas, P. Serna, *A molecular mechanism for the chemoselective hydrogenation of substituted nitroaromatics with nanoparticles of gold on TiO_2 catalysts: A cooperative effect between gold and the support*. J. Am. Chem. Soc. 129 (2007) 16230-16237.

[3.24] K.-I. Shimizu, Y. Miyamoto, T. Kawasaki, T. Tanji, Y. Tai, A. Satsuma, *Chemoselective hydrogenation of nitroaromatics by supported gold catalysts: Mechanistic reasons of size- and support-dependent activity and selectivity*. J. Phys. Chem. C 113 (2009) 17803-17810.

[3.25] X. Wang, N. Perret, J.J. Delgado, G. Blanco, X. Chen, C.M. Olmos, S. Bernal, M.A. Keane, *Reducible support effects in the gas phase hydrogenation of p-chloronitrobenzene over gold*. J. Phys. Chem. C 117 (2013) 994-1005.

[3.26] M. Li, X. Wang, N. Perret, M.A. Keane, *Enhanced production of benzyl alcohol in the gas phase continuous hydrogenation of benzaldehyde over Au/Al_2O_3*. Catal. Commun. 46 (2014) 187-191.

[3.27] C. Mohr, H. Hofmeister, P. Claus, *The influence of real structure of gold catalysts in the partial hydrogenation of acrolein*. J. Catal. 213 (2003) 86-94.

[3.28] P. Claus, A. Bruckner, C. Mohr, H. Hofmeister, *Supported gold nanoparticles from quantum dot to mesoscopic size scale: Effect of electronic and structural properties on catalytic hydrogenation of conjugated functional groups*. J. Am. Chem. Soc. 122 (2000) 11430-11439.

[3.29] F. Cárdenas-Lizana, S. Gómez-Quero, L. Kiwi-Minsker, M.A. Keane, *Gold nano-particles supported on hematite and magnetite as highly selective catalysts for the hydrogenation of nitro-aromatics*. Int. J. Nanotechnol. 9 (2012) 92-112.

[3.30] X. Wang, N. Perret, M.A. Keane, *Gas phase hydrogenation of nitrocyclohexane over supported gold catalysts*. Appl. Catal. A: Gen. 467 (2013) 575-584.

[3.31] G.C. Bond, *Chemisorption and reactions of small molecules on small gold particles*. Molecules 17 (2012) 1716-1743.

[3.32] J. Lenz, B.C. Campo, M. Alvarez, M.A. Volpe, *Liquid phase hydrogenation of α, β-unsaturated aldehydes over gold supported on iron oxides*. J. Catal. 267 (2009) 50-56.

[3.33] X. Zhang, H. Shi, B.-Q. Xu, *Vital roles of hydroxyl groups and gold oxidation states in Au/ZrO_2 catalysts for 1,3-butadiene hydrogenation*. J. Catal. 279 (2011) 75-87.

[3.34] G. Jacobs, T.K. Das, Y.Q. Zhang, J.L. Li, G. Racoillet, B.H. Davis, *Fischer-Tropsch synthesis: Support, loading, and promoter effects on the reducibility of cobalt catalysts*. Appl. Catal. A: Gen. 233 (2002) 263-281.

[3.35] B. Campo, C. Petit, M.A. Volpe, *Hydrogenation of crotonaldehyde on different Au/CeO_2 catalysts*. J. Catal. 254 (2008) 71-78.

[3.36] L. Delannoy, N. Weiher, N. Tsapatsaris, A.M. Beesley, L. Nchari, S.L.M. Schroeder, C. Louis, *Reducibility of supported gold (III) precursors: Influence of the metal oxide support and consequences for CO oxidation activity*. Top. Catal. 44 (2007) 263-273.

[3.37] M. Ousmane, L.F. Liotta, G. Di-Carlo, G. Pantaleo, A.M. Venezia, G. Deganello, L. Retailleau, A. Boreave, A. Giroir-Fendler, *Supported Au catalysts for low-*

temperature abatement of propene and toluene, as model VOCs: Support effect. Appl. Catal. B: Environ. 101 (2011) 629-637.

[3.38] F. Arena, P. Famulari, G. Trunfio, G. Bonura, F. Frusteri, L. Spadaro, *Probing the factors affecting structure and activity of the Au/CeO_2 system in total and preferential oxidation of CO*. Appl. Catal. B: Environ. 66 (2006) 81-91.

[3.39] D. Andreeva, V. Idakiev, T. Tabakova, L. Ilieva, P. Falaras, A. Bourlinos, A. Travlos, *Low-temperature water-gas shift reaction over Au/CeO_2 catalysts*. Catal. Today 72 (2002) 51-57.

[3.40] G. Jacobs, S. Ricote, P.M. Patterson, U.M. Graham, A. Dozier, S. Khalid, E. Rhodus, B.H. Davis, *Low temperature water-gas shift: Examining the efficiency of Au as a promoter for ceria-based catalysts prepared by CVD of a Au precursor*. Appl. Catal. A: Gen. 292 (2005) 229-243.

[3.41] S. Scire, C. Crisafulli, S. Minico, G.G. Condorelli, A. Di-Mauro, *Selective oxidation of CO in H_2-rich stream over gold/iron oxide: An insight on the effect of catalyst pretreatment*. J. Mol. Catal. A: Chem. 284 (2008) 24-32.

[3.42] C. Amorim, M.A. Keane, *Catalytic hydrodechlorination of chloroaromatic gas streams promoted by Pd and Ni: The role of hydrogen spillover*. J. Hazard. Mater. 211 (2012) 208-217.

[3.43] F. Benseradj, F. Sadi, M. Chater, *Hydrogen spillover studies on diluted Rh/Al_2O_3 catalyst*. Appl. Catal. A: Gen. 228 (2002) 135-144.

[3.44] R. Prins, *Hydrogen spillover: Facts and fiction*. Chem. Rev. 112 (2012) 2714-2738.

[3.45] A.G. Boudjahem, S. Monteverdi, M. Mercy, D. Ghanbaja, M.M. Bettahar, *Nickel nanoparticles supported on silica of low surface area: Hydrogen chemisorption and TPD and catalytic properties*. Catal. Lett. 84 (2002) 115-122.

[3.46] M.V. Ganduglia-Pirovano, A. Hofmann, J. Sauer, *Oxygen vacancies in transition metal and rare earth oxides: Current state of understanding and remaining challenges*. Surf. Sci. Rep. 62 (2007) 219-270.

[3.47] F. Boccuzzi, A. Chiorino, M. Manzoli, D. Andreeva, T. Tabakova, *FTIR study of the low-temperature water-gas shift reaction on Au/Fe_2O_3 and Au/TiO_2 catalysts*. J. Catal. 188 (1999) 176-185.

[3.48] T. Tabakova, F. Boccuzzi, M. Manzoli, D. Andreeva, *FTIR study of low-temperature water-gas shift reaction on gold/ceria catalyst*. Appl. Catal. A: Gen. 252 (2003) 385-397.

[3.49] T. Tabakova, G. Avgouropoulos, J. Papavasiliou, M. Manzoli, F. Boccuzzi, K. Tenchev, F. Vindigni, T. Ioannides, *CO-free hydrogen production over Au/CeO_2-Fe_2O_3 catalysts: Part 1. Impact of the support composition on the performance for the preferential CO oxidation reaction*. Appl. Catal. B: Environ. 101 (2011) 256-265.

[3.50] G.C. Bond, C. Louis, D.T. Thompson, *Catalysis by gold*, G.J. Hutchings (Ed.), Imperial College Press, London, 2006.

[3.51] G.L. Haller, D.E. Resasco, *Metal support interaction: Group VIII metals and reducible oxides*. Adv. Catal. 36 (1989) 173-235.

[3.52] N. Perret, X. Wang, L. Delannoy, C. Potvin, C. Louis, M.A. Keane, *Enhanced selective nitroarene hydrogenation over Au supported on β-Mo_2C and β-MO_2C/Al_2O_3*. J. Catal. 286 (2012) 172-183.

[3.53] F. Moreau, G.C. Bond, A.O. Taylor, *Gold on titania catalysts for the oxidation of carbon monoxide: Control of pH during preparation with various gold contents*. J. Catal. 231 (2005) 105-114.

[3.54] L.F. Liotta, G. Pantaleo, F. Puleo, A.M. Venezia, *Au/CeO_2-SBA-15 catalysts for CO oxidation: Effect of ceria loading on physic-chemical properties and catalytic performances*. Catal. Today 187 (2012) 10-19.

[3.55] A.M. Visco, F. Neri, G. Neri, A. Donato, C. Milone, S. Galvagno, *X-ray photoelectron spectroscopy of Au/Fe_2O_3 catalysts*. Phys. Chem. Chem. Phys. 1 (1999) 2869-2873.

[3.56] S. Arrii, F. Morfin, A.J. Renouprez, J.L. Rousset, *Oxidation of CO on gold supported catalysts prepared by laser vaporization: Direct evidence of support contribution*. J. Am. Chem. Soc. 126 (2004) 1199-1205.

[3.57] S. Schimpf, M. Lucas, C. Mohr, U. Rodemerck, A. Bruckner, J. Radnik, H. Hofmeister, P. Claus, *Supported gold nanoparticles: In-depth catalyst characterization and application in hydrogenation and oxidation reactions*. Catal. Today 72 (2002) 63-78.

[3.58] Y.F. Han, Z.Y. Zhong, K. Ramesh, F.X. Chen, L.W. Chen, T. White, Q.L. Tay, S.N. Yaakub, Z. Wang, *Au promotional effects on the synthesis of H_2O_2 directly from H_2 and O_2 on supported Pd-Au alloy catalysts*. J. Phys. Chem. C 111 (2007) 8410-8413.

[3.59] W. Deng, A.I. Frenkel, R. Si, M. Flytzani-Stephanopoulos, *Reaction-relevant gold structures in the low temperature water-gas shift reaction on Au-CeO_2*. J. Phys. Chem. C 112 (2008) 12834-12840.

[3.60] W. Deng, C. Carpenter, N. Yi, M. Flytzani-Stephanopoulos, *Comparison of the activity of Au/CeO_2 and Au/Fe_2O_3 catalysts for the CO oxidation and the water-gas shift reactions*. Top. Catal. 44 (2007) 199-208.

[3.61] A.N. Pestryakov, V.V. Lunin, A.N. Kharlanov, D.I. Kochubey, N. Bogdanchikova, A.Y. Stakheev, *Influence of modifying additives on electronic state of supported gold*. J. Mol. Struct. 642 (2002) 129-136.

[3.62] S. Peters, S. Peredkov, M. Neeb, W. Eberhardt, M. Al-Hada, *Size-dependent XPS spectra of small supported Au-clusters*. Surf. Sci. 608 (2013) 129-134.

[3.63] A. Saadi, R. Merabiti, Z. Rassoul, M.M. Bettahar, *Benzaldehyde hydrogenation over supported nickel catalysts*. J. Mol. Catal. A: Chem. 253 (2006) 79-85.

[3.64] A. Saadi, Z. Rassoul, M.M. Bettahar, *Gas phase hydrogenation of benzaldehyde over supported copper catalysts*. J. Mol. Catal. A: Chem. 164 (2000) 205-216.

[3.65] M. Arai, A. Obata, Y. Nishiyama, *Catalytic features of a low-temperature reduced alumina-supported platinum catalyst: Activity and selectivity in the liquid-phase hydrogenation of benzaldehyde and nitrobenzene*. React. Kinet. Catal. Lett. 61 (1997) 275-280.

[3.66] C.T. Campbell, C.H.F. Peden, *Oxygen vacancies and catalysis on ceria surfaces*. Science 309 (2005) 713-714.

[3.67] C. Milone, C. Crisafulli, R. Ingoglia, L. Schipilliti, S. Galvagno, *A comparative study on the selective hydrogenation of α, β-unsaturated aldehyde and ketone to unsaturated alcohols on Au supported catalysts*. Catal. Today 122 (2007) 341-351.

[3.68] M.A. Keane, *Gas phase hydrogenation/hydrogenolysis of benzaldehyde and o-tolualdehyde over Ni/SiO_2*. J. Mol. Catal. A: Chem. 118 (1997) 261-269.

[3.69] M.A. Vannice, D. Poondi, *The effect of metal-support interactions on the hydrogenation of benzaldehyde and benzyl alcohol*. J. Catal. 169 (1997) 166-175.

[3.70] H. He, H.X. Dai, L.H. Ng, K.W. Wong, C.T. Au, *Pd-, Pt-, and Rh-loaded $Ce_{0.6}Zr_{0.35}Y_{0.05}O_2$ three-way catalysts: An investigation on performance and redox properties*. J. Catal. 206 (2002) 1-13.

[3.71] J.A. Rodriguez, S. Ma, P. Liu, J. Hrbek, J. Evans, M. Pérez, *Activity of CeO_x and TiO_x nanoparticles grown on Au(111) in the water-gas shift reaction*. Science 318 (2007) 1757-1760.

[3.72] T.J. Huang, H.J. Lin, T.C. Yu, *A comparison of oxygen-vacancy effect on activity behaviors of carbon dioxide and steam reforming of methane over supported nickel catalysts*. Catal. Lett. 105 (2005) 239-247.

[3.73] C. Doornkamp, V. Ponec, *The universal character of the Mars and Van Krevelen mechanism*. J. Mol. Catal. A: Chem. 162 (2000) 19-32.

[3.74] A. Sepúlveda-Escribano, E. Coloma, F. Rodríguez-Reinoso, *Promoting effect of ceria on the gas phase hydrogenation of crotonaldehyde over platinum catalysts*. J. Catal. 178 (1998) 649-657.

[3.75] S. Sitthisa, T. Sooknoi, Y. Ma, P.B. Balbuena, D.E. Resasco, *Kinetics and mechanism of hydrogenation of furfural on Cu/SiO_2 catalysts*. J. Catal. 277 (2011) 1-13.

[3.76] N. Perret, X. Wang, T. Onfroy, C. Calers, M.A. Keane, *Selectivity in the gas phase hydrogenation of 4-nitrobenzaldehyde over supported Au catalysts*. J. Catal. 309 (2014) 333-342.

[3.77] A. Maltha, S.C. van Wermeskerken, T.L.F. Favre, P. Angevaare, E.J. Grootendorst, C.A. Koutstaal, A.P. Zuur, V. Ponec, *On the surface chemistry of oxides in the reaction of nitro compounds*. Catal. Today 10 (1991) 387-391.

Chapter 4

Gold Promoted Imine Formation by Selective Gas Phase Reductive Coupling of Nitrobenzene with Benzaldehyde

In the previous chapters, selective hydrogenation of benzaldehyde and nitrobenzene to benzyl alcohol and aniline has been established over supported Au catalysts. This chapter evaluates the feasibility of imine (*N*-benzylideneaniline) synthesis by gas-phase reductive coupling of nitrobenzene with benzaldehyde using nano-scale supported Au.

4.1 Introduction

Tandem catalytic coupling processes that combine multi-step reactions in one ‘‘pot” enhance process efficiency by minimising reaction steps with maximum catalyst utilisation [4.1]. Tandem coupled systems involving cyclisation [4.2], cycloaddition [4.3] and Michael-aldol [4.4] reactions have drawn on homogeneous catalysis. The requirement for catalyst separation and reuse limits efficiency but this can be circumvented by switching to heterogeneous catalysis. Solid catalysts (montmorillonite [4.5], β-zeolite [4.6], $NaAlO_2$ [4.7], Rh/Zr-β-zeolite [4.8] and Pd/MgO [4.9]) have been used in pressurised (up to 5 bar) batch liquid phase tandem reactions for the synthesis of ethers, glycidol, alkylcyclohexanols and nabumetone. Continuous gas phase operation has clear benefits in terms of reduced downtime and higher throughout but there is limited work on catalytic tandem reactions [4.10-4.12]. We can flag butanol synthesis (13% yield) *via* a tandem gas phase hydroformylation-hydrogenation of propene and synthesis gas over a SiO_2 supported Ru complex (Shvo catalyst) and supported Rh catalyst [4.10] and ethylene dimerization-isomerization to 2-butene over supported Ni [4.12].

Imines, widely used as organic intermediates in the manufacture of fine chemicals, pharmaceuticals and agrochemicals [4.13], are typically prepared by multi-step processes *via* amine synthesis from the corresponding nitro-reactant [4.14]. Dehydrogenative condensation of alcohols with amines to give imines has been established in liquid phase [4.15-4.19] with promising results achieved over supported Au [4.20,4.21]. Selectivities up to 99% have been reported in batch imine synthesis over

hydroxyapatite [4.20] and TiO_2 [4.21] supported Au by coupled reaction of alcohols (benzyl alcohol, cinnamyl alcohol and 1-phenylethanol) with aniline, 1-hexylamine and benzylamine. Oxidative condensation of benzylamines has been studied in liquid phase operation (T = 373 K, P_{O_2} = 5 bar) with exclusivity to imines achieved over (Al_2O_3, TiO_2, carbon and graphite) supported Au [4.22,4.23]. The multi-step process (nitro → amine → imine) requiring conventional multiple reactor operation is still a decided drawback. Use of nitrocompounds as feedstock in the coupled system can increase efficiency by incorporating the nitro → amine reduction step (**Fig. 4.1**, step **(I)**) in the overall process.

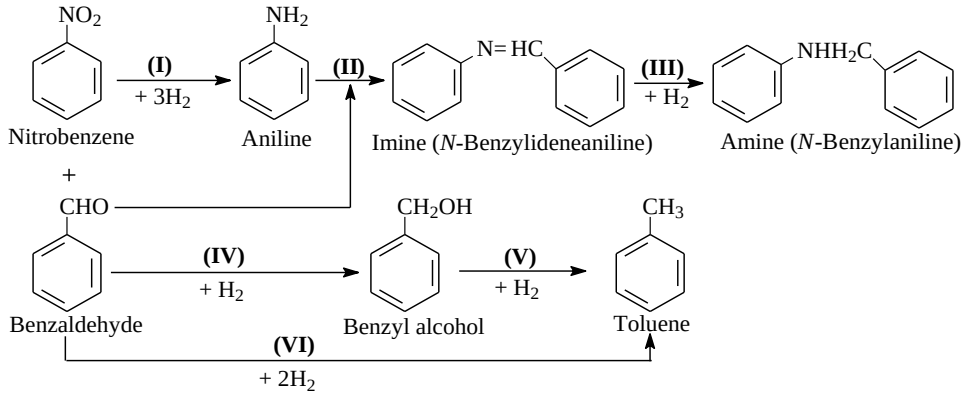

Fig. 4.1: Reaction scheme for the reductive coupling of nitrobenzene with benzaldehyde.

Application of supported Au catalysts in one-pot reductive coupling has not been examined in detail and we could not find any report of nitroarene-aldehyde gas phase reductive coupling. Santos *et al.* [4.24] demonstrated one-step synthesis of imine from substituted (vinyl and brominated) nitrobenzene and aromatic aldehydes (benzaldehyde and cinnamaldehyde) over Au/TiO_2 in batch liquid phase (T = 393 K, P_{H_2} = 4-12 bar). We herein evaluate the viability of imine preparation by gas phase continuous reductive coupling of nitrobenzene and benzaldehyde (as model reactants) over Au. As illustrated in **Fig. 4.1**, nitrobenzene reduction is a critical step in determining imine production as it supplies aniline for the condensation reaction. We have previously reported Au particle size and support nature (reducibility) played a crucial role in determining catalytic activity of $–NO_2$ reduction over supported Au catalysts [4.25]. We have considered the role of support reducibility on performance using a series of oxides (TiO_2, Fe_2O_3, Al_2O_3, ZrO_2 and MgO). Supported Pd is a commercial catalyst for nitrobenzene hydrogenation to aniline and has been utilised in reductive coupling reaction [4.26]. Selective nitroarene adsorption *via* the $–NO_2$ function on TiO_2 and the

metal-TiO_2 interface serves to enhance amine production rate [4.27], we have included Pd/TiO_2 as a benchmark. It has been shown utilisation of sequential catalyst beds to promote tandem gas phase hydroformylation-hydrogenation [4.10]. We evaluate the efficacy of multiple catalyst bed on enhancing the target imine yield in this study.

4.2 Experimental

4.2.1 Catalyst Preparation and Activation

The supports employed in this study were obtained from commercial sources (γ-Al_2O_3 (Puralox, Condea Vista), TiO_2 (P25, Degussa) and MgO (Sigma-Aldrich)) or synthesised (α-Fe_2O_3 and ZrO_2) following the procedures described in detail elsewhere [4.28,4.29]. Gold on MgO was prepared by impregnation of MgO (10 g) with aqueous $HAuCl_4$ (Sigma-Aldrich, 99%, 5×10^{-2} M, 50 cm^3). The slurry was heated (at 2 K min^{-1}) to 353 K under vigorous stirring (600 rpm) and maintained in a He purge for 5 h. Gold incorporation (on γ-Al_2O_3, TiO_2, α-Fe_2O_3 and ZrO_2) was prepared by deposition-precipitation with urea as basification agent. An aqueous solution of urea (100-fold excess) and $HAuCl_4$ ($3\text{-}7 \times 10^{-3}$ M, 400 cm^3) was added to the support (10-30 g). The suspension was stirred (600 rpm) and heated (at 2 K min^{-1}) to 353 K, where the pH progressively increased to reach *ca.* 6-8 after 3-4 h as a result of urea decomposition. The solid obtained was separated by filtration, washed with distilled water and dried in 45 cm^3 min^{-1} He at 373 K for 5 h. A supported Pd benchmark was synthesised by precipitation of $Pd(NO_3)_2$ (Sigma-Aldrich, 99%, 4×10^{-3} M, 300 cm^3) on TiO_2 (10 g), adding aqueous Na_2CO_3 (2 M) dropwise until pH >10 to ensure Pd deposition (as $Pd(OH)_2$) [4.30]. The slurry was heated (at 2 K min^{-1}) to 353 K and maintained for 4 h. The solid was separated by filtration, washed with distilled water and dried under vacuum at 333 K for 12 h. The catalyst precursors were sieved (ATM fine test sieves) to mean particle diameter = 75 μm. Samples were activated in 60 cm^3 min^{-1} H_2 at 2-5 K min^{-1} to 423-603 K, held for 1 h and passivated at ambient temperature in 1% v/v O_2/He for *ex situ* characterisation.

4.2.2 Catalyst Characterisation

Metal content was measured by atomic absorption spectroscopy using a Shimadzu AA-6650 spectrometer with an air-acetylene flame from the diluted extract in aqua regia (25% v/v HNO_3/HCl). Temperature programmed reduction (TPR) and H_2

chemisorption were conducted on the commercial CHEM-BET 3000 (Quantachrome Instrument) unit with data acquisition/manipulation using the TPR Win^{TM} software. Samples were loaded into a U-shaped Pyrex glass cell (3.76 mm i.d.) and heated in 17 cm^3 min^{-1} (Brooks mass flow controlled) 5% v/v H_2/N_2 at 2-5 K min^{-1} to 423-603 K, which was maintained until the signal returned to baseline. The effluent gas passed through a liquid N_2 trap and H_2 consumption was monitored by a thermal conductivity detector (TCD). The activated sample was swept with 65 cm^3 min^{-1} N_2 for 1.5 h, cooled to reaction temperature (413 K) and subjected to H_2 chemisorption by pulse (10 μl) titration. In blank tests there was no measurable H_2 uptake over support alone. Oxygen chemisorption post-TPR was employed to determine the extent of support reduction, where samples were reduced as described above, swept with 65 cm^3 min^{-1} He for 1.5 h, cooled to 413 K with pulse (50 μl) O_2 titration. It has been demonstrated that Au contribution to total O_2 adsorbed is negligible [4.31]. Nitrogen adsorption-desorption isotherms were obtained using the commercial Micromeritics Gemini 2390p system. Prior to analysis, the samples were outgassed at 423 K for 1 h in N_2. Total specific surface area (SSA) was obtained using the standard BET method. Metal particle morphology (size and shape) was examined by scanning transmission electron microscopy (STEM, JEOL 2200FS), employing Gatan Digital Micrograph 1.82 for data acquisition/manipulation. Samples for analysis were prepared by dispersion in acetone and deposited on a holey carbon/Cu grid (300 Mesh). The surface area weighted mean metal size (d_{STEM}) was based on a count of at least 300 particles according to

$$d_{STEM} = \frac{\sum_i n_i d_i^3}{\sum_i n_i d_i^2} \qquad \textbf{(4.1)}$$

where n_i is the number of particles of diameter d_i.

4.2.3 Catalytic Procedure

Catalyst testing was carried out at atmospheric pressure and 413 K *in situ* after activation in a continuous flow fixed bed tubular reactor (i.d. = 15 mm). A layer of borosilicate glass beads served as preheating zone where the reactant was vaporised and reached reaction temperature before contacting the catalyst bed. Isothermal conditions (±1 K) were maintained by diluting the catalyst bed with ground glass (75 μm), which was mixed thoroughly with the catalyst before loading into the reactor. Reaction temperature was continuously monitored by a thermocouple inserted in a thermowell

within the catalyst bed. The reactant(s) (benzaldehyde and/or nitrobenzene) was(were) delivered as an ethanolic solution to the reactor *via* a glass/teflon air-tight syringe and teflon line using a microprocessor controlled infusion pump (Model 100 kd Scientific) at a fixed calibrated flow rate. A co-current flow of organic reactant and H_2 was maintained at $GHSV = 2 \times 10^4$ h^{-1}. The molar metal to inlet organic molar feed rate (n/F) spanned the range $1.3 \times 10^{-3} - 5.8 \times 10^{-2}$ h. Catalyst performance for multiple Au/TiO_2 beds in series was tested where each catalyst bed was separated by glass wool (1 cm); catalyst activation followed the procedure given above. In blank tests, passage of each reactant (and mixture) in a stream of H_2 through the empty reactor or over each support did not result in any detectable conversion. The reactor effluent was condensed in a liquid nitrogen trap for subsequent analysis using a Perkin-Elmer Auto System XL gas chromatograph equipped with a programmed split/splitless injector and a flame ionisation detector, employing a DB-1 (50 m × 0.33 mm i.d., 0.20 μm film thickness) capillary column (J&W Scientific). Data acquisition and manipulation were performed using the Turbochrom Workstation Version 6.3.2 (for Windows) chromatography data system. Benzaldehyde (Fluka, ≥98%), nitrobenzene (Riedel-de Haën, ≥99%), benzyl alcohol (Riedel-de Haën, ≥99%), aniline (Riedel-de Haën, ≥99%), *N*-benzylideneaniline (Sigma Aldrich, 99%), *N*-benzylaniline (Sigma Aldrich, 99%) and ethanol (Sigma Aldrich, ≥99%) were used without further purification. All the gases employed (H_2, O_2, N_2 and He) were of high purity (>99.98%, BOC). Reactant (i) fractional conversion (X) is defined by

$$X_{\mathrm{i}} = \frac{[reactant]_{\mathrm{i,\,in}} - [reactant]_{\mathrm{i,\,out}}}{[reactant]_{\mathrm{i,\,in}}} \qquad \textbf{(4.2)}$$

and selectivity (S) to product "j" is given by

$$S_{\mathrm{j}}(\%) = \frac{[product]_{\mathrm{j,\,out}}}{[reactant]_{\mathrm{i,\,in}} - [reactant]_{\mathrm{i,\,out}}} \times 100 \qquad \textbf{(4.3)}$$

Yield (Y) to product "j" was obtained from

$$Y_{\mathrm{j}}(\%) = \frac{[product]_{\mathrm{j,\,out}}}{[reactant]_{\mathrm{i,\,in}}} \times 100 \qquad \textbf{(4.4)}$$

where subscripts "in" and "out" refer to the inlet and outlet gas streams, respectively. Catalytic activity is also quantified in terms of initial conversion ($X_{\mathrm{i},0}$), reactant consumption rate (R, $mol_{reactant}$ mol_{metal}^{-1} h^{-1}) and turnover frequency (TOF, rate per active site) calculated using

$$TOF\ (\mathrm{h}^{-1}) = \frac{R}{D} \qquad \textbf{(4.5)}$$

where D the metal dispersion (surface to total metal atoms) was obtained from STEM measurements [4.29]. Repeated reactions with different samples from the same batch of catalyst delivered raw data reproducibility that was better than ±6% with a carbon mass balance ≥ 95%.

4.3 Results and Discussion

Given the promoting effect of TiO_2 and metal-TiO_2 interface on activation/reduction of $–NO_2$ function, Au/TiO_2 and Pd/TiO_2 were chosen as the starting catalysts here.

4.3.1 Au/TiO_2 *vs.* Pd/TiO_2

4.3.1.1 Catalyst Characteristics

The physicochemical properties of TiO_2 supported Au and Pd are shown in **Table 4.1**, where both exhibit an equivalent metal loading (0.8 mol%) and SSA (52-53 $m^2\ g^{-1}$).

Table 4.1: Physicochemical characteristics of oxide supported Au and Pd catalysts.

Catalyst	Au/TiO_2	Pd/TiO_2	Au/Fe_2O_3	Au/Al_2O_3	Au/ZrO_2	Au/MgO
Metal loading (mol%)	0.8	0.8	0.8	0.5	0.5	0.7
SSA ($m^2\ g^{-1}$)	52	53	38	166	93	24
TPR T_{max} (K)	373	350[a]/566[b]	363	451	476	512
TPR H_2 consumption (μmol g^{-1})	170[c]/147[d]	34/99[d]	593[c]/74[d]	87[c]/84[d]	56[c]/61[d]	5[c]/256[d]
H_2 chemisorption (μmol g_{metal}^{-1})[e]	146	5015	76	318	137	26
Metal size range (nm)	1-6	1-7	1-5	1-8	3-12	1-15
Mean size (d_{STEM}, nm)	3.2	3.4	2.9	4.3	7.0	7.7
O_2 uptake (μmol g^{-1})[e]	8	-	168	1	3	<1

[a,b]T_{max} associated with negative and positive peak, respectively; [c]value obtained from TPR analysis; [d]calculated value for $Au^{3+} \rightarrow Au^0$ (or $Pd^{2+} \rightarrow Pd^0$); [e] measurement at 413 K.

The TPR profile for Au/TiO_2 (**Fig. 4.2(A)**) displays a positive peak at 373 K, where H_2 consumption (170 μmol g^{-1}, see **Table 4.1**) exceeded that required for the $Au^{3+} \rightarrow Au^0$ step (147 μmol g^{-1}), suggesting partial support reduction. A single TPR peak (T_{max} = 350-408 K) has been recorded elsewhere during activation of Au/TiO_2 and attributed to combined Au precursor reduction and Ti^{4+} conversion to Ti^{3+} at the metal/support interface [4.32]. The TPR profile of Pd/TiO_2 (**Fig. 4.2(B)**) is characterised by a negative (H_2 release) signal at T_{max} = 350 K and a positive (H_2 consumption) peak at T_{max} = 566

K, consistent with results reported by Babu *et al.* [4.30] for Pd/TiO_2. The lower temperature peak can be attributed to Pd hydride decomposition where Pd can absorb H_2 at ambient temperature and pressures >0.02 atm to form the hydride [4.33], which is thermally unstable and decomposes during TPR at 331-353 K [4.30,4.34]. Hydride composition (H/Pd ratio) is dependent on Pd size where the value obtained in this study (= 0.28 mol mol^{-1}) falls within the range (0.10-0.52) reported for a well dispersed Pd phase (2-10 nm) [4.35]. The positive signal at higher temperature can be attributed to reduction of oxidised Pd and/or support reduction ($Ti^{4+} \rightarrow Ti^{3+}$) [4.30].

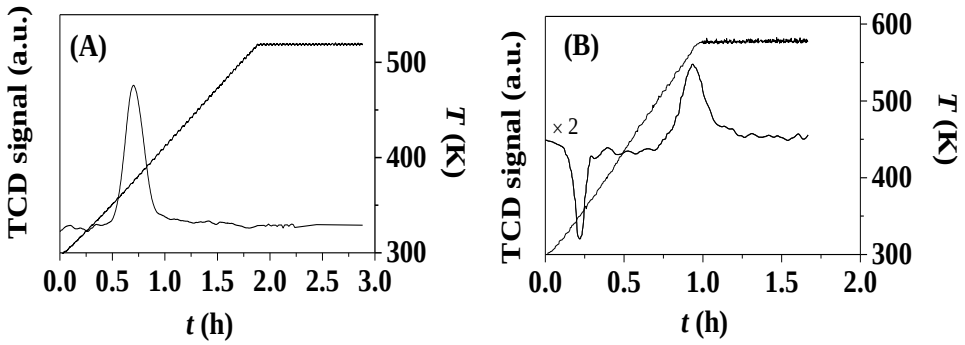

Fig. 4.2: Temperature programmed reduction (TPR) profiles for (A) Au/TiO_2 and (B) Pd/TiO_2.

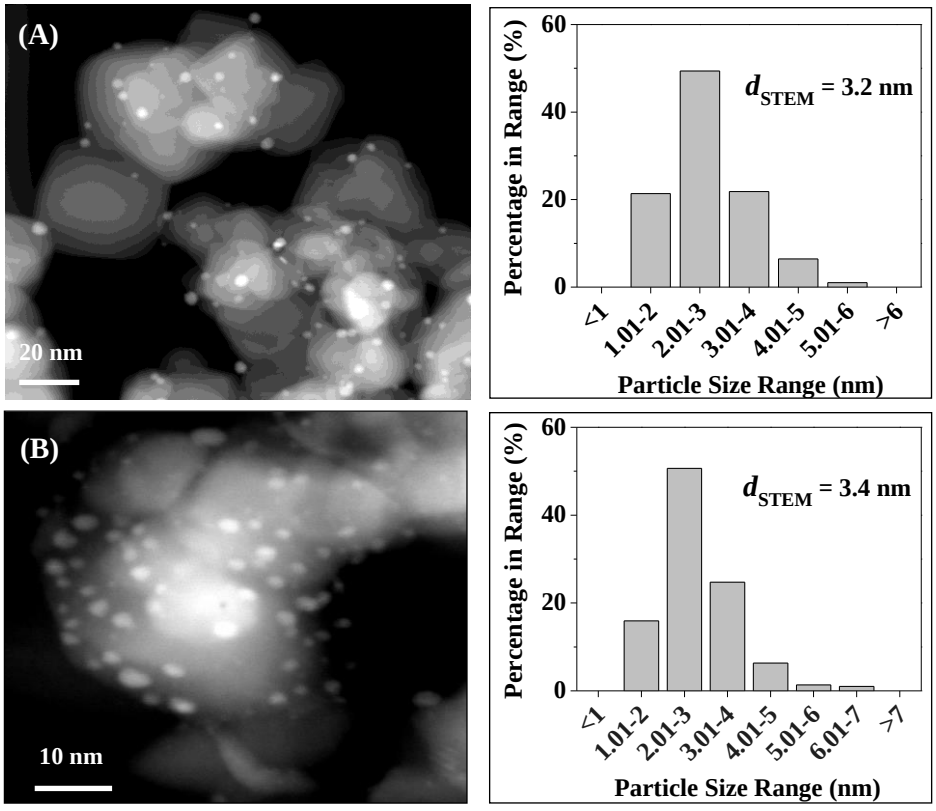

Fig. 4.3: Representative STEM images and associated particle size distribution histograms for (A) Au/TiO_2 and (B) Pd/TiO_2.

Metal particle morphology (size and shape) was evaluated by STEM analysis; representative images and associated particle size histograms are provided in **Fig. 4.3**. Both catalysts displayed quasi-spherical shaped particles with similar size distributions and surface area weighted mean (3.2-3.4 nm). Metal particle size has been shown to impact on catalytic hydrogenation activity, particularly in the case of Au catalysts where particles <10 nm have been identified as critical for hydrogen activation [4.36] and hydrogenation activity [4.31]. Hydrogen chemisorption under reaction conditions (413 K) is given in **Table 4.1** where uptake on Au/TiO_2 (146 μmol g_{Au}^{-1}) was significantly higher than that (16-46 μmol g_{Au}^{-1}) recorded at ambient temperature [4.37]. Bus *et al.* [4.38] have shown that H_2 chemisorption is favored at higher temperature (298 → 373 K) over nano-scale Au on Al_2O_3. Pd/TiO_2 exhibited appreciably larger uptake (5015 μmol g_{Pd}^{-1}) than that recorded for Au/TiO_2. Borgschulte *et al*. [4.39] have studied the catalytic activity of pure metal film in H_2 adsorption and reported up to three orders of magnitude higher H_2 uptake rate over Pd than Au. This can be attributed to a lower H_2 dissociation energy barrier for Pd due to the unfilled *d* band [4.31,4.39].

Table 4.2: Pseudo-first order rate constants (*k*) and product selectivity ($S_{product}$, %) in individual hydrogenation of nitrobenzene and benzaldehyde, and in the reductive coupling of nitrobenzene with benzaldehyde; *Reaction conditions*: *T* = 413 K, *P* = 1 atm.

Feed	Nitrobenzene		Benzaldehyde			Nitrobenzene + Benzaldehyde			
Catalyst	k (h^{-1})	$S_{aniline}$ (%)	k (h^{-1})	$S_{benzyl\ alcohol}$ (%)	$S_{toluene}$ (%)	k (h^{-1})	S_{imine} (%)	S_{amine} (%)	$S_{toluene}$ (%)
Au/TiO_2	32	100	8	100	-	36	99	1	-
Pd/TiO_2	1214	100	91	5	95	110	83	-	17

4.3.1.2 Catalytic Results

The tandem coupling process requires greater activity in the reduction of nitrobenzene to aniline (**Fig. 4.1**, step **(I)**) than benzaldehyde hydrogenation and/or hydrogenolysis to ensure aniline supply for subsequent condensation (step **(II)**). We first investigated stand-alone hydrogenation of nitrobenzene and benzaldehyde over Au/TiO_2 and Pd/TiO_2, and the results are presented in **Table 4.2**. Nitrobenzene hydrogenation over both catalysts generated aniline as sole product. Conversion of benzaldehyde over Au/TiO_2 was fully selective to benzyl alcohol while Pd/TiO_2 favoured hydrogenolysis to toluene (selectivity = 95%). The applicability of a pseudo-

first order kinetic treatment has been established elsewhere for the hydrogenation of nitrobenzene [4.40] and benzaldehyde [4.41] where the following expression applies

$$\ln\left[\frac{1}{(1-X_{i,0})}\right] = k\left(\frac{n_{metal}}{F}\right) \qquad \textbf{(4.6)}$$

(n_{metal}/F) has the physical meaning of contact time. The extracted rate constants (k, h^{-1}) are given in **Table 4.2**, where Pd/TiO_2 delivered appreciably higher rates than Au/TiO_2 for both reactions which can be linked to the greater H_2 chemisorption capacity recorded in **Table 4.1**. The rate of nitrobenzene hydrogenation was higher than that of benzaldehyde which agrees with reaction thermodynamics where nitrobenzene → aniline ($\Delta G_{413\ K}$ = -436 ± 1 kJ mol^{-1}) is more favourable than benzaldehyde hydrogenation (to benzyl alcohol, $\Delta G_{413\ K}$ = -24 ± 2 kJ mol^{-1}) or hydrogenolysis (to toluene, $\Delta G_{413\ K}$ = -108 ± 3 kJ mol^{-1}). Higher (at least by four fold) nitrobenzene reduction rate relative to benzaldehyde reaction meets the prerequisite for the tandem process.

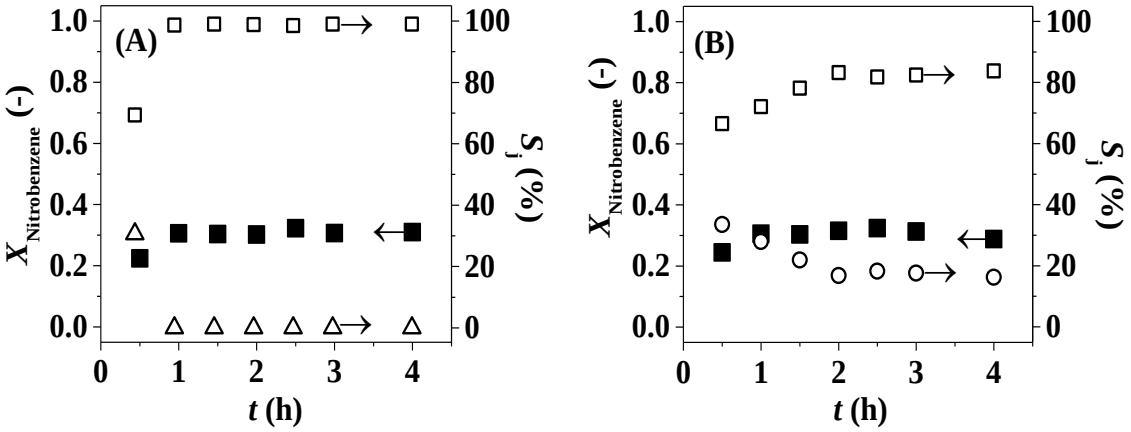

Fig. 4.4: Variation of fractional nitrobenzene conversion (*X*, ■) and product selectivity (S_j, □: imine, ○: toluene, Δ: aniline) with time on-stream over (A) Au/TiO_2 and (B) Pd/TiO_2. *Reaction conditions*: *T* = 413 K, *P* = 1 atm.

Temporal variation of conversion and product selectivity in nitrobenzene + benzaldehyde reductive coupling over Au/TiO_2 **(A)** and Pd/TiO_2 **(B)** is presented in **Fig. 4.4**. In both cases, activity increased to attain steady state after 1 h on-stream. In terms of selectivity, aniline from nitrobenzene reduction (**Fig. 4.1**, step **(I)**) was detected as a secondary product over Au/TiO_2 during the first 0.5 h with conversion to the target imine (**Fig. 4.1**, step **(II)**) at extended reaction times. In contrast, reaction over Pd/TiO_2 resulted in significant toluene formation (S ~ 20%) at steady state, resulting from hydrogenolysis (**Fig. 4.1**, steps **(V/VI)**) in addition to nitro group reduction. The generation of imine over both catalysts demonstrates successful tandem reaction in

continuous gas phase operation. Imine formation (99% selectivity) over Au/TiO_2 (with trace amine, step **(III)** in **Fig. 4.1**) with no detectable by-products from benzaldehyde hydrogenation (to benzyl alcohol) or hydrogenolysis (to toluene) is important in terms of clean synthesis. We could not find any directly comparable studies in continuous gas phase operation. We should note that the highest imine selectivity (≤ 93%) in liquid phase reductive coupling of nitrobenzene + benzaldehyde over Au/TiO_2 [4.24] was lower than that achieved in this study. Moreover, amine and benzyl alcohol were detected as significant by-products ($S_{imine} \leq 80\%$) for reaction over Pt/Al_2O_3 [4.42]. The pseudo-first order rate constants (based on steady state and nitrobenzene conversion) for the coupled reaction are given in **Table 4.2**, where Pd/TiO_2 again delivered greater activity than Au/TiO_2. The tandem reaction over Au/TiO_2 generated a similar rate constant to that of stand-alone nitrobenzene reduction, suggesting that imine formation in the coupled reaction is controlled by the nitrobenzene → aniline step. Liu *et al*. [4.19] have noted that the hydrogenation of nitrobenzene to aniline is much slower than aniline condensation with benzaldehyde. Lower tandem reaction rate over Pd/TiO_2 than the stand-alone nitrobenzene reduction can be linked to the occurrence of benzaldehyde hydrogenolysis that resulted in decreased rate.

4.3.2 Oxides Supported Au

The results presented above have established imine synthesis *via* gas phase coupled reactions over Au/TiO_2 where nitrobenzene hydrogenation is rate-determining. Nitroarene hydrogenation over supported Au catalysts has been shown to depend on the surface chemistry and redox properties of the support [4.43] and Au particle size [4.44]. We probe both variables by examining the catalytic action of Au (of varying size) on reducible and non-reducible carriers.

4.3.2.1 Catalyst Characterisation

The SSA recorded (in **Table 4.1**) for the supported Au catalysts range from 24 $m^2 g^{-1}$ (Au/MgO) to 166 $m^2 g^{-1}$ (Au/Al_2O_3) and fall within values reported in the literature [4.45-4.48]. The TPR profiles (not shown) were similar to Au/TiO_2 with a single H_2 consumption peak with T_{max} in the range 363-512 K (**Table 4.1**) [4.37,4.45,4.49]. Hydrogen consumption during TPR showed a dependency on support redox character where values recorded for Au on non-reducible oxides matched the amount required for metal precursor reduction (Au/Al_2O_3 and Au/ZrO_2). The appreciably lower

consumption during TPR of Au/MgO (prepared by impregnation) can be attributed to metal reduction pre-TPR, during catalyst preparation and drying as reported by Margitfalvi *et al.* for Au/MgO also prepared by impregnation [4.50]. Excess H_2 consumption for Au/Fe_2O_3 can be ascribed to partial reduction of the support. Oxygen chemisorption post-TPR was employed to determine the extent of support reduction. Uptake on Au/Fe_2O_3 and Au/TiO_2 is consistent with support reduction and correlates with excess H_2 consumption and the formation of oxygen vacancies [4.51,4.52]. The mean Au sizes given in **Table 4.1** suggest a dependence of metal dispersion on support reducibility. Smaller Au particles were formed on the reducible (Fe_2O_3 and TiO_2) carriers where the stabilising effect of surface oxygen vacancies can inhibit sintering [4.53]. The largest mean size (7.7 nm) associated with Au/MgO (1-15 nm) is the result of synthesis by less controlled impregnation that is known to generate weak precursor/support interactions leading to particles agglomeration during pre-treatment [4.54]. Okumura *et al*. [4.55] reported Au/Al_2O_3 (1% w/w) prepared by deposition-precipitation and impregnation exhibited mean Au particle sizes of 2.5 nm and 37 nm, respectively. Hydrogen chemisorption (**Table 4.1**) under reaction conditions (413 K) revealed highest uptake over Au/Al_2O_3 (318 μmol g_{Au}^{-1}) with lowest uptake over Au/MgO (26 μmol g_{Au}^{-1}). There is some consensus that H_2 chemisorption is favoured on smaller Au particles (1-10 nm, supported on Al_2O_3) that possess a higher fraction of low coordinated Au atoms at corners and edge sites [4.38]. Moreover, hydrogen adsorption/dissociation on Au supported on (Al_2O_3, TiO_2, Fe_2O_3, ZrO_2 and CeO_2) can spillover onto support [4.56-4.58], where larger surface area can accommodate greater spillover hydrogen [4.59]. H_2 uptake can be linked to SSA (Au/Al_2O_3 > Au/ZrO_2 > Au/TiO_2 > Au/Fe_2O_3 > Au/MgO). Au/ZrO_2 exhibits higher SSA (than Au/TiO_2), but the occurrence of larger Au particles (73% >5 nm *vs*. 1% >5 nm for Au/TiO_2) decreased hydrogen chemisorption.

4.3.2.2 Catalytic Results

Turnover frequencies (*TOF*) and imine selectivity at the steady state in the reductive coupling of nitrobenzene with benzaldehyde are presented in **Fig. 4.5**. High (97-99%) selectivity to imine with trace amine production was common to all the Au catalysts with no evidence of benzyl alcohol and/or toluene formation. As a general observation, *TOF* increased ($6 \rightarrow 103$ h^{-1}) with decreasing ($7.7 \rightarrow 3.2$ nm, Au/MgO < Au/ZrO_2 < Au/Al_2O_3 < Au/TiO_2) mean Au size. This response finds agreement with

reports in the literature showing sympathetic structure sensitivity for the hydrogenation of nitroarenes over supported Au [4.25] but we provide here first evidence that this effect extends to tandem reactions. It should be noted that Au/Fe_2O_3 with the smallest mean Au size (2.9 nm) and greatest oxygen vacancy density deviates from this trend. This can be tentatively attributed to stronger binding of nitro-group at these vacancy sites that can stabilise surface adsorbed nitrobenzene and inhibit $–NO_2$ activation/ reduction [4.60]. Moreover, loss of metal character for smaller Au nano-particles that particularly applies to Au/Fe_2O_3 (40% particles ≤ 2 nm) has been shown to result in decreased hydrogenation activity [4.61]. Increased *TOF* ($6 \rightarrow 103\ h^{-1}$) can also be linked to H_2 chemisorption capacity ($26 \rightarrow 146\ \mu mol\ g_{Au}^{-1}$, $Au/MgO < Au/Fe_2O_3 < Au/ZrO_2 < Au/TiO_2$). But reaction over Au/Al_2O_3 with the highest H_2 uptake ($318\ \mu mol\ g_{Au}^{-1}$) delivered a lower *TOF* than Au/TiO_2 ($146\ \mu mol\ g_{Au}^{-1}$). Nitro-group polarisation plays a critical factor in determining reaction rate and application of the selective energy transfer (SET) has established $–NO_2$ activation at TiO_2 and/or $Au\text{-}TiO_2$ interface sites [4.62]. Boronat *et al*. [4.27], studying the hydrogenation of nitrostyrene by *in situ* IR analysis and quantum chemical calculations, attributed greater *TOF* to aminostyrene over Au/TiO_2 ($173\ h^{-1}$) relative to Au/SiO_2 ($10\ h^{-1}$) to $–NO_2$ activation at the $Au\text{-}TiO_2$ interface. A high Au dispersion on TiO_2 serves to extend the $Au\text{-}TiO_2$ interface and can contribute to the enhanced *TOF*. The specific rate of the tandem reactions converged with that recorded for nitrobenzene hydrogenation for all the catalysts (**Fig. 4.5**), further demonstrating nitrobenzene → aniline as rate determining.

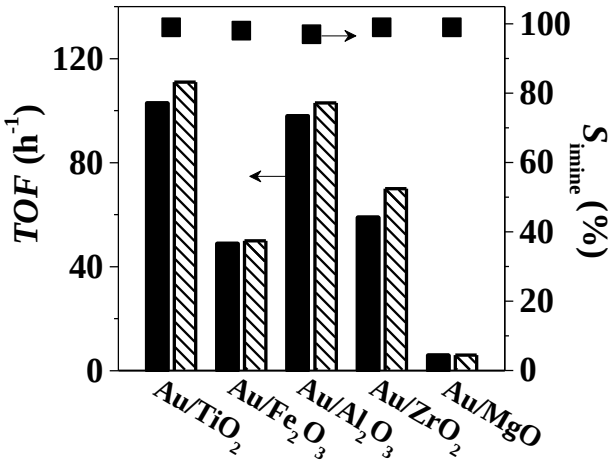

Fig. 4.5: Turnover frequency (*TOF*) in terms of aniline (in the stand-alone hydrogenation of nitrobenzene, hatched bar) and imine (in the coupled reaction, solid bar) formation and selectivity to imine in the coupled system (■) over the series of oxide supported Au catalysts. *Reaction conditions*: *T* = 413 K, *P* = 1 atm.

4.3.3 Use of Multiple Catalyst Beds

The tests to this point have established structure sensitivity in imine production over Au with the highest specific activity over Au/TiO_2 (**Fig. 4.5**). However, productivity (30% yield, see entry 1 in **Table 4.3**) is still low. It has been shown that a configuration of discrete catalyst beds in series, each at operated at low contact time (n/F), served to enhance nitrile hydrogenation to benzylamine over Pd/Al_2O_3 with retaining target selectivity [4.63] and the effective use of sequential or "stacked" catalyst beds to promote each reaction (in the corresponding catalyst bed) with enhanced catalytic activity in hydrodesulphurisation [4.64]. We considered the possible benefits of multiple Au/TiO_2 bed operation in the sequential hydrogenation-condensation reaction.

Table 4.3: Fractional conversion (X), product selectivity ($S_{product}$, %) and imine yield (Y_{imine}, %) in the reductive coupling of nitrobenzene with benzaldehyde using single and multiple catalyst beds in series; *Reaction conditions*: T = 413 K, P = 1 atm.

Catalyst	Catalyst bed	Catalyst mass (g)	n/F (10^{-3} h)	X (-)	S_{imine} (%)	S_{amine} (%)	Y_{imine} (%)
Au/TiO_2	single	0.02	8.5	0.30	99	1	30
		0.04	17	0.34	99	1	34
	triple	0.04	17	0.62	95	5	59
		0.06	26	0.75	93	7	70

Use of a triple bed arrangement resulted in a two-fold increase in overall conversion at an imine selectivity of 95% (**Table 4.3**). In the single bed, increasing the mass of catalyst (0.02 → 0.04 g) did not result in a proportional increase in activity (entries 1-2 in **Table 4.3**). In addition to the promotional effect of low n/F related to each bed, the enhanced conversion for triple bed can also be attributed to extended residence time with increased aniline conversion *via* condensation that in turn enhances fractional hydrogenation of nitrobenzene to aniline in the tandem (nitrobenzene → aniline → imine) reaction. The marginal drop in selectivity was due to amine formation *via* consecutive hydrogenation of the imine (**Fig. 4.1**, step **(III)**). Enhanced activity has also been observed in the hydrodesulphurisation of gas oil using a double bed of Ni/Al_2O_3 and Mo/Al_2O_3 with Al_2O_3 as spacer [4.65] and in the selective catalytic reduction of NO_2 with hydrocarbons using $Pd/SZ\text{-}Co_x/CeO_2$ dual beds [4.66]. We demonstrate that multiple beds of a single supported metal catalyst can also promote tandem reaction. There is possible competition for the same sites in the hydrogenation of imine (**Fig. 4.1**, step (**III**)) with nitrobenzene → aniline (**Fig. 4.1**, step (**I**)) that can impact on product

distribution. A mixed feedstock of nitrobenzene/*N*-benzylideneaniline was used to probe this possible effect and the consumption rates of each reactant over Au/TiO_2 as a function of inlet reactant ratio can be compared in **Fig. 4.6**. Nitrobenzene hydrogenation rates (26-45 $mol_{\text{-}NO_2}\ mol_{Au}^{-1}\ h^{-1}$) were appreciably greater than imine hydrogenation (2-14 $mol_{\text{-}C=N}\ mol_{Au}^{-1}\ h^{-1}$), regardless of nitrobenzene/imine ratio. This suggests preferential $–NO_2$ group (relative to –C=N) activation/reduction. As imine content in the feed was increased, nitrobenzene hydrogenation rate was lowered with a concomitant increase in imine consumption. This can account for amine production at higher conversions in the coupled reaction using catalyst beds in series. The results presented in this study can serve as a basis for process intensification with an alternative catalytic tandem reaction for sustainable imine synthesis. Enhanced imime selectivity and continuous operation at ambient pressure represent a significant advancement over current pressurised batch liquid operations.

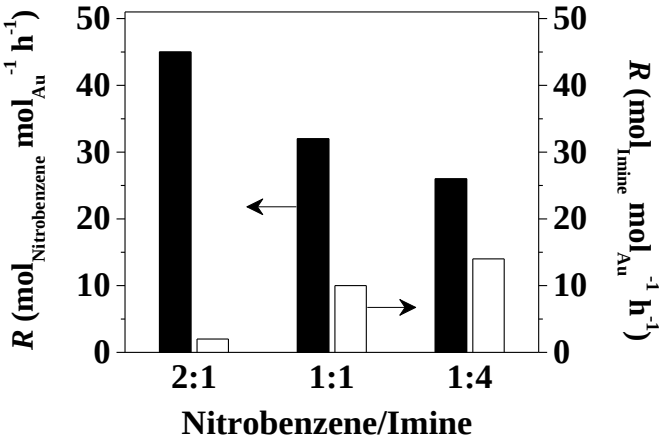

Fig. 4.6: Nitrobenzene (solid bar) and imine (open bar) consumption rate as a function of inlet nitrobenzene/imine ratio for the hydrogenation of nitrobenzene + imine mixtures. *Reaction conditions*: *T* = 413 K, *P* = 1 atm.

4.4 Conclusion

Nano-scale Au (mean = 2.9-7.7 nm) on a series of oxide (TiO_2, Fe_2O_3, Al_2O_3, ZrO_2 and MgO) supports generated high selectivity to the target imine (*N*-benzylideneaniline) in the reductive coupling of nitrobenzene and benzaldehyde in continuous gas phase operation. Under the same reaction conditions Pd/TiO_2 (mean Pd size = 3.4 nm) delivered a higher reaction rate but generated toluene (from benzaldehyde hydrogenolysis) as a significant by-product, resulting in lower imine selectivity (83%). Turnover frequencies ($6 \rightarrow 103\ h^{-1}$) were dependent on Au size where rate increased with decreasing Au size ($7.7 \rightarrow 3.2$ nm) that can be linked to greater H_2 chemisorption

capacity for smaller Au particles. Lower *TOF* over Au (mean = 2.9 nm) on reducible Fe_2O_3 can be attributed to an anchoring of the nitro group to surface oxygen vacancies that suppresses reactivity. Reaction rates in the coupled reaction coincided with stand-alone nitrobenzene hydrogenation, suggesting that the latter is the rate-determining step. Use of a triple Au/TiO_2 bed arrangement in series served to further increase imine yield (from 30% to 70%) in a single pass conversion. This study has established the viability of a catalytic tandem process for continuous imine production.

4.5 References

[4.1] Y. Shiraishi, K. Fujiwara, Y. Sugano, S. Ichikawa, T. Hirai, *N-monoalkylation of amines with alcohols by tandem photocatalytic and catalytic reactions on TiO_2 loaded with Pd nanoparticles*. ACS Catal. 3 (2013) 312-320.

[4.2] K.T. Yip, M. Yang, K.L. Law, N.Y. Zhu, D. Yang, *Pd(II)-catalyzed enantioselective oxidative tandem cyclization reactions: Synthesis of indolines through C-N and C-C bond formation*. J. Am. Chem. Soc. 128 (2006) 3130-3131.

[4.3] K. Wakabayashi, H. Yorimitsu, K. Oshima, *Cobalt-catalyzed tandem radical cyclization and cross-coupling reaction: Its application to benzyl-substituted heterocycles*. J. Am. Chem. Soc. 123 (2001) 5374-5375.

[4.4] Y. Yamamoto, N. Momiyama, H. Yamamoto, *Enantioselective tandem O-nitroso aldol/Michael reaction*. J. Am. Chem. Soc. 126 (2004) 5962-5963.

[4.5] S.M. Landge, M. Berryman, B. Toeroek, *Microwave-assisted solid acid-catalyzed one-pot synthesis of isobenzofuran-1(3H)-ones*. Tetrahedron Lett. 49 (2008) 4505-4508.

[4.6] A. Corma, M. Renz, *A general method for the preparation of ethers using water-resistant solid Lewis acids*. Angew. Chem. Int. Edit. 46 (2007) 298-300.

[4.7] R. Bai, H. Zhang, F. Mei, S. Wang, T. Li, Y. Gu, G. Li, *One-pot synthesis of glycidol from glycerol and dimethyl carbonate over a highly efficient and easily available solid catalyst $NaAlO_2$*. Green Chem. 15 (2013) 2929-2934.

[4.8] Y. Nie, S. Jaenicke, H. van Bekkum, G.-K. Chuah, *Stereoselective cascade hydrogenation of 4-tert-butylphenol and p-cresol over Zr-zeolite beta-supported rhodium*. J. Catal. 246 (2007) 223-231.

[4.9] M.J. Climent, A. Corma, S. Iborra, M. Mifsud, *MgO nanoparticle-based multifunctional catalysts in the cascade reaction allows the green synthesis of anti-inflammatory agents*. J. Catal. 247 (2007) 223-230.

[4.10] D.G. Hanna, S. Shylesh, P.A. Parada, A.T. Bell, *Hydrogenation of butanal over silica-supported Shvo's catalyst and its use for the gas-phase conversion of propene to butanol via tandem hydroformylation and hydrogenation*. J. Catal. 311 (2014) 52-58.

[4.11] Y.C. Zhang, T.Q. Ma, J.Q. Zhao, *Study on the conversion of glycerol to nitriles over a $Fe_{19.2}K_{0.2}/\gamma$-Al_2O_3 catalyst*. J. Catal. 313 (2014) 92-103.

[4.12] J. Scholz, V. Hager, X.J. Wang, F.T.U. Kohler, M. Sternberg, M. Haumann, N. Szesni, K. Meyer, P. Wasserscheid, *Ethylene to 2-butene in a continuous gas phase reaction using SILP-type cationic nickel catalysts*. ChemCatChem 6 (2014) 162-169.

[4.13] J. Chen, S.J. Huang, J. Lin, W.P. Su, *Recyclable palladium catalyst for facile synthesis of imines from benzyl alcohols and nitroarenes*. Appl. Catal. A: Gen. 470 (2014) 1-7.

[4.14] M.T. Schuemperli, C. Hammond, I. Hermans, *Developments in the aerobic oxidation of amines*. ACS Catal. 2 (2012) 1108-1117.

[4.15] J.W. Kim, K. Yamaguchi, N. Mizuno, *Heterogeneously catalyzed selective N-alkylation of aromatic and heteroaromatic amines with alcohols by a supported ruthenium hydroxide*. J. Catal. 263 (2009) 205-208.

[4.16] J. He, K. Yamaguchi, N. Mizuno, *Selective synthesis of secondary amines via N-alkylation of primary amines and ammonia with alcohols by supported copper hydroxide catalysts*. Chem. Lett. 39 (2010) 1182-1183.

[4.17] A. Corma, T. Rodenas, M.J. Sabater, *A bifunctional Pd/MgO solid catalyst for the one-pot selective N-monoalkylation of amines with alcohols*. Chem. Eur. J. 16 (2010) 254-260.

[4.18] J.H. Cho, J.H. Park, T.-S. Chang, G. Seo, C.-H. Shin, *Reductive amination of 2-propanol to monoisopropylamine over Co/γ-Al_2O_3 catalysts*. Appl. Catal. A: Gen. 417 (2012) 313-319.

[4.19] H. Liu, G.-K. Chuah, S. Jaenicke, *N-alkylation of amines with alcohols over alumina-entrapped Ag catalysts using the "borrowing hydrogen" methodology*. J. Catal. 292 (2012) 130-137.

[4.20] H. Sun, F.-Z. Su, J. Ni, Y. Cao, H.-Y. He, K.-N. Fan, *Gold supported on hydroxyapatite as a versatile multifunctional catalyst for the direct tandem synthesis of imines and oximes*. Angew. Chem. Int. Edit. 48 (2009) 4390-4393.

[4.21] S. Kegnaes, J. Mielby, U.V. Mentzel, C.H. Christensen, A. Riisager, *Formation of imines by selective gold-catalysed aerobic oxidative coupling of alcohols and amines under ambient conditions*. Green Chem. 12 (2010) 1437-1441.

[4.22] B. Zhu, M. Lazar, B.G. Trewyn, R.J. Angelici, *Aerobic oxidation of amines to imines catalyzed by bulk gold powder and by alumina-supported gold*. J. Catal. 260 (2008) 1-6.

[4.23] A. Grirrane, A. Corma, H. Garcia, *Highly active and selective gold catalysts for the aerobic oxidative condensation of benzylamines to imines and one-pot, two-step synthesis of secondary benzylamines*. J. Catal. 264 (2009) 138-144.

[4.24] L.L. Santos, P. Serna, A. Corma, *Chemoselective synthesis of substituted imines, secondary amines, and β-amino carbonyl compounds from nitroaromatics through cascade reactions on gold catalysts*. Chem. Eur. J. 15 (2009) 8196-8203.

[4.25] F. Cárdenas-Lizana, M.A. Keane, *The development of gold catalysts for use in hydrogenation reactions*. J. Mater. Sci. 48 (2013) 543-564.

[4.26] M.E. Domine, M.C. Hernández-Soto, Y. Pérez, *Development of metal nanoparticles supported materials as efficient catalysts for reductive amination reactions using high-throughput experimentation*. Catal. Today 159 (2011) 2-11.

[4.27] M. Boronat, P. Concepción, A. Corma, S. González, F. Illas, P. Serna, *A molecular mechanism for the chemoselective hydrogenation of substituted nitroaromatics with nanoparticles of gold on TiO_2 catalysts: A cooperative effect between gold and the support*. J. Am. Chem. Soc. 129 (2007) 16230-16237.

[4.28] F. Cárdenas-Lizana, S. Gómez-Quero, L. Kiwi-Minsker, M.A. Keane, *Gold nano-particles supported on hematite and magnetite as highly selective catalysts for the hydrogenation of nitro-aromatics*. Int. J. Nanotechnol. 9 (2012) 92-112.

[4.29] M. Li, X. Wang, N. Perret, M.A. Keane, *Enhanced production of benzyl alcohol in the gas phase continuous hydrogenation of benzaldehyde over Au/Al_2O_3*. Catal. Commun. 46 (2014) 187-191.

[4.30] N.S. Babu, N. Lingaiah, N. Pasha, J.V. Kumar, P.S.S. Prasad, *Influence of particle size and nature of Pd species on the hydrodechlorination of chloroaromatics: Studies on Pd/TiO_2 catalysts in chlorobenzene conversion*. Catal. Today 141 (2009) 120-124.

[4.31] G.C. Bond, C. Louis, D.T. Thompson, *Catalysis by gold*, G.J. Hutchings (Ed.), Imperial College Press, London, 2006.

[4.32] M. Ousmane, L.F. Liotta, G. Di-Carlo, G. Pantaleo, A.M. Venezia, G. Deganello, L. Retailleau, A. Boreave, A. Giroir-Fendler, *Supported Au catalysts for low-temperature abatement of propene and toluene, as model VOCs: Support effect*. Appl. Catal. B: Environ. 101 (2011) 629-637.

[4.33] W.J. Shen, M. Okumura, Y. Matsumura, M. Haruta, *The influence of the support on the activity and selectivity of Pd in CO hydrogenation*. Appl. Catal. A: Gen. 213 (2001) 225-232.

[4.34] H.B. Huang, X.G. Ye, H.L. Huang, L. Zhang, D.Y.C. Leung, *Mechanistic study on formaldehyde removal over Pd/TiO_2 catalysts: Oxygen transfer and role of water vapor*. Chem. Eng. J. 230 (2013) 73-79.

[4.35] C.M. Mendez, H. Olivero, D.E. Damiani, M.A. Volpe, *On the role of Pd β-hydride in the reduction of nitrate over Pd based catalyst*. Appl. Catal. B: Environ. 84 (2008) 156-161.

[4.36] M. Manzoli, A. Chiorino, F. Vindigni, F. Boccuzzi, *Hydrogen interaction with gold nanoparticles and clusters supported on different oxides: A FTIR study*. Catal. Today 181 (2012) 62-67.

[4.37] F. Cárdenas-Lizana, S. Gómez-Quero, N. Perret, M.A. Keane, *Gold catalysis at the gas-solid interface: Role of the support in determining activity and selectivity in the hydrogenation of m-dinitrobenzene*. Catal. Sci. Technol. 1 (2011) 652-661.

[4.38] E. Bus, J.T. Miller, J.A. van Bokhoven, *Hydrogen chemisorption on Al_2O_3-supported gold catalysts*. J. Phys. Chem. B 109 (2005) 14581-14587.

[4.39] A. Borgschulte, R.J. Westerwaal, J.H. Rector, H. Schreuders, B. Dam, R. Griessen, *Catalytic activity of noble metals promoting hydrogen uptake*. J. Catal. 239 (2006) 263-271.

[4.40] F. Cárdenas-Lizana, Z.M. Pedro, S. Gómez-Quero, M.A. Keane, *Gas phase hydrogenation of nitroarenes: A comparison of the catalytic action of titania supported gold and silver*. J. Mol. Catal. A: Chem. 326 (2010) 48-54.

[4.41] N. Perret, F. Cárdenas-Lizana, M.A. Keane, *Selective hydrogenation of benzaldehyde to benzyl alcohol over Au/Al_2O_3*. Catal. Commun. 16 (2011) 159-164.

[4.42] M. Arai, A. Obata, Y. Nishiyama, *Catalytic features of a low-temperature reduced alumina-supported platinum catalyst: Activity and selectivity in the liquid-phase hydrogenation of benzaldehyde and nitrobenzene*. React. Kinet. Catal. Lett. 61 (1997) 275-280.

[4.43] K.-I. Shimizu, Y. Miyamoto, T. Kawasaki, T. Tanji, Y. Tai, A. Satsuma, *Chemoselective hydrogenation of nitroaromatics by supported gold catalysts: Mechanistic reasons of size- and support-dependent activity and selectivity*. J. Phys. Chem. C 113 (2009) 17803-17810.

[4.44] U. Hartfelder, C. Kartusch, M. Makosch, M. Rovezzi, J. Sa, J.A. van Bokhoven, *Particle size and support effects in hydrogenation over supported gold catalysts*. Catal. Sci. Technol. 3 (2013) 454-461.

[4.45] X. Zhang, H. Shi, B.-Q. Xu, *Vital roles of hydroxyl groups and gold oxidation states in Au/ZrO_2 catalysts for 1,3-butadiene hydrogenation*. J. Catal. 279 (2011) 75-87.

[4.46] G. Jacobs, T.K. Das, Y.Q. Zhang, J.L. Li, G. Racoillet, B.H. Davis, *Fischer-Tropsch synthesis: Support, loading and promoter effects on the reducibility of cobalt catalysts*. Appl. Catal. A: Gen. 233 (2002) 263-281.

[4.47] M. Zdražil, *MgO-supported Mo, CoMo and NiMo sulfide hydrotreating catalysts*. Catal. Today 86 (2003) 151-171.

[4.48] C. Milone, C. Crisafulli, R. Ingoglia, L. Schipilliti, S. Galvagno, *A comparative study on the selective hydrogenation of α, β-unsaturated aldehyde and ketone to unsaturated alcohols on Au supported catalysts*. Catal. Today 122 (2007) 341-351.

[4.49] S. Gómez-Quero, F. Cárdenas-Lizana, M.A. Keane, *Unique selectivity in the hydrodechlorination of 2,4-dichlorophenol over hematite-supported Au*. J. Catal. 303 (2013) 41-49.

[4.50] J.L. Margitfalvi, M. Hegedűs, A. Szegedi, I. Sajó, *Modification of Au/MgO catalysts used in low temperature CO oxidation with Mn and Fe*. Appl. Catal. A: Gen. 272 (2004) 87-97.

[4.51] F. Boccuzzi, A. Chiorino, M. Manzoli, D. Andreeva, T. Tabakova, *FTIR study of the low-temperature water-gas shift reaction on Au/Fe_2O_3 and Au/TiO_2 catalysts*. J. Catal. 188 (1999) 176-185.

[4.52] T. Tabakova, F. Boccuzzi, M. Manzoli, D. Andreeva, *FTIR study of low-temperature water-gas shift reaction on gold/ceria catalyst*. Appl. Catal. A: Gen. 252 (2003) 385-397.

[4.53] L.F. Liotta, G. Pantaleo, F. Puleo, A.M. Venezia, *Au/CeO_2-SBA-15 catalysts for CO oxidation: Effect of ceria loading on physic-chemical properties and catalytic performances*. Catal. Today 187 (2012) 10-19.

[4.54] G.C. Bond, D.T. Thompson, *Catalysis by gold*. Catal. Rev. 41 (1999) 319-388.

[4.55] M. Okumura, T. Akita, M. Haruta, *Hydrogenation of 1,3-butadiene and of crotonaldehyde over highly dispersed Au catalysts*. Catal. Today 74 (2002) 265-269.

[4.56] D.A. Panayotov, J.T. Yates, *Spectroscopic detection of hydrogen atom spillover from Au nanoparticles supported on TiO_2: Use of conduction band electrons*. J. Phys. Chem. C 111 (2007) 2959-2964.

[4.57] S.E. Collins, J.M. Cíes, E. Río, M. López-Haro, S. Trasobares, J.J. Calvino, J.M. Pintado, S. Bernal, *Hydrogen interaction with a ceria-zirconia supported gold catalyst: Influence of CO co-adsorption and pretreatment conditions*. J. Phys. Chem. C 111 (2007) 14371-14379.

[4.58] D. Andreeva, *Low temperature water gas shift over gold catalysts*. Gold Bull. 35 (2002) 82-88.

[4.59] X. Wang, N. Perret, M.A. Keane, *Gas phase hydrogenation of nitrocyclohexane over supported gold catalysts*. Appl. Catal. A: Gen. 467 (2013) 575-584.

[4.60] A. Maltha, T.L.F. Favre, H.F. Kist, A.P. Zuur, V. Ponec, *Manganese oxides as catalysts for the selective reduction of nitrobenzene to nitrosobenzene*. J. Catal. 149 (1994) 364-374.

[4.61] P. Claus, A. Bruckner, C. Mohr, H. Hofmeister, *Supported gold nanoparticles from quantum dot to mesoscopic size scale: Effect of electronic and structural properties on catalytic hydrogenation of conjugated functional groups*. J. Am. Chem. Soc. 122 (2000) 11430-11439.

[4.62] M.A. Keane, R. Larsson, *Isokinetic behavior in the gas phase hydrogenation of nitroarenes over Au/TiO_2: Application of the selective energy transfer model*. React. Kinet. Mech. Catal. 106 (2012) 267-288.

[4.63] Y. Hao, M. Li, F. Cárdenas-Lizana, M.A. Keane, *Selective production of benzylamine via gas phase hydrogenation of benzonitrile over supported Pd catalysts.* Catal. Lett. 146 (2016) 109-117.

[4.64] M. Villarroel, E. Camu, N. Escalona, P. Avila, S.B. Rasmussen, P. Baeza, F. Gil-Llambías, *Synergisms via hydrogen spillover between some transition metals during hydrodesulphurization: Increased activity towards conversion of refractory molecules*. Appl. Catal. A: Gen. 399 (2011) 63-68.

[4.65] M. Villarroel, P. Baeza, N. Escalona, J. Ojeda, B. Delmon, F.J. Gil-Liambías, *M_D//Mo and M_D//W [M_D = Mn, Fe, Co, Ni, Cu and Zn] promotion via spillover hydrogen in hydrodesulfurization*. Appl. Catal. A: Gen. 345 (2008) 152-157.

[4.66] P. Gawade, A.M.C. Alexander, R. Clark, U.S. Ozkan, *The role of oxidation catalyst in dual-catalyst bed for after-treatment of lean burn natural gas exhaust*. Catal. Today 197 (2012) 127-136.

Chapter 5

Combined Catalytic Action of Supported Cu and Au in Imine Production from Benzyl Alcohol with Nitrobenzene

Chapter 4 has established selective synthesis of imine by reductive coupling of nitrobenzene with benzaldehyde (using external hydrogen) over supported Au catalysts. This chapter proposes an alternative route for imine production from benzyl alcohol and nitrobenzene in the absence of external hydrogen over supported Cu and Au catalysts.

5.1 Introduction

Higher substituted imines are extensively used as intermediates in the manufacture of fine chemicals, pharmaceuticals and agrochemicals [5.1]. Conventional production draws on reductive amination (alkylation) of aldehydes/ketones with amines that are derived from the reduction of nitro-compounds in excess or pressurised (4-12 bar) H_2 [5.2-5.4]. Hydrogen is not a naturally occurring feedstock and current production (*ca.* 95%) is fossil fuel based, notably by methane steam reforming and coal gasification [5.5]. Issues linked to sustainable H_2 production are now the driver for the search of more efficient routes to imines. Work to date has focused on batch liquid phase catalytic oxidation of amines [5.6] (*e.g.* benzylamine over Au [5.7] and Cu [5.8]) and oxidative condensation of alcohols with amines [5.9] (*e.g.* benzyl alcohol and aniline over Cu [5.10], Pd [5.11] and Au [5.12]) at high (O_2/air) pressures (up to 5 atm). But the use of amine as reactant with multi-step process (nitro → amine → imine) involved in oxidation

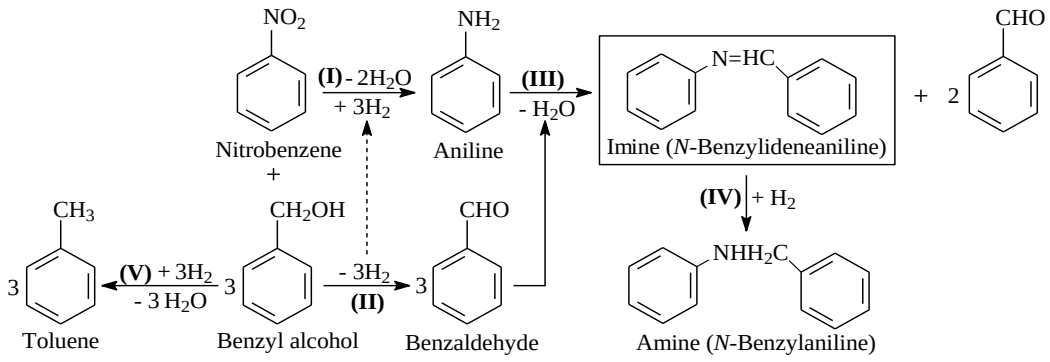

Fig. 5.1: Reaction network in the coupled benzyl alcohol and nitrobenzene reactions. *Note*: dashed arrow represents hydrogen transfer; target imine product is framed.

is still a decided drawback [5.13]. We propose to integrate the nitro- → amine reduction step (**Fig. 5.1**, step **(I)**) and reaction with aldehyde (step **(III)**) in a "one pot" imine production that circumvents conventional multiple reactor operation. Moreover, alcohol dehydrogenation (step **(II)**) is used to generate hydrogen that is utilised in $–NO_2$ hydrogenation. This removes the requirement for an external supply of pressurised H_2 and can be step-changing in terms of sustainability and process efficiency.

Synthesis of imines *via* coupling of alcohol dehydrogenation with nitro-compound reduction has not been studied to any significant extent. The viability of batch liquid phase coupling of benzyl alcohol dehydrogenation (as hydrogen donor) with nitrobenzene hydrogenation has been demonstrated for reaction over $Mg_6Al_2(OH)_{16}CO_3$ supported Pd but with amine (>7% yield) generated as by-product [5.14]. Imine synthesis from nitrobenzene and furfural has been reported for Pd-Au/Al_2O_3 (with CH_3OH as hydrogen source) [5.15] and from nitroarenes and benzaldehyde over iron powder (with HCl as hydrogen donor) [5.16] in batch mode. A move from batch to continuous processing provides significant benefits in terms of economics, high throughput and quality control. This has been identified as a priority for sustainable production in the pharmaceutical and fine chemical sector [5.17]. Studies of continuous gas phase operation employing a hydrogen ''borrowing'' strategy have predominantly focused on coupling of dehydrogenation and hydrogenation [5.18-5.21] with no report of cross-coupling of alcohols with nitro- reactants for imine synthesis. Baiker *et al*. [5.22,5.23] studied the formation of dimethyldodecylamine by gas phase cross-coupling of dimethylamine and 1-dodecanol over Cu/Al_2O_3 and observed loss of activity and selectivity in the absence of external hydrogen supply. Deactivation has been a feature of coupling reactions involving alcohols and amines over supported Cu and Ni catalysts and was attributed to nitride formation, coking and amine deposition [5.24].

We have previously established the coupling of nitrobenzene reduction (to aniline) with benzaldehyde for imine synthesis using external hydrogen over supported Au catalysts in continuous gas phase operation in **Chapter 4**. In this study, we have extended that work to evaluate the feasibility of imine production in the absence of external H_2 supply by combining Cu/SiO_2 with supported Au catalysts using benzyl alcohol and nitrobenzene as model reactants. Nitroarene hydrogenation over supported Au shows a dependency on support reducibility [5.25], where Au on TiO_2 and MgO carriers has exhibited differences in chemoselective amine production rates [5.26]. We

also evaluate hydrogen utilisation efficiency and catalyst stability as two critical considerations for imine production.

5.2 Experimental

5.2.1 Catalyst Preparation and Activation

Cu/SiO_2 was prepared by deposition-precipitation with NaOH (Riedel-de Haën, 99%) as precipitation agent. Silica powder (Sigma-Aldrich, 20 g) was dispersed in an aqueous solution of $Cu(NO_3)_2$ (Sigma-Aldrich, 99%, 0.03 M, 200 cm^3). The suspension was stirred (600 rpm) at ambient temperature for 1 h, NaOH (2 M) added dropwise until pH >10 to ensure complete copper deposition as $Cu(OH)_2$ [5.27]. The mixture was heated in air to 353 K with subsequent ageing for 4 h to facilitate homogeneous deposition [5.27]. The solid obtained was separated by filtration, washed with distilled water until pH = 7 and dried at 393 K in air over night. The dried sample was calcined in air (at 10 K min^{-1} to 723 K for 4 h) to generate a supported copper oxide (CuO) [5.27]. Gold on MgO (Sigma-Aldrich, 10 g) was prepared by impregnation with aqueous $HAuCl_4$ (Sigma-Aldrich, 99%, 5×10^{-2} M, 50 cm^3). The slurry was heated (at 2 K min^{-1}) to 353 K under vigorous stirring (600 rpm) and maintained in a He purge for 5 h. Gold on TiO_2 (P25, Degussa) was prepared by deposition-precipitation using urea (Riedel-de Haën, 99%) as basification agent. An aqueous solution of urea (100 fold excess) and $HAuCl_4$ (5×10^{-3} M, 400 cm^3) was added to the support (15 g) and the suspension stirred and heated to 353 K (2 K min^{-1}). The pH progressively increased to reach *ca.* 7 after 3-4 h as a result of thermal decomposition of urea. The supported Au catalyst precursor was separated by filtration, washed with distilled water and dried in 45 cm^3 min^{-1} He at 373 K for 5 h. The catalyst precursors were sieved (ATM fine test sieves) to mean particle diameter = 75 μm. Prior to *ex situ* characterisation and catalytic testing, samples were activated in 60 cm^3 min^{-1} H_2 at 2-4 K min^{-1} to 523-545 K, held for 1-2 h and passivated at ambient temperature in 1% v/v O_2/He.

5.2.2 Catalyst Characterisation

Metal loading was determined by atomic absorption spectroscopy (Shimadzu AA-6650 spectrometer with an air-acetylene flame) analysis of the diluted extract in aqua regia (25% v/v HNO_3/HCl). Temperature programmed reduction (TPR) and H_2 chemisorption were conducted on the CHEM-BET 3000 (Quantachrome Instrument)

unit with data acquisition/manipulation using the TPR Win^{TM} software. The sample was loaded into a U-shaped Pyrex glass cell (3.76 mm i.d.) and heated in 17 cm^3 min^{-1} (Brooks mass flow controlled) 5% v/v H_2/N_2 at 2-4 K min^{-1} to 523-545 K. The activated samples were swept with 65 cm^3 min^{-1} N_2 for 1.5 h, cooled to reaction temperature (498 K) and subjected to H_2 chemisorption by pulse (10 μl) titration. The effluent gas passed through a liquid N_2 trap and H_2 consumption was monitored by a thermal conductivity detector (TCD). In blank tests there was no measurable H_2 uptake on the (SiO_2, MgO or TiO_2) supports. Nitrogen adsorption-desorption isotherms were obtained using the Micromeritics Gemini 2390p system. Prior to analysis, the samples were outgassed at 423 K for 1 h in N_2. Total specific surface area (SSA) and cumulative pore volumes were obtained using standard BET and BJH analysis. Metal particle morphology (size and shape) was examined by scanning transmission electron microscopy (STEM, JEOL 2200FS field emission gun-equipped unit), employing Gatan Digital Micrograph 1.82 for data acquisition/manipulation. Samples for analysis were prepared by dispersion in acetone and deposited on a holey carbon/Cu grid (300 Mesh). Surface area weighted mean metal size (*d*) was based on a count of up to 800 nanoparticles according to

$$d = \frac{\sum_i n_i d_i^3}{\sum_i n_i d_i^2} \qquad \textbf{(5.1)}$$

where n_i is the number of particles of diameter d_i. Thermogravimetric analysis (TGA) and differential scanning calorimetry (DSC) of the samples *pre*- and/or *post*-reaction was performed on a SDT Q600 simultaneous TGA/DSC analyser (TA Instrument) by monitoring temporal mass and heat flow changes with temperature. The samples (*ca.* 10 mg) were heated in 100 cm^3 min^{-1} air at 373 K for 1 h and ramped to 1073 K (at 20 K min^{-1}). Elemental (C, H and N) analysis for samples *post*-reaction was carried out on an Exeter CE-400 elemental analyser. X-ray photoelectron spectroscopic (XPS) analysis was conducted on an Axis Ultra instrument (Kratos Analytical) under ultra-high vacuum conditions (<10^{-8} Torr) with a monochromatic Al Kα radiation (1486 eV). The C1*s*, Cu 2$p_{3/2}$, Au 4$f_{5/2}$ and 4$f_{7/2}$, N1*s* and Si 2*p* spectra were collected. Characteristic Cu 2$p_{3/2}$ binding energies (BE) for metallic Cu and CuO are 932.8 eV [5.28] and 934.0 eV [5.29]. Values in the 83.7-84.0 eV and 87.8-88.2 eV ranges for 4$f_{7/2}$ and 4$f_{5/2}$ levels have been reported elsewhere [5.30] for metallic Au. We define adventitious carbon as any carbon associated with the air exposed samples [5.31]. The C1*s* profile for this adventitious carbon is characterised by a principal peak at 284.5 eV, indicative of alkyl species (C–C, C–H) [5.32], and was used as an internal standard to compensate for

charging effects. The spectra were calibrated against the Si 2*p* (of SiO_2, BE = 103.5 eV) [5.33] and fitted with abstraction of the Shirley background using the Gaussian-Lorentzian function in XPSPEAK 41.

5.2.3 Catalytic Procedure

Reactions (stand-alone benzyl alcohol dehydrogenation and nitrobenzene hydrogenation and cross-coupling) were carried out at atmospheric pressure, *in situ* after activation in a continuous flow fixed bed vertical glass reactor (i.d. = 15 mm) at 423-523 K. A layer of borosilicate glass beads served as preheating zone, ensuring that the reactant(s) (benzyl alcohol and/or nitrobenzene) was (were) vaporised and reached reaction temperature before contacting the catalyst. Isothermal conditions (±1 K) were maintained by diluting the catalyst with ground glass (75 μm) and continuously monitored by a thermocouple inserted in a thermowell within the catalyst bed. The reactant(s) was (were) delivered to the reactor *via* a glass/teflon air-tight syringe and teflon line using a microprocessor controlled infusion pump (Model 100 kd Scientific). Dehydrogenation of benzyl alcohol and hydrogenation of nitrobenzene were tested separately in a co-current flow of N_2 with benzyl alcohol ($GHSV = 1.0 \times 10^4$ h^{-1}, molar metal to reactant feed rate $n_{metal}/F = 3.8 \times 10^{-3} – 5.0 \times 10^{-2}$ h) and H_2 with nitrobenzene ($GHSV = 1.0 \times 10^4$ h^{-1}, $n_{metal}/F = 8.0 \times 10^{-3} – 1.2 \times 10^{-2}$ h), respectively. The coupled reaction was carried out in a N_2 flow ($GHSV = 2.0 \times 10^3$ h^{-1}, $n_{metal}/F = 1.2 \times 10^{-1} – 3.6 \times 10^{-1}$ h). In blank tests passage of each reactant through the empty reactor or over the (SiO_2, MgO or TiO_2) support alone did not result in any detectable conversion. The reactor effluent was condensed in a liquid nitrogen trap for subsequent analysis using a Perkin-Elmer Auto System XL gas chromatograph equipped with a programmed split/splitless injector and a flame ionization detector, employing a DB-1 (50 m × 0.33 mm i.d., 0.20 μm film thickness) capillary column (J&W Scientific). Data acquisition and manipulation were performed using the TurboChrom Workstation Version 6.3.2 (for Windows) chromatography data system. Benzyl alcohol (Riedel-de Haën, ≥99%), benzaldehyde (Fluka, ≥98%), nitrobenzene (Riedel-de Haën, ≥99%), aniline (Sigma-Aldrich, ≥99%), toluene (Sigma-Aldrich, 99%), *N*-benzylideneaniline (Sigma-Aldrich, 99%) and *N*-benzylaniline (Sigma-Aldrich, 99%) were used as received without further purification. The (H_2, N_2, O_2 and He) gases were of high purity (BOC, >99.98 %). Reactant (i) fractional conversion (X_i) is defined by

$$X_i = \frac{[reactant]_{i,\,in} - [reactant]_{i,\,out}}{[reactant]_{i,\,in}} \quad \textbf{(5.2)}$$

and composition (N_j) with respect to outlet product (j) is given by

$$N_j\,(\%) = \frac{[compotent]_{j,out}}{\sum_{j=1}^{n}[compotent]_{j,out}} \times 100 \quad \textbf{(5.3)}$$

where subscripts "in" and "out" refer to the inlet and outlet gas streams, respectively. Catalytic activity for stand-alone dehydrogenation and hydrogenation is also quantified in terms of initial conversion ($X_{i,0}$), which was obtained as described elsewhere [5.34]; imine formation rate (R, mmol mol_{metal}^{-1} h^{-1}) and product ratio (benzaldehyde to imine, $N_{C=O}/N_{C=N}$) in the cross-coupling reaction were obtained from the time on-stream measurements. Repeated reaction with different samples from the same batch of catalyst delivered raw data reproducibility and mass balances within ±5%.

Table 5.1: Physicochemical characteristics of Cu/SiO_2, Au/TiO_2 and Au/MgO.

		Cu/SiO_2	Au/TiO_2	Au/MgO
Metal loading (% w/w)		1.8	1.9	3.4
Specific surface area (SSA, $m^2\,g^{-1}$)		192	52	24
Pore volume ($cm^3\,g^{-1}$)		0.34	0.07	0.04
TPR	T_{max} (K)	545	378	510
	H_2 consumption ($\mu mol\,g^{-1}$)	281[a]/281[b]	170[a]/143[b]	5[a]/256[b]
H_2 chemisorption ($\mu mol\,g_{metal}^{-1}$)[c]		37	185	19
d (nm)[d]		3.1	3.2	7.7
Particle size range (nm)[d]		1-6	1-6	1-15

[a]experimental value obtained from TPR analysis; [b]calculated value for $Cu^{2+} \rightarrow Cu^0$ and $Au^{3+} \rightarrow Au^0$; [c]measurement at reaction temperature (498 K); [d]from STEM analysis.

5.3 Results and Discussion

5.3.1 Cu/SiO_2: Characterisation (*Pre*-reaction) and Catalysis (Stand-Alone and Coupled Reactions)

The physicochemical characteristics of Cu/SiO_2 given in **Table 5.1** reveal a SSA lower than that of the silica support (223 $m^2\,g^{-1}$) but a comparable pore volume (SiO_2 = 0.35 $cm^3\,g^{-1}$). Activation by TPR (**Fig. 5.2(AI)**) generated a positive (H_2 consumption)

peak at the final isothermal hold (545 K) where the H_2 consumed matched the requirements for $Cu^{2+} \rightarrow Cu^0$ reduction (**Table 5.1**). Hydrogen chemisorption capacity is a critical catalyst characteristic for hydrogenation applications. We have noted previously low ambient temperature H_2 chemisorption on Cu/SiO_2 (25 µmol g_{Cu}^{-1}) that can be linked to the filled *d* band [5.35]. Hydrogen uptake on Cu is an activated process, where Cu/SiO_2 showed a higher uptake (37 µmol g_{Cu}^{-1}) under reaction condition (498 K). This value is appreciably lower than that recorded for silica supported hydrogenation metals such as Pd (1650 µmol g_{Pd}^{-1}) [5.36] and Ni (614 µmol g_{Ni}^{-1}) [5.37]. STEM analysis (**Fig. 5.2(AII)**) revealed presence of discrete Cu particles at the nano-scale (1-6 nm, **Fig. 5.2(AIII)**) with a surface area weighted mean of 3.1 nm.

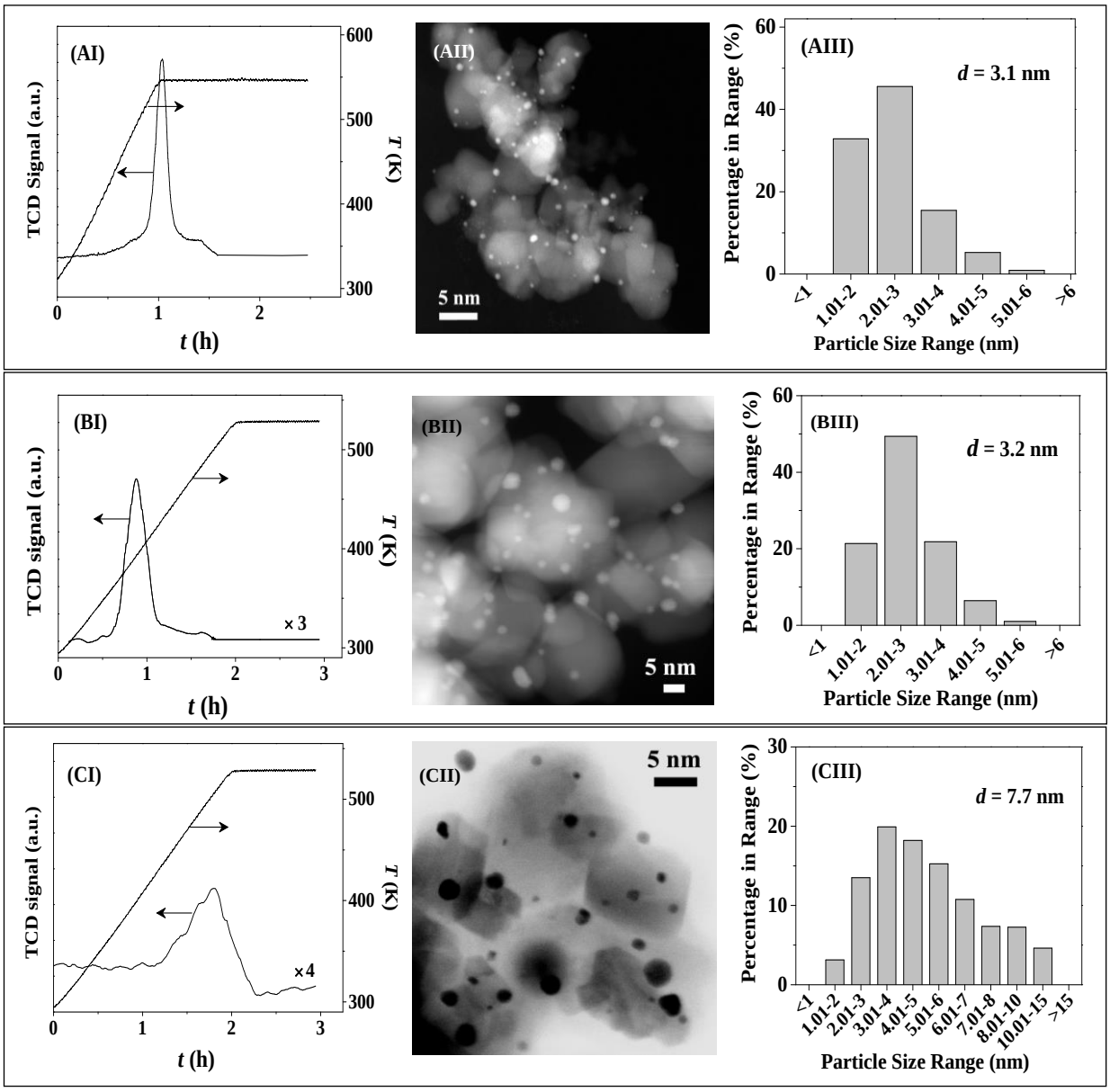

Fig. 5.2: (I) Temperature programmed reduction (TPR) profiles, (II) representative STEM images and (III) associated metal particle size distribution histograms for (A) Cu/SiO_2, (B) Au/TiO_2 and (C) Au/MgO.

The coupled dehydrogenation-hydrogenation system requires a higher dehydrogenation rate compared with hydrogenation to ensure a sufficient H_2 supply for reaction. We first examined separately the dehydrogenation of benzyl alcohol (in N_2) and hydrogenation of nitrobenzene (using an external H_2 supply) over Cu/SiO_2. Benzyl alcohol dehydrogenation generated benzaldehyde (**Fig. 5.1**, step **(II)**) as the sole product over the 423-498 K temperature range. Limited toluene formation (≤10% selectivity, step **(V)** in **Fig. 5.1**) was observed for reaction at 523 K. Full selectivity to the target benzaldehyde at $T < 498$ K is consistent with the reported reaction over $K\text{-}Cu/TiO_2$ [5.38], while benzyl alcohol hydrogenolysis (over Cu/MgO) to toluene required temperatures ≥513 K [5.39]. We have previously established pseudo-first order kinetic behaviour for catalytic dehydrogenation (of 2-butanol) and nitroarene hydrogenation [5.40] where the following expression applies

$$\ln\left[\frac{1}{(1-X_{i,0})}\right] = k\left(\frac{n_{Cu}}{F}\right) \qquad \textbf{(5.4)}$$

and n_{Cu}/F has the physical meaning of contact time. The associated Arrhenius plots (423-498 K) using the extracted rate constants (k) are presented in **Fig. 5.3** with an associated apparent activation energy for the dehydrogenation reaction of 37 kJ mol^{-1}. We could not find any reported activation energy for a comparable benzyl alcohol dehydrogenation to benzaldehyde and the value (20 kJ mol^{-1}) recorded for *n*-octyl alcohol dehydrogenation (over $Cu/Al_2O_3\text{-}MgO$) is relatively lower [5.41]. Nitrobenzene hydrogenation (**Fig. 5.1**, step **(I)**) over Cu/SiO_2 resulted in exclusive production of aniline with no hydrodenitrogenation or aromatic ring reduction. The apparent activation energy (32 kJ mol^{-1}, **Fig. 5.3**) falls within the range (12-54 kJ mol^{-1}) recorded

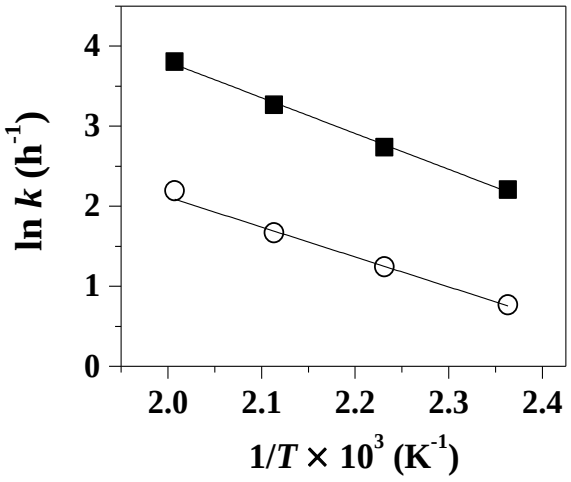

Fig. 5.3: Arrhenius plots for stand-alone (■) dehydrogenation of benzyl alcohol and (○) hydrogenation of nitrobenzene over Cu/SiO_2. *Reaction conditions*: T = 423-498 K, P = 1 atm.

for reaction over supported Ag [5.42], Pd [5.43] and Ni [5.44] catalysts. A four-fold higher benzyl alcohol dehydrogenation rate relative to nitrobenzene hydrogenation meets the prerequisite for our coupled system (reaction stoichiometry = 3).

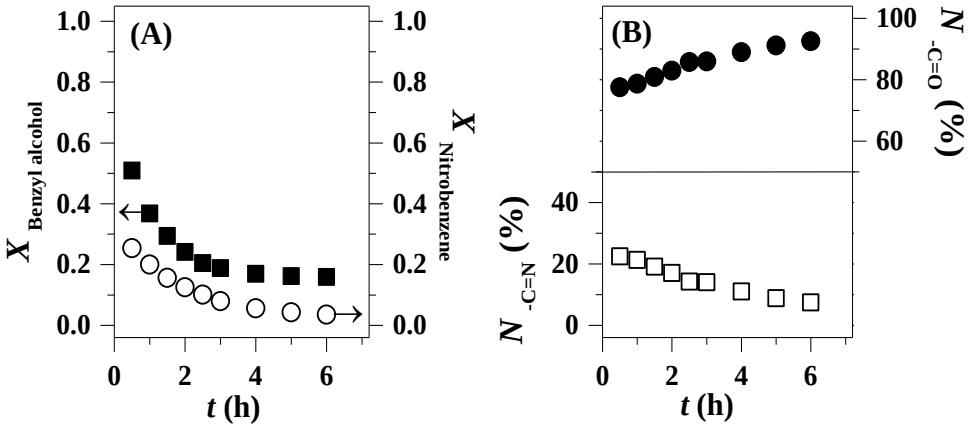

Fig. 5.4: (A) Variation of fractional conversion (X_i, ■: benzyl alcohol, ○: nitrobenzene) and (B) product composition (N_j, □: imine, ●: benzaldehyde) with time on-stream for the coupled benzyl alcohol and nitrobenzene reactions over Cu/SiO_2. *Reaction conditions*: T = 498 K, –OH/–NO_2 = 3, P = 1 atm.

The coupled reaction of benzyl alcohol and nitrobenzene in N_2, *i.e.* absence of an external H_2 supply, was examined over Cu/SiO_2 at 498 K where the highest selective benzyl alcohol dehydrogenation rate was achieved. Temporal variations in conversion and product composition are shown in **Fig. 5.4**. The coupled reaction generated imine and benzaldehyde with no detectable hydrogenolysis to toluene (step **(V)**, **Fig. 5.1**) and/or amine from further hydrogenation of imine (**step (IV)**). This represents the first reported continuous imine synthesis *via* coupling alcohol dehydrogenation and nitro-group hydrogenation without external H_2. The generation of imine in N_2 demonstrates that the catalyst "borrows" hydrogen generated from alcohol dehydrogenation (step **(II)**) with an "auto-transfer" in the catalytic reduction of nitrobenzene to aniline (step **(I)**). As aniline is a strong nucleophile it undergoes facile condensation with benzaldehyde to the target imine (step **(III)**) [5.45]. This represents innovation in process intensification and enhanced sustainability relative to conventional multi-stepped methodologies that require an external H_2 supply [5.2-5.4,5.8,5.10]. A temporal decline in activity and imine production was observed (**Fig. 5.4**). Baiker [5.22] studying the gas phase (T = 510 K, P = 1 atm) cross-coupling alkylation of dimethylamine with 1-dodecanol over Cu/Al_2O_3 reported a severe loss of activity that was ascribed to the formation of copper nitride (Cu_3N) by Cu interaction with NH_3 generated from disproportionation of dimethylamine.

Reaction temperature is a critical variable that can impact on reactant/intermediate activation, which in turn influences reaction rate and product distribution [5.46]. Imine formation rate (R), molar product (benzaldehyde/imine) ratio ($N_{\text{-C=O}}/N_{\text{-C=N}}$) and hydrogen utilisation efficiency, expressed as the ratio of mol H_2 generated from benzyl alcohol dehydrogenation to mol imine produced (H_2/–C=N) are presented as a function of temperature (448-498 K) in **Table 5.2**. An increase in temperature (to 498 K) at the reaction stoichiometry (inlet alcohol/nitroarene (–OH/–NO_2) = 3) resulted in a greater imine formation rate (by a factor of over 50) with a higher imine composition in the product and improved H_2 utilisation. The increased reaction rate can be attributed to greater hydrogen availability (from the Arrhenius plot in **Fig. 5.3**) in tandem with the increased H_2 chemisorption capacity of Cu/SiO_2 at higher temperatures as determined from H_2 titration measurements. It should however be noted that product ratio ($N_{\text{-C=O}}/N_{\text{-C=N}}$) was greater than that (= 2) shown in the reaction scheme (**Fig. 5.1**) and H_2/–C=N exceeded the stoichiometry requirement (= 3) for full H_2 utilisation (**Table 5.2**), necessitating further process and parameter optimisation.

Table 5.2: Effect of reaction temperature (T) and inlet (alcohol/nitroarene) molar reactant ratio (–OH/–NO_2) on imine formation rate (R), molar (benzaldehyde/imine) product ratio ($N_{\text{-C=O}}/N_{\text{-C=N}}$) and hydrogen utilisation efficiency (mol H_2 generated from alcohol dehydrogenation per mol imine product (H_2/–C=N)) in the coupled benzyl alcohol and nitrobenzene reactions over Cu/SiO_2; *Reaction conditions*: T = 448-498 K, P = 1 atm.

T (K)	–OH/–NO_2	R (mmol mol_{Cu}^{-1} h^{-1})	$N_{\text{-C=O}}/N_{\text{-C=N}}$	H_2/–C=N
448	3	7	20.3	40
473	3	66	6.8	10
498	3	358	3.8	6
498	1	67	3.7	6
498	9	468	4.4	8

It has been demonstrated that –OH/–NO_2 is a critical parameter in determining product distribution in liquid phase cross-coupling [5.14]. A higher –OH/–NO_2 served to increase imine formation rate (R) as shown in **Table 5.2**. This result suggests competition between nitrobenzene and benzyl alcohol for surface sites where higher alcohol content in the feed favours alcohol dehydrogenation (with greater hydrogen release) that enhanced the hydrogenation step. Shimizu *et al*. [5.47] proposed that

dehydrogenation was rate determining in the coupled reaction of aniline with benzyl alcohol in N_2 for amine (*N*-benzylaniline) synthesis over Ni/Al_2O_3. Hydrogen utilisation (H_2/–C=N) and product ratio ($N_{\text{-C=O}}/N_{\text{-C=N}}$) was largely insensitive to variations in –OH/–NO_2 (**Table 5.2**). Incomplete H_2 utilisation can be linked to the low hydrogenation activity of Cu catalysts. Incorporation of a second metal with greater hydrogenation capability can serve as a means of increasing imine production rate. A critical prerequisite is that the second metal must not promote side-reactions (*e.g.* benzyl alcohol hydrogenolysis and imine hydrogenation). Supported Pd, Pt and Ni exhibit high activity in the reduction of unsaturated functions (*e.g.* –NO_2 and –C=O) but promote hydrogenolysis, generating a range of by-products (*e.g.* toluene) [5.48, 5.49]. In contrast, nano-scale Au has displayed unique chemoselectivity for hydrogenation of –NO_2 with other reactive groups (*e.g.* –C=O) [5.4] and was chosen in this study as a suitable candidate to improve hydrogen utilisation directed at higher imine production rates.

5.3.2 Au/TiO_2 and Au/MgO Characterisation (*Pre*-reaction) and Catalysis (Stand -Alone (Benzyl Alcohol) Dehydrogenation and (Nitrobenzene) Reduction)

Titania supported Au was chosen here given facilitated adsorption/activation of –NO_2 on TiO_2 and at the Au-TiO_2 interface with enhanced selective nitroarene reduction rates [5.26]. In order to probe possible support effects we have also examined the performance of Au/MgO as an additive in the cross coupled reaction. The TPR profile of Au/TiO_2 (**Fig. 5.2(BI)**) exhibits a single H_2 consumption peak (T_{max} = 378 K) that exceeds the amount needed for Au^{3+} reduction to Au^0 (**Table 5.1**), suggesting partial support reduction [5.50]. Reduction of Au/MgO (**Fig. 5.2(CI)**) generated a broader higher temperature (T_{max} = 510 K) signal, where H_2 consumption was appreciably lower (**Table 5.1**) than that required for precursor reduction and can be ascribed to reduction *pre*-TPR during catalyst synthesis and drying [5.51]. Representative STEM images **(BII**, **CII)** and particle size distributions **(BIII**, **CIII)** are provided in **Fig. 5.2**. Au/TiO_2 is characterised by a narrow particle size range (1-6 nm) and a mean (3.2 nm) close to that of Cu/SiO_2. In contrast, Au/MgO bore larger Au particles (1-15 nm, mean = 7.7 nm), which is a consequence of preparation by impregnation that generates weak precursor-support interaction resulting in mobility and agglomeration during thermal treatment [5.52]. Gold particle size <10 nm has been identified as critical for significant activity in hydrogenation applications [5.35]. A significantly higher H_2 chemisorption

capacity was recorded for Au/TiO_2 relative to Au/MgO (**Table 5.1**) that can be linked to the smaller Au particle size [5.53] and a contribution due to the $Au\text{-}TiO_2$ interface [5.54] which facilitates H_2 activation/dissociation. The performance of Au/TiO_2 and Au/MgO can be assessed against Cu/SiO_2 in the stand-alone benzyl alcohol dehydrogenation and hydrogenation of nitrobenzene in **Fig. 5.5**. The results establish lower (by an order of magnitude) dehydrogenation rates for the two Au catalysts (**Fig. 5.5(A)**). The negligible activity for gas phase alcohol dehydrogenation over supported Au recorded in this work is consistent with results for ethanol dehydrogenation over silica supported Au at $T < 523$ K [5.55]. Au/TiO_2 delivered an appreciably higher nitrobenzene hydrogenation rate than Cu/SiO_2 and Au/MgO (**Fig. 5.5(B)**) and can be correlated to the H_2 chemisorption values in **Table 5.1** and the promotional effect of TiO_2 and the $Au\text{-}TiO_2$ interface for $–NO_2$ activation.

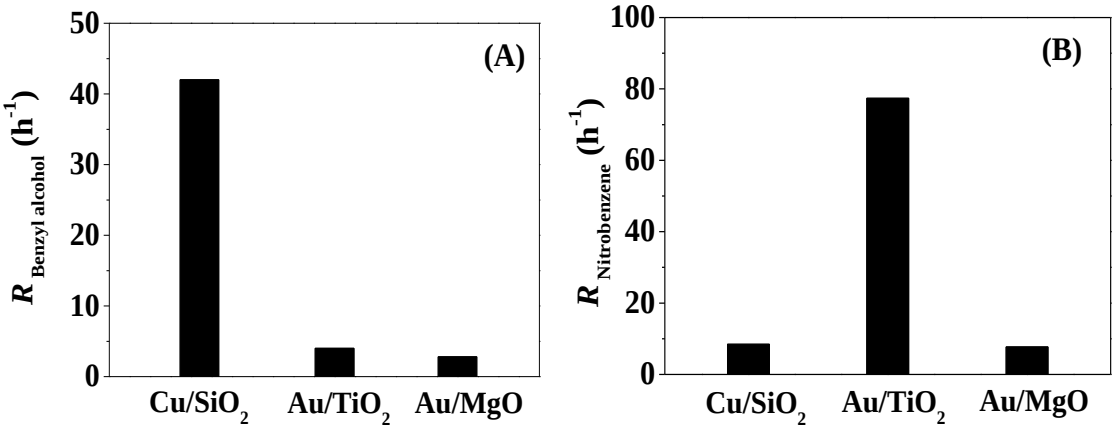

Fig. 5.5: Reaction rates for (A) dehydrogenation of benzyl alcohol and (B) hydrogenation of nitrobenzene over Cu/SiO_2, Au/TiO_2 and Au/MgO. *Reaction conditions*: T = 498 K, P = 1 atm.

5.3.3 Cu/SiO_2 combined with Au/TiO_2 and Au/MgO: Catalytic Response in Coupled Reaction

We first assessed the catalytic action of mixed (Cu + Au) catalysts by varying the Cu/Au molar ratio (10, 20 and 80). The results are presented in **Table 5.3** and **Fig. 5.6** where benzaldehyde and target *N*-benzylideneaniline were the only detected products. Imine production was enhanced upon incorporating Au/TiO_2 with Cu/SiO_2 where rate increased at higher Au content (Cu/Au from 80 to 10). This demonstrates the contribution of Au/TiO_2 to harness the hydrogen (generated from dehydrogenation, **Fig. 5.1**, step **(II)**) and promote nitroarene reduction (step **(I)**) with subsequent condensation (aniline + aldehyde) to imine (step **(III)**). We envision a synergism between Au and Cu

Table 5.3: Imine formation rate (*R*), molar (benzaldehyde/imine) product ratio ($N_{\text{-C=O}}/N_{\text{-C=N}}$) and hydrogen utilisation efficiency (mol H_2 generated from alcohol dehydrogenation per mol imine produced (H_2/–C=N)) as a function of Cu/Au molar ratio for the coupled benzyl alcohol and nitrobenzene reactions over Cu/SiO_2 and oxide supported Au + Cu physical mixtures; *Reaction conditions*: *T* = 498 K, *P* = 1 atm, inlet alcohol/nitroarene molar ratio (–OH/–NO_2) = 3.

Catalyst	Cu/Au	R (mmol mol_{Cu}^{-1} h^{-1})	$N_{\text{-C=O}}/N_{\text{-C=N}}$	H_2/–C=N
Cu/SiO_2	-	358	3.8	6
Cu/SiO_2 +Au/TiO_2	80	609	4.4	6
Cu/SiO_2 +Au/TiO_2	20	1219	2.6	4
Cu/SiO_2 +Au/TiO_2	10	1407	2.0	3
Cu/SiO_2 +Au/MgO	20	368	4.9	6
Cu/SiO_2 +Au/MgO	10	961	2.9	4

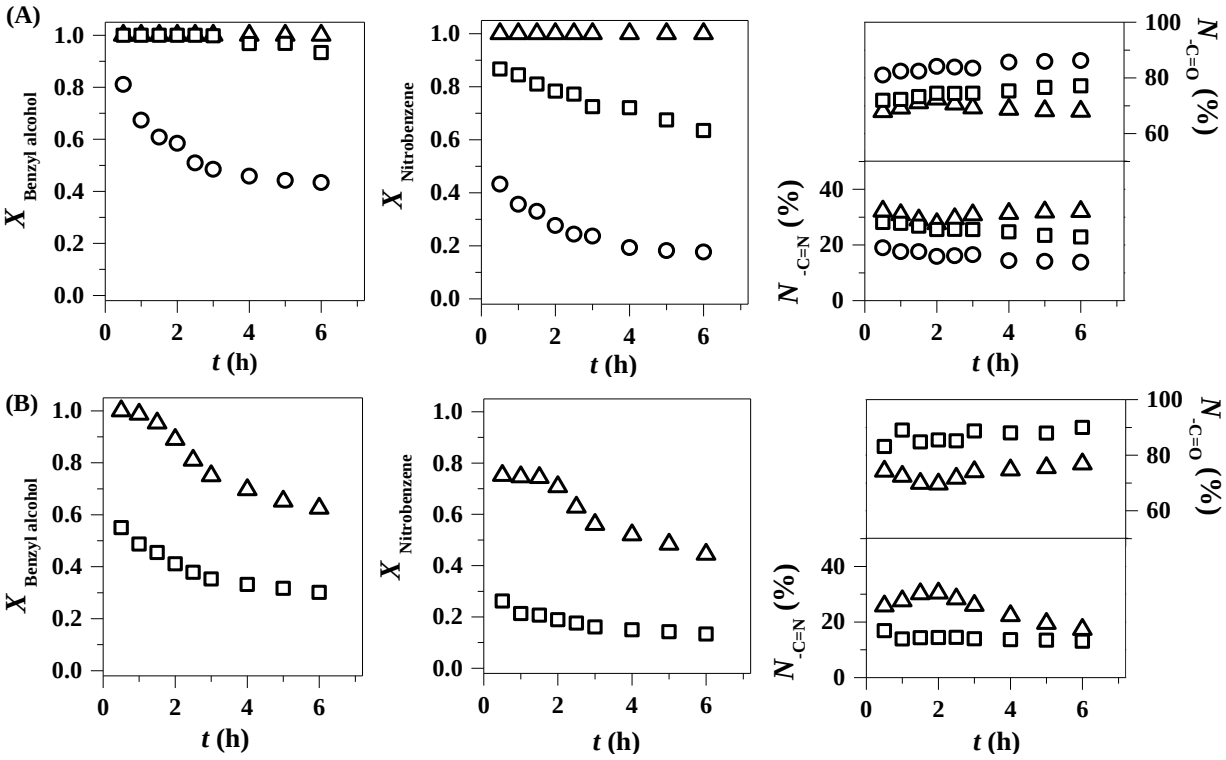

Fig. 5.6: Variation of fractional conversion (X_i) and product composition (N_j) with time on-stream for the coupled benzyl alcohol and nitrobenzene reactions as a function of Cu/Au ratio (△: 10, □: 20 and ○: 80) over (A) Cu/SiO_2 + Au/TiO_2 and (B) Cu/SiO_2 + Au/MgO physical mixtures. *Reaction conditions*: *T* = 498 K, –OH/–NO_2 = 3, *P* = 1 atm.

that is illustrated in the schematic representation in **Fig. 5.7**. The supported Cu phase promotes alcohol dehydrogenation with hydrogen abstraction (step **(I)**). Fridman *et al.*

[5.56] have proposed a two-step H abstraction mechanism for Cu catalysed cyclohexanol dehydrogenation where interaction between metal and the abstracted hydrogen resulted in the formation of transient Ru-H [5.57], Ag-H [5.45] and Ni-H [5.47]. Hydrogen on Cu sites (Cu-H) can "spillover" across the Cu-SiO_2 interface, the physical interface with Au/TiO_2 and onto Au sites (step **(II)**) [5.58] with auto-transfer in

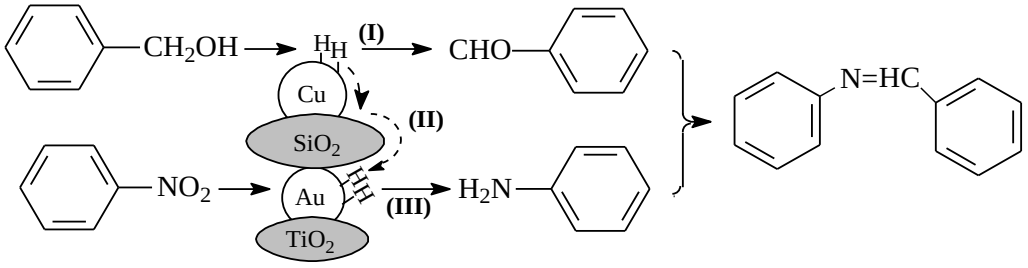

Fig. 5.7: Schematic illustrating Cu-Au cooperation effect in imine production.

the catalytic conversion of nitrobenzene to aniline (step **(III)**). Further hydrogenation of imine to *N*-benzylaniline (**Fig. 5.1**, step **(IV)**) was not observed which may be due to competition with nitrobenzene for surface hydrogen. We obtained full hydrogen utilisation (H_2/–C=N = 3) and imine formation ($N_{\text{-C=O}}/N_{\text{-C=N}}$ = 2) over Cu/SiO_2 + Au/TiO_2 at Cu/Au = 10. This represents unprecedented performance in terms of atom efficiency and hydrogen usage relative to conventional batch liquid phase reactions conducted in pressurised H_2 (P_{H_2} = 4-12 bar) [5.4]. Moreover, activity and selectivity in the coupled reactions over Cu/SiO_2 + Au/TiO_2 (Cu/Au = 10) were invariant for up to 6 h on-stream (**Fig. 5.6(A)**), which represents a marked improvement in stability relative to reaction over Cu/SiO_2 (**Fig. 5.4(A)**). We could find no published study where the catalytic response in coupled reactions over physically combined Cu + Au catalysts has been investigated. We should note published work where physical mixtures of (graphite) supported Pd (or Pt) with supported bimetallic Fe-Ce exhibited higher stability and activity relative to the individual catalysts in the hydrogenation-isomerisation of 1,3-butadiene to butane [5.59]. Incorporation of Au/MgO with Cu/SiO_2 (**Table 5.3**, **Fig. 5.6(B)**) also served to enhance imine production rate with increasing Au content (Cu/Au = 20 → 10). This is again indicative of a cooperative effect in terms of alcohol dehydrogenation at Cu sites (**Fig. 5.7**, step **(I)**) with hydrogen release that works in tandem with –NO_2 hydrogenation on Au/MgO (**Fig. 5.7**, step **(III)**). The promotional effect was not as significant as that observed with Au/TiO_2, which can be attributed to the facilitated adsorption/activation of –NO_2 on TiO_2 and at the Au-TiO_2

interface, greater hydrogen chemisorption capacity (**Table 5.1**) with resultant higher nitrobenzene reduction activity (**Fig. 5.5(B)**) of the latter [5.26].

5.3.4 Cu/SiO_2 and Cu/SiO_2 combined with Au/TiO_2: Characterisation (*Post*-reaction)

Given the decline in activity with time on-stream over Cu/SiO_2 (**Fig. 5.4(A)**) we subjected a spent sample to characterisation measurements in order to arrive at a possible cause for catalyst deactivation. We also carried through the same analyses for a spent Au/TiO_2 + Cu/SiO_2 (Cu/Au = 10) physical mixture that delivered full conversion/hydrogen utilisation over 6 h on-stream (**Fig. 5.6(A)**). Catalyst deactivation in reactions involving alcohols and amines (or nitro-compounds) has been ascribed to active site occlusion/poisoning (*e.g.* nitride formation [5.22], coke [5.60] and amine/nitro-compound deposition [5.24]) and/or changes to the oxidation state of the active metal [5.61]. Analysis by XPS provides information on surface composition and the chemical/electronic state of the supported metal phase. Spectra over the C1*s* **(A)** and Cu $2p_{3/2}$ **(B)** binding energy (BE) regions are shown in **Fig. 5.8**. The C1*s* profile for unused Cu/SiO_2 **(AI)** exhibits a contribution due to adventitious carbon (BE = 284.5 eV) with a secondary peak (BE = 286.1 eV) corresponding to C–OH or C–O–C [5.32].

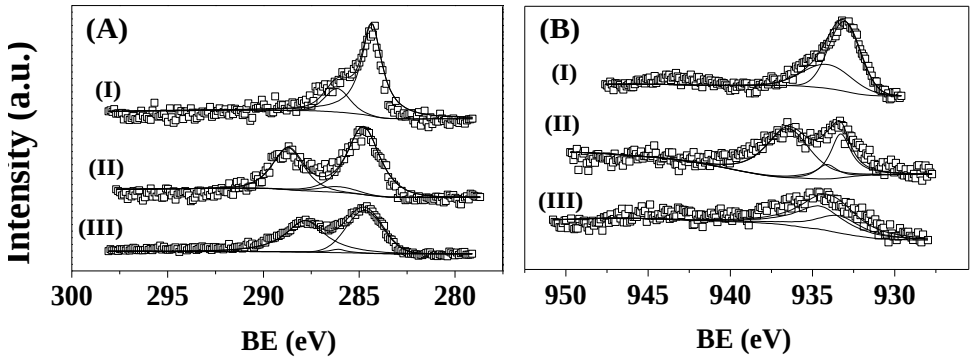

Fig. 5.8: XPS spectra: (A) C1*s* and (B) Cu $2p_{3/2}$ (I) *pre*- and (II) *post*-reaction over Cu/SiO_2 and (III) after reaction over Cu/SiO_2 + Au/TiO_2; experimental data are given by □ where lines represent the fits with peak.

An additional peak at 288.7 eV for the spent Cu/SiO_2 **(AII)** can be tentatively linked to the carboxyl functionality in benzoate species (BE = 288.6-289.1 eV) [5.62]. The Cu $2p_{3/2}$ spectrum for the passivated unused Cu/SiO_2 **(BI)** presents a principal peak at BE = 933.2 eV characteristic of electron deficient copper ($Cu^{\delta+}$ = 933.0-933.6 eV) [5.63]. The spectrum also shows a secondary peak at higher BE = 934.1 eV that corresponds to

CuO (BE = 934.0 eV [5.29]) and may be due to surface Cu oxidation during passivation [5.64]. *Post*-reaction **(BII)**, a peak at higher BE (936.5 eV) suggests a surface ionic Cu species [5.65.5.66] that can be ascribed to copper benzoate formation. A decrease in CuO was accompanied which can be tentatively attributed to the transformation (of CuO) to copper benzoate. The formation of a surface benzoate has been proposed elsewhere [5.67] for reaction of benzaldehyde over oxide (SiO_2, TiO_2, ZrO_2 and CeO_2) supported Cu under similar reaction conditions (T = 373-623 K) to those used in this work. The occurrence of Cu benzoate resulting from surface reaction of benzaldehyde with water (release from $–NO_2$ reduction) can reduce the number of available active sites and inhibits benzyl alcohol dehydrogenation, limiting hydrogen generation and subsequent nitrobenzene reduction and imine formation. The spectrum for the used Cu/SiO_2 over the N1*s* region (396-400 eV, not shown) did not present any detectable signals and we have no evidence for the formation of copper nitride and/or nitrogenous species (T = 510 K, P = 1 atm) as has been proposed elsewhere [5.22].

The XPS profile of the (Au + Cu) physical mixture *post*-reaction (**Fig. 5.8(AIII)**) exhibits a C1*s* peak at 287.8 eV that falls within the BE range (287.3-287.9 eV) reported for –C=O species [5.68-5.70], and can be attributed to benzaldehyde deposition on catalyst surface. Liu and co-authors [5.69] attributed a C1*s* signal at 287.8 eV to aldehyde deposition on copper surface during furfural hydrogenation. In contrast to the spent Cu/SiO_2, there was no detectable C1*s* signal attributable to a benzoate. The absence of –C=O peak can be linked to the transformation of benzaldehyde to benzoate. In the Cu $2p_{3/2}$ BE range (**Fig. 5.8(BIII)**), peaks characteristic of $Cu^{\delta+}$ and CuO were observed with no signal at BE > 936 eV for Au/TiO_2 + Cu/SiO_2. This suggests suppressed benzoate formation in the presence of Au/TiO_2. The incorporation of Au/TiO_2 with Cu/SiO_2 provides a more efficient site for nitrobenzene hydrogenation and aniline condensation with benzaldehyde (**Fig. 5.7**). This can act to ameliorate Cu deactivation as benzaldehyde reaction and $–NO_2$ reduction (with H_2O generation) proceeds at Au sites. The BE for Au $4f_{7/2}$ (83.2 ± 0.2 eV) and Au $4f_{5/2}$ (86.7 ± 0.2 eV) were lower than the reference Au^0 (84.0 eV and 87.8 eV) [5.71], suggesting the formation of an electron rich ($Au^{\delta-}$) phase as a result of electron donation from TiO_2 [5.72]. There was no measurable difference in Au BE *pre*- and *post*-reaction (profiles not shown).

The possible formation of carbonaceous deposits was further evaluated by TGA-DSC and elemental (C, H and N) analysis; the results are presented in **Fig. 5.9**. *Pre*-reaction, Cu/SiO_2 **(I)** and Cu/SiO_2 + Au/TiO_2 **(II)** exhibited a similar (2-3% w/w) mass loss at $T \leq 373$ K due to water removal (**Fig. 5.9(A)**). Both spent samples displayed an additional higher temperature mass loss that can be attributed to combustion of carbonaceous species [5.60]. Elemental analysis (see inset Table in **Fig. 5.9(A)**) revealed a higher carbon content on the spent Cu/SiO_2 relative to the physical mixture.

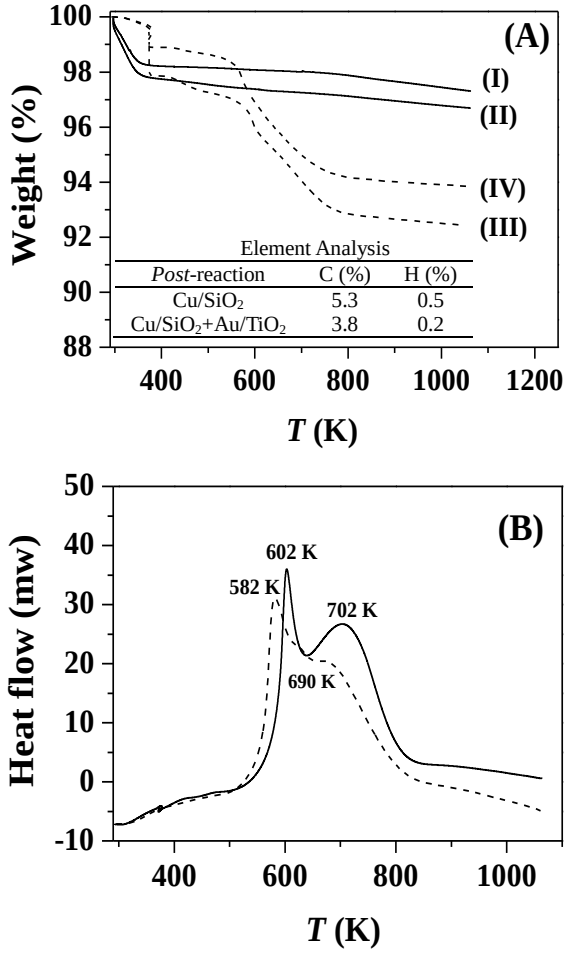

Fig. 5.9: (A) TGA profiles for catalysts *pre*-reaction (solid lines: (I) Cu/SiO_2; (II) Cu/SiO_2 + Au/TiO_2) and *post*-reaction (dashed lines: (III) Cu/SiO_2; (IV) Cu/SiO_2 + Au/TiO_2); Inset table: element (C, H and N) analysis and (B) DSC analysis of Cu/SiO_2 (solid line) and Cu/SiO_2 + Au/TiO_2 (dashed line) *post*-reaction.

There was no measurable N content, consistent with XPS results. The DSC profile of the spent Cu/SiO_2 (**Fig. 5.9(B)**) exhibits two exothermic mass losses (at 602 K and 702 K) during the temperature program oxidation, indicative of different structural carbon deposits on the catalyst surface after reaction. The lower temperature exothermic mass loss matches that (553-613 K) corresponding to combustion of amorphous aromatic

carbonaceous species [5.73,5.74]. Based on the DSC work of Siqueira *et al.* [5.75], the exothermic mass loss at higher temperature can be attributed to combustion of (copper) benzoate species. The DSC profile for the used Cu/SiO_2 + Au/TiO_2 mixture presents a principal mass loss at lower temperature (582 K) with a secondary shoulder at 690 K. This can be taken as indicative of limited deposition of surface benzoate as suggested by the XPS analysis.

5.4 Conclusion

We have established the viability of ‘‘hydrogen-free’’ imine (*N*-benzylideneaniline) production *via* continuous gas phase cross coupling of benzyl alcohol dehydrogenation with nitrobenzene hydrogenation and condensation over physical mixtures of supported Cu and Au catalysts. Dehydrogenation of benzyl alcohol to benzaldehyde over Cu/SiO_2 (mean Cu size = 3.1 nm) delivered a ten-fold higher rate than Au/TiO_2 (mean Au size = 3.2 nm) where the latter exhibited significantly greater H_2 chemisorption capacity and nitrobenzene hydrogenation rate. Reaction over Cu/SiO_2 promoted cross coupling to imine where an increase in temperature and inlet reactant alcohol/nitroarene ratio (–OH/–NO_2) served to enhance imine formation. The Cu catalyst suffered severe temporal decline in activity and selectivity that is linked to carbon (benzoate species from XPS and TGA-DSC measurements) deposition where low hydrogen utilisation is due to the low hydrogenation capacity of Cu. Incorporation of Au/TiO_2 with Cu/SiO_2 resulted in (4-fold) higher imine production rate with full hydrogen utilisation at Cu/Au = 10. We attribute this effect to synergism between Cu and Au where hydrogen release from benzyl alcohol dehydrogenation on Cu was transferred to Au for nitrobenzene reduction (to aniline) and subsequent condensation with benzaldehyde to the imine. The promotional effect of Au/TiO_2 was greater than that observed with the addition of Au/MgO and can be attributed to the greater H_2 chemisorption capability and –NO_2 reduction capacity of the former. Coupled reaction over Cu + Au exhibited stable performance with time on-stream where predominant hydrogenation and condensation on Au sites circumvents Cu deactivation. Our results establish the feasibility of continuous stable gas phase synthesis of imine using a ‘‘hydrogen borrowing’’ strategy over combined supported Cu and Au catalysts.

5.5 References

[5.1] W.J. Cui, Q. Xiao, S. Sarina, W.L. Ao, M.X. Xie, H.Y. Zhu, Z. Bao, *Au-Pd alloy nanoparticle catalyzed selective oxidation of benzyl alcohol and tandem synthesis of imines at ambient conditions*. Catal. Today 235 (2014) 152-159.

[5.2] R.D. Patil, S. Adimurthy, *Catalytic methods for imine synthesis*. Asian J. Org. Chem. 2 (2013) 726-744.

[5.3] A. Srivani, P.S.S. Prasad, N. Lingaiah, *Reductive amination of carbonyl compounds over silica supported palladium exchanged molybdophosphoric acid catalysts*. Catal. Lett. 142 (2012) 389-396.

[5.4] L.L. Santos, P. Serna, A. Corma, *Chemoselective synthesis of substituted imines, secondary amines, and β-amino carbonyl compounds from nitroaromatics through cascade reactions on gold catalysts*. Chem. Eur. J. 15 (2009) 8196-8203.

[5.5] E. Cetinkaya, I. Dincer, G.F. Naterer, *Life cycle assessment of various hydrogen production methods*. Int. J. Hydrogen Energ. 37 (2012) 2071-2080.

[5.6] M. Largeron, *Protocols for the catalytic oxidation of primary amines to imines*. Eur. J. Org. Chem. 2013 (2013) 5225-5235.

[5.7] A. Grirrane, A. Corma, H. Garcia, *Highly active and selective gold catalysts for the aerobic oxidative condensation of benzylamines to imines and one-pot, two-step synthesis of secondary benzylamines*. J. Catal. 264 (2009) 138-144.

[5.8] L. Al-Hmoud, C.W. Jones, *Reaction pathways over copper and cerium oxide catalysts for direct synthesis of imines from amines under aerobic conditions*. J. Catal. 301 (2013) 116-124.

[5.9] L.L. Zhang, W.T. Wang, A.Q. Wang, Y.T. Cui, X.F. Yang, Y.Q. Huang, X.Y. Liu, W.G. Liu, J.Y. Son, H.S. Oji, T. Zhang, *Aerobic oxidative coupling of alcohols and amines over Au-Pd/resin in water: Au/Pd molar ratios switch the reaction pathways to amides or imines*. Green Chem. 15 (2013) 2680-2684.

[5.10] H.W. Tian, X.C. Yu, Q. Li, J.X. Wang, Q. Xu, *General, green, and scalable synthesis of imines from alcohols and amines by a mild and efficient copper-catalyzed aerobic oxidative reaction in open air at room temperature*. Adv. Synth. Catal. 354 (2012) 2671-2677.

[5.11] L. Jiang, L.L. Jin, H.W. Tian, X.Q. Yuan, X.C. Yu, Q. Xu, *Direct and mild palladium-catalyzed aerobic oxidative synthesis of imines from alcohols and amines under ambient conditions*. Chem. Commun. 47 (2011) 10833-10835.

[5.12] H. Sun, F.-Z. Su, J. Ni, Y. Cao, H.-Y. He, K.-N. Fan, *Gold supported on hydroxyapatite as a versatile multifunctional catalyst for the direct tandem synthesis of imines and oximes*. Angew. Chem. Int. Edit. 48 (2009) 4390-4393.

[5.13] M.T. Schuemperli, C. Hammond, I. Hermans, *Developments in the aerobic oxidation of amines*. ACS Catal. 2 (2012) 1108-1117.

[5.14] J. Chen, S.J. Huang, J. Lin, W.P. Su, *Recyclable palladium catalyst for facile synthesis of imines from benzyl alcohols and nitroarenes*. Appl. Catal. A: Gen. 470 (2014) 1-7.

[5.15] Y. Xiang, Q. Meng, X. Li, J. Wang, *In situ hydrogen from aqueous-methanol for nitroarene reduction and imine formation over an Au-Pd/Al_2O_3 catalyst*. Chem. Commun. 46 (2010) 5918-5920.

[5.16] A.L. Korich, T.S. Hughes, *A facile, one-pot procedure for forming diarylimines from nitroarenes and benzaldehydes*. Synlett. 16 (2007) 2602-2604.

[5.17] R.J. Giraud, P.A. Williams, A. Sehgal, E. Ponnusamy, A.K. Phillips, J.B. Manley, *Implementing green chemistry in chemical manufacturing: A survey report*. ACS Sustain. Chem. Eng. 2 (2014) 2237-2242.

[5.18] A. Malaika, M. Kozłowski, *Modification of activated carbon with different agents and catalytic performance of products obtained in the process of ethylbenzene dehydrogenation coupled with nitrobenzene hydrogenation*. Chem. Eng. J. 171 (2011) 1348-1355.

[5.19] Y.L. Zhu, J. Yang, G.Q. Dong, H.Y. Zheng, H.H. Zhang, H.W. Xiang, Y.W. Li, *An environmentally benign route to gamma-butyrolactone through the coupling of hydrogenation and dehydrogenation*. Appl. Catal. B: Environ. 57 (2005) 183-190.

[5.20] B.M. Nagaraja, A.H. Padmasri, P. Seetharamulu, K.H.P. Reddy, B.D. Raju, K.S.R. Rao, *A highly active Cu-MgO-Cr_2O_3 catalyst for simultaneous synthesis of furfuryl alcohol and cyclohexanone by a novel coupling route: Combination of furfural hydrogenation and cyclohexanol dehydrogenation*. J. Mol. Catal. A: Chem. 278 (2007) 29-37.

[5.21] B.M. Nagaraja, A.H. Padmasri, B.D. Raju, K.S.R. Rao, *Production of hydrogen through the coupling of dehydrogenation and hydrogenation for the synthesis of cyclohexanone and furfuryl alcohol over different promoters supported on Cu-MgO catalysts*. Int. J. Hydrogen Energ. 36 (2011) 3417-3425.

[5.22] A. Baiker, *Catalytic amination of aliphatic-alcohols: The role of hydrogen as inhibitor for catalyst deactivation*. Ind. Eng. Chem. Res. Prod. Dev. 20 (1981) 615-618.

[5.23] A. Baiker, D. Monti, Y.S. Fan, *Deactivation of copper, nickel and cobalt catalysts by interaction with aliphatic amines*. J. Catal. 88 (1984) 81-88.

[5.24] G. Guillena, D.J. Ramon, M. Yus, *Hydrogen autotransfer in the N-alkylation of amines and related compounds using alcohols and amines as electrophiles*. Chem. Rev. 110 (2010) 1611-1641.

[5.25] T. Mitsudome, K. Kaneda, *Gold nanoparticle catalysts for selective hydrogenations*. Green Chem. 15 (2013) 2636-2654.

[5.26] M. Boronat, P. Concepción, A. Corma, S. González, F. Illas, P. Serna, *A molecular mechanism for the chemoselective hydrogenation of substituted nitroaromatics with nanoparticles of gold on TiO_2 catalysts: A cooperative effect between gold and the support*. J. Am. Chem. Soc. 129 (2007) 16230-16237.

[5.27] Z. Huang, F. Cui, J. Xue, J. Zuo, J. Chen, C. Xia, *Cu/SiO_2 catalysts prepared by hom- and heterogeneous deposition-precipitation methods: Texture, structure, and catalytic performance in the hydrogenolysis of glycerol to 1,2-propanediol*. Catal. Today 183 (2012) 42-51.

[5.28] J.P. Espinós, J. Morales, A. Barranco, A. Caballero, J.P. Holgado, A.R. González-Elipe, *Interface effects for Cu, CuO, and Cu_2O deposited on SiO_2 and ZrO_2: XPS determination of the valence state of copper in Cu/SiO_2 and Cu/ZrO_2 catalysts*. J. Phys. Chem. B 106 (2002) 6921-6929.

[5.29] J. Gong, H. Yue, Y. Zhao, S. Zhao, L. Zhao, J. Lv, S. Wang, X. Ma, *Synthesis of ethanol via syngas on Cu/SiO_2 catalysts with balanced Cu^0-Cu^+ sites*. J. Am. Chem. Soc. 134 (2012) 13922-13925.

[5.30] A.M. Visco, F. Neri, G. Neri, A. Donato, C. Milone, S. Galvagno, *X-ray photoelectron spectroscopy of Au/Fe_2O_3 catalysts*. Phys. Chem. Chem. Phys. 1 (1999) 2869-2873.

[5.31] T.L. Barr, S. Seal, *Nature of the use of adventitious carbon as a binding energy standard*. J. Vac. Sci. Technol. A 13 (1995) 1239-1246.

[5.32] M.C. Biesinger, B.P. Payne, A.P. Grosvenor, L.W.M. Lau, A.R. Gerson, R.S. Smart, *Resolving surface chemical states in XPS analysis of first row transition metals, oxides and hydroxides: Cr, Mn, Fe, Co and Ni*. Appl. Surf. Sci. 257 (2011) 2717-2730.

[5.33] J. Kleiman, M. Tagawa, *Protection of materials and structures from the space environment*, Y. Kimoto (Ed.), Springer, Berlin, 2013.

[5.34] M. Li, X. Wang, N. Perret, M.A. Keane, *Enhanced production of benzyl alcohol in the gas phase continuous hydrogenation of benzaldehyde over Au/Al_2O_3*. Catal. Commun. 46 (2014) 187-191.

[5.35] G.C. Bond, C. Louis, D.T. Thompson, *Catalysis by gold*, G.J. Hutchings (Ed.), Imperial College Press, London, 2006.

[5.36] S. Jujjuri, M.A. Keane, *Catalytic hydrodechlorination at low hydrogen partial pressures: Activity and selectivity response*. Chem. Eng. J. 157 (2010) 121-130.

[5.37] K.V. Murthy, P.M. Patterson, G. Jacobs, B.H. Davis, M.A. Keane, *An exploration of activity loss during hydrodechlorination and hydrodebromination over Ni/SiO_2*. J. Catal. 223 (2004) 74-85.

[5.38] J. Fan, Y.H. Dai, Y.L. Li, N.F. Zheng, J.F. Guo, X.Q. Yan, G.D. Stucky, *Low-temperature, highly selective, gas-phase oxidation of benzyl alcohol over mesoporous K-Cu-TiO_2 with stable copper(I) oxidation state*. J. Am. Chem. Soc. 131 (2009) 15568-15569.

[5.39] R.K. Marella, C.K.P. Neeli, S.R.R. Kamaraju, D.R. Burri, *Highly active Cu/MgO catalysts for selective dehydrogenation of benzyl alcohol into benzaldehyde using neither O_2 nor H_2 acceptor*. Catal. Sci. Technol. 2 (2012) 1833-1838.

[5.40] F. Cárdenas-Lizana, S. Gómez-Quero, C.J. Baddeley, M.A. Keane, *Tunable gas phase hydrogenation of m-dinitrobenzene over alumina supported Au and Au-Ni*. Appl. Catal. A: Gen. 387 (2010) 155-165.

[5.41] M.E. Crivello, C.F. Perez, S.N. Mendieta, S.G. Casuscelli, G.A. Eimer, V.R. Elias, E.R. Herrero, *n-Octyl alcohol dehydrogenation over copper catalysts*. Catal. Today 133 (2008) 787-792.

[5.42] G.D. Yadav, R.K. Mewada, *Novelties of azobenzene synthesis via selective hydrogenation of nitrobenzene over nano-fibrous Ag-OMS-2: Mechanism and kinetics*. Chem. Eng. J. 221 (2013) 500-511.

[5.43] I.I. Obraztsova, N.K. Eremenko, Y.N. Velyakina, *Reaction kinetics of nitrobenzene hydrogenation on a palladium catalyst supported on nanodiamonds*. Kinet. Catal. 49 (2008) 401-406.

[5.44] J. Wang, Z. Yuan, R. Nie, Z. Hou, X. Zheng, *Hydrogenation of nitrobenzene to aniline over silica gel supported nickel catalysts*. Ind. Eng. Chem. Res. 49 (2010) 4664-4669.

[5.45] H. Liu, G.-K. Chuah, S. Jaenicke, *N-alkylation of amines with alcohols over alumina-entrapped Ag catalysts using the "borrowing hydrogen" methodology*. J. Catal. 292 (2012) 130-137.

[5.46] V. Zamlynny, L. Kubelkova, E. Baburek, K. Jiratova, J. Novakova, *Amination of cyclohexanol over metallosilicate-based materials*. Appl. Catal. A: Gen. 169 (1998) 119-125.

[5.47] K. Shimizu, N. Imaiida, K. Kon, S. Siddiki, A. Satsuma, *Heterogeneous Ni catalysts for N-alkylation of amines with alcohols*. ACS Catal. 3 (2013) 998-1005.

[5.48] A. Corma, P. Serna, *Chemoselective hydrogenation of nitro compounds with supported gold catalysts*. Science 313 (2006) 332-334.

[5.49] N. Perret, F. Cárdenas-Lizana, M.A. Keane, *Selective hydrogenation of benzaldehyde to benzyl alcohol over Au/Al_2O_3*. Catal. Commun. 16 (2011) 159-164.

[5.50] X.D. Jiang, Y.P. Zhang, J. Jiang, Y.S. Rong, Y.C. Wang, Y.C. Wu, C.X. Pan, *Characterization of oxygen vacancy associates within hydrogenated TiO_2: A positron annihilation study*. J. Phys. Chem. C 116 (2012) 22619-22624.

[5.51] J.L. Margitfalvi, M. Hegedűs, A. Szegedi, I. Sajó, *Modification of Au/MgO catalysts used in low temperature CO oxidation with Mn and Fe*. Appl. Catal. A: Gen. 272 (2004) 87-97.

[5.52] G.C. Bond, D.T. Thompson, *Catalysis by gold*. Catal. Rev. 41 (1999) 319-388.

[5.53] E. Bus, J.T. Miller, J.A. van Bokhoven, *Hydrogen chemisorption on Al_2O_3-supported gold catalysts*. J. Phys. Chem. B 109 (2005) 14581-14587.

[5.54] I. Nakamura, H. Mantoku, T. Furukawa, A. Takahashi, T. Fujitani, *Influence of Au and TiO_2 structures on hydrogen dissociation over TiO_2/Au(100)*. Surf. Sci. 606 (2012) 1581-1585.

[5.55] Y. Guan, E.J.M. Hensen, *Ethanol dehydrogenation by gold catalysts: The effect of the gold particle size and the presence of oxygen*. Appl. Catal. A: Gen. 361 (2009) 49-56.

[5.56] V.Z. Fridman, A.A. Davydov, K. Titievsky, *Dehydrogenation of cyclohexanol on copper-containing catalysts: II. The pathways of the cyclohexanol dehydrogenation reaction to cyclohexanone on copper-active sites in oxidation state Cu^0 and Cu^+*. J. Catal. 222 (2004) 545-557.

[5.57] K. Yamaguchi, J. He, T. Oishi, N. Mizuno, *The "borrowing hydrogen strategy" by supported ruthenium hydroxide catalysts: Synthetic scope of symmetrically and unsymmetrically substituted amines*. Chem. Eur. J. 16 (2010) 7199-7207.

[5.58] R. Prins, *Hydrogen spillover: Facts and fiction*. Chem. Rev. 112 (2012) 2714-2738.

[5.59] H. Chang, J. Phillips, *Catalytic synergism in physical mixtures of supported iron-cerium and supported noble metal for hydroisomerization of 1,3-butadiene*. Langmuir 13 (1997) 477-482.

[5.60] F. Cárdenas-Lizana, X. Wang, D. Lamey, M. Li, M.A. Keane, L. Kiwi-Minsker, *An examination of catalyst deactivation in p-chloronitrobenzene hydrogenation over supported gold*. Chem. Eng. J. 255 (2014) 695-704.

[5.61] P. Forzatti, L. Lietti, *Catalyst deactivation*. Catal. Today 52 (1999) 165-181.

[5.62] X.-H. Guan, G.-H. Chen, C. Shang, *ATR-FTIR and XPS study on the structure of complexes formed upon the adsorption of simple organic acids on aluminum hydroxide*. J. Environ. Sci. 19 (2007) 438-443.

[5.63] S.D. Jones, L.M. Neal, M.L. Everett, G.B. Hoflund, H.E. Hagelin-Weaver, *Characterization of ZrO_2-promoted Cu/ZnO/nano-Al_2O_3 methanol steam reforming catalysts*. Appl. Surf. Sci. 256 (2010) 7345-7353.

[5.64] F. Cárdenas-Lizana, B. Bridier, C.C.K. Shin, J. Pérez-Ramírez, L. Kiwi-Minsker, *Promotional effect of Ni in the selective gas-phase hydrogenation of chloronitrobenzene over Cu-based catalysts*. ChemCatChem 4 (2012) 668-673.

[5.65] C. Moreno-Castilla, F.J. Maldonado-Hódar, A.F. Pérez-Cadenas, *Physicochemical surface properties of Fe, Co, Ni, and Cu-doped monolithic organic aerogels*. Langmuir 19 (2003) 5650-5655.

[5.66] E. Cano, C.L. Torres, J.M. Bastidas, *An XPS study of copper corrosion originated by formic acid vapour at 40% and 80% relative humidity*. Mater. Corros. 52 (2001) 667-676.

[5.67] A. Saadi, Z. Rassoul, M.M. Bettahar, *Gas phase hydrogenation of benzaldehyde over supported copper catalysts*. J. Mol. Catal. A: Chem. 164 (2000) 205-216.

[5.68] B. Singh, Y.Y. Fang, B.C.C. Cowie, L. Thomsen, *NEXAFS and XPS characterisation of carbon functional groups of fresh and aged biochars*. Org. Geochem. 77 (2014) 1-10.

[5.69] D.X. Liu, D. Zemlyanov, T.P. Wu, R.J. Lobo-Lapidus, J.A. Dumesic, J.T. Miller, C.L. Marshall, *Deactivation mechanistic studies of copper chromite catalyst for selective hydrogenation of 2-furfuraldehyde*. J. Catal. 299 (2013) 336-345.

[5.70] R. Maiti, A. Midya, C. Narayana, S.K. Ray, *Tunable optical properties of graphene oxide by tailoring the oxygen functionalities using infrared irradiation*. Nanotechnology 25 (2014).

[5.71] A. Retnakumari, S. Setua, D. Menon, P. Ravindran, H. Muhammed, T. Pradeep, S. Nair, M. Koyakutty, *Molecular-receptor-specific, non-toxic, near-infrared-emitting Au cluster-protein nanoconjugates for targeted cancer imaging*. Nanotechnology 21 (2010).

[5.72] Y.F. Han, Z.Y. Zhong, K. Ramesh, F.X. Chen, L.W. Chen, T. White, Q.L. Tay, S.N. Yaakub, Z. Wang, *Au promotional effects on the synthesis of H_2O_2 directly from H_2 and O_2 on supported Pd-Au alloy catalysts*. J. Phys. Chem. C 111 (2007) 8410-8413.

[5.73] V.H. Vu, J. Belkouch, A. Ould-Dris, B. Taouk, *Removal of hazardous chlorinated VOCs over Mn-Cu mixed oxide based catalyst*. J. Hazard. Mater. 169 (2009) 758-765.

[5.74] Y.X. Cui, X.S. Zhou, Q. Sun, L. Shi, *Vapor-phase synthesis of 3-methylindole from glycerol and aniline over zeolites-supported Cu-based catalysts*. J. Mol. Catal. A: Chem. 378 (2013) 238-245.

[5.75] A.B. Siqueira, E.Y. Ionashiro, C.T. Carvalho, G. Bannach, E.C. Rodrigues, M. Ionashiro, *Synthesis, characterization and thermal behaviour of solid-state compounds of benzoates with some bivalent transition metal ions*. Quim. Nova 30 (2007) 318-322.

Chapter 6

"Hydrogen Free" Production of 2-Butanone and Aniline over Cu/SiO_2 *via* Reaction Coupling

In this chapter, a coupled reaction system for the simultaneous production of 2-butanone (from 2-butanol dehydrogenation) and aniline (from nitrobenzene hydrogenation) over Cu/SiO_2 in continuous gas phase operation without an external H_2 supply is examined with copper structure-sensitivity. Hydrogen utilisation efficiency is compared with conventional hydrogenation using pressurised hydrogen.

6.1 Introduction

Catalytic hydrogenation is essential in the manufacture of bulk and fine chemicals [6.1]. These processes are typically conducted where hydrogen is far in excess of stoichiometric requirements and is taken from an external pressurised supply that is generated using fossil fuel based technologies [6.2]. Issues of sustainable production and safe handling are now drivers for alternative sources of hydrogen and/or hydrogen donors. Several hydrogen carriers including hydrazine [6.3], ammonia-borane complexes [6.4], esters [6.5], alcohols [6.6] and acids [6.7] have been employed in homogeneous and heterogeneous transfer hydrogenation but application is hampered due to the required separation steps for catalyst reuse. A continuous heterogeneous catalytic system that combines dehydrogenation with hydrogen release that is utilised in hydrogenation represents an alternative approach that circumvents the requirement for an external hydrogen supply. Moreover, the formation of two commercial products (from both dehydrogenation and hydrogenation) offers clear advantages over conventional transfer hydrogenation processes in terms of sustainable chemical manufacture. It is striking that the number of published studies on coupled heterogeneous catalysis systems is so limited. This is possibly due to the requirement for a catalytic component active for both dehydrogenation and hydrogenation. Nonetheless, we can flag the coupling of ethylbenzene dehydrogenation with nitrobenzene hydrogenation over Pt/C [6.8], the butanediol/maleic anhydride combination over Cu-Zn [6.9] and cyclohexanol/furfural conversion over Cu based catalysts [6.10,6.11]. Differences in reactivity of the two reactants, the possibility of

cross reaction between the target products and/or reactants and ease of product separation are crucial considerations. Nagaraja *et al.* [6.10,6.11] studying coupled cyclohexanol dehydrogenation/furfural hydrogenation demonstrated that product yields were constrained by hydrogen generation due to the thermodynamic equilibrium that controls the dehydrogenation step. Climent and co-workers [6.12] examined the coupling of glycols with 1,2-dinitrobenzene and reported cross reaction of dicarbonyl compounds (formed from glycol dehydrogenation) and phenylenediamine (generated from 1,2-dinitrobenzene reduction) to generate quinoxaline.

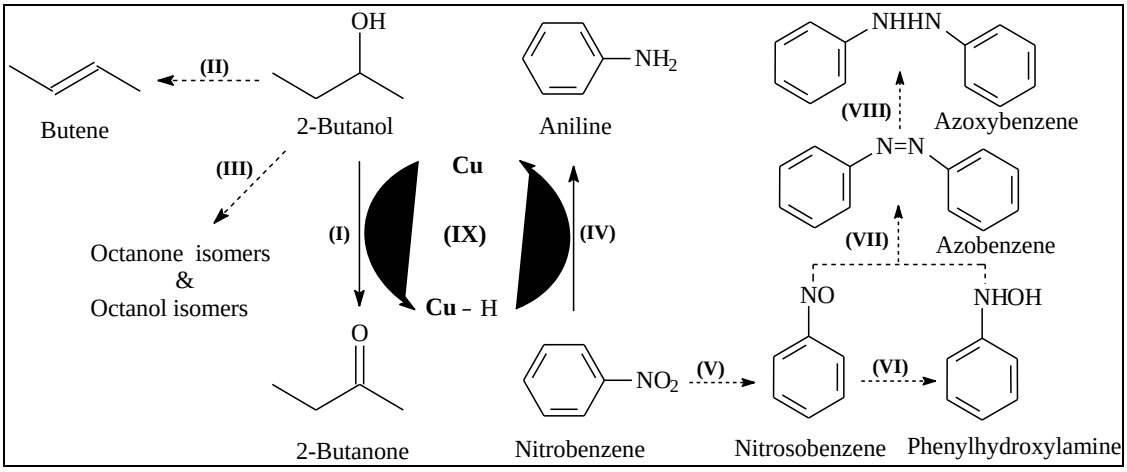

Fig. 6.1: Schematic reaction scheme for 2-butanol dehydrogenation to the target (I) 2-butanone and undesired (II) dehydration to butene and (III) dimerisation to octanone and/or octanol isomers; nitrobenzene hydrogenation to the target (IV) aniline, the intermediates (V) nitrosobenzene and (VI) phenylhydroxylamine and undesired condensation to (VII) azobenzene and (VIII) azoxybenzene; (IX) coupled system; solid arrows denote target reactions while dashed arrows indicate routes to undesired intermediates and products.

The selective catalytic dehydrogenation of 2-butanol to 2-butanone (**Fig. 6.1** step **(I)**), used as a solvent for gums, resins, cellulose acetate and nitrocellulose coatings and vinyl films, is an important industrial process [6.13]. The reaction has been primarily conducted over oxide supported Cu [6.14-6.16] although application of Ag [6.17] and Pd [6.18] based catalysts has also been reported. High selectivity to the target 2-butanone is challenging due to possible formation of butene *via* dehydration (step **(II)**) [6.14,6.19] and/or dimerisation to octanone/octanol isomers (step **(III)**) [6.16]. Aniline is used in the manufacture of dyes, pigments, herbicides and a range of pharmaceuticals [6.20]. Commercial production *via* catalytic hydrogenation of nitrobenzene (step **(IV)**) mainly draws on liquid-phase reaction over supported Ni [6.21,6.22], Pt [6.23-6.25] and Pd [6.26,6.27] but the formation of toxic by-products (nitrosobenzene **(V)**,

phenylhydroxylamine **(VI)**, azobenzene **(VII)** and azoxybenzene **(VIII)**, see **Fig. 6.1**) and the necessity for high reaction pressures (2-50 atm) [6.21,6.27] are still major drawbacks. In this study we have investigated, for the first time, the feasibility of sustainable (ambient pressure) gas phase continuous production of aniline and 2-butanone over Cu/SiO_2 in the absence of an external hydrogen supply by coupling 2-butanol dehydrogenation with nitrobenzene hydrogenation. We correlate catalyst performance with surface structural properties and evaluate hydrogen utilisation efficiency, as a critical sustainability parameter, for the independent and coupled reactions.

6.2 Experimental

6.2.1 Materials and Catalyst Preparation

Two (15.9 and 1.8% w/w) Cu/SiO_2 catalysts were prepared by deposition-precipitation with NaOH (Riedel-de Haën). The (fumed) SiO_2 support and $Cu(NO_3)_2$ were supplied by Sigma-Aldrich and used as received. The silica powder (20 g) was dispersed in a solution (200 cm^3) of $Cu(NO_3)_2$ (0.25 and 0.03 M for high and low loadings, respectively). The suspension was stirred (600 rpm) at room temperature for 1 h, followed by addition of an aqueous NaOH solution (2 M) until pH >10, heated to 353 K and aged under vigorous stirring for 4 h to ensure homogeneous copper deposition [6.28]. The solid was separated by filtration, washed with distilled water (until pH = 7) and dried at 393 K overnight. The dried sample was calcined in air (at 10 K min^{-1} to 723 K for 4 h) to generate a supported copper oxide (CuO) phase [28] and sieved (ATM fine test sieves) to mean particle diameter = 75 μm. Before reaction, the catalyst precursor was activated in 60 cm^3 min^{-1} H_2 at 4 K min^{-1} to 543 K, which was maintained for 2 h. Samples were passivated at ambient temperature in 1% v/v O_2/He for *ex situ* characterisation.

6.2.2 Catalyst Characterisation

Copper loading was determined by atomic absorption spectroscopy using a Shimadzu AA-6650 spectrometer with an air-acetylene flame from the diluted extract in aqua regia (25% v/v HNO_3/HCl). Temperature programmed reduction (TPR) and H_2 chemisorption measurements were conducted on the commercial CHEM-BET 3000 (Quantachrome Instrument) unit with data acquisition/manipulation using the TPR

Win^{TM} software. Samples were loaded into a U-shaped Pyrex glass cell (3.76 mm i.d.) and heated in 17 cm^3 min^{-1} (Brooks mass flow controlled) 5% v/v H_2/N_2 at 4 K min^{-1} to 543 K, swept with 65 cm^3 min^{-1} N_2 for 1.5 h, cooled to ambient temperature and subjected to H_2 chemisorption by pulse (10 μl) titration. In a blank test, there was no measurable H_2 uptake on the SiO_2 support alone. The effluent gas passed through a liquid N_2 trap and H_2 consumption was monitored by a thermal conductivity detector (TCD). Nitrogen adsorption-desorption isotherms were obtained using the commercial Micromeritics Gemini VII 2390p system. Prior to analysis, the samples were outgassed at 423 K for 1 h in N_2. Total specific surface area (SSA) and cumulative pore volume were obtained using the standard BET method and BJH analysis, respectively. Powder X-ray diffractograms (XRD) were recorded on a Bruker/Siemens D500 incident X-ray diffractometer using Cu Kα radiation. Samples were scanned at 0.01º $step^{-1}$ over the range $30º \leq 2\theta \leq 85º$ and the diffractograms identified against the JCPDS-ICDD reference (Cu (04-0836)). Copper particle morphology (size and shape) post-TPR was examined by scanning transmission electron microscopy (STEM, JEOL 2200FS), employing Gatan Digital Micrograph 1.82 for data acquisition/manipulation. Samples for analysis were prepared by dispersion in acetone and deposited on a holey carbon/Cu grid (300 Mesh). The surface area weighted mean Cu size (d) was based on a count of up to 800 particles

$$d = \frac{\sum_i n_i d_i^3}{\sum_i n_i d_i^2} \qquad \textbf{(6.1)}$$

where n_i is the number of particles of diameter d_i. X-ray photoelectron spectroscopic (XPS) analysis was conducted on an Axis Ultra instrument (Kratos Analytical) at ultra-high vacuum conditions ($<10^{-8}$ Torr) with a monochromatic Al Kα radiation (1486 eV). The Cu $2p_{3/2}$ spectra were collected and binding energies (BE) calibrated with respect to the C 1*s* peak (284.5 eV). The Cu $2p_{3/2}$ spectra were fitted with abstraction of the Shirley background using the Gaussian-Lorentzian function in XPSPEAK 41.

6.2.3 Catalytic Procedure

Reactions (stand-alone 2-butanol dehydrogenation and nitrobenzene hydrogenation and coupled dehydrogenation/hydrogenation) were carried out at atmospheric pressure *in situ* after catalyst activation in a continuous flow fixed bed vertical glass reactor (i.d. = 15 mm) at 423-523 K under operating conditions that ensured negligible heat/mass

transport limitations. A layer of borosilicate glass beads served as preheating zone where the reactant(s) (2-butanol and/or nitrobenzene) was (were) vaporised and reached reaction temperature before contacting the catalyst bed. Isothermal conditions (±1 K) were maintained by diluting the catalyst bed with ground glass (75 μm); the ground glass was mixed thoroughly with the catalyst before insertion into the reactor. Reaction temperature was continuously monitored by a thermocouple inserted in a thermowell within the catalyst bed. The reactant(s) was (were) delivered to the reactor *via* a glass/teflon air-tight syringe and teflon line using a microprocessor controlled infusion pump (Model 100 kd Scientific). The independent (uncoupled) reactions were conducted in a co-current flow of N_2 with 2-butanol ($GHSV = 5 \times 10^3$ h^{-1}, molar Cu to reactant feed rate (n_{Cu}/F) = 8.8×10^{-4} - 1.2×10^{-2} h, $X = 0.04$-0.29) or H_2 with nitrobenzene ($GHSV = 1 \times 10^4$ h^{-1}, $n_{Cu}/F = 6 \times 10^{-3}$ - 3×10^{-2} h, $X = 0.03$-0.16). The coupled reaction was carried out in N_2 ($GHSV = 1.2 \times 10^3$ h^{-1}, $n_{Cu}/F = 3 \times 10^{-2}$ - 6×10^{-2} h). In a series of blank tests, passage of each reactant in a stream of H_2 or N_2 through the empty reactor or over the (SiO_2) support alone did not result in any detectable conversion. The reactor effluent was condensed in a liquid nitrogen trap for subsequent analysis using a Perkin-Elmer Auto System XL gas chromatograph equipped with a programmed split/splitless injector and a flame ionisation detector, employing a DB-1 (50 m × 0.33 mm i.d., 0.20 μm film thickness) capillary column (J&W Scientific). Data acquisition and manipulation were performed using the TurboChrom Workstation Version 6.3.2 (for Windows) chromatography data system. 2-Butanol (Sigma-Aldrich, ≥99%), 2-butanone (Sigma-Aldrich, ≥99%), nitrobenzene (Riedel-de Haën, ≥99%) and aniline (Sigma-Aldrich, ≥99%) were used without further purification. All gases (O_2, H_2, N_2 and He) were of high purity (>99.98%, BOC). Reactant (i) fractional conversion (X) is defined by

$$X_{\mathrm{i}} = \frac{[reactant]_{\mathrm{i,\ in}} - [reactant]_{\mathrm{i,\ out}}}{[reactant]_{\mathrm{i,\ in}}} \qquad \textbf{(6.2)}$$

and yield (Y) to product (j) is obtained from

$$Y_{\mathrm{j}}(\%) = \frac{[product]_{\mathrm{j,\ out}}}{[reactant]_{\mathrm{i,\ in}}} \times 100 \qquad \textbf{(6.3)}$$

where subscripts "in" and "out" refer to the inlet and outlet gas streams, respectively. Catalytic activity is quantified in terms of initial reactant consumption rate (R_0, $mol_{reactant}$ mol_{Cu}^{-1} h^{-1}) extracted from time on-stream measurements. Turnover frequency (*TOF*, rate per active site) is obtained from

$$TOF\ (\mathrm{h}^{-1}) = \frac{R_0}{D} \qquad \textbf{(6.4)}$$

where D is the metal dispersion (surface $atom_{Cu}$/total $atom_{Cu}$) determined from STEM measurements. Repeated reactions using different samples from the same batch of catalyst delivered raw data reproducibility and mass balance to within ±5%.

6.3 Results and Discussion

6.3.1 Catalyst Characterisation

The physico-chemical properties of the two Cu/SiO_2 catalysts used in this study are recorded in **Table 6.1**. The SSA and cumulative pore volume of the activated catalysts were lower than that of the starting SiO_2 support (223 $m^2\ g^{-1}$, 0.35 $cm^3\ g^{-1}$). Guerreiro *et al*. [6.29] attributed a decrease in SSA (425 → 198 $m^2\ g^{-1}$) for (2.6% w/w) Cu/SiO_2 relative to the starting SiO_2 to modifications to the support pore structure caused by the high solution pH (11.5) used in catalyst preparation. The TPR profiles (**Fig. 6.2(AI-AII)**)

Table 6.1: Copper loading, specific surface area (SSA), cumulative pore volume, H_2 consumption during temperature programmed reduction (TPR), Cu particle size range and mean (*d*), ambient temperature H_2 chemisorption and principal XPS Cu $2p_{3/2}$ binding energy (BE).

Cu content (%, w/w)	15.9	1.8
SSA ($m^2\ g^{-1}$)	163	192
Pore volume ($cm^3\ g^{-1}$)	0.26	0.34
TPR H_2 consumption (mmol g_{Cu}^{-1})	18.6	15.6
Cu size range (nm)	1-15	1-6
d (nm)	7.8	3.1
H_2 chemisorption (μmol g_{Cu}^{-1})	7	25
XPS Cu $2p_{3/2}$ BE (eV)	932.8	933.2

for both catalyst precursors are similar and characterised by H_2 consumption (see **Table 6.1**) at the final isothermal hold (543 K) that was close to that required for Cu^{2+} reduction to Cu^0 (16 mmol g_{Cu}^{-1}). Reduction over the 410-550 K temperature range has been reported elsewhere for the transformation of bulk CuO to zero valent Cu [6.28]. Smith and co-workers [6.30], investigating the reduction of Cu/SiO_2 as a function of

temperature by *in situ* XRD, proposed a stepwise $Cu^{2+} \rightarrow Cu^{+} \rightarrow Cu^{0}$ sequence where metallic copper prevailed at T >523 K. Structural analysis of the activated Cu/SiO_2 by XRD generated the diffractograms presented in **Fig. 6.2(B)**. The XRD pattern of the Cu rich sample **(I)** exhibits diffraction peaks at 2θ = 43.6°, 50.8° and 73.9° that match Cu (111), (200) and (220) planes (JCPDS-ICDD Cu (04-0836)). There was no detectable signals due to bulk copper oxides (tenorite (CuO, 2θ = 35.5°, 38.7° and 48.7° (05-0661)) or cuprite (Cu_2O, 2θ = 36.6° (05-0667))), confirming full reduction to metallic copper following TPR. The XRD pattern for the lower loaded Cu/SiO_2 **(II)** was featureless and the absence of Cu diffraction peaks suggests the presence of a well dispersed metal phase. It should be noted Grunwaldt *et al*. [6.31] did not observe any XRD peaks for 4.5% w/w Cu/ZnO prepared by precipitation, which they attributed to high Cu dispersion (Cu size <3 nm).

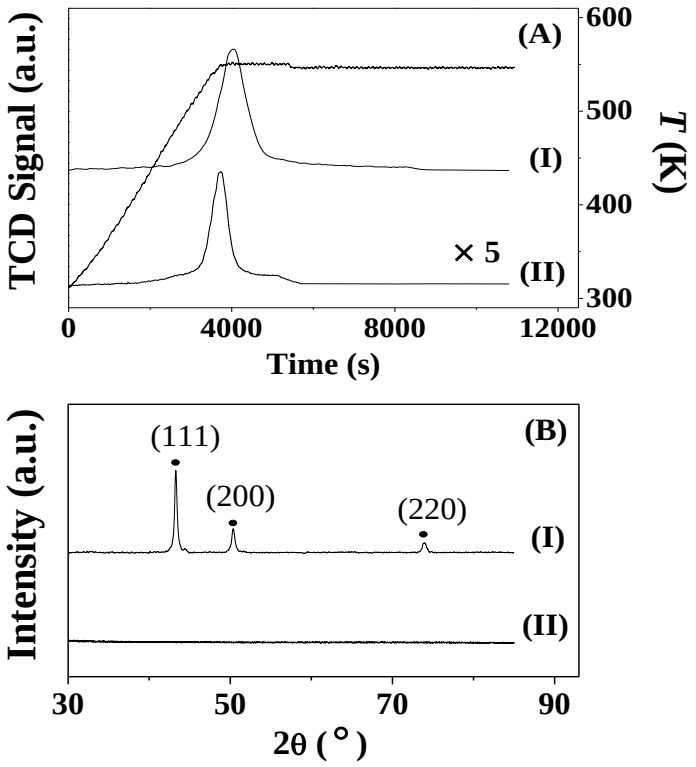

Fig. 6.2: (A) Temperature programmed reduction (TPR) profiles and (B) XRD patterns associated with (I) 15.9% and (II) 1.8% w/w Cu/SiO_2.

Copper particle morphology (size and shape) was analysed by STEM analysis and representative images are provided in **Fig. 6.3** for 15.9% w/w **(AI)** and 1.8% w/w Cu/SiO_2 **(AII)**. In both cases, the metal particles exhibit a quasi-spherical shape. Huang *et al*. [6.28] reported the formation of fibrous and spherical particles in 30% w/w Cu/SiO_2 prepared by deposition-precipitation and activated (in H_2) at 553 K that they attributed to copper phyllosilicate and copper nano-crystals, respectively. The metal

particles associated with the higher loading fall within a relatively broad size range (1-15 nm) with 80% of the total particle count below 6 nm (**Fig. 6.3(BI)**) to give a surface area weighted mean of 7.8 nm (**Table 6.1**). The 1.8% w/w loading is characterised by a narrower size distribution (1-6 nm, **Fig. 6.3(BII)**) with an associated mean of 3.1 nm and

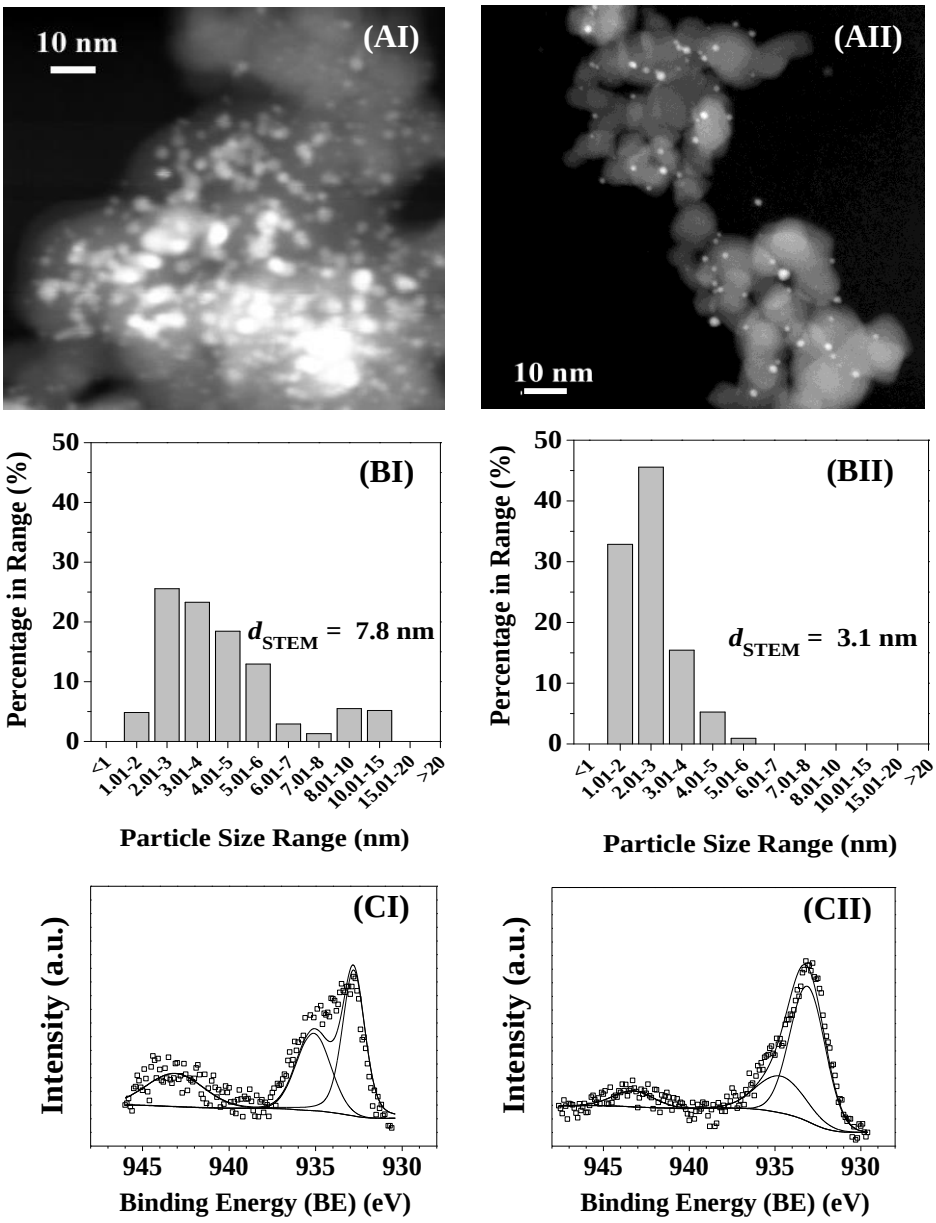

Fig. 6.3: (A) Representative STEM images with (B) associated Cu particle size distribution histograms and (C) XPS spectra over the Cu $2p_{3/2}$ core level for (I) 15.9% and (II) 1.8% w/w Cu/SiO_2.

the majority of particles in the 1-3 nm interval, which can account for the absence of XRD signal due to Cu (see **Fig. 6.2(BII)**). The higher Cu loading must be subjected to particle agglomeration during thermal treatment that resulted in the larger mean size [6.32]. Lambert and co-workers [6.33] also observed bigger metal particles (2 → 30 nm) in Cu/SiO_2 co-gelled xerogel catalysts with increasing loading (0.1-4.5% w/w).

Hydrogen chemisorption is a critical catalyst characteristic in hydrogenation applications. Ambient temperature H_2 uptake for both catalysts (**Table 6.1**) falls within the range of values (0.8-158 μmol g_{Cu}^{-1}) reported elsewhere for (Al_2O_3 [6.34] and C [6.35]) supported Cu samples. We can note here that H_2 uptake was significantly lower than that reported elsewhere for typical oxide supported transition metal catalysts, *e.g.* Pd/SiO_2 (120 μmol g_{Pd}^{-1}) [6.36] and Ni/SiO_2 (600 μmol g_{Ni}^{-1}) [6.37], which can account for the observed lower activity reported for Cu catalysts in hydrogenation reactions [6.38]. The markedly lower specific H_2 chemisorption associated with the higher Cu loading (**Table 6.1**) is consistent with the reported limited H_2 chemisorption capacity for larger (>3 nm) Cu particles [6.39]. XPS measurements were conducted to evaluate the electronic properties of the supported Cu phase in both catalysts. The spectra over the Cu $2p_{3/2}$ binding energy (BE) region are shown in **Fig. 6.3(C)** and the BE values are given in **Table 6.1**. The Cu $2p_{3/2}$ profile for the passivated 15.9% w/w Cu/SiO_2 **(I)** presents a principal peak at BE = 932.8 eV, which matches the value reported for reduced Cu^0 species [6.40]. The main XPS signal appears at higher BE (= 933.2 eV) for 1.8% w/w Cu/SiO_2, suggesting the presence of electron deficient ($Cu^{\delta+}$ and/or Cu^+) surface species (Cu^{2+} BE = 934.0 eV [6.41]). Support interactions and metal particle size (coordination number) can impact on the electronic character of the metal phase with associated shifts in BE [6.42]. The formation of Cu-O-M bonds at the Cu-oxide interface and contributions due to bridging oxygens with different electronic properties from the bulk oxide can modify the electronic structure of supported Cu. Chen *et al.* [6.43] have attributed the occurrence of partially electropositive Cu nanoparticles (2.9 nm) on SiO_2 to electron transfer to the support oxygens. Moreover, a displacement to higher BE (by 0.5-1.0 eV) with decreasing metal particle size (from bulk → Cu_3 cluster) has been reported elsewhere for Cu clusters deposited on a silicon wafer [6.44]. In this work more than 30% of the total Cu content in the lower loaded sample exhibited sizes <2 nm, which can contribute to the positive Cu $2p_{3/2}$ BE shift. Both spectra exhibit two additional peaks at higher BE characteristic of surface Cu^{2+} species (XPS peak at *ca.* 934-936 eV with a satellite peak around 943-944 eV) that can result from (surface) oxidation during the passivation step conducted for *ex situ* characterisation, as reported previously [6.45].

6.3.2 Catalytic Response

We first examined independently the dehydrogenation of 2-butanol (in N_2) and nitrobenzene hydrogenation (using an external H_2 supply) over both Cu/SiO_2 catalysts

in the 423-523 K temperature range; the results are presented in **Fig. 6.4**. Dehydrogenation of 2-butanol resulted in exclusive production of 2-butanone with no detectable dehydration (step **(II)** in **Fig. 6.1**) and/or dimerisation (step **(III)** in **Fig. 6.1**). This is significant given the number of studies that have failed to achieve full selectivity to 2-butanone [6.14,6.16]. The exclusive production of 2-butanone achieved in this study can be associated with the lower reaction temperature employed. Keuler and co-workers [6.14] reported a decrease in 2-butanone selectivity (from 100 → 83%) with increasing temperature (513 → 663 K) over Cu/SiO_2 due to 2-butene formation. Fang *et al.* [6.16] observed 2-butanol dimerisation (to octanone and octanol isomers) over surface acid sites on $Cu/Zn\text{-}Al_2O_3$ at higher temperatures and equivalent degree of conversion to that in our work (≤0.3). The applicability of a pseudo-first order kinetic treatment has been established for the catalytic dehydrogenation of cyclohexane [6.46] and hydrogenation of dinitrobenzene [6.47] where the following expression applies

$$\ln\left[\frac{1}{(1-X_{i,0})}\right] = k\left(\frac{n_{Cu}}{F}\right) \qquad \textbf{(6.5)}$$

$X_{i,0}$ is the initial fractional conversion; (n_{Cu}/F) has the physical meaning of contact time.

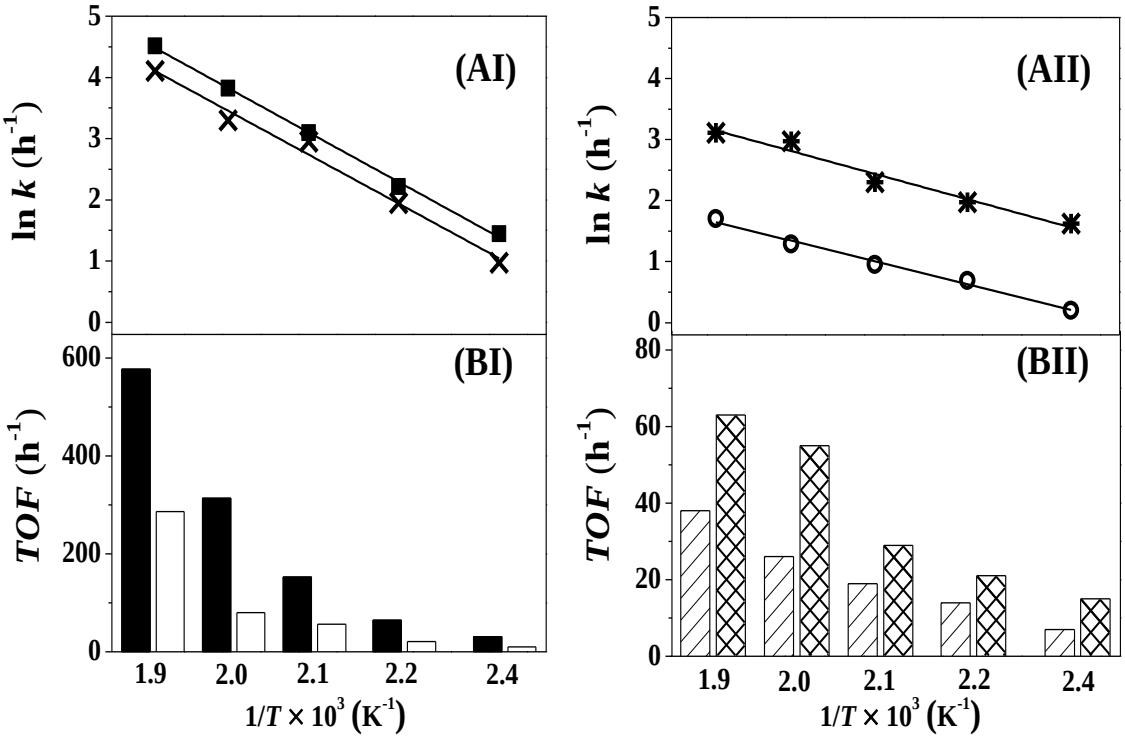

Fig. 6.4: (A) Arrhenius plot and (B) turnover frequency (*TOF*) as a function of reaction temperature (*T*) for stand-alone (I) 2-butanol dehydrogenation and (II) nitrobenzene hydrogenation over 15.9% w/w Cu/SiO_2 (■, ○, solid and hatched bars) and 1.8% w/w (×, ✳, open and cross-hatched bars). *Reaction conditions*: *T* = 423-523 K, *P* = 1 atm.

The associated Arrhenius plots using the extracted rate constants (*k*) for both catalysts are presented in **Fig. 6.4(AI)** where an equivalent apparent activation energy (56±1 kJ mol^{-1}) was obtained, close to that (65 kJ mol^{-1}) reported for reaction over $Cu/ZnO/Al_2O_3$ [6.48]. In order to compare the intrinsic activity of the two catalysts, which bear different Cu size distributions and mean (**Fig. 6.3(A-B)**), 2-butanol specific activity or turnover frequency (*TOF*) was calculated (see section 2.3) and the temperature dependence is illustrated in **Fig. 6.4(BI)**. The Cu rich catalyst (mean = 7.8 nm) delivered a specific dehydrogenation rate that was three times greater than that for the lower loading (mean = 3.1 nm). This response suggests antipathetic structure sensitivity where enhanced intrinsic dehydrogenation efficiency is associated with larger Cu nanoparticles (3.1→7.8 nm). Lambert *et al.* [6.15] also recorded a greater 2-butanol dehydrogenation rate over Cu/SiO_2 with larger Cu size (from 3 to 30 nm). Differences in catalytic dehydrogenation performance over metal nanoparticles have been ascribed to variations in active site electronic character. Fridman *et al.* [6.49] have proposed a two-step mechanism for Cu^0 catalysed cyclohexanol dehydrogenation where abstraction of the second H from the alkoxide intermediate generated by H elimination from the hydroxyl group was rate determining. Shimizu and co-workers, studying the mechanism of alcohol dehydrogenation over Ni/Al_2O_3 [6.50] and Pt/Al_2O_3 [6.51] by *in situ* IR spectra, reported that C-H activation/dissociation of the alkoxide intermediate occurred on zero valent Ni and Pt sites. The higher *TOF* obtained with 15.9% w/w Cu/SiO_2 can be linked to the uncharged (from XPS analysis) character of the Cu sites that must facilitate adsorption of the alkoxide intermediate *via* interaction with the polarised carbon and abstraction of the second H atom. This step is not favoured to the same extent on 1.8% w/w Cu/SiO_2 due to the presence of surface electron deficient species that inhibit dehydrogenation activity due to repulsive effects with respect to the polarised alkoxide.

Gas phase nitrobenzene hydrogenation over Cu/SiO_2 generated aniline as sole product. Industrial aniline production *via* high pressure (2-50 atm) batch liquid-phase hydrogenation over supported Pd [6.27] or Pt [6.52] catalysts generates toxic by-products (phenylhydroxylamine **(VI)**, azobenzene **(VII)**, and azoxybenzene **(VIII)**, see **Fig. 6.1**). In contrast to dehydrogenation, the lower loaded Cu/SiO_2 delivered a (two-fold) higher *TOF* (**Fig. 6.4(BII)**), *i.e.*, sympathetic structure sensitivity with higher intrinsic hydrogenation efficiency over smaller Cu nanoparticles (7.8 → 3.1 nm). We can correlate this with the greater levels of H_2 chemisorption recorded in **Table 6.1** on

smaller supported Cu particles. The extracted apparent activation energies obtained from the Arrhenius plots (**Fig. 6.4(AII)**) were very close for both Cu loadings (29 ± 3 kJ mol^{-1}) and within the range (12-54 kJ mol^{-1}) reported for nitrobenzene hydrogenation over supported Ag [6.53], Pd [6.54] and Ni [6.22] catalysts. An essential requirement for effective dehydrogenation-hydrogenation coupling is that the former proceeds at a greater rate than the latter in order to ensure a sufficient H_2 supply. This prerequisite is only met by the higher loaded Cu/SiO_2 catalyst and, consequently, we employed 15.9% w/w Cu/SiO_2 to test the viability of the coupled system.

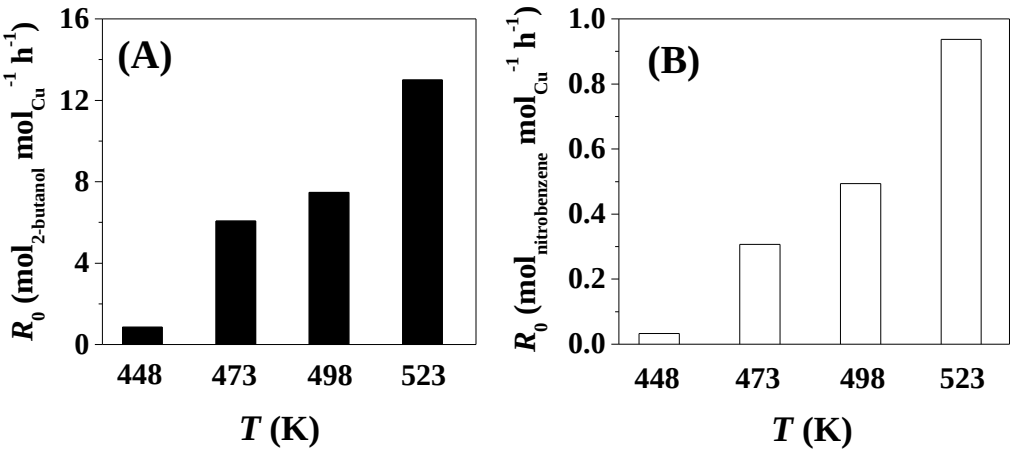

Fig. 6.5: Variation of initial reaction rate (R_0) as a function of temperature (T) in the coupled system with respect to (A) dehydrogenation of 2-butanol and (B) hydrogenation of nitrobenzene for reaction over 15.9% w/w Cu/SiO_2. *Reaction conditions*: T = 448-523 K, P = 1 atm, 2-butanol/nitrobenzene molar ratio = 35.

The results in terms of the temperature (448-523 K) dependence of reaction rate for the coupled system are presented in **Fig. 6.5** with respect to **(A)** 2-butanone and **(B)** aniline production**.** The coupled system was 100% selective to the two target products where the generation of aniline (in N_2 as carrier) demonstrates that the catalyst "borrowed" hydrogen generated in the dehydrogenation step with an "auto-transfer" in the catalytic conversion of nitrobenzene. Both products can be readily separated by standard distillation given the (105 K) difference in boiling points. An increase in activity at higher reaction temperature was observed for both reactions. This is consistent with the endothermicity of 2-butanol dehydrogenation (ΔH = 54-57 kJ mol^{-1}) [6.55] while the greater amount of hydrogen generated at elevated temperature resulted in increased aniline production. In addition to the hydrogen source, utilisation efficiency is a critical parameter that must be optimised to ensure sustainability. Hydrogen usage can be evaluated from the entries in **Fig. 6.6** where the mol ratio of H_2 (generated *via* 2-butanol dehydrogenation **(A)** or as an external pressurised hydrogen supply **(B)**) to

aniline formation (H_2/Aniline) is plotted as a function of temperature. The H_2/Aniline ratio for "stand-alone" nitrobenzene hydrogenation (using conventional pressurised H_2)

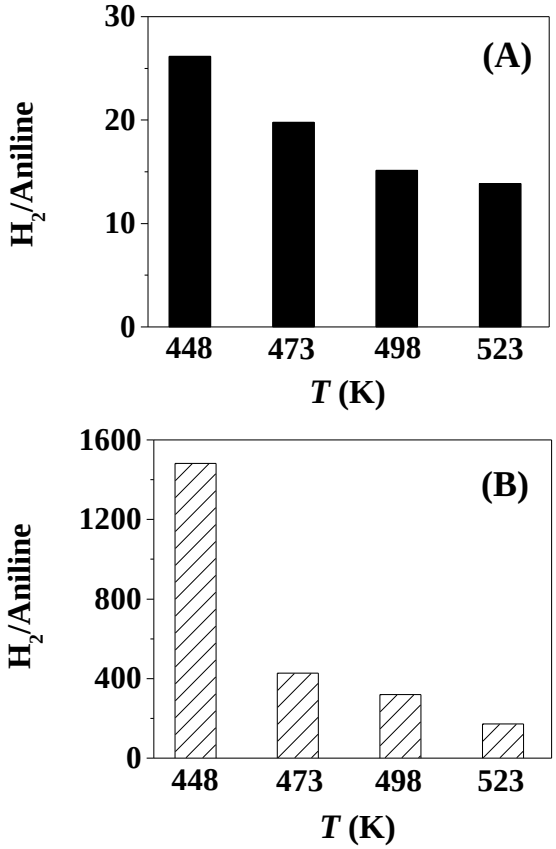

Fig. 6.6: Temperature dependence of hydrogen utilisation efficiency over 15.9% w/w Cu/SiO_2 represented as the molar ratio of hydrogen supplied to aniline generated (H_2/Aniline) for (A) coupled system (H_2 generated from *in situ* 2-butanol dehydrogenation) and (B) stand-alone nitrobenzene hydrogenation. *Reaction conditions*: *T* = 448-523 K, *P* = 1 atm, 2-butanol/nitrobenzene molar ratio = 35.

was up to 500 times greater than the stoichiometric (=3) requirement. This represents gross inefficiency in terms of unreacted hydrogen, highlighting a severe sustainability gap. Such limited H_2 utilisation can be attributed to the low capacity of Cu to chemisorb and activate H_2 [6.34,6.35] as established in the pulse titration measurements given in **Table 6.1**. In contrast, the coupled system exhibited dramatically lower H_2/Aniline, demonstrating significantly improved hydrogen utilisation, *i.e.*, the hydrogen generated *in situ via* catalytic dehydrogenation is more efficient as $–NO_2$ reductant. Effective transfer and use of hydrogen in the coupled system can involve participation of abstracted hydrogen species that interact with copper (Cu-H, see step **(IX)** in **Fig. 6.1**). Nagaraja *et al*. [6.10] and Sawadjoon *et al*. [6.56] reached a similar conclusion in their analysis of the gas phase coupling of cyclohexanol dehydrogenation with furfural hydrogenation (*T* = 453-523 K, *P* = 1 atm) over Cu-MgO-Cr_2O_3 and liquid phase coupling of alcohol hydrogenolysis with formic acid as hydrogen donor (*T* = 353 K, *P* =

1 atm) over Pd/carbon, respectively. Moreover, there is evidence in the literature for the formation of transitory metal-H (Cu-H [6.57], Ru-H [6.58], Ag-H [6.59] and Ni-H [6.60]) species (*via* interaction with hydrogen abstracted from alcohols) that can serve as a source of reactive hydrogen. In this study, the abstracted hydrogen associated with copper (Cu-H) must participate in the nitrobenzene hydrogenation step. This supply of reactive hydrogen circumvents limitations associated with H_2 activation/dissociation by Cu and contributes to enhanced hydrogen utilisation. The benefits in terms of atom efficiency and sustainability are immediate while replacement of compressed H_2 has important safety implications for large scale production.

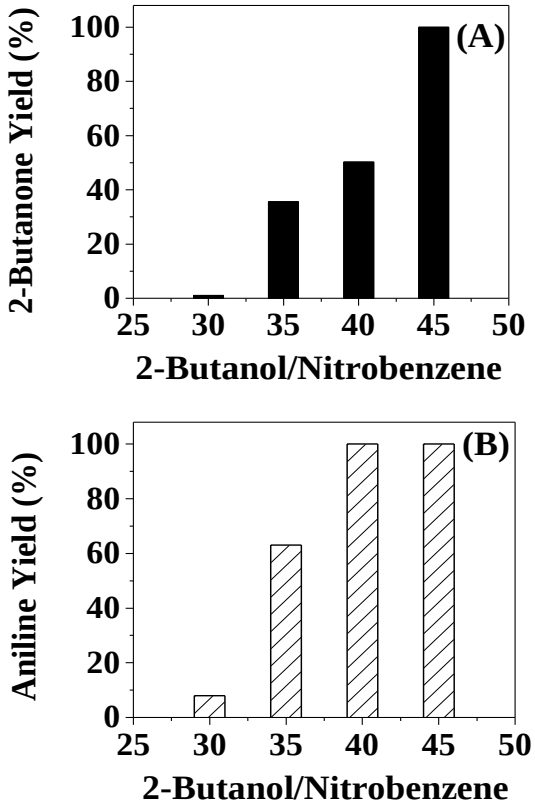

Fig. 6.7: Yield of (A) 2-butanone and (B) aniline as a function of inlet 2-butanol/ nitrobenzene molar ratio in the coupled dehydrogenation of 2-butanol and hydrogenation of nitrobenzene over 15.9% w/w Cu/SiO_2. *Reaction conditions*: P = 1 atm, T = 473 K, 2-butanol/nitrobenzene molar ratio = 30-45.

It has been demonstrated [6.61,6.62] that the inlet H_2/nitroarene ratio is a critical parameter in determining amine production rate where variations in H_2 partial pressure impact on the available surface hydrogen. With the goal of further improving performance of the coupled system we examined the effect of modifying the 2-butanol/nitrobenzene molar feed ratio; the results obtained are shown in **Fig. 6.7**. An

increase in 2-butanol/nitrobenzene served to increase the yield of both 2-butanone and aniline to reach 100% at 2-butanol/nitrobenzene = 45. A higher inlet ratio facilitates dehydrogenation with greater hydrogen release that, in turn, serves to promote nitrobenzene hydrogenation. This represents unprecedented coupling performance with respect to the literature where reported aniline yields have been below 80% (coupled with dehydrogenation of ethylbenzene [6.63] and butanediol [6.64]). In addition to thermodynamic constraints associated with hydrogen generation, Nagaraja *et al.* [6.10] concluded that the coupling of cyclohexanol dehydrogenation with furfural hydrogenation resulted in competitive adsorption on copper sites that inhibited hydrogen utilisation. Competition between 2-butanol and nitrobenzene for adsorption sites may be reflected in the observed (**Fig. 6.7**) dependence of product yield on reactant ratio. Nevertheless, adjustment of the feed composition allows full conversion to both target products, demonstrating the feasibility of applying catalytic dehydrogenation as an *in situ* source of hydrogen for reduction reactions.

6.4 Conclusion

The results presented in this study establish the viability of *in situ* hydrogen generation (from 2-butanol dehydrogenation) and direct utilisation (in nitrobenzene hydrogenation) over Cu/SiO_2 (15.9 and 1.8% w/w) for the production of commercially important products (2-butanone and aniline). Dehydrogenation of 2-butanol is structure-sensitive with a higher *TOF* over 15.9% w/w Cu/SiO_2 with larger (mean = 7.8 nm) Cu particles. The larger nanoscale Cu^0 (from XPS analysis) facilitates adsorption of the alkoxide intermediate *via* interaction with the polarised carbon and abstraction of the second H atom. In contrast, enhanced *TOF* in the hydrogenation of nitrobenzene has been recorded over 1.8% w/w Cu/SiO_2 that exhibited smaller Cu nanoparticles (mean = 3.1 nm) with greater H_2 chemisorption capacity. Exclusive production of both 2-butanone and aniline at full conversion has been achieved in the coupling of 2-butanol dehydrogenation with nitrobenzene hydrogenation over 15.9% w/w Cu/SiO_2 in the absence of an external H_2 supply. Hydrogen utilisation efficiency was appreciably greater (by a factor of up to 50) in the coupled system relative to conventional stand-alone hydrogenation using pressurised hydrogen. This response can be attributed to the generation of reactive hydrogen associated with the Cu sites (Cu-H) that is effectively transferred for $–NO_2$ reduction and circumvents the limitations associated with H_2 activation/dissociation by Cu. Our results open new possibilities for sustainable "hydrogen free" hydrogenation processes.

6.5 References

[6.1] M. Irfan, T.N. Glasnov, C.O. Kappe, *Heterogeneous catalytic hydrogenation reactions in continuous-flow reactors*, ChemSusChem 4 (2011) 300-316.

[6.2] R. Kothari, D. Buddhi, R.L. Sawhney, *Comparison of environmental and economic aspects of various hydrogen production methods*, Renew. Sust. Energ. Rev. 12 (2008) 553-563.

[6.3] P.L. Gkizis, M. Stratakis, I.N. Lykakis, *Catalytic activation of hydrazine hydrate by gold nanoparticles: Chemoselective reduction of nitro compounds into amines*, Catal. Commun. 36 (2013) 48-51.

[6.4] E. Vasilikogiannaki, C. Gryparis, V. Kotzabasaki, I.N. Lykakis, M. Stratakis, *Facile reduction of nitroarenes into anilines and nitroalkanes into hydroxylamines via the rapid activation of ammonia borane complex by supported gold nanoparticles*, Adv. Synth. Catal. 355 (2013) 907-911.

[6.5] C. Zheng, S.L. You, *Transfer hydrogenation with Hantzsch esters and related organic hydride donors*, Chem. Soc. Rev. 41 (2012) 2498-2518.

[6.6] F. Alonso, P. Riente, M. Yus, *Nickel nanoparticles in hydrogen transfer reactions*, Acc. Chem. Res. 44 (2011) 379-391.

[6.7] A. Wang, Z. Yang, J. Liu, Q. Gui, X. Chen, Z. Tan, J.-C. Shi, *Pd-catalyzed reduction of aldehydes to alcohols using formic acid as the hydrogen donor*, Synth. Commun. 44 (2014) 280-288.

[6.8] A. Malaika, M. Kozłowski, *Modification of activated carbon with different agents and catalytic performance of products obtained in the process of ethylbenzene dehydrogenation coupled with nitrobenzene hydrogenation*, Chem. Eng. J. 171 (2011) 1348-1355.

[6.9] Y.L. Zhu, J. Yang, G.Q. Dong, H.Y. Zheng, H.H. Zhang, H.W. Xiang, Y.W. Li, *An environmentally benign route to gamma-butyrolactone through the coupling of hydrogenation and dehydrogenation*, Appl. Catal. B: Environ. 57 (2005) 183-190.

[6.10] B.M. Nagaraja, A.H. Padmasri, P. Seetharamulu, K.H.P. Reddy, B.D. Raju, K.S.R. Rao, *A highly active Cu-MgO-Cr_2O_3 catalyst for simultaneous synthesis of furfuryl alcohol and cyclohexanone by a novel coupling route: Combination of furfural hydrogenation and cyclohexanol dehydrogenation*, J. Mol. Catal. A: Chem. 278 (2007) 29-37.

[6.11] B.M. Nagaraja, A.H. Padmasri, B.D. Raju, K.S.R. Rao, *Production of hydrogen through the coupling of dehydrogenation and hydrogenation for the synthesis of*

cyclohexanone and furfuryl alcohol over different promoters supported on Cu-MgO catalysts, Int. J. Hydrogen Energ. 36 (2011) 3417-3425.

[6.12] M.J. Climent, A. Corma, J.C. Hernandez, A.B. Hungría, S. Iborra, S. Martínez-Silvestre, *Biomass into chemicals: One-pot two- and three-step synthesis of quinoxalines from biomass-derived glycols and 1,2-dinitrobenzene derivatives using supported gold nanoparticles as catalysts*, J. Catal. 292 (2012) 118-129.

[6.13] W.G. Zhang, D.H. Yu, X.J. Ji, H. Huang, *Efficient dehydration of bio-based 2,3-butanediol to butanone over boric acid modified HZSM-5 zeolites*, Green Chem. 14 (2012) 3441-3450.

[6.14] J.N. Keuler, L. Lorenzen, S. Miachon, *The dehydrogenation of 2-butanol over copper-based catalysts: Optimising catalyst composition and determining kinetic parameters*, Appl. Catal. A: Gen. 218 (2001) 171-180.

[6.15] S. Lambert, C. Cellier, F. Ferauche, E.M. Gaigneaux, B. Heinrichs, *On the structure-sensitivity of 2-butanol dehydrogenation over Cu/SiO_2 cogelled xerogel catalysts*, Catal. Commun. 8 (2007) 2032-2036.

[6.16] D. Fang, W. Ren, Z. Liu, X. Xu, L. Xu, H. Lue, W. Liao, H. Zhang, *Synthesis and applications of mesoporous $Cu-Zn-Al_2O_3$ catalyst for dehydrogenation of 2-butanol*, J. Natur. Gas Chem. 18 (2009) 179-182.

[6.17] S. Lambert, N. Tcherkassova, C. Cellier, F. Ferauche, B. Heinrichs, P. Grange, J.P. Pirard, *Ag/SiO_2 and Cu/SiO_2 cogelled xerogel catalysts for benzene combustion and 2-butanol dehydrogenation*, E. Gaigneaux, D.E. DeVos, P. Grange, P.A. Jacobs, J.A. Martens, P. Ruiz, G. Poncelet (Eds.), Scientific bases for the preparation of heterogeneous catalysts, Elsevier Science, Amsterdam, 2002.

[6.18] J.N. Keuler, L. Lorenzen, *The dehydrogenation of 2-butanol in a Pd-Ag membrane reactor*, J. Membr. Sci. 202 (2002) 17-26.

[6.19] Z.L. Wang, H.C. Ma, W.C. Zhu, G.J. Wang, *Characterization of $Cu-ZnO-Cr_2O_3/SiO_2$ catalysts and application to dehydrogenation of 2-butanol to 2-butanone*, React. Kinet. Catal. Lett. 76 (2002) 271-279.

[6.20] H.-U. Blaser, H. Steiner, M. Studer, *Selective catalytic hydrogenation of functionalised nitroarenes: An update*, ChemCatChem 1 (2009) 210-221.

[6.21] J. Relvas, R. Andrade, F.G. Freire, F. Lemos, P. Araujo, M.J. Pinho, C.P. Nunes, F.R. Ribeiro, *Liquid Phase hydrogenation of nitrobenzene over an industrial Ni/SiO_2 supported catalyst*, Catal. Today 133 (2008) 828-835.

[6.22] J. Wang, Z. Yuan, R. Nie, Z. Hou, X. Zheng, *Hydrogenation of nitrobenzene to aniline over silica gel supported nickel catalysts*, Ind. Eng. Chem. Res. 49 (2010) 4664-4669.

[6.23] M.C.M. Perez, C.S.M. deLecea, A.L. Solano, *Platinum supported on activated carbon cloths as catalyst for nitrobenzene hydrogenation*, Appl. Catal. A: Gen. 151 (1997) 461-475.

[6.24] G.C. Torres, E.L. Jablonski, G.T. Baronetti, A.A. Castro, S.R. deMiguel, O.A. Scelza, M.D. Blanco, M.A.P. Jimenez, J.L.G. Fierro, *Effect of the carbon pre-treatment on the properties and performance for nitrobenzene hydrogenation of Pt/C catalysts*, Appl. Catal. A: Gen. 161 (1997) 213-226.

[6.25] P. Yang, W. Zhang, Y. Du, X. Wang, *Hydrogenation of nitrobenzenes catalyzed by platinum nanoparticle core-polyaryl ether trisacetic acid ammonium chloride dendrimer shell nanocomposite*, J. Mol. Catal. A: Chem. 260 (2006) 4-10.

[6.26] P. Sangeetha, P. Seetharamulu, K. Shanthi, S. Narayanan, K.S.R. Rao, *Studies on Mg-Al oxide hydrotalcite supported Pd catalysts for vapor phase hydrogenation of nitrobenzene*, J. Mol. Catal. A: Chem. 273 (2007) 244-249.

[6.27] C. Willocq, V. Dubois, Y.Z. Khimyak, M. Devillers, S. Hermans, *Hydrogenation of nitrobenzene over Pd/C catalysts prepared from molecular carbonyl-phosphine palladium clusters*, J. Mol. Catal. A: Chem. 365 (2012) 172-180.

[6.28] Z. Huang, F. Cui, J. Xue, J. Zuo, J. Chen, C. Xia, *Cu/SiO_2 catalysts prepared by hom- and heterogeneous deposition-precipitation methods: Texture, structure, and catalytic performance in the hydrogenolysis of glycerol to 1,2-propanediol*, Catal. Today 183 (2012) 42-51.

[6.29] E.D. Guerreiro, O.F. Gorriz, G. Larsen, L.A. Arrua, *Cu/SiO_2 catalysts for methanol to methyl formate dehydrogenation: A comparative study using different preparation techniques*, Appl. Catal. A: Gen. 204 (2000) 33-48.

[6.30] M.L. Smith, A. Campos, J.J. Spivey, *Reduction processes in Cu/SiO_2, Co/SiO_2, and $CuCo/SiO_2$ catalysts*, Catal. Today 182 (2012) 60-66.

[6.31] J.D. Grunwaldt, A.M. Molenbroek, N.Y. Topsøe, H. Topsøe, B.S. Clausen, *In situ investigations of structural changes in Cu/ZnO catalysts*, J. Catal. 194 (2000) 452-460.

[6.32] C.S. Chen, W.H. Cheng, S.S. Lin, *Study of iron-promoted Cu/SiO_2 catalyst on high temperature reverse water gas shift reaction*, Appl. Catal. A: Gen. 257 (2004) 97-106.

[6.33] S. Lambert, C. Cellier, P. Grange, J.P. Pirard, B. Heinrichs, *Synthesis of Pd/SiO_2, Ag/SiO_2, and Cu/SiO_2 cogelled xerogel catalysts: Study of metal dispersion and catalytic activity*, J. Catal. 221 (2004) 335-346.

[6.34] S.C. Chou, C.T. Yeh, T.H. Chang, *Adsorption of hydrogen on dispersed copper-rhodium bimetallic crystallites*, J. Phys. Chem. B 101 (1997) 5828-5833.

[6.35] J.J. Liu, L.L. Zhang, J.T. Zhang, T. Liu, X.S. Zhao, *Bimetallic ruthenium-copper nanoparticles embeded in mesoporous carbon as an effective hydrogenation catalyst*, Nanoscale 5 (2013) 11044-11050.

[6.36] S. Jujjuri, E. Ding, S.G. Shore, M.A. Keane, *A characterization of Ln-Pd/SiO_2 (Ln=La, Ce, Sm, Eu, Gd and Yb): Correlation of surface chemistry with hydrogenolysis activity*, J. Mol. Catal. A: Chem. 272 (2007) 96-107.

[6.37] K.V. Murthy, P.M. Patterson, G. Jacobs, B.H. Davis, M.A. Keane, *An exploration of activity loss during hydrodechlorination and hydrodebromination over Ni/SiO_2*, J. Catal. 223 (2004) 74-85.

[6.38] S. Sitthisa, D.E. Resasco, *Hydrodeoxygenation of furfural over supported metal catalysts: A comparative study of Cu, Pd and Ni*, Catal. Lett. 141 (2011) 784-791.

[6.39] V. Subbaramaiah, V.C. Srivastava, I.D. Mall, *Catalytic activity of Cu/SBA-15 for peroxidation of pyridine bearing wastewater at atmospheric condition*, AIChE J. 59 (2013) 2577-2586.

[6.40] J.P. Espinos, J. Morales, A. Barranco, A. Caballero, J.P. Holgado, A.R. Gonzalez-Elipe, *Interface effects for Cu, CuO, and Cu_2O deposited on SiO_2 and ZrO_2: XPS determination of the valence state of copper in Cu/SiO_2 and Cu/ZrO_2 catalysts*, J. Phys. Chem. B 106 (2002) 6921-6929.

[6.41] J. Gong, H. Yue, Y. Zhao, S. Zhao, L. Zhao, J. Lv, S. Wang, X. Ma, *Synthesis of ethanol via syngas on Cu/SiO_2 catalysts with balanced Cu^0-Cu^+ sites*, J. Am. Chem. Soc. 134 (2012) 13922-13925.

[6.42] P.S. Bagus, E.S. Ilton, C.J. Nelin, *The interpretation of XPS spectra: Insights into materials properties*, Surf. Sci. Rep. 68 (2013) 273-304.

[6.43] C.S. Chen, J.H. Lin, T.W. Lai, B.H. Li, *Active sites on Cu/SiO_2 prepared using the atomic layer epitaxy technique for a low-temperature water-gas shift reaction*, J. Catal. 263 (2009) 155-166.

[6.44] N. Ferretti, B. Balkaya, A. Vollmer, M. Neeb, W. Eberhardt, *Inner-shell photoelectron spectroscopy of size-selected Cu-clusters on Si*, J. Electron. Spectrosc. 156 (2007) 124-127.

[6.45] F. Cárdenas-Lizana, B. Bridier, C.C.K. Shin, J. Perez-Ramirez, L. Kiwi-Minsker, *Promotional effect of Ni in the selective gas-phase hydrogenation of chloronitrobenzene over Cu-based catalysts*, ChemCatChem 4 (2012) 668-673.

[6.46] D.H. Parker, C.L. Pettiettehall, Y.Z. Li, R.T. McIver, J.C. Hemminger, *Kinetic-study of the initial stage of dehydrogenation of cyclohenxane on the Pt(111) surface*, J. Phys. Chem. 96 (1992) 1888-1894.

[6.47] F. Cárdenas-Lizana, S. Gómez-Quero, C.J. Baddeley, M.A. Keane, *Tunable gas phase hydrogenation of m-dinitrobenzene over alumina supported Au and Au-Ni*, Appl. Catal. A: Gen. 387 (2010) 155-165.

[6.48] D. Fang, X. Jiang, Z. Wang, Z. Qiu, H. Zhang, *Kinetics of dehydrogenaiton of 2-butanol on Cu/ZnO/Al_2O_3 catalyst*, Petrochem. Tech. 40 (2011) 49-54.

[6.49] V.Z. Fridman, A.A. Davydov, K. Titievsky, *Dehydrogenation of cyclohexanol on copper-containing catalysts: II. The pathways of the cyclohexanol dehydrogenation reaction to cyclohexanone on copper-active sites in oxidation state Cu^0 and Cu^+*, J. Catal. 222 (2004) 545-557.

[6.50] K. Shimizu, K. Kon, K. Shimura, S. Hakim, *Acceptor-free dehydrogenation of secondary alcohols by heterogeneous cooperative catalysis between Ni nanoparticles and acid-base sites of alumina supports*, J. Catal. 300 (2013) 242-250.

[6.51] K. Kon, S. Siddiki, K.I. Shimizu, *Size- and support-dependent Pt nanocluster catalysis for oxidant-free dehydrogenation of alcohols*, J. Catal. 304 (2013) 63-71.

[6.52] Z. Sun, Y. Zhao, Y. Xie, R. Tao, H. Zhang, C. Huang, Z. Liu, *The solvent-free selective hydrogenation of nitrobenzene to aniline: An unexpected catalytic activity of ultrafine Pt nanoparticles deposited on carbon nanotubes*, Green Chem. 12 (2010) 1007-1011.

[6.53] G.D. Yadav, R.K. Mewada, *Novelties of azobenzene synthesis via selective hydrogenation of nitrobenzene over nano-fibrous Ag-OMS-2: Mechanism and kinetics*, Chem. Eng. J. 221 (2013) 500-511.

[6.54] I.I. Obraztsova, N.K. Eremenko, Y.N. Velyakina, *Reaction kinetics of nitrobenzene hydrogenation on a palladium catalyst supported on nanodiamonds*, Kinet. Catal. 49 (2008) 401-406.

[6.55] A.H. Cubberley, M.B. Mueller, *Equilibrium studies on the dehydrogenation of primary and secondary alcohols: I. 2-Butanol, 2-octanol, cyclopentanol and benzyl alcohol*, J. Am. Chem. Soc. 68 (1946) 1149-1151.

[6.56] S. Sawadjoon, A. Lundstedt, J.S.M. Samec, *Pd-catalyzed transfer hydrogenolysis of primary, secondary, and tertiary benzylic alcohols by formic acid: A mechanistic study*, ACS Catal. 3 (2013) 635-642.

[6.57] J. He, K. Yamaguchi, N. Mizuno, *Selective synthesis of secondary amines via N-alkylation of primary amines and ammonia with alcohols by supported copper hydroxide catalysts*, Chem. Lett. 39 (2010) 1182-1183.

[6.58] K. Yamaguchi, J. He, T. Oishi, N. Mizuno, *The "borrowing hydrogen strategy" by supported ruthenium hydroxide catalysts: Synthetic scope of symmetrically and unsymmetrically substituted amines*, Chem. Eur. J. 16 (2010) 7199-7207.

[6.59] H. Liu, G.-K. Chuah, S. Jaenicke, *N-alkylation of amines with alcohols over alumina-entrapped Ag catalysts using the "borrowing hydrogen" methodology*, J. Catal. 292 (2012) 130-137.

[6.60] K. Shimizu, N. Imaiida, K. Kon, S. Siddiki, A. Satsuma, *Heterogeneous Ni catalysts for N-alkylation of amines with alcohols*, ACS Catal. 3 (2013) 998-1005.

[6.61] X. Wang, N. Perret, M.A. Keane, *The role of hydrogen partial pressure in the gas phase hydrogenation of p-chloronitrobenzene over alumina supported Au and Pd: A consideration of reaction thermodynamics and kinetics*, Chem. Eng. J. 210 (2012) 103-113.

[6.62] C. Torres, C. Campos, J.L.G. Fierro, M. Oportus, P. Reyes, *Nitrobenzene hydrogenation on Au/TiO_2 and Au/SiO_2 catalyst: Synthesis, characterization and catalytic activity*, Catal. Lett. 143 (2013) 763-771.

[6.63] A.L. Sun, Z.F. Qin, J.G. Wang, *Reaction coupling of ethylbenzene dehydrogenation with nitrobenzene hydrogenation*, Catal. Lett. 79 (2002) 33-37.

[6.64] K.H.P. Reddy, R. Rahul, S.S.V. Reddy, B.D. Raju, K.S.R. Rao, *Coupling of 1,4-butanediol dehydrogenation reaction with the hydrogenation of nitrobenzene over Cu/MgO catalysts*, Catal. Commun. 10 (2009) 879-883.

Chapter 7

Conversion of Benzyl Alcohol to Benzylamine *via* Dehydrogenation/Amination/Reduction over Cu and Au

Conversion of benzyl alcohol *via* a tandem dehydrogenation/amination/reduction reaction as an alternative for benzylamine synthesis over Cu/SiO_2 in the continuous gas phase operation is investigated in this chapter where the effect of Au/TiO_2 on the product distribution is identified.

7.1 Introduction

Benzylamine is widely utilised as a corrosion inhibitor and intermediate in the manufacture of pharmaceuticals, detergents and nylon fibres [7.1]. The conventional manufacturing route *via* stoichiometric reaction of benzyl chloride with NH_3 produces significant quantities of solid waste (*e.g.* NH_4Cl) with HCl and/or Cl_2 release [7.2]. Catalytic hydrogenation of benzonitrile to benzylamine has been examined in the liquid phase over (Al_2O_3 and SiO_2) supported metals (Ni [7.3,7.4], Pd [7.5,7.6], Pt [7.7,7.8], Ru [7.9] and Co [7.10]) but the simultaneous generation of secondary/tertiary amines and toluene over these metals is a decided drawback. Use of NH_3 [7.4,7.11], a biphasic medium (H_2O-CO_2 [7.12], aqueous NaH_2PO_4-CH_2Cl_2 [7.13]) and elevated pressure (10-83 bar) is necessary to inhibit side-reactions. A search through the literature has revealed only two studies of gas phase reaction (over Cu/MgO [7.1] and Ni/Al_2O_3 [7.14]) that resulted in benzylamine yields <70%. Catalytic reductive amination of benzaldehyde with NH_3 without additives (NaH_2PO_4, CH_2Cl_2) represents an alternative route (**Fig. 7.1** (path **A→B**)) to benzylamine. This reaction has been studied using soluble

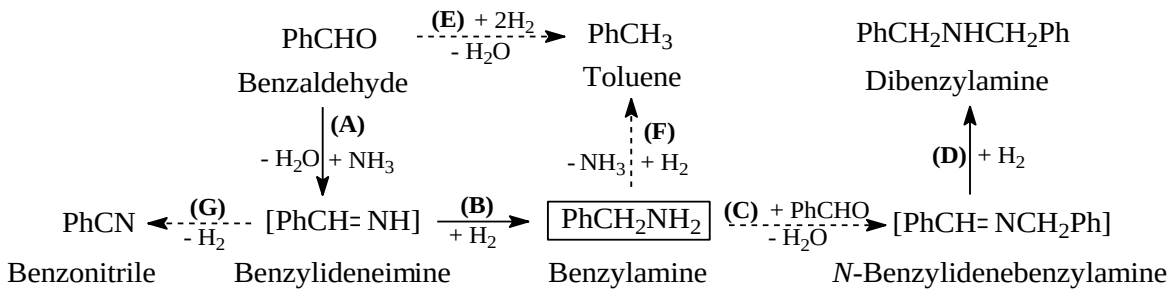

Fig. 7.1: Reaction pathways for reductive amination of benzaldehyde (solid arrow: target pathway; dashed arrow: side-reaction pathway).

metal (Rh [7.15] and Ti [7.16]) complex, supported metal (Pd/C [7.17], Ru/C [7.18-7.20] and Ni/SiO_2 [7.21]) and Pt nanowires [7.22] in the liquid phase (T = 298-408 K, P = 1-65 bar) but we could not find any reported instance of gas phase operation. Selective conversion of benzaldehyde to benzylamine (66-86% yield) has been achieved over a Rh complex ($[Rh(cod)Cl]_2$ [7.15]) and Ru/C [7.19] with *N*-benzylidenebenzylamine (**Fig. 7.1** (step **C**)) and dibenzylamine (step **D**) as by-products. Reaction over Pd/C [7.17] and Pt nanowires [7.22] promoted condensation of benzylamine with benzaldehyde to *N*-benzylidenebenzylamine and subsequent hydrogenation to dibenzylamine. Moreover, hydrogenolysis of benzaldehyde (**Fig. 7.1** step **(E)**) or benzylamine (step **(F)**) can generate toluene while benzylideneimine dehydrogenation (**Fig. 7.1** step **(G)**) results in the formation of benzonitrile [7.5]. Use of benzyl alcohol as feedstock in a reaction with NH_3 has been proposed for benzylamine production in homogeneous (Ru complex) systems at high pressure (P_{NH_3} = 7.5 bar) with benzylamine yields ≤86% [7.23]. Heterogeneous catalysis studies have entirely focused on liquid phase reaction over $Ru(OH)_x/TiO_2$ [7.24] and $Cu(OH)_x/Al_2O_3$ [7.25] where there has been no detectable benzylamine formation.

A move from batch to continuous processes presents a number of advantages in terms of product/catalyst separation, reduced downtime, product quality control and process safety [7.26]. Although there has been no reported study of continuous benzylamine production from benzaldehyde or benzyl alcohol, we can flag the application of Cu catalysts (copper chromite [7.27] and Cu/ZrO_2 [7.28]) in the gas phase reductive amination of cyclohexanone and cyclohexanol (with NH_3) which has shown (at least two-fold) higher yield to the target cyclohexylamine when compared with that achieved over Al_2O_3 supported Pd, Pt, Ru and Rh. In this study, we assess the viability of benzylamine production from the reductive amination of benzaldehyde generated *via* benzyl alcohol dehydrogenation where the hydrogen released is used in hydrogenation. This tandem dehydrogenation/amination/reduction in continuous gas phase operation represents a significant advancement in terms of sustainable amine production. It has been previously (in **Chapter 5**) demonstrated that Cu/SiO_2 is effective in benzyl alcohol dehydrogenation to benzaldehyde and was accordingly employed in this study to promote the first step of the tandem reaction. But supported Cu shows low hydrogenation rate in coupling nitrobenzene reduction with benzyl alcohol dehydrogenation. Nano-scale supported Au has displayed higher selective rates in the

reduction of unsaturated functionalities (*e.g.* –C=O and –C=N) relative to Cu [7.29] and negligible activity in the gas phase dehydrogenation (at T < 523 K) [7.30]. This can facilitate benzylideneimine reduction to the target benzylamine without promoting dehydrogenation to benzonitrile or benzaldehyde hydrogenolysis to toluene (**Fig. 7.1**). We evaluate the efficacy of Au/TiO_2 incorporation to control product distribution and increase benzylamine production.

7.2 Experimental

7.2.1 Catalyst Preparation

Silica supported Cu was prepared by deposition-precipitation with NaOH (Riedel-de Haën, 99%) as precipitation agent. The (fumed) SiO_2 support (20 g, Sigma-Aldrich) was dispersed in a solution of $Cu(NO_3)_2$ (Sigma-Aldrich, 99%, 0.03 M, 200 cm^3). The suspension was stirred (600 rpm) at ambient temperature for 1 h with addition of aqueous NaOH (2 M) until pH >10 to ensure complete deposition of $Cu(OH)_2$, heated to 353 K and aged under vigorous stirring for 4 h [7.31]. The solid obtained was separated by filtration, washed with distilled water (until pH = 7) and dried in air at 393 K overnight. The dried sample was calcined in air (at 10 K min^{-1} to 723 K for 4 h) to generate a supported CuO phase [7.31]. Synthesis of Au/TiO_2 by deposition-precipitation employed urea (Riedel-de Haën, 99%) as basification agent. An aqueous solution of urea (100 fold excess) and $HAuCl_4$ (Sigma-Aldrich, 99%, 5×10^{-3} M, 400 cm^3) was added to the support (15 g) and the suspension stirred and heated to 353 K (2 K min^{-1}). The pH progressively increased to *ca.* 7 after 3-4 h as a result of thermal decomposition of urea [7.32]. The solid obtained was separated by filtration, washed with distilled water at ambient temperature until Cl free (based on the $AgNO_3$ test) and dried in 45 cm^3 min^{-1} He at 373 K for 5 h. The catalyst precursors were sieved (ATM fine test sieves) to mean particle diameter = 75 μm. Before reaction, the catalysts precursors were activated in 60 cm^3 min^{-1} H_2 at 2-4 K min^{-1} to 523-543 K, held for 1-2 h and passivated at ambient temperature in 1% v/v O_2/He for *ex situ* characterisation.

7.2.2 Catalyst Characterisation

Metal loading was determined by atomic absorption spectroscopy using a Shimadzu AA-6650 spectrometer with an air-acetylene flame from the diluted extract in aqua regia (25% v/v HNO_3/HCl). Temperature programmed reduction (TPR) and H_2

chemisorption were conducted on the CHEM-BET 3000 (Quantachrome Instrument) unit with data acquisition/manipulation using the TPR Win^{TM} software. The catalyst was loaded into a U-shaped Pyrex glass cell (3.76 mm i.d.) and heated in 17 cm^3 min^{-1} (Brooks mass flow controlled) 5% v/v H_2/N_2 at 2-4 K min^{-1} to 523-543 K. The activated samples were swept with 65 cm^3 min^{-1} N_2 for 1.5 h, cooled to reaction temperature (498 K) and subjected to H_2 chemisorption by pulse (10 μl) titration. The effluent gas passed through a liquid N_2 trap and H_2 consumption was monitored by a thermal conductivity detector (TCD). In blank tests there was no measurable H_2 uptake on the supports alone. Nitrogen adsorption-desorption isotherms were obtained using the Micromeritics Gemini 2390p system. Prior to analysis, samples were outgassed at 423 K for 1 h in N_2 and the total specific surface area (SSA) obtained using the standard BET method. Metal particle morphology (size and shape) was examined by scanning transmission electron microscopy (STEM, JEOL 2200FS field emission gun-equipped unit), employing Gatan Digital Micrograph 1.82 for data acquisition/manipulation. Samples for analysis were prepared by dispersion in acetone and deposited on a holey carbon/Cu grid (300 Mesh). Surface area weighted mean metal size (d) was based on a count of up to 800 particles according to

$$d = \frac{\sum_i n_i d_i^3}{\sum_i n_i d_i^2} \qquad \textbf{(7.1)}$$

where n_i is the number of particles of diameter d_i. X-ray photoelectron spectroscopic (XPS) analysis was conducted on an Axis Ultra instrument (Kratos Analytical) under ultra-high vacuum conditions ($<10^{-8}$ Torr) with a monochromatic Al Kα radiation (1486 eV). The Cu $2p_{3/2}$ and Au $4f_{7/2}$ spectra were collected and binding energies (BE) calibrated with respect to the C 1*s* peak (284.5 eV).

7.2.3 Catalytic Procedure

Reactions (reductive amination of benzaldehyde (Fluka, ≥98%), dehydrogenation or reductive amination of benzyl alcohol (Riedel-de Haën, ≥99%)) were carried out at atmospheric pressure *in situ* following catalyst activation in a continuous flow fixed bed vertical glass reactor (i.d. = 15 mm) at 423-498 K. A layer of borosilicate glass beads served as preheating zone, ensuring that the reactant was vaporised and reached reaction temperature before contacting the catalyst bed. Isothermal conditions (±1 K) were maintained by diluting the catalyst bed with ground glass (75 μm); the ground glass was

physically mixed thoroughly with catalyst before insertion into the reactor. Reaction temperature was continuously monitored by a thermocouple inserted in a thermowell within the catalyst bed. Solutions of benzaldehyde or benzyl alcohol in cyclohexane (Sigma-Aldrich, 99.5%) were delivered to the reactor *via* a glass/teflon air-tight syringe and teflon line using a microprocessor controlled infusion pump (Model 100 kd Scientific) at a fixed calibrated flow rate. Reductive amination of benzaldehyde was conducted in a co-current flow of carrier (N_2 and/or H_2) and NH_3 ($GHSV = 5 \times 10^3$ h^{-1}, molar Cu to reactant feed rate (n_{Cu}/F) = 3.6×10^{-1} h). Benzyl alcohol dehydrogenation was conducted in a co-current flow of N_2 with benzyl alcohol ($GHSV = 1.0 \times 10^4$ h^{-1}, molar metal to reactant feed rate $n_{metal}/F = 3.8 \times 10^{-3} - 5.0 \times 10^{-2}$ h). The reaction of benzyl alcohol with NH_3 was carried out in a co-current flow of N_2 and/or H_2 ($GHSV = 2 \times 10^3$ h^{-1}, $n_{metal}/F = 2.4 \times 10^{-1} - 2.8 \times 10^{-1}$ h). In blank tests, passage of each reactant in a stream of H_2 or N_2 through the empty reactor or over the (SiO_2 or TiO_2) support alone did not result in any detectable conversion. The reactor effluent was condensed in a liquid nitrogen trap for subsequent analysis using a Perkin-Elmer Auto System XL gas chromatograph equipped with a programmed split/splitless injector and a flame ionisation detector, employing a DB-1 (50 m × 0.33 mm i.d., 0.20 μm film thickness) capillary column (J&W Scientific). Benzylamine (Acros Organics, 99%), benzonitrile (Acros Organics, 99%), dibenzylamine (Acros Organics, 98%), *N*-benzylidenebenzylamine (Sigma-Aldrich, 99%) and toluene (Fisher scientific, 99%) were used without further purification. All gases (H_2, N_2, O_2 and He) were of high purity (BOC, >99.98%). Reactant (i) conversion (X) is defined by

$$X_i\,(\%) = \frac{[reactant]_{i,\,in} - [reactant]_{i,\,out}}{[reactant]_{i,\,in}} \times 100 \qquad \textbf{(7.2)}$$

and selectivity (S) to product (j) is given by

$$S_j(\%) = \frac{[product]_{j,\,out}}{[reactant]_{i,\,in} - [reactant]_{i,\,out}} \times 100 \qquad \textbf{(7.3)}$$

Yield (Y) to product (j) was obtained from

$$Y_j(\%) = \frac{[product]_{j,\,out}}{[reactant]_{i,\,in}} \times 100 \qquad \textbf{(7.4)}$$

where subscripts "in" and "out" refer to the inlet and outlet gas streams, respectively. Repeated reactions with different samples from the same batch of catalyst delivered raw data reproducibility and carbon mass balance that were within ±5 %.

7.3 Results and Discussion

7.3.1 Cu/SiO_2: Characterisation and Catalytic Response in the Reductive Amination of Benzaldehyde

The physicochemical properties of Cu/SiO_2 are given in **Table 7.1**, where the SSA is similar to that (192-199 $m^2\ g^{-1}$) reported for (fumed) SiO_2 supported Ni [7.33] and Pd [7.34]. The TPR profile of Cu/SiO_2 (not shown) is characterised by a single positive peak at the final isothermal hold (T = 543 K) with associated H_2 consumption (**Table** 7.**1**)

Table 7.1: Metal loading, specific surface area (SSA), temperature maxima (T_{max}) and H_2 consumption during temperature programmed reduction (TPR), metal size range and mean (d), principal XPS binding energy (BE) and H_2 chemisorption at 498 K.

	Cu/SiO_2	Au/TiO_2
Metal loading (% w/w)	1.8	1.9
SSA ($m^2\ g^{-1}$)	192	52
TPR T_{max} (K)	543	373
TPR H_2 consumption (μmol g^{-1})	281[a]/281[b]	170[a]/143[b]
Metal particle size range (nm)	1-6	1-6
d (nm)	3.1	3.2
XPS Cu $2p_{3/2}$ or Au $4f_{7/2}$ BE (eV)	933.2	83.2
H_2 uptake (μmol g_{metal}^{-1})	37	185

[a]value obtained from TPR analysis; [b]theoretical value for $Cu^{2+} \rightarrow Cu^0$ and $Au^{3+} \rightarrow Au^0$.

matching that required for Cu^{2+} reduction to Cu^0. Copper particle morphology was analysed by STEM and a representative image is provided in **Fig. 7.2(AI)** where Cu particles exhibit a quasi-spherical shape consistent with the observations of Zhu *et al.* for Cu/SiO_2 prepared by deposition-precipitation [7.35]. The associated particle size distribution (**Fig. 7.2(AII)**) is at the nano-scale (1-6 nm) with a surface weighted mean size of 3.1 nm. Hydrogen chemisorption (at 498 K) was significantly lower than that reported for Ni/SiO_2 (600 μmol g_{Ni}^{-1}) [7.33] and Pd/SiO_2 (120 μmol g_{Pd}^{-1}) [7.34]. This can be attributed to the high activation energy barrier for dissociative adsorption and low binding strength of dissociated hydrogen atoms on Cu due to the filled *d* band [7.36,7.37]. XPS analysis was conducted to evaluate the electronic properties of the

supported metal phase. The Cu $2p_{3/2}$ XPS signal (spectrum not shown) presents a principal peak at BE = 933.2 eV (**Table 7.1**) characteristic of electron deficient ($Cu^{\delta+}$) surface species ($Cu^{\delta+}$ = 933.0-933.6 eV) [7.38]. The characterisation results establish formation of electron deficient nano-scale (1-6 nm) Cu particles.

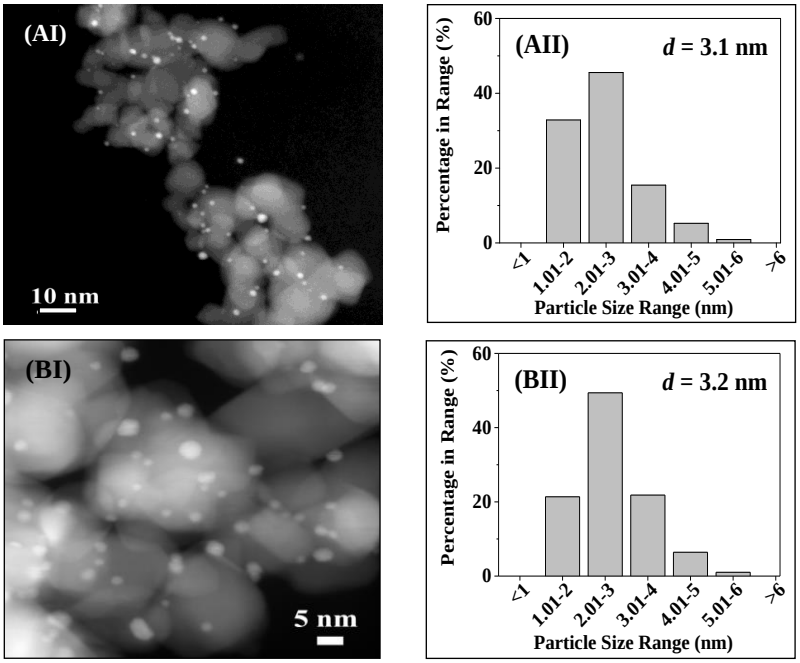

Fig. 7.2: (I) Representative STEM image and (II) associated particle size distribution histogram for (A) Cu/SiO_2 and (B) Au/TiO_2.

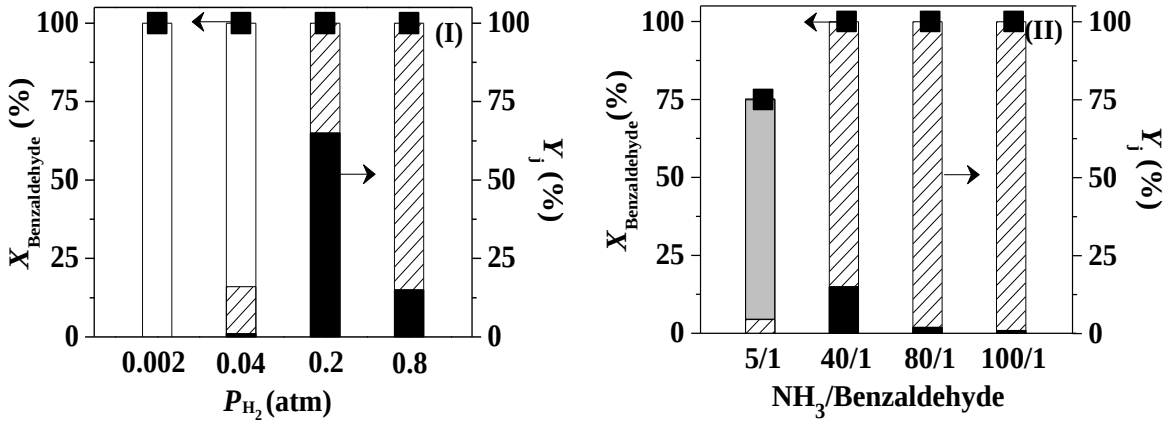

Fig. 7.3: Effect of variations in (I) H_2 partial pressure (P_{H_2}, NH_3/Benzaldehyde = 40) and (II) inlet NH_3/Benzaldehyde (P_{H_2} = 0.8 atm) on aldehyde conversion ($X_{Benzaldehyde}$, ■) and product yield (Y_j, open bars: benzonitrile, gray bars: toluene, solid bars: *N*-benzylidenebenzylamine, hatched bars: dibenzylamine) in the reductive amination of benzaldehyde over Cu/SiO_2. *Reaction conditions*: T = 498 K, P = 1 atm.

In the reductive amination of aldehydes and ketones, the H_2 and NH_3 content in the feed are critical parameters in determining surface concentration of reactive species, product distribution and ultimate amine production rate [7.18,7.39]. The effect of varying H_2 partial pressure **(I)** and inlet NH_3/Benzaldehyde molar ratio **(II)** on catalytic performance can be assessed from the entries in **Fig. 7.3**. Full conversion of benzaldehyde to benzonitrile (**Fig. 7.1**, paths **(A)+(G)**) was observed for reaction in N_2 and at the reaction stoichiometry for benzylamine formation (P_{H_2} = 0.002 atm), indicating exclusive amination of –C=O to –C=N (step **(A)**) and dehydrogenation of –C=N to –C≡N (step **(G)**). An increase in H_2 partial pressure (from 0.002 to 0.8 atm) resulted in a progressive shift from benzonitrile to a predominant dibenzylamine formation (to 85% yield). This result indicates a move from dehydrogenation (step **(G)**) to a combined hydrogenation + condensation path **(B→C→D)**). Suppressed hydrogenation activity in diluted H_2 can be linked to the low capacity of Cu to chemisorb/activate H_2 (as shown in **Table 7.1**). The primary amine (benzylamine) as a strong nucleophile undergoes facile condensation with benzaldehyde (step **(C)**) [7.23]. This accounts for the predominant formation of *N*-benzylidenebenzylamine and dibenzylamine (at elevated H_2 partial pressure) observed in this study. An increase in NH_3/Benzaldehyde (from 5 to 100) served to increase benzaldehyde conversion (to 100% at ≥40) with a shift of principal product from toluene (70% yield at 5) to dibenzylamine (99% yield at 100). This can be linked to competition between NH_3 and H_2 for surface sites where increased NH_3 content in the feed which favours benzaldehyde amination with condensation (**Fig. 7.1**, path **(A→D)**) over benzaldehyde hydrogenolysis (**Fig. 7.1**, step **(E)**). Likewise, Kirumakki *et al.* [7.39] observed that increased NH_3 concentration promoted cyclohexanone amination and condensation to *N*-cyclohexylcyclohexanimine over zeolites Hβ and HY (T = 523 K). It must be stressed that reaction of benzaldehyde (with NH_3) over Cu/SiO_2 did not generate any detectable benzylamine in the product stream. Formation of the target amine requires circumventing the condensation reaction (step **(C)** in **Fig. 7.1**).

7.3.2 Cu/SiO_2: Catalytic Response in the Benzyl Alcohol Reaction

The use of benzyl alcohol as a feedstock can (i) minimise undesired formation of secondary products (*N*-benzylidenebenzylamine and dibenzylamine) due to the lower reactivity of the alcohol than benzaldehyde in condensation reactions [7.40] and (ii) serve as hydrogen donor *via* hydrogen release from dehydrogenation (to benzaldehyde)

which can initiate the reductive amination shown in **Fig. 7.1**. The benzyl alcohol and NH_3 content in the feed can influence surface concentration of reactive species, H_2 generation and product distribution. The catalytic response in the conversion of benzyl alcohol (in N_2) over Cu/SiO_2 as a function of inlet NH_3/Benzyl alcohol is presented in **Fig. 7.4**. Full conversion was achieved at NH_3/Benzyl alcohol ≤10. In the amination of alcohols with NH_3, alcohol dehydrogenation has been proposed as rate-determining [7.41]. Decreased conversions at higher NH_3/Benzyl alcohol suggests competition with

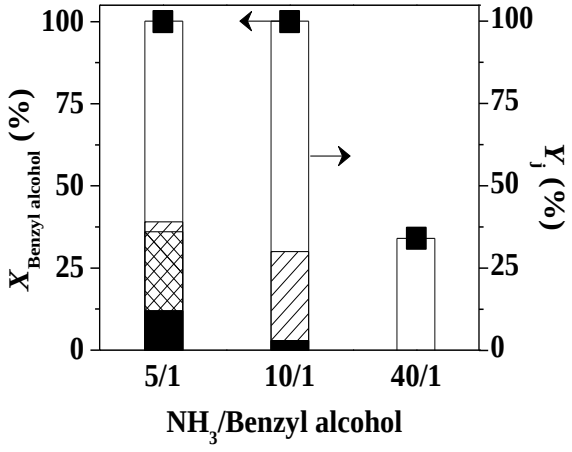

Fig. 7.4: Effect of variations in inlet NH_3/Benzyl alcohol on alcohol conversion ($X_{Benzyl\ alcohol}$, ■) and product yield (Y_j, open bars: benzonitrile, solid bars: *N*-benzylidenebenzylamine, hatched bars: dibenzylamine, cross hatched bars: benzaldehyde) for the reaction of benzyl alcohol (in N_2) with NH_3 over Cu/SiO_2. *Reaction conditions*: T = 498 K, P = 1 atm.

NH_3 for surface active sites. Reaction at NH_3/Benzyl alcohol = 40 generated benzonitrile as sole product consistent with consecutive dehydrogenation/amination/ dehydrogenation steps (benzyl alcohol → benzaldehyde → benzylideneimine → benzonitrile). Hu *et al*. [7.42] and Zhang *et al*. [7.43], studying the gas phase amination of ethanol with NH_3 in 5% H_2/N_2 over $Cu/\gamma\text{-}Al_2O_3$ (T = 523-563 K) or in N_2 over Co-Ni/Al_2O_3 (T = 693 K) reported acetonitrile as principal (>80% selectivity) product. Formation of *N*-benzylidenebenzylamine and dibenzylamine at lower NH_3/Benzyl alcohol (≤10) establishes the viability of transfer hydrogenation of the intermediate imines to amines using hydrogen released from benzyl alcohol dehydrogenation. Unconverted benzaldehyde was detected at the lowest NH_3/Benzyl alcohol (= 5) where the NH_3 supply is insufficient and must limit the extent of benzaldehyde amination (**Fig. 7.1**, step **(A)**). This is consistent with incomplete aldehyde conversion at NH_3/Benzaldehyde = 5 shown in **Fig. 7.3(II)**. Fischer *et al*. [7.44] have suggested that excess NH_3 (>20) favoured 1,3-propanediol amination over unsupported Co catalysts.

In contrast to benzaldehyde reaction, toluene from hydrogenolysis was restricted due to inadequate H_2 supply. It is important to note that, regardless of inlet NH_3/Benzyl alcohol, dehydrogenation to benzonitrile was the prevailing reaction ($S_{Benzonitrile} \geq 61\%$). This points to inefficient hydrogenation (**Fig. 7.1**, step **(B)**) where hydrogen generated from dehydrogenation is not effectively utilised by Cu/SiO_2 for amine production. This limitation can be addressed by incorporating a second catalyst to promote hydrogenation to benzylamine. A critical prerequisite is that the second metal must not promote side-reactions (*e.g.* hydrogenolysis and denitrogenation). Conventional supported transition metal (Pd, Pt and Ni) hydrogenation catalysts exhibit high activity for the hydrogenation of unsaturated functions (–C=O, –C≡N and –C=N) but low selectivity due to hydrogenolysis, decarbonylation and denitrogenation [7.45]. In contrast, nano-scale supported Au has displayed unique hydrogenation chemoselectivity [7.29,7.46]. We have established synergism in physical mixtures of Au/TiO_2 and Cu/SiO_2 in **Chapter 5** where supported Au enhances selective nitro- hydrogenation rate *via* utilisation of hydrogen from coupled benzyl alcohol dehydrogenation over Cu. Application of combined Au/TiO_2 and Cu/SiO_2 mixtures in the tandem process can promote selective hydrogenation of benzylideneimine to benzylamine. Au/TiO_2 was accordingly chosen in this study as a suitable candidate.

7.3.3 Au/TiO_2 Characterisation and Catalytic Response of $Cu/SiO_2 + Au/TiO_2$ in the Benzyl Alcohol Reaction

The SSA of Au/TiO_2 (**Table 7.1**) matches that (50 $m^2 g^{-1}$) reported elsewhere [7.47] for Au/TiO_2 prepared by deposition-precipitation. Hydrogen consumption (T_{max} = 373 K) during TPR exceeded the requirement for $Au^{3+} \rightarrow Au^0$ reduction, suggesting a partial support ($Ti^{4+} \rightarrow Ti^{3+}$) reduction [7.48]. Gold particle size <10 nm has been identified as an essential requirement for significant hydrogen adsorption/activation and hydrogenation activity [7.37]. STEM analysis (**Fig. 7.2(BI)**) has established Au size at the nano-scale (1-6 nm) and a mean (3.2 nm) close to that for Cu on SiO_2. Hydrogen chemisorption at reaction conditions (498 K) on Au/TiO_2 was appreciably greater than that recorded for Cu/SiO_2 (**Table 7.1**), consistent with that reported by Borgschulte *et al*. [7.49] who reported higher hydrogen uptake rate over Au film than Cu film (460-540 K). XPS analysis was employed to evaluate the electronic properties of supported Au phase. The XPS profile (not shown) over the Au $4f_{7/2}$ region is characterised by a lower BE (**Table 7.1**) than that which is characteristic of Au^0 (BE = 84.0 eV) [7.50],

suggesting electron donation from the support with the generation of $Au^{\delta-}$ surface species [7.51].

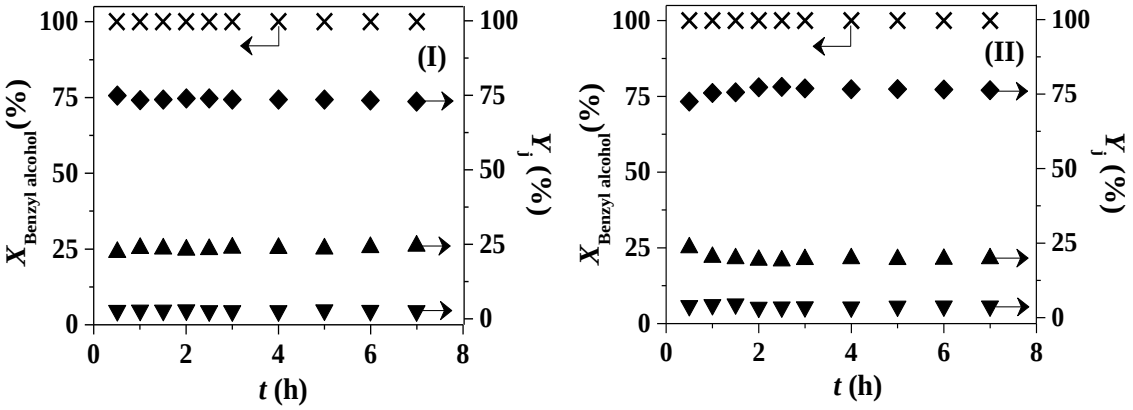

Fig. 7.5: Temporal variation in alcohol conversion ($X_{Benzyl\ alcohol}$, ×) and product yield (Y_j, ▲: benzylamine, ◆: benzonitrile, ▼: toluene) in the reaction of benzyl alcohol (in N_2) with NH_3 over Cu/SiO_2 + Au/TiO_2 as a function of Cu/Au molar ratio ((I): 10, (II): 5). *Reaction conditions*: T = 498 K, P = 1 atm, NH_3/Benzyl alcohol = 40.

The performance of Au/TiO_2 has been assessed against Cu/SiO_2 in the stand-alone dehydrogenation of benzyl alcohol (at 498 K), where lower (by an order of magnitude) dehydrogenation rate was obtained over Au. This is consistent with literature that has shown negligible catalytic activity for gas phase alcohol dehydrogenation over supported Au at temperatures <523 K [7.30]. In the reaction of benzyl alcohol with NH_3 (in N_2) over Cu/SiO_2 + Au/TiO_2, hydrogen generation (*via* dehydrogenation) depends on Cu content. This hydrogen contributes to benzylideneimine hydrogenation (**Fig. 7.1**, step **(B)**). The effect of variations in Cu/Au molar ratio on conversion and product yield was evaluated for two representative values (5 and 10) and the results are presented in **Fig. 7.5**. Full conversion of the alcohol ($X_{Benzyl\ alcohol}$) was achieved and maintained for 7 h on-stream. As in reaction over Cu/SiO_2 alone, benzonitrile was the principal product but benzylamine was generated as a significant secondary product over the mixture with trace quantities of toluene (yield = 3%). There was no detectable formation of *N*-benzylidenebenzylamine or dibenzylamine. Product distribution was equivalent for both Cu/Au ratios. The generation of benzylamine demonstrates that the inclusion of Au/TiO_2 facilitated benzylideneimine hydrogenation without further condensation to *N*-benzylidenebenzylamine and/or dibenzylamine (**Fig. 7.1**, steps **(C)** and **(D)**). This can be attributed to the greater H_2 chemisorption capacity of Au/TiO_2 relative to Cu/SiO_2 (**Table 7.1**) that more effectively captures and utilises the hydrogen generated in the alcohol dehydrogenation. Moreover, Au/TiO_2 and Cu/SiO_2 combination serves to

promote dehydrogenation (to benzaldehyde) and hydrogenation (to benzylamine) on isolated metal sites and inhibit condensation. We envision a synergism between Au/TiO_2 and Cu/SiO_2 that is illustrated in **Fig. 7.6**. The supported copper phase promotes

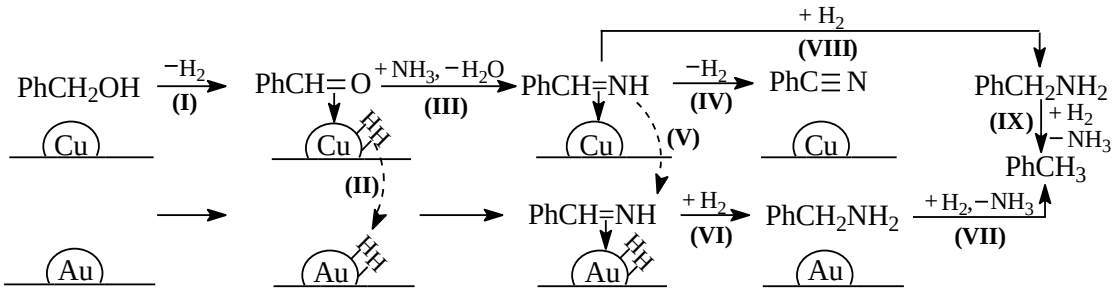

Fig. 7.6: Reaction scheme illustrating the proposed Cu-Au cooperation effect in benzylamine production.

dehydrogenation of benzyl alcohol to benzaldehyde to generate Cu-H species (step **(I)**) [7.52]. The extracted atomic hydrogen can spillover across the Cu-support interface [7.53] and the physical boundary with Au/TiO_2 [7.53] onto Au sites (step **(II)**). The benzaldehyde that generated on Cu from benzyl alcohol dehydrogenation reacts with NH_3 to form the intermediate benzylideneimine (step **(III)**) that can undergo dehydrogenation to benzonitrile (step **(IV)**). The latter undesired step is favoured under hydrogen lean conditions (see **Fig. 7.3(I)**) which limit hydrogenation to benzylamine. Benzylideneimine desorbs from electron-deficient $Cu^{\delta+}$ (from XPS analysis) as a result of repulsion with the polarised $–C^{\delta+}=N$ function. The imine adsorbs on electron-rich $Au^{\delta-}$ *via* interaction with –C=N (step **(V)**) and is hydrogenated to benzylamine (step **(VI)**). In contrast to reaction over Cu/SiO_2, the incorporation of Au serves as an additional and more efficient site for benzylideneimine hydrogenation to benzylamine while Cu is responsible for the alcohol dehydrogenation to benzaldehyde. The generation of amine and aldehyde on two isolated metal sites (Au and Cu, respectively) inhibits condensation with a consequent enhancement of benzylamine selectivity. Toluene formation is possible through the hydrogenolysis of benzylamine [7.5], but depends on hydrogen availability and is not a significant feature of reaction over $Cu/SiO_2 + Au/TiO_2$.

In order to address the limitations in terms of available surface reactive hydrogen (generated from benzyl alcohol dehydrogenation), we examined the possibility of enhancing benzylamine production by supplying hydrogen (P_{H_2} = 0.04 atm) in the feed;

time on-stream results are presented in **Fig. 7.7**. Full benzyl alcohol conversion was maintained for 7 h on-stream where the supply of external H_2 resulted in a two-fold increase in benzylamine yield (46%), decreased benzonitrile production with increased

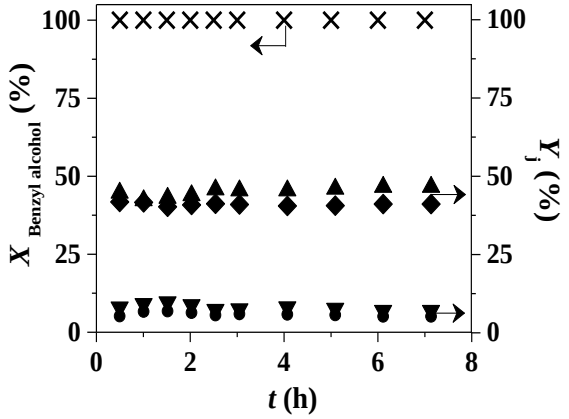

Fig. 7.7: Temporal variation of alcohol conversion ($X_{\text{Benzyl alcohol}}$, ×) and product yield ($Y_j$, ▲: benzylamine, ◆: benzonitrile, ▼: toluene, ●: dibenzylamine) in the reaction of benzyl alcohol with NH_3 over Cu/SiO_2 + Au/TiO_2 with additional external H_2 supply in the feed. *Reaction conditions*: P_{H_2} = 0.04 atm, T = 498 K, NH_3/Benzyl alcohol = 40.

toluene (8%) and the appearance of dibenzylamine (6%) in the product stream. As presented in **Table 7.2**, a further increase in P_{H_2} (to 0.08 atm) elevated benzylamine yield (to 58%) with a consequent increase in condensation-hydrogenation to dibenzylamine (17%) and hydrogenolysis to toluene (13%). Provision of H_2 in the feed served to increase the available surface hydrogen and hydrogenation of *N*-benzylideneimine over Au (**Fig. 7.6**, step **(VI)**) and/or Cu (step **(VIII)**). Reaction temperature is a critical variable that impacts on reactant/intermediate activation, which in turn influences activity and product distribution in reductive amination [7.27]. We addressed temperature effects in this tandem reaction system (at P_{H_2} = 0.04 atm) and the results are presented in **Fig. 7.8**. A decrease in temperature from 498 to 448 K served

Table 7.2: Effect of H_2 partial pressure (P_{H_2}) on product yield (Y_j, %) in the reaction of benzyl alcohol with NH_3 over Cu/SiO_2 + Au/TiO_2; *Reaction conditions*: T = 498 K, Cu/Au = 10, NH_3/Benzyl alcohol = 40.

P_{H_2} (atm)	$Y_{\text{Benzylamine}}$ (%)	$Y_{\text{Benzonitrile}}$ (%)	Y_{Toluene} (%)	$Y_{\text{Dibenzylamine}}$ (%)
0.04	46	40	8	6
0.08	58	12	13	17

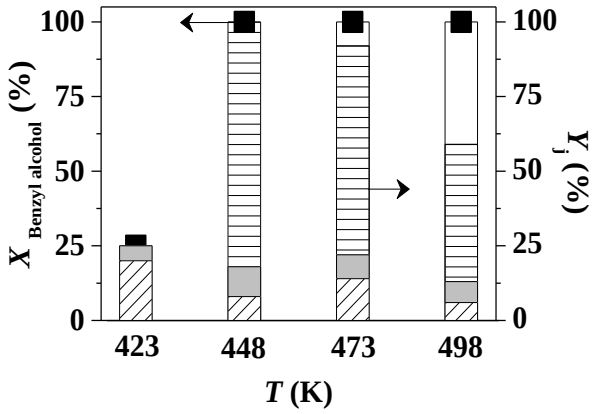

Fig. 7.8: Effect of temperature on alcohol conversion ($X_{Benzyl\ alcohol}$, ■) and product yield (Y_j, horizontal lined bars: benzylamine, open bars: benzonitrile, gray bars: toluene, hatched bars: dibenzylamine) in the reaction of benzyl alcohol with NH_3 over Cu/SiO_2 + Au/TiO_2 with additional external H_2 supply in the feed. *Reaction conditions*: P_{H_2} = 0.04 atm, NH_3/Benzyl alcohol = 40.

to increase benzylamine yield to 81%. Toluene yield (*ca*. 10%) remained largely unchanged and there was no benzonitrile formed. This result is in line with the report of Zamlynny *et al*. [7.41] who attributed higher aniline selectivity in the reductive amination of cyclohexanol with increasing temperature (473 → 573 K) to a shift in reaction equilibrium in favour of cyclohexylamine dehydrogenation. A further decrease in temperature (to 423 K) was accompanied by a severe decline in conversion with dibenzylamine as principal product. We can tentatively attribute this response to inefficient activation/dehydrogenation of benzyl alcohol and reductive amination of benzaldehyde (**Fig. 7.1**, path **(A→B)**) with a consequent lower activity and condensation-hydrogenation of unconverted benzaldehyde with benzylamine to *N*-benzylidenebenzylamine and then to dibenzylamine. To the best of our knowledge, this is the first report of selective benzylamine synthesis from benzyl alcohol *via* a tandem dehydrogenation/amination/reduction reaction in continuous gas phase operation. The highest yield (81%) achieved exceeds that reported for gas phase hydrogenation of benzonitrile (<70% yield) [7.1,7.14]. Batch liquid phase amination of benzyl alcohol did not result in detectable benzylamine formation [7.24,7.25]. Moreover, efficient utilisation of a H_2 lean feed represents a significant advancement in terms of process efficiency and sustainability when compared with conventional hydrogenation using excess pressurised H_2.

7.4 Conclusion

This study has established the viability of a tandem dehydrogenation/amination/ reduction route for high throughout production of benzylamine from benzyl alcohol over Cu/SiO_2 (1-6 nm, mean = 3.1 nm) and Au/TiO_2 (1-6 nm, mean = 3.2 nm) in continuous gas phase operation. Reductive amination of benzaldehyde (as feed) over Cu/SiO_2 generated dibenzylamine as predominant product (yield up to 99%) with no detectable benzylamine due to the facile condensation with benzaldehyde. We have demonstrated transfer hydrogenation for reaction of benzyl alcohol with NH_3 (in N_2) over Cu/SiO_2 using hydrogen from benzyl alcohol dehydrogenation. Benzonitrile was the principal product due to limited hydrogenation capacity of Cu/SiO_2. This was addressed by incorporating Au/TiO_2 (as a physical mixture) that shows five times higher hydrogen chemisorption capacity relative to Cu/SiO_2 under reaction conditions. Combination of Au/TiO_2 with Cu/SiO_2 served to suppress condensation of benzylamine with benzaldehyde leading to enhanced benzylamine production. We have established a reaction synergism between Cu/SiO_2 and Au/TiO_2 where the supported Cu phase is responsible for coupled benzyl alcohol dehydrogenation/amination and Au facilitates hydrogenation to benzylamine. The formation of the intermediate benzaldehyde and product benzylamine on two isolated metal sites inhibited condensation to *N*-benzylidenebenzylamine and dibenzylamine. An unprecedented benzylamine yield (up to 81%) in continuous mode was achieved through an optimisation of H_2 partial pressure and reaction temperature.

7.5 References

[7.1] R.K. Marella, K.S. Koppadi, Y. Jyothi, K.S.R. Rao, D.R. Burri, *Selective gas-phase hydrogenation of benzonitrile into benzylamine over Cu-MgO catalysts without using any additives*. New J. Chem. 37 (2013) 3229-3235.

[7.2] X.J. Cui, X.C. Dai, Y.Q. Deng, F. Shi, *Development of a general non-noble metal catalyst for the benign amination of alcohols with amines and ammonia*. Chem. Eur. J. 19 (2013) 3665-3675.

[7.3] H. Cheng, X. Meng, C. Wu, X. Shan, Y. Yu, F. Zhao, *Selective hydrogenation of benzonitrile in multiphase reaction systems including compressed carbon dioxide over Ni/Al_2O_3 catalyst*. J. Mol. Catal. A: Chem. 379 (2013) 72-79.

[7.4] S.P. Bawane, S.B. Sawant, *Reaction kinetics of the liquid-phase hydrogenation of benzonitrile to benzylamine using Raney nickel catalyst*. Chem. Eng. J. 103 (2004) 13-19.

[7.5] J.J.W. Bakker, A.G. van der Neut, M.T. Kreutzer, J.A. Moulijn, F. Kapteijn, *Catalyst performance changes induced by palladium phase transformation in the hydrogenation of benzonitrile*. J. Catal. 274 (2010) 176-191.

[7.6] Y.M. López-De Jesús, C.E. Johnson, J.R. Monnier, C.T. Williams, *Selective hydrogenation of benzonitrile by alumina-supported Ir-Pd Catalysts*. Top. Catal. 53 (2010) 1132-1137.

[7.7] S. Gőbölös, N. Mahata, I. Borbáth, M. Hegedűs, J.L. Margitfalvi, *Hydrogenation of benzonitrile on Sn-Pt/SiO_2 catalysts prepared by introducing $SnEt_4$ to Pt/SiO_2: Role of tin*. React. Kinet. Catal. Lett. 74 (2001) 345-352.

[7.8] H. Khajavi, H.A. Stil, H. Kuipers, J. Gascon, F. Kapteijn, *Shape and transition state selective hydrogenations using egg-shell Pt-MIL-101(Cr) catalyst*. ACS Catal. 3 (2013) 2617-2626.

[7.9] M.H.G. Prechtl, J.D. Scholten, J. Dupont, *Tuning the selectivity of ruthenium nanoscale catalysts with functionalised ionic liquids: Hydrogenation of nitriles*. J. Mol. Catal. A: Chem. 313 (2009) 74-78.

[7.10] J. Krupka, J. Pasek, *Nitrile hydrogenation on solid catalysts: New insights into the reaction mechanism*. Curr. Org. Chem. 16 (2012) 988-1004.

[7.11] S. Gomez, J.A. Peters, T. Maschmeyer, *The reductive amination of aldehydes and ketones and the hydrogenation of nitriles: Mechanistic aspects and selectivity control*. Adv. Synth. Catal. 344 (2002) 1037-1057.

[7.12] H. Yoshida, Y. Wang, S. Narisawa, S.-I. Fujita, R. Liu, M. Arai, *A multiphase reaction medium including pressurized carbon dioxide and water for selective hydrogenation of benzonitrile with a Pd/Al_2O_3 catalyst*. Appl. Catal. A: Gen. 456 (2013) 215-222.

[7.13] L. Hegedűs, T. Máthé, *Selective heterogeneous catalytic hydrogenation of nitriles to primary amines in liquid phase: Part I. Hydrogenation of benzonitrile over palladium*. Appl. Catal. A: Gen. 296 (2005) 209-215.

[7.14] C.V. Rode, M. Arai, M. Shirai, Y. Nishiyama, *Gas-phase hydrogenation of nitriles by nickel on various supports*. Appl. Catal. A: Gen. 148 (1997) 405-413.

[7.15] T. Gross, A.M. Seayad, M. Ahmad, M. Beller, *Synthesis of primary amines: First homogeneously catalyzed reductive amination with ammonia*. Org. Lett. 4 (2002) 2055-2058.

[7.16] B. Miriyala, S. Bhattacharyya, J.S. Williamson, *Chemoselective reductive alkylation of ammonia with carbonyl compounds: Synthesis of primary and symmetrical secondary amines*. Tetrahedron 60 (2004) 1463-1471.

[7.17] A.W. Heinen, J.A. Peters, H. van Bekkum, *The reductive amination of benzaldehyde over Pd/C catalysts: Mechanism and effect of carbon modifications on the selectivity*. Eur. J. Org. Chem. 13 (2000) 2501-2506.

[7.18] S. Gomez, J.A. Peters, J.C. van der Waal, W.Z. Zhou, T. Maschmeyer, *Preparation of benzylamine by highly selective reductive amination of benzaldehyde over Ru on an acidic activated carbon support as the catalyst*. Catal. Lett. 84 (2002) 1-5.

[7.19] S. Gomez, J.A. Peters, J.C. van der Waal, T. Maschmeyer, *High-throughput experimentation as a tool in catalyst design for the reductive amination of benzaldehyde*. Appl. Catal. A: Gen. 254 (2003) 77-84.

[7.20] S. Gomez, J.A. Peters, J.C. van der Waal, P.J. van den Brink, T. Maschmeyer, *The rationalization of catalyst behaviour in the reductive amination of benzaldehyde with ammonia using a simple computer model*. Appl. Catal. A: Gen. 261 (2004) 119-125.

[7.21] A. Rahman, S.B. Jonnalagadda, *Robust and selective reductive amination of aldehydes and ketones with Ni-boride-silica catalysts system at low temperature*. Oxid. Commun. 35 (2012) 99-109.

[7.22] F. Qi, L. Hu, S. Lu, X. Cao, H. Gu, *Selective synthesis of secondary amines by Pt nanowire catalyzed reductive amination of aldehydes and ketones with ammonia*. Chem. Commun. 48 (2012) 9631-9633.

[7.23] C. Gunanathan, D. Milstein, *Selective synthesis of primary amines directly from alcohols and ammonia*. Angew. Chem. Int. Edit. 47 (2008) 8661-8664.

[7.24] K. Yamaguchi, J. He, T. Oishi, N. Mizuno, *The "borrowing hydrogen strategy" by supported ruthenium hydroxide catalysts: Synthetic scope of symmetrically and unsymmetrically substituted amines*. Chem. Eur. J. 16 (2010) 7199-7207.

[7.25] J. He, K. Yamaguchi, N. Mizuno, *Selective synthesis of secondary amines via N-alkylation of primary amines and ammonia with alcohols by supported copper hydroxide catalysts*. Chem. Lett. 39 (2010) 1182-1183.

[7.26] J.F. Jenck, F. Agterberg, M.J. Droescher, *Products and processes for a sustainable chemical industry: A review of achievements and prospects*. Green Chem. 6 (2004) 544-556.

[7.27] J. Becker, J.P.M. Niederer, M. Keller, W.F. Holderich, *Amination of cyclohexanone and cyclohexanol/cyclohexanone in the presence of ammonia and hydrogen using copper or a group VIII metal supported on a carrier as the catalyst*. Appl. Catal. A: Gen. 197 (2000) 229-238.

[7.28] K.V.R. Chary, K.K. Seela, D. Naresh, P. Ramakanth, *Characterization and reductive amination of cyclohexanol and cyclohexanone over Cu/ZrO_2 catalysts*. Catal. Commun. 9 (2008) 75-81.

[7.29] T. Mitsudome, K. Kaneda, *Gold nanoparticle catalysts for selective hydrogenations*. Green Chem. 15 (2013) 2636-2654.

[7.30] Y. Guan, E.J.M. Hensen, *Ethanol dehydrogenation by gold catalysts: The effect of the gold particle size and the presence of oxygen*. Appl. Catal. A: Gen. 361 (2009) 49-56.

[7.31] Z. Huang, F. Cui, J. Xue, J. Zuo, J. Chen, C. Xia, *Cu/SiO_2 catalysts prepared by hom- and heterogeneous deposition-precipitation methods: Texture, structure, and catalytic performance in the hydrogenolysis of glycerol to 1,2-propanediol*. Catal. Today 183 (2012) 42-51.

[7.32] X. Wang, N. Perret, M.A. Keane, *The role of hydrogen partial pressure in the gas phase hydrogenation of p-chloronitrobenzene over alumina supported Au and Pd: A consideration of reaction thermodynamics and kinetics*. Chem. Eng. J. 210 (2012) 103-113.

[7.33] K.V. Murthy, P.M. Patterson, G. Jacobs, B.H. Davis, M.A. Keane, *An exploration of activity loss during hydrodechlorination and hydrodebromination over Ni/SiO_2*. J. Catal. 223 (2004) 74-85.

[7.34] S. Jujjuri, E. Ding, S.G. Shore, M.A. Keane, *A characterization of $Ln\text{-}Pd/SiO_2$ (Ln=La, Ce, Sm, Eu, Gd and Yb): Correlation of surface chemistry with hydrogenolysis activity*. J. Mol. Catal. A: Chem. 272 (2007) 96-107.

[7.35] Y.-Y. Zhu, S.-R. Wang, L.-J. Zhu, X.-L. Ge, X.-B. Li, Z.-Y. Luo, *The Influence of copper particle dispersion in Cu/SiO_2 catalysts on the hydrogenation synthesis of ethylene glycol*. Catal. Lett. 135 (2010) 275-281.

[7.36] M. Pozzo, D. Alfe, *Hydrogen dissociation and diffusion on transition metal (= Ti, Zr, V, Fe, Ru, Co, Rh, Ni, Pd, Cu, Ag)-doped Mg(0001) surfaces*. Int. J. Hydrogen Energ. 34 (2009) 1922-1930.

[7.37] G.C. Bond, C. Louis, D.T. Thompson, *Catalysis by gold*, G.J. Hutchings (Ed.), Imperial College Press, London, 2006.

[7.38] S.D. Jones, L.M. Neal, M.L. Everett, G.B. Hoflund, H.E. Hagelin-Weaver, *Characterization of ZrO_2-promoted Cu/ZnO/nano-Al_2O_3 methanol steam reforming catalysts*. Appl. Surf. Sci. 256 (2010) 7345-7353.

[7.39] S.R. Kirumakki, M. Papadaki, K.V.R. Chary, N. Nagaraju, *Reductive amination of cyclohexanone in the presence of cyclohexanol over zeolites Hβ and HY*. J. Mol. Catal. A: Chem. 321 (2010) 15-21.

[7.40] M. Hamid, P.A. Slatford, J.M.J. Williams, *Borrowing hydrogen in the activation of alcohols*. Adv. Synth. Catal. 349 (2007) 1555-1575.

[7.41] V. Zamlynny, L. Kubelkova, E. Baburek, K. Jiratova, J. Novakova, *Amination of cyclohexanol over metallosilicate-based materials*. Appl. Catal. A: Gen. 169 (1998) 119-125.

[7.42] Y.F. Hu, J.P. Cao, J. Deng, B.Y. Cui, M.W. Tan, J.F. Li, H.S. Zhang, *Synthesis of acetonitrile from ethanol via reductive amination over Cu/γ-Al_2O_3*. React. Kinet. Mech. Catal. 106 (2012) 127-139.

[7.43] Y. Zhang, Y. Zhang, C. Feng, C. Qiu, Y. Wen, J. Zhao, *Amination of ethanol to acetonitrile over Ni-doped Co/γ-Al_2O_3 catalyst*. Catal. Commun. 10 (2009) 1454-1458.

[7.44] A. Fischer, M. Maciejewski, T. Burgi, T. Mallat, A. Baiker, *Cobalt-catalyzed amination of 1,3-propanediol: Effects of catalyst promotion and use of supercritical ammonia as solvent and reactant*. J. Catal. 183 (1999) 373-383.

[7.45] A. Corma, P. Serna, *Chemoselective hydrogenation of nitro compounds with supported gold catalysts*. Science 313 (2006) 332-334.

[7.46] H.-U. Blaser, H. Steiner, M. Studer, *Selective catalytic hydrogenation of functionalised nitroarenes: An update*. ChemCatChem 1 (2009) 210-221.

[7.47] V. Jovic, W.-T. Chen, D. Sun-Waterhouse, M.G. Blackford, H. Idriss, G.I.N. Waterhouse, *Effect of gold loading and TiO_2 support composition on the activity of Au/TiO_2 photocatalysts for H_2 production from ethanol-water mixtures*. J. Catal. 305 (2013) 307-317.

[7.48] M. Ousmane, L.F. Liotta, G. Di-Carlo, G. Pantaleo, A.M. Venezia, G. Deganello, L. Retailleau, A. Boreave, A. Giroir-Fendler, *Supported Au catalysts for low-temperature abatement of propene and toluene, as model VOCs: Support effect*. Appl. Catal. B: Environ. 101 (2011) 629-637.

[7.49] A. Borgschulte, R.J. Westerwaal, J.H. Rector, H. Schreuders, B. Dam, R. Griessen, *Catalytic activity of noble metals promoting hydrogen uptake*. J. Catal. 239 (2006) 263-271.

[7.50] S. Arrii, F. Morfin, A.J. Renouprez, J.L. Rousset, *Oxidation of CO on gold supported catalysts prepared by laser vaporization: Direct evidence of support contribution*. J. Am. Chem. Soc. 126 (2004) 1199-1205.

[7.51] Y.F. Han, Z.Y. Zhong, K. Ramesh, F.X. Chen, L.W. Chen, T. White, Q.L. Tay, S.N. Yaakub, Z. Wang, *Au promotional effects on the synthesis of H_2O_2 directly from H_2 and O_2 on supported Pd-Au alloy catalysts*. J. Phys. Chem. C 111 (2007) 8410-8413.

[7.52] V.Z. Fridman, A.A. Davydov, K. Titievsky, *Dehydrogenation of cyclohexanol on copper-containing catalysts: II. The pathways of the cyclohexanol dehydrogenation reaction to cyclohexanone on copper-active sites in oxidation state Cu^0 and Cu^+*. J. Catal. 222 (2004) 545-557.

[7.53] R. Prins, *Hydrogen spillover: Facts and fiction*. Chem. Rev. 112 (2012) 2714-2738.

Chapter 8

Selective Hydrogenation of Furfural to Furfuryl Alcohol over Au/Al_2O_3

Previous chapters employ petroleum based raw material for the production of high value chemicals. This chapter considers gas phase hydrogenation of biomass derived furfural for selective continuous production of furfuryl alcohol over Au/Al_2O_3.

8.1 Introduction

Furfural is a biomass derived heterocyclic aldehyde that is attracting increasing attention as a renewable, non-petroleum based raw material for the production of a diversity of high value products [8.1]. A primary route for conversion of furfural is selective hydrogenation to furfuryl alcohol, used in the manufacture of resins, rubbers and fibres [8.2]. Selectivity is crucial where decarbonylation (path **(I)**), furan ring reduction (paths **(II)**, **(IV)** and **(VI)**) and hydrogenolysis (path **(V)**) generate a range of by-products as shown in **Fig. 8.1**. Furfural hydrogenation has been examined in both liquid and gas phase operation, where different metal catalysts (Pd [8.3], Pt [8.4], Ni [8.5] and Cu [8.6]) have exhibited diverse product distributions. Noble metals (Pd and Pt) generally catalyse decarbonylation to furan and promote hydrogenation to tetrahydrofurfuryl alcohol and hydrogenolysis to 2-methylfuran [8.3,8.4]. Incorporation

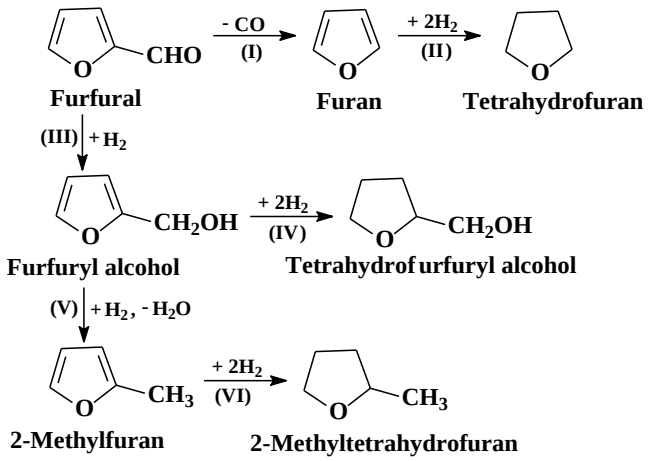

Fig. 8.1: Reaction pathways for furfural hydrogenation.

of additives such as Sn and Ge serve to alter metal site electronic character (*via* electron donation) that favours adsorption/activation of the carbonyl group and enhances selectivity to the target alcohol [8.7]. Raney Ni exhibits low selectivity (75%) to furfuryl alcohol but modification with heteropolyacid salts ($Cu_{1.5}PMo_{12}$) increased alcohol selectivity (98%) although no rationale was provided to account for this effect [8.8]. Incorporation of Ce, Fe and Co to Ni-B polarises/activates the carbonyl function resulting in preferential formation of furfuryl alcohol [8.9-8.11].

Taking an overview of the literature, Cu catalysts are the most selective to furfuryl alcohol in both liquid and gas phase operation [8.12-8.17]. Batch liquid phase reaction has been predominantly conducted at elevated H_2 pressure (10-20 bar) [8.6,8.12]. A move from batch to continuous processes presents advantages in terms of product/catalyst separation, reduced downtime, product quality control and process safety [8.18]. In continuous operation, Liu *et al*. [8.14] reported 90% selectivity to furfuryl alcohol over a commercial copper chromite but with the generation of toxic Cr_2O_3 waste. Application of Cu/MgO [8.15,8.16] and Cu/C [8.17] can overcome this limitation and these systems are used as the benchmark in this study. Supported Au nano-particles have shown unique selectivity for –C=O reduction in the presence of other functionalities (*e.g.* C=C) [8.19]. However, we could not find any reported application of supported Au catalysts in furfural hydrogenation beyond the observation by Hong *et al.* [8.20] of negligible activity (1% conversion) for Au/SiO_2 in liquid phase reaction at high pressure (10 bar). We should note the work of Ohyama *et al.* [8.21] who reported alcohol formation (*ca.* 65% selectivity) from 2-hydroxylmethyl-5-furfural over Au/Al_2O_3 in batch liquid operation at elevated pressure (38 bar). In previous work [8.22] we have demonstrated full selectivity in the gas phase reduction of benzaldehyde to benzyl alcohol over Au/Al_2O_3. In this study, we have adopted Au/Al_2O_3 as a model catalyst, assess for the first time the gas phase continuous hydrogenation of furfural and provide a comparison with the benchmark supported Cu.

8.2 Experimental

8.2.1 Materials and Catalyst Preparation

Au/Al_2O_3 (1.1% w/w) was prepared by deposition-precipitation using urea (Riedel-de Haën, 99%) as basification agent. An aqueous solution of urea (100-fold urea excess) and $HAuCl_4$ (Sigma-Aldrich, 99%, 4.4×10^{-6} mol cm^{-3}, 400 cm^3) was added to the γ-

Al_2O_3 support (Puralox, Condea Vista, 30 g). The suspension was stirred and heated to 353 K (2 K min^{-1}) and the pH progressively increased to reach *ca.* 7 after 3 h as a result of urea decomposition [8.23]. The solid obtained was separated by filtration, washed with distilled water until chlorine free (based on the $AgNO_3$ test) and dried in He (45 cm^3 min^{-1}) at 373 K (2 K min^{-1}) for 5 h. The catalyst precursor was sieved (ATM fine test sieves) to a mean particle diameter = 75 μm. Catalyst activation by temperature programmed (2 K min^{-1} to 603 K) reduction (TPR in 60 cm^3 min^{-1} H_2) ensured metal precursor reduction ($Au^{3+} \rightarrow Au^0$) [8.22]. The activated sample was passivated in 1% v/v O_2/He for 1 h at ambient temperature for *ex situ* characterisation.

8.2.2 Catalyst Characterisation

The Au content was measured by atomic absorption spectroscopy (Shimadzu AA-6650 spectrometer) from the diluted extract in aqua regia (25% v/v HNO_3/HCl). X-ray diffractograms (XRD) were recorded on a Bruker/Siemens D500 incident X-ray diffractometer using Cu Kα radiation with a scan rate of 0.02º $step^{-1}$ over the range 20º ≤ 2θ ≤ 80º. The diffractogram was identified against JCPDS-ICDD reference standards, *i.e.* Au (04-0784) and γ-Al_2O_3 (10-0425). Nitrogen physisorption was performed using the Micromeritics Gemini 2390p system, where the sample was outgassed at 423 K for 1 h in N_2 prior to analysis. Total specific surface area (SSA) was calculated using the standard BET method with cumulative pore volume and pore radius from BJH analysis of the desorption isotherm. Hydrogen chemisorption (pulse 10 μl titration at 298 K and 413 K) following TPR (in 17 cm^3 min^{-1} (Brooks mass flow controlled) 5% v/v H_2/N_2 to 603 K at 2 K min^{-1}) was conducted on the CHEM-BET 3000 (Quantachrome Instrument) unit with data acquisition/manipulation using the TPR Win™ software as outlined previously [8.22]. In a blank test, there was no measurable H_2 uptake on the Al_2O_3 support. X-ray photoelectron spectroscopic (XPS) analysis was performed on a VG ESCA spectrometer equipped with monochromatised Al Kα radiation (1486 eV). The sample was adhered to conducting carbon tape, mounted in the sample holder and subjected to ultra-high vacuum conditions (<10^{-8} Torr). Full range surveys (Au $4f_{5/2}$ and $4f_{7/2}$ spectra) were collected where binding energies (BE) were calibrated with respect to the C1*s* peak (284.5 eV). The Au 4*f* spectra were fitted with abstraction of the Shirley background using the Gaussian-Lorentzian function in XPSPEAK 41. Gold particle morphology (shape and size) was examined by scanning transmission electron microscopy (STEM, JEOL 2200FS field emission gun-equipped unit), employing Gatan

Digital Micrograph 1.82 for data acquisition/manipulation. Samples for analysis were prepared by dispersion in acetone and deposited on a holey carbon/Cu grid (300 Mesh). The surface area weighted mean Au size (*d*) was based on a count of 300 particles according to

$$d = \frac{\sum_i n_i d_i^3}{\sum_i n_i d_i^2} \qquad \textbf{(8.1)}$$

where n_i is the number of particles of diameter d_i.

8.2.3 Catalytic Procedure

The hydrogenation of furfural (Sigma-Aldrich, 99%) was carried out at atmospheric pressure over the 383-523 K temperature range, *in situ* after activation in a continuous flow fixed bed tubular reactor (15 mm i.d.). A layer of borosilicate glass beads served as preheating zone, ensuring that the furfural reactant was vaporised and reached reaction temperature before contacting the catalyst bed. Isothermal conditions (±1 K) were maintained by diluting the catalyst bed with ground glass (75 μm). Reaction temperature was continuously monitored by a thermocouple inserted in a thermowell within the catalyst bed. Furfural was delivered as a *n*-butanolic (Sigma-Aldrich, >99%) solution to the reactor *via* a glass/teflon air-tight syringe and teflon line using a microprocessor controlled infusion pump (Model 100 kd Scientific) at a fixed calibrated flow rate with a co-current flow of H_2 in excess (250-1500) of the stoichiometry requirement for furfuryl alcohol formation; $GHSV = 5 \times 10^3 - 3 \times 10^4$ h^{-1}. The catalyst mass to inlet furfural molar feed rate (*W/F*) spanned the range 100 - 300 g mol^{-1} h. In blank tests, passage of furfural in a stream of H_2 through the empty reactor or over the (Al_2O_3) support alone did not result in any detectable conversion. The reactor effluent was condensed in a liquid nitrogen trap for subsequent analysis using a Perkin-Elmer Auto System XL gas chromatograph equipped with a programmed split/splitless injector and a flame ionization detector, employing a DB-1 (50 m × 0.33 mm i.d., 0.20 μm film thickness) capillary column (J&W Scientific). Data acquisition and manipulation were performed using the TurboChrom Workstation Version 6.3.2 (for Windows) chromatography data system. Reactant/products (in **Fig. 8.1**) were used as supplied (Sigma-Aldrich, 99%) for identification/analysis. All gases (O_2, H_2, N_2 and He) were of high purity (BOC, >99.98%). Furfural fractional conversion (*X*) is defined by

$$X = \frac{[\,furfural\,]_{in} - [\,furfural\,]_{out}}{[\,furfural\,]_{in}} \quad \textbf{(8.2)}$$

and selectivity (S) to product (j) is given by

$$S_j\,(\%) = \frac{[\,product\,]_{j,\,out}}{[\,furfural\,]_{in} - [\,furfural\,]_{out}} \times 100 \quad \textbf{(8.3)}$$

where the subscripts "in" and "out" refer to the inlet and outlet gas streams. Catalytic activity is quantified in terms of furfural consumption rate (R) obtained from

$$R\,(\mu\text{mol h}^{-1}) = X_0 \times F \quad \textbf{(8.4)}$$

where initial fractional conversion (X_0) was extracted from time on-stream measurements as described elsewhere [8.22]. Turnover frequency (*TOF*, rate per active site) was calculated using

$$TOF\ (\text{h}^{-1}) = \frac{R}{n_{Au} \times D} \quad \textbf{(8.5)}$$

where n_{Au} is the number moles of Au in the catalyst bed and D is the Au dispersion determined by STEM [8.22]. Repeated reactions with different samples from the same batch of catalyst delivered raw data reproducibility and a carbon mass balance that were within ±5%.

Table 8.1: Gold loading, specific surface area (SSA), pore volume, mean pore radius, temperature maxima (T_{max}) and H_2 consumption during temperature programmed reduction (TPR), mean Au size from STEM analysis (d) and H_2 chemisorption (at 413 K) for Au/Al_2O_3.

Loading (% w/w)	SSA ($m^2\,g^{-1}$)	Pore volume ($cm^3\,g^{-1}$)	Pore radius (Å)	T_{max} (K)	H_2 consumption ($mol_{H_2}\,mol_{Au}^{-1}$)	d (nm)	H_2 chemisorption ($\mu mol\,g_{Au}^{-1}$)
1.1	166	0.36	29	451	1.5	4.3	318

8.3 Results and Discussion

8.3.1 Catalyst Characterisation

Analysis of catalyst structure by XRD (diffractogram not shown) revealed diffraction peaks at 2θ = 37.6°, 39.5°, 45.9° and 67.0° due to γ-Al_2O_3 (JCPDS-ICDD 10-0425). There was no detectable signal for metallic Au (2θ = 38.1°, 44.3°, 64.6° and 77.5°; JCPDS-ICDD 04-0784), suggesting the formation of a well dispersed phase, *i.e.*

Au particle size below XRD (<5 nm) detection limits [8.24]. Nitrogen adsorption/ desorption isotherms (**Fig. 8.2(I)**) show a hysteresis loop at $P/P_0 > 0.6$ characteristic of mesoporous materials (type IV, IUPAC classification) [8.25]. This is consistent with the mesoporosity of γ-Al_2O_3 (from Puralox) with mean pore radius in the 30-41 Å range [8.26,8.27]. A decrease in total surface area, pore volume and radius was observed for Au/Al_2O_3 (**Table 8.1**) relative to the starting support (SSA = 191 $m^2\ g^{-1}$, pore volume = 0.45 $cm^3\ g^{-1}$ and pore radius = 31 Å), which can be linked to the partial pore filling during

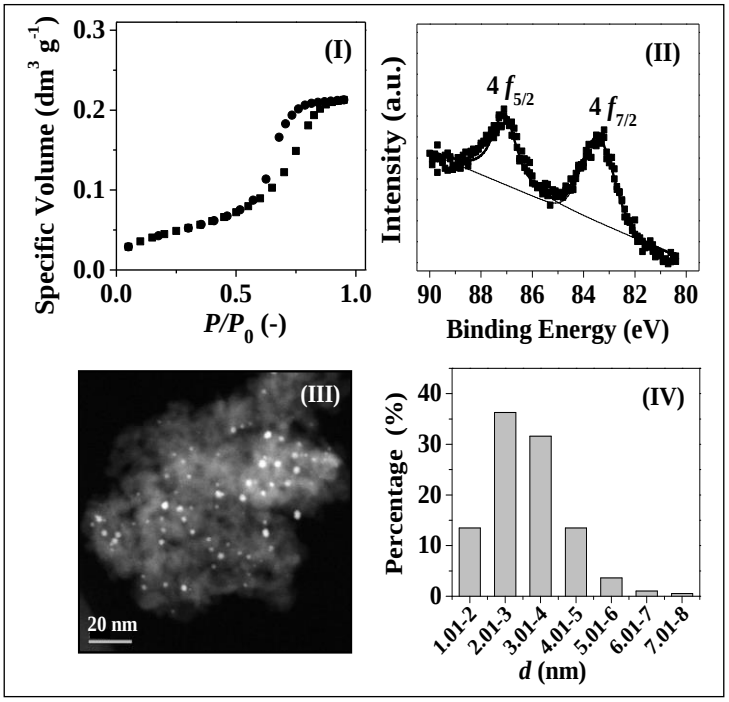

Fig. 8.2: (I) N_2 adsorption-desorption isotherm, (II) XPS spectra, (III) representative STEM image and (IV) associated Au size distribution histogram for Au/Al_2O_3.

catalyst preparation [8.28]. Temperature programmed reduction of Au/Al_2O_3 (profile not shown) generated a positive H_2 consumption signal with a temperature maximum (T_{max}) at 451 K, in agreement with the results reported by Liu and Yang [8.29] for Au/Al_2O_3 prepared by deposition-precipitation. Hydrogen consumption during TPR (**Table 8.1**) matched that (1.5 $mol_{H_2}\ mol_{Au}^{-1}$) required for the reduction of the Au^{3+} precursor to metallic Au. The XPS spectrum over the Au 4*f* binding energy (BE) region (**Fig. 8.2(II)**) exhibited two peaks with binding energy (BE = 87.0 eV and 83.4 eV) corresponding to $4f_{5/2}$ and $4f_{7/2}$ levels, respectively. The $4f_{7/2}$ BE is lower than that characteristic of metallic Au (84.0 eV) [8.30], suggesting electron donation from the support to generate $Au^{\delta-}$. Arrii *et al*. [8.30] have also reported a downward shift in the BE of Au/γ-Al_2O_3 (Au $4f_{7/2}$ = 83.1 eV). STEM analysis (**Fig. 8.2(III)**) confirmed the

presence of nano-sized gold particles (1-8 nm, **Fig. 8.2(IV)**) and a surface area weighted mean (4.3 nm) that falls within the interval (3-5 nm) reported by Costello *et al*. [8.31] for Au/Al_2O_3 (1.1% w/w) prepared by deposition-precipitation. Supported Au is known to exhibit lower efficiency for H_2 chemisorption compared to standard hydrogenation metals (Ni, Pd and Pt) due to the filled 3*d* band where measurable H_2 uptake is associated with small (<10 nm) Au particles that bear a greater number of edge and corner sites [8.32]. Hydrogen chemisorption on Au/Al_2O_3 is an activated process [8.32] and uptake under reaction conditions (413 K, **Table 8.1**) was appreciably higher than that (36 μmol g_{Au}^{-1}) recorded at ambient temperature (298 K). Bus *et al.* [8.33] demonstrated higher H_2 adsorption capacity for Au/Al_2O_3 with an increase in temperature (298-373 K). The characterisation results demonstrate formation of nano-scale $Au^{\delta-}$ particles (mean = 4.3 nm) with a narrow size distribution and significant (318 μmol g_{Au}^{-1}) H_2 uptake under reaction conditions.

8.3.2 Catalytic Activity and Selectivity

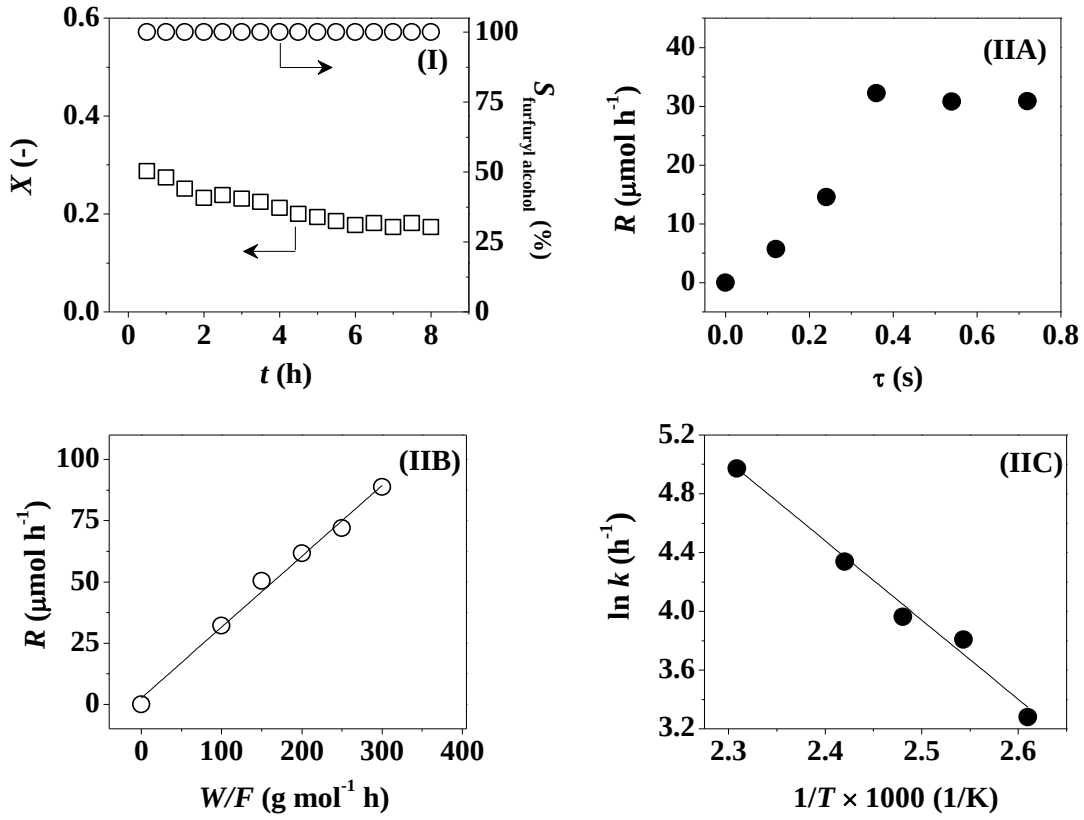

Fig. 8.3: (I) Variation of furfural fractional conversion (□) and furfuryl alcohol selectivity (○) with time on-stream (*T* = 413 K, *P* = 1 atm, *τ* = 0.36 s, *W*/*F* = 100 g mol^{-1} h). (II) Tests to establish kinetic control for furfural hydrogenation over Au/Al_2O_3: Dependence of consumption rate (*R*) on (A) contact time *τ* (*T* = 413 K, *P* = 1 atm, *W*/*F* = 100 g mol^{-1} h) and (B) *W*/*F* (*T* = 413 K, *P* = 1 atm, *τ* = 0.36 s); (C) Arrhenius plot (*T* = 383-433 K, *P* = 1 atm, *τ* = 0.36 s, *W*/*F* = 100 g mol^{-1} h).

Representative time on-stream conversion and selectivity profiles for reaction at 413 K are shown in **Fig. 8.3(I)**, where furfural was solely converted to the target furfuryl alcohol, *i.e.* exclusive reduction of the carbonyl group (**Fig. 8.1**, path **(III)**). To the best of our knowledge this is the first report of 100% selectivity to furfuryl alcohol over Au catalysts. This result is significant in the light of the negligible activity recorded for reaction over (SiO_2) supported Au in batch mode [8.20]. Moreover, by-product formation has been a feature of furfural hydrogenation over Pd [8.3], Pt [8.4] and Ni [8.8] catalysts. A meaningful evaluation of the catalytic response requires that the reaction is operated under kinetic control, free heat/mass transfer constraints. These possible limitations were assessed using standard diagnostic tests (effect of contact time, catalyst mass to reactant feed rate and reaction temperature) [8.34] and the results are presented in **Fig. 8.3(II)**. Furfural consumption rate increased with contact time (at τ <0.36 s, **(A)**), indicative of interparticle transport limitations that inhibit hydrogenation. Rate was insensitive to contact time at $\tau \geq 0.36$ s, demonstrating minimal external diffusion constraints; τ was set at 0.36 s in subsequent tests. Variation in catalyst mass to furfural feed rate (W/F) was used to probe the effect of possible reactant concentration gradients on performance. Hydrogenation rate (at $X \leq 0.9$) displayed a linear correlation with respect to W/F (passing through the origin, **(B)**) and we can discount contributions due to internal and/or external mass transport on the observed activity. The applicability of pseudo-first order kinetics has been demonstrated elsewhere [8.35]. The Arrhenius plot **(C)** delivered an apparent activation energy (ΔE_a = 45 kJ mol^{-1}) close to that (50 kJ mol^{-1}) reported for reaction over Cu/SiO_2 [8.36]. This activation energy is higher than the reported furfural adsorption energy (<30 kJ mol^{-1}) [8.36] and typical values (<15 kJ mol^{-1}) for surface diffusion of gases [8.37], confirming that the reaction was under chemical kinetic control (at $\tau \geq 0.36$ s, W/F = 100-300 g mol^{-1} h and T = 383-433 K).

Reaction exclusivity to furfuryl alcohol was maintained over 383-433 K (**Fig. 8.4**). An increase in temperature (to 523 K) resulted in higher turnover frequencies (*TOF*) but with a switch from exclusive –C=O reduction to predominant hydrogenolysis (to 2-methylfuran, path **(V)** in **Fig. 8.1**). This result suggests that higher temperatures facilitate activation of –C=O for subsequent hydrogenolytic cleavage (steps **(III)** and **(V)**). Similar behaviour has been reported for Cu/MgO [8.16] where reaction temperatures ≥473 K favoured 2-methylfuran formation. Reduction of furfural to furfuryl alcohol has been proposed to proceed *via* nucleophilic addition where the

nucleophile (dissociated H) attacks the electrophilic –C=O group to form an alkoxide (or hydroxyl-alkyl) intermediate with subsequent protonation to yield the alcohol [8.36].

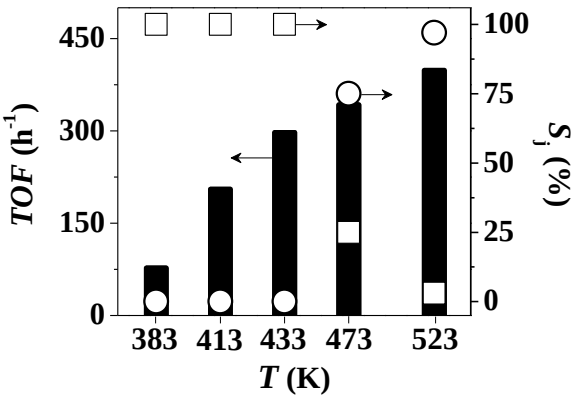

Fig. 8.4: Dependence of furfural *TOF* (bars) and selectivity to furfuryl alcohol (□) and 2-methylfuran (○) with temperature over Au/Al_2O_3.

Theoretical (DFT) calculations have demonstrated perpendicular adsorption of furfural on Cu *via* the oxygen lone pair of the carbonyl group as the most stable configuration for reduction to the alcohol [8.36]. Adsorption *via* the furan ring (parallel to the metal surface) has been proposed to account for decarbonylation (to furan, path **(I)**) and furan ring reduction (to tetrahydrofurfurylalcohol, path **(IV)**) over supported Pd [8.3,8.38]. Support surface properties can impact on carbonyl group adsorption where FTIR analysis has established benzaldehyde interaction with Al^{3+} sites on alumina to generate a surface benzoate as reactive intermediate to the alcohol [8.39]. We have confirmed, by pyridine titration coupled with FTIR, that the Lewis acidity of alumina facilitates selective activation and reduction of –C=O to the alcohol at low temperatures (423-443 K) in the gas phase hydrogenation of nitrobenzaldehyde [8.40]. Moreover, electron-rich Au particles have been shown to favour selective activation/reduction of carbonyl group in benzalacetone [8.41] and acrolein [8.42] hydrogenation. Surface Lewis acid sites on Al_2O_3 and electron-rich Au particles (determined from XPS analysis) can then contribute to selective hydrogenation of furfural to furfuryl alcohol at $T \leq 433$ K. It is important to note that Au/Al_2O_3 not only delivered full selectivity to the target furfuryl alcohol but delivered a higher *TOF* than the values reported for Cu/MgO (18-140 h^{-1}) [8.15,8.16] and Cu/C (65-115 h^{-1}) [8.17] at higher reaction temperatures (453-498 K) and which we can take as the current benchmark. The higher selective hydrogenation rate can be linked to the greater capacity of nano-sized Au to chemisorb/activate H_2 (318 µmol g_{Au}^{-1} in this work) relative to supported Cu (0.8 µmol g_{Cu}^{-1} for Cu/C [8.43]). The results presented in this study have established Au/Al_2O_3 as a viable catalyst for the

exclusive continuous high throughout production of furfuryl alcohol from furfural.

8.4 Conclusion

We report the exclusive formation of furfuryl alcohol in the continuous atmospheric pressure hydrogenation of furfural (383-433 K, ΔE_a = 45 kJ mol^{-1}) over nano-scale $Au^{\delta-}$ (1-8 nm, mean = 4.3 nm) on Al_2O_3 under conditions of chemical control (at $\tau \geq 0.36$ s, W/F = 100-300 g mol^{-1} h). Reaction over Au/Al_2O_3 delivered a *TOF* that was significantly greater than the benchmark Cu catalysts operated at higher temperatures (453-498 K).

8.5 References

[8.1] M.M. Villaverde, T.F. Garetto, A.J. Marchi, *Liquid-phase transfer hydrogenation of furfural to furfuryl alcohol on Cu-Mg-Al catalysts*, Catal. Commun. 58 (2015) 6-10.

[8.2] D. Vargas-Hernández, J.M. Rubio-Caballero, J. Santamaría-González, R. Moreno-Tost, J.M. Mérida-Robles, M.A. Pérez-Cruz, A. Jiménez-López, R. Hernández-Huesca, P. Maireles-Torres, *Furfuryl alcohol from furfural hydrogenation over copper supported on SBA-15 silica catalysts*, J. Mol. Catal. A: Chem. 383 (2014) 106-113.

[8.3] S. Sitthisa, P. Trung, T. Prasomsri, T. Sooknoi, R.G. Mallinson, D.E. Resasco, *Conversion of furfural and 2-methylpentanal on Pd/SiO_2 and $Pd-Cu/SiO_2$ catalysts*, J. Catal. 280 (2011) 17-27.

[8.4] V.V. Pushkarev, N. Musselwhite, K.J. An, S. Alayoglu, G.A. Somorjai, *High structure sensitivity of vapor-phase furfural decarbonylation/hydrogenation reaction network as a function of size and shape of Pt nanoparticles*, Nano Lett. 12 (2012) 5196-5201.

[8.5] Y. Nakagawa, H. Nakazawa, H. Watanabe, K. Tomishige, *Total hydrogenation of furfural over a silica-supported nickel catalyst prepared by the reduction of a nickel nitrate precursor*, ChemCatChem 4 (2012) 1791-1797.

[8.6] M. Lesiak, M. Binczarski, S. Karski, W. Maniukiewicz, J. Rogowski, E. Szubiakiewicz, J. Berlowska, P. Dziugan, I. Witonska, *Hydrogenation of furfural over $Pd-Cu/Al_2O_3$ catalysts: The role of interaction between palladium and copper on determining catalytic properties*, J. Mol. Catal. A: Chem. 395 (2014) 337-348.

[8.7] A.B. Merlo, V. Vetere, J.M. Ramallo-López, F.G. Requejo, M.L. Casella, *Liquid-phase furfural hydrogenation employing silica-supported PtSn and PtGe catalysts*

prepared using surface organometallic chemistry on metals techniques, React. Kinet. Mech. Catal. 104 (2011) 467-482.

[8.8] B.J. Liu, L.H. Lu, B.C. Wang, T.X. Cai, K. Iwatani, *Liquid phase selective hydrogenation of furfural on Raney nickel modified by impregnation of salts of heteropolyacids*, Appl. Catal. A: Gen. 171 (1998) 117-122.

[8.9] H.S. Luo, H.I. Li, L. Zhuang, *Furfural hydrogenation to furfuryl alcohol over a novel Ni-Co-B amorphous alloy catalyst*, Chem. Lett. (2001) 404-405.

[8.10] H.X. Li, H.S. Luo, L. Zhuang, W.L. Dai, M.H. Qiao, *Liquid phase hydrogenation of furfural to furfuryl alcohol over the Fe-promoted Ni-B amorphous alloy catalysts*, J. Mol. Catal. A: Chem. 203 (2003) 267-275.

[8.11] H.X. Li, S.Y. Zhang, H.S. Luo, *A Ce-promoted Ni-B amorphous alloy catalyst (Ni-Ce-B) for liquid-phase furfural hydrogenation to furfuryl alcohol*, Mater. Lett. 58 (2004) 2741-2746.

[8.12] M.M. Villaverde, N.M. Bertero, T.F. Garetto, A.J. Marchi, *Selective liquid-phase hydrogenation of furfural to furfuryl alcohol over Cu-based catalysts*, Catal. Today 213 (2013) 87-92.

[8.13] H.Y. Zheng, Y.L. Zhu, B.T. Teng, Z.Q. Bai, C.H. Zhang, H.W. Xiang, Y.W. Li, *Towards understanding the reaction pathway in vapour phase hydrogenation of furfural to 2-methylfuran*, J. Mol. Catal. A: Chem. 246 (2006) 18-23.

[8.14] D.X. Liu, D. Zemlyanov, T.P. Wu, R.J. Lobo-Lapidus, J.A. Dumesic, J.T. Miller, C.L. Marshall, *Deactivation mechanistic studies of copper chromite catalyst for selective hydrogenation of 2-furfuraldehyde*, J. Catal. 299 (2013) 336-345.

[8.15] B.M. Nagaraja, V.S. Kumar, V. Shasikala, A.H. Padmasri, B. Sreedhar, B.D. Raju, K.S.R. Rama, *A highly efficient Cu/MgO catalyst for vapour phase hydrogenation of furfural to furfuryl alcohol*, Catal. Commun. 4 (2003) 287-293.

[8.16] B.M. Nagaraja, A.H. Padmasri, B.D. Raju, K.S.R. Rama, *Vapor phase selective hydrogenation of furfural to furfuryl alcohol over Cu-MgO coprecipitated catalysts*, J. Mol. Catal. A: Chem. 265 (2007) 90-97.

[8.17] R. Rao, R.T.K. Baker, M.A. Vannice, *Furfural hydrogenation over carbon-supported copper*, Catal. Lett. 60 (1999) 51-57.

[8.18] J.F. Jenck, F. Agterberg, M.J. Droescher, *Products and processes for a sustainable chemical industry: A review of achievements and prospects*, Green Chem. 6 (2004) 544-556.

[8.19] T. Mitsudome, K. Kaneda, *Gold nanoparticle catalysts for selective hydrogenations*, Green Chem. 15 (2013) 2636-2654.

[8.20] Y.-C. Hong, K.-Q. Sun, G.-R. Zhang, R.-Y. Zhong, Q. Xu, *Fully dispersed Pt entities on nano-Au dramatically enhance the activity of gold for chemoselective hydrogenation catalysis*, Chem. Commun. 47 (2011) 1300-1302.

[8.21] J. Ohyama, A. Esaki, Y. Yamamoto, S. Arai, A. Satsuma, *Selective hydrogenation of 2-hydroxymethyl-5-furfural to 2,5-bis(hydroxymethyl)furan over gold sub-nano clusters*, RSC Adv. 3 (2013) 1033-1036.

[8.22] M. Li, X. Wang, N. Perret, M.A. Keane, *Enhanced production of benzyl alcohol in the gas phase continuous hydrogenation of benzaldehyde over Au/Al_2O_3*, Catal. Commun. 46 (2014) 187-191.

[8.23] X. Wang, N. Perret, M.A. Keane, *The role of hydrogen partial pressure in the gas phase hydrogenation of p-chloronitrobenzene over alumina supported Au and Pd: A consideration of reaction thermodynamics and kinetics*, Chem. Eng. J. 210 (2012) 103-113.

[8.24] G.C. Bond, C. Louis, D.T. Thompson, *Catalysis by gold*, G.J. Hutchings (Ed.), Imperial College Press, London, 2006.

[8.25] I. Chorkendorff, J.W. Niemantsverdriet, *Concept of modern catalysis and kinetics*, Wiley-VCH, Weinheim, 2003.

[8.26] K. Lehnert, P. Claus, *Influence of Pt particle size and support type on the aqueous-phase reforming of glycerol*, Catal. Commun. 9 (2008) 2543-2546.

[8.27] E. Kok, N. Cant, D. Trimm, J. Scott, *The effect of support and synthesis method on the methanation activity of alumina-supported cobalt-ruthenium-lanthana catalysts*, Catal. Today 178 (2011) 79-84.

[8.28] S. Jujjuri, E. Ding, S.G. Shore, M.A. Keane, *A characterization of Ln-Pd/SiO_2 (Ln=La, Ce, Sm, Eu, Gd and Yb): Correlation of surface chemistry with hydrogenolysis activity*, J. Mol. Catal. A: Chem. 272 (2007) 96-107.

[8.29] S.Y. Liu, S.M. Yang, *Complete oxidation of 2-propanol over gold-based catalysts supported on metal oxides*, Appl. Catal. A: Gen. 334 (2008) 92-99.

[8.30] S. Arrii, F. Morfin, A.J. Renouprez, J.L. Rousset, *Oxidation of CO on gold supported catalysts prepared by laser vaporization: Direct evidence of support contribution*, J. Am. Chem. Soc. 126 (2004) 1199-1205.

[8.31] C.K. Costello, M.C. Kung, H.S. Oh, Y. Wang, H.H. Kung, *Nature of the active site for CO oxidation on highly active Au/γ-Al_2O_3*, Appl. Catal. A: Gen. 232 (2002) 159-168.

[8.32] G.C. Bond, *Chemisorption and reactions of small molecules on small gold particles*, Molecules 17 (2012) 1716-1743.

[8.33] E. Bus, J.T. Miller, J.A. van Bokhoven, *Hydrogen chemisorption on Al_2O_3-supported gold catalysts*, J. Phys. Chem. B 109 (2005) 14581-14587.

[8.34] S. Jujjuri, M.A. Keane, *Catalytic hydrodechlorination at low hydrogen partial pressures: Activity and selectivity response*, Chem. Eng. J. 157 (2010) 121-130.

[8.35] N. Perret, F. Cárdenas-Lizana, M.A. Keane, *Selective hydrogenation of benzaldehyde to benzyl alcohol over Au/Al_2O_3*, Catal. Commun. 16 (2011) 159-164.

[8.36] S. Sitthisa, T. Sooknoi, Y. Ma, P.B. Balbuena, D.E. Resasco, *Kinetics and mechanism of hydrogenation of furfural on Cu/SiO_2 catalysts*, J. Catal. 277 (2011) 1-13.

[8.37] K. Wang, S.Z. Qiao, X.J. Hu, *Study of isosteric heat of adsorption and activation energy for surface diffusion of gases on activated carbon using equilibrium and kinetics information*, Sep. Purif. Technol. 34 (2004) 165-176.

[8.38] V. Vorotnikov, G. Mpourmpakis, D.G. Vlachos, *DFT study of furfural conversion to furan, furfuryl alcohol, and 2-methylfuran on Pd (111)*, ACS Catal. 2 (2012) 2496-2504.

[8.39] C.A. Koutstaal, P. Angevaare, V. Ponec, *Surface chemistry of benzoyl compounds on oxides: An FT-IR study*, J. Catal. 143 (1993) 573-582.

[8.40] N. Perret, X. Wang, T. Onfroy, C. Calers, M.A. Keane, *Selectivity in the gas-phase hydrogenation of 4-nitrobenzaldehyde over supported Au catalysts*, J. Catal. 309 (2014) 333-342.

[8.41] C. Milone, R. Ingoglia, L. Schipilliti, C. Crisafulli, G. Neri, S. Galvagno, *Selective hydrogenation of α, β-unsaturated ketone to α, β-unsaturated alcohol on gold-supported iron oxide catalysts: Role of the support*, J. Catal. 236 (2005) 80-90.

[8.42] P. Claus, A. Bruckner, C. Mohr, H. Hofmeister, *Supported gold nanoparticles from quantum dot to mesoscopic size scale: Effect of electronic and structural properties on catalytic hydrogenation of conjugated functional groups*, J. Am. Chem. Soc. 122 (2000) 11430-11439.

[8.43] J.J. Liu, L.L. Zhang, J.T. Zhang, T. Liu, X.S. Zhao, *Bimetallic ruthenium-copper nanoparticles embeded in mesoporous carbon as an effective hydrogenation catalyst*, Nanoscale 5 (2013) 11044-11050.

Chapter 9

Role of Support Oxygen Vacancies in the Gas Phase Furfural Hydrogenation over Gold

In the previous chapter, reaction exclusivity to furfuryl alcohol was established over Au/Al_2O_3. In this chapter, the possible role of support (surface oxygen vacancies) is investigated by comparison with reducible oxides (TiO_2 and CeO_2) supported Au in the selective gas phase reduction of furfural where the catalytic behaviour is linked to the critical catalyst characterisation.

9.1 Introduction

Oxygen vacancies in metal oxides (*e.g.* titanium, cerium, iron and vanadium oxides) are defects generated by the loss of lattice oxygen as a result of high temperature annealing (≥673 K) in ultra-high vacuum (UHV) [9.1], chemical reduction (by H_2 or CO) [9.2] and/or electron irradiation [9.3,9.4]. The formation and properties of these surface imperfections have been the subject of theoretical (DFT) and experimental (UPS, XPS, EELS, IR, EPR, STM) work [9.4-9.6]. Oxygen vacancies have been identified as active sites in catalytic water-gas shift [9.7], steam reforming of oxygenates [9.8], CO oxidation [9.9] and hydrodeoxygenation [9.10]. Moreover, the presence of these defects can modify the electronic characteristics (*via* electron transfer) [9.11], particle size (by stabilisation at vacancy sites) [9.12] and chemical properties (metal-support interaction) [9.13] of the supported metal phase (Pt [9.7], Ag [9.11], Au [9.12,9.13] and Pd [9.14]) which impact on reactant adsorption/activation.

Hydrogenation is a key process in the food, petrochemical, pharmaceutical and agrochemical sectors [9.15]. The effect of surface oxygen vacancies on catalytic hydrogenation is still the subject of debate. Enhanced activity and (–C=O reduction) selectivity reported for Pt/CeO_2 [9.16] and Au/Fe_2O_3 [9.17] in the hydrogenation of crotonaldehyde and benzalacetone was attributed to a facilitated activation of the carbonyl function on oxygen vacancies and/or electron-rich metal nano-particles. On the other hand, a (3-fold) decrease in crotonaldehyde hydrogenation activity was observed following incorporation of CeO_2 (by impregnation with $Ce(NO_3)_3$) on Ru/Al_2O_3 and

ascribed to strong –C=O interaction with surface oxygen deficient sites [9.18]. Tian *et al*. [9.19] studying the hydrogenation of cinnamaldehdye over Au/CeO_2 suggested a preferential –C=C– adsorption on $Au^{\delta+}$ (from electrons transfer to support defects) to explain decreased selectivity to –C=O reduction. In the hydrogenation of *p*-chloronitrobenzene unwanted hydrodechlorination was reported for $Au/Ce_{0.62}Zr_{0.38}O_2$ and ascribed to C–Cl scission at oxygen vacancy sites [9.20]. In this study, we consider the role of surface oxygen vacancies (on reducible TiO_2 and CeO_2) in determining the catalytic action of supported Au in the gas phase hydrogenation of –C=O using furfural as model reactant. We also assess the catalytic action of Au on non-reducible alumina as a benchmark.

9.2 Experimental

9.2.1 Materials and Catalyst Preparation

Commercial TiO_2 (P25, Degussa) and CeO_2 (Sigma-Aldrich) were used as received. The supported Au catalysts were prepared by deposition-precipitation using urea (Riedel-de Haën, 99%, 100-fold excess) with $HAuCl_4$ (Sigma-Aldrich, 99%, 1.5×10^{-3} - 3.0×10^{-3} M, 400 cm^3). A suspension with the oxide carrier (10 g) was heated to 353 K (2 K min^{-1}) where the pH progressively increased to *ca.* 7 after 3-4 h as a result of urea decomposition [9.21]. The solid obtained was separated by filtration, washed with distilled water until chlorine free (from $AgNO_3$ test) and dried in He (45 cm^3 min^{-1}) at 373 K (2 K min^{-1}) for 5 h. The resultant samples were sieved (ATM fine test sieves) to mean particle diameter = 75 μm, activated at 2 K min^{-1} to 523 K in 60 cm^3 min^{-1} H_2, cooled to ambient temperature and passivated in 1% v/v O_2/He for 1 h for *ex situ* characterisation. Synthesis and activation of the benchmark (0.6 mol%) Au/Al_2O_3 catalyst is described in detail elsewhere [9.22].

9.2.2 Catalyst Characterisation

The Au content was measured by atomic absorption spectroscopy (Shimadzu AA-6650 spectrometer with an air-acetylene flame) from the diluted extract in aqua regia (25% v/v HNO_3/HCl). Temperature programmed reduction (TPR), H_2 and O_2 chemisorption measurements were conducted on the CHEM-BET 3000 (Quantachrome Instrument) unit with data acquisition/manipulation using the TPR Win™ software. Samples were loaded into a U-shaped Pyrex glass cell (3.76 mm i.d.) and heated in 17

cm^3 min^{-1} (Brooks mass flow controlled) 5% v/v H_2/N_2 to 523 K at 2 K min^{-1}. The effluent gas passed through a liquid N_2 trap and H_2 consumption was monitored by a thermal conductivity detector (TCD). The activated samples were swept with 65 cm^3 min^{-1} N_2 for 1.5 h, cooled to 413 K and subjected to H_2 chemisorption by pulse (10 μl) titration. In blank tests, there was no measurable H_2 uptake on the oxide supports alone. Oxygen chemisorption post-TPR was employed to determine the extent of support reduction, where the samples were reduced as described above, swept with 65 cm^3 min^{-1} He for 1.5 h, cooled to 413 K and subjected to pulse (50 μl) O_2 titration. It has been demonstrated previously that Au contribution to total O_2 adsorbed is negligible [9.23]. Nitrogen physisorption was performed using the commercial Micromeritics Gemini 2390p system. The samples were outgassed at 423 K for 1 h prior to analysis. Total specific surface area (SSA) was calculated by standard BET. X-ray diffractograms (XRD) were recorded on a Bruker/Siemens D500 incident X-ray diffractometer using Cu Kα radiation, scanning at 0.02º per step over the range $20º \leq 2\theta \leq 80º$. The diffractograms were identified against the JCPDS-ICDD reference standards, *i.e.* Au (04-0784), anatase-TiO_2 (21-1272), rutile-TiO_2 (21-1276), CeO_2 (43-1002) and Ce_2O_3 (23-1048). Gold particle morphology was examined by scanning transmission electron microscopy (STEM, JEOL 2200FS field emission gun-equipped unit), employing Gatan Digital Micrograph 1.82 for data acquisition/manipulation. Samples for analysis were prepared by dispersion in acetone and deposited on a holey carbon/Cu grid (300 Mesh). The surface area weighted mean Au particle size (d) was based on a count of at least 300 particles, according to

$$d = \frac{\sum_i n_i d_i^3}{\sum_i n_i d_i^2} \qquad \textbf{(9.1)}$$

where n_i is the number of particles of diameter d_i.

9.2.3 Catalytic Procedure

Hydrogenation of furfural (Sigma-Aldrich, 99%) was carried out at atmospheric pressure and 413-523 K *in situ* after activation in a continuous flow fixed bed tubular reactor (15 mm i.d.). Reactions were conducted under operating conditions that ensured negligible mass/heat transport limitations. A layer of borosilicate glass beads served as preheating zone, ensuring that the furfural reactant was vaporised and reached reaction temperature before contacting the catalyst. Isothermal conditions (±1 K) were ensured by diluting the catalyst bed with ground glass (75 μm); the ground glass was mixed

thoroughly with catalyst before loading into the reactor. Reaction temperature was continuously monitored by a thermocouple inserted in a thermowell within the catalyst bed. Furfural was delivered as *n*-butanolic (Sigma-Aldrich, >99%) solutions to the reactor *via* a glass/teflon air-tight syringe and teflon line using a microprocessor controlled infusion pump (Model 100 kd Scientific) at a fixed calibrated flow rate. A co-current flow of furfural and H_2 was adjusted to $GHSV = 1 \times 10^4$ h^{-1}. The molar Au to inlet reactant molar feed rate (n/F) spanned the range $4.0 \times 10^{-3} - 3.0 \times 10^{-2}$ h. Passage of furfural in a stream of H_2 through the empty reactor or over support alone did not result in any detectable conversion. The reactor effluent was condensed in a liquid N_2 trap for subsequent analysis using a Perkin-Elmer Auto System XL gas chromatograph equipped with a programmed split/splitless injector and a flame ionisation detector, employing a DB-1 (50 m × 0.33 mm i.d., 0.20 μm film thickness) capillary column (J&W Scientific). Data acquisition and manipulation were performed using the TurboChrom Workstation Version 6.3.2 (for Windows) chromatography data system. Furfuryl alcohol and 2-methylfuran were used as supplied (from Sigma-Aldrich, 99%) for product identification/analysis. All gases (O_2, H_2, N_2 and He) were of high purity (>99.98%, BOC). Furfural fractional conversion (X) is defined by

$$X = \frac{[\,furfural\,]_{in} - [\,furfural\,]_{out}}{[\,furfural\,]_{in}} \qquad \textbf{(9.2)}$$

and selectivity (S) to product (j) is given by

$$S_j\,(\%) = \frac{[\,product\,]_{j,\,out}}{[\,furfural\,]_{in} - [\,furfural\,]_{out}} \times 100 \qquad \textbf{(9.3)}$$

where the subscripts "in" and "out" refer to the inlet and outlet gas streams. Turnover frequency (*TOF*, rate per active site) was calculated based on Au dispersion from STEM as described elsewhere [9.22]. Repeated reactions with different samples from the same batch of catalyst delivered raw data reproducibility and a carbon mass balance that were within ±5 %.

9.3 Results and Discussion

9.3.1 Catalyst Characterisation

The physicochemical characteristics of Au/TiO_2 and Au/CeO_2 are given in **Table 9.1**. Both samples contained a similar Au loading (0.7-0.8 mol%) and the SSA match

values reported for TiO_2 (50 m^2 g^{-1}) [9.24] and CeO_2 (36-67 m^2 g^{-1}) [9.11] supported Au catalysts. XRD analysis of Au/TiO_2 (**Fig. 9.1(I)**) revealed a mixture of tetragonal anatase (2θ = 25.3°, 37.8°, 48.1° and 62.8°) and rutile (2θ = 27.4°, 36.1°, 41.2°, 54.3°, 56.6°, 69.0° and 69.8°) phases, where the anatase : rutile ratio (5:1) is consistent with Degussa P25 [9.25]. The XRD pattern of Au/CeO_2 (**Fig. 9.1(II)**) presents principal peaks (at 2θ = 28.6°, 33.1°, 47.5° and 56.3°) characteristic of CeO_2 with no evidence of Ce_2O_3 (2θ = 29.5°) formation from bulk ($CeO_2 \rightarrow Ce_2O_3$) reduction. In both cases, there were no diffraction peaks due to Au, diagnostic of a well dispersed (<5 nm) metal phase [9.23]. This was confirmed by STEM analysis (**Fig. 9.2**) where both samples exhibited quasi-spherical Au nanoparticles with a similar narrow size range (1-6 nm) and mean (**Table 9.1**). The TPR profile of Au/TiO_2 (**Fig. 9.3(I)**) shows a single peak (T_{max} = 376 K)

Table 9.1: Gold loading, specific surface area (SSA), mean Au particle size from STEM analysis (*d*), H_2 consumption during TPR, H_2/O_2 uptake and support standard redox potential (E_{redox}) associated with Au/TiO_2 and Au/CeO_2.

Catalyst	Au/TiO_2	Au/CeO_2
Au loading (mol%)	0.8	0.7
SSA (m^2 g^{-1})	52	64
d (nm)	3.2	2.8
TPR H_2 consumption (μmol g^{-1})	174[a]/147[b]	495[a]/61[b]
H_2 uptake[c] (μmol g_{Au}^{-1})	146	87
E_{redox} (V)	-0.6	1.6
O_2 uptake[c] (μmol g^{-1})	8	90

[a]from TPR analysis; [b]H_2 required for for $Au^{3+} \rightarrow Au^0$; [c]measured at 413 K.

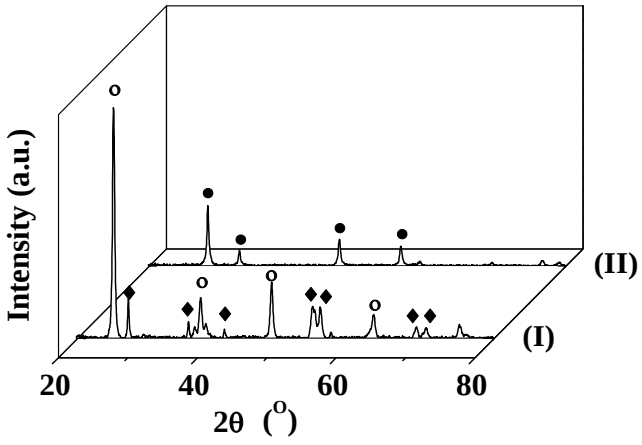

Fig. 9.1: XRD patterns for (I) Au/TiO_2 (○: anatase; ♦: rutile) and (II) Au/CeO_2 (●: CeO_2).

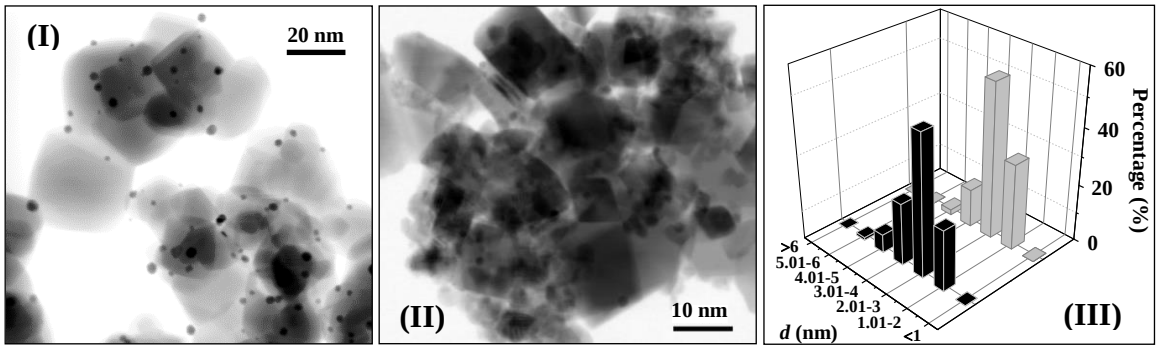

Fig. 9.2: (I-II) Representative STEM images and (III) associated particle size distribution histograms for (I) Au/TiO_2 (black bars) and (II) Au/CeO_2 (grey bars).

with an associated H_2 consumption that exceeded the amount required for the formation of Au^0 (**Table 9.1**) but far lower than that (6200 μmol g^{-1}) required for $Ti^{4+} \rightarrow Ti^{3+}$. This suggests a partial reduction of the support, notably at the Au-support interface [9.26]. Reduction of Au/CeO_2 (**Fig. 9.3(II)**) exhibited a single H_2 consumption peak at higher T_{max} (418 K). Liu and Yang [9.27] reported a dependency of Au^{3+} reducibility on support redox properties where weaker interactions with TiO_2 compared with CeO_2 rendered the Au^{3+} component more susceptible to reduction. In the TPR of Au/CeO_2, H_2 consumed was greater than requirements for Au precursor reduction but far lower than bulk $Ce^{4+} \rightarrow Ce^{3+}$ transformation (2900 μmol g^{-1}). The higher H_2 uptake during the activation of Au/CeO_2 relative to Au/TiO_2 suggests a greater degree of support reduction. This agrees with the higher redox potential of CeO_2 (**Table 9.1**), which is an indicator of a more facile reduction. In contrast, TPR analysis of Al_2O_3 supported Au (d = 4.3 nm) taken as a benchmark in this study generated an equivalent H_2 consumption (87 μmol g^{-1}) to the theoretical value (84 μmol g^{-1}) for $Au^{3+} \rightarrow Au^0$, confirmation of support non-reducibility.

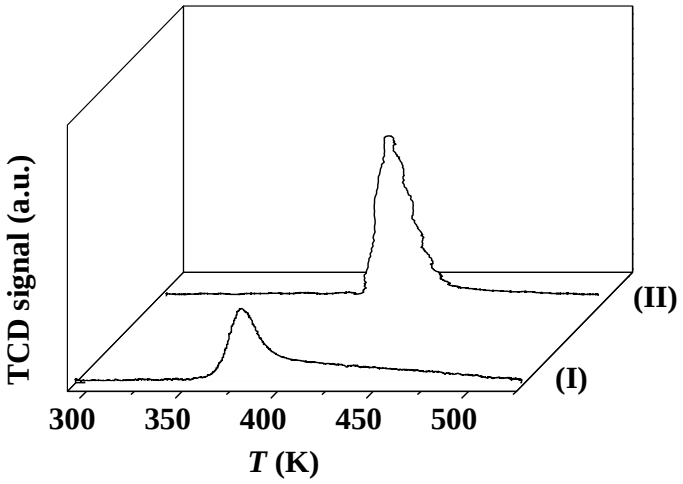

Fig. 9.3: TPR profiles for (I) Au/TiO_2 and (II) Au/CeO_2.

It has been demonstrated that the number of surface oxygen vacancies can be accurately quantified by oxygen titration [9.28,9.29]. Oxygen chemisorption (post-TPR) under reaction conditions (413 K) was employed to determine the extent of support reduction. The values (presented in **Table 9.1**) are comparable to those reported for TiO_2 and CeO_2 supported Au [9.30]. Decreasing O_2 uptake (Au/CeO_2 > Au/TiO_2 > Au/Al_2O_3 (1 μmol g^{-1})) matched the sequence of lower support redox potential ($E_{redox,\ CeO_2}$ = 1.6 V > $E_{redox,\ TiO_2}$ = -0.6 V > $E_{redox,\ Al_2O_3}$ = -1.7 V) and decreasing H_2 consumption during TPR. Oxygen vacancy formation in TiO_2 has been established by *in situ* EPR following reduction (in H_2) over 573-1073 K [9.31]. Boccuzzi *et al.* [9.32] using FTIR spectroscopy demonstrated H_2 dissociation on Au supported on TiO_2 (reduced at 523 K) with spillover that resulted in surface reduction. It has been established (by DFT calculation and STM) that bare ceria surfaces can be reduced ($Ce^{4+} \rightarrow Ce^{3+}$) to generate oxygen defects (post-activation in H_2 over 400-900 K) [9.6,9.33]. Addition of Au on ceria facilitates support reduction (273-573 K) during TPR [9.34]. The performance of supported Au catalysts in hydrogenation is determined by the surface capacity for H_2 adsorption/dissociation [9.23]. Hydrogen chemisorption (at 413 K, **Table 9.1**) was appreciably higher than that (28-63 μmol g_{Au}^{-1}) recorded at ambient temperature [9.35] suggesting that H_2 uptake is an activated process. Chemisorption on Au/TiO_2 was measurably higher than Au/CeO_2. Gold particle size and support interactions impact on H_2 chemisorption [9.36-9.38]. Corner and edge sites associated with smaller Au particles (<10 nm) have been identified as active for H_2 dissociation on Au/CeO_2 [9.36]. Gold particle size distribution is nearly equivalent for both samples (**Fig. 9.2(III)**) and the greater H_2 chemisorption capacity of Au/TiO_2 can be attributed to increased H_2 uptake at the Au-TiO_2 interface [9.38,9.39]. Moreover, lower uptake on Au/CeO_2 can be linked to metal encapsulation due to Au diffusion into the bulk (573-673 K) that is facilitated by oxygen vacancies on CeO_2 [9.40,9.41]. The characterisation results demonstrate the generation of nano-scale (mean = 3.0 ± 0.2 nm) Au particles on TiO_2 and CeO_2 and a greater density of surface oxygen vacancies on Au/CeO_2.

9.3.2 Catalytic Response

A search through the literature did not produce any reported application of TiO_2 or CeO_2 supported Au catalysts in furfural hydrogenation. We can flag the work of Ohyama *et al.* [9.42] on the high pressure (3.8 MPa) liquid phase hydrogenation of 2-hydroxylmethyl-5-furfural where reaction over Au/TiO_2 resulted in furan ring opening

and Au/CeO_2 promoted carbonyl group reduction at a (ten-fold) lower activity. Higher selectivity to alcohol was ascribed to (ceria) surface basicity but no reason was provided

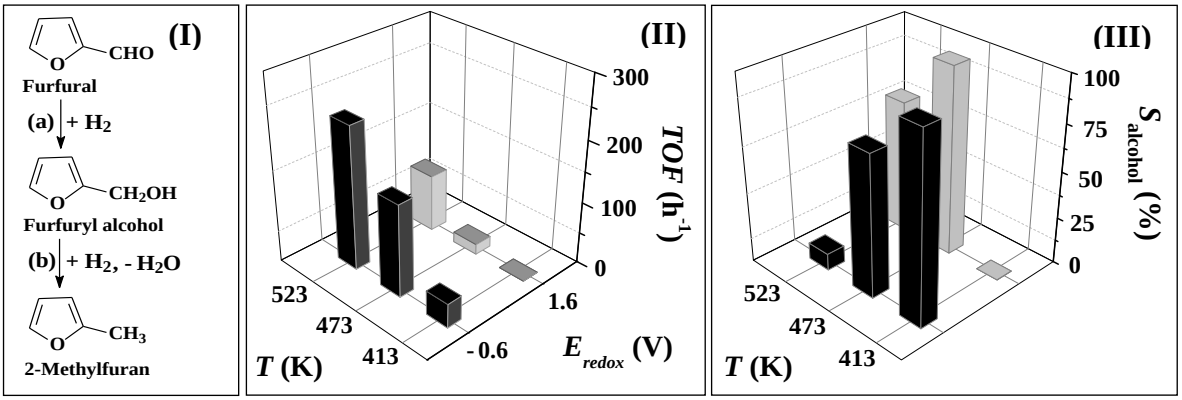

Fig. 9.4: (I) Simplified reaction scheme for furfural hydrogenation; (II) Variation of turnover frequency (*TOF*) and (III) furfuryl alcohol selectivity ($S_{alcohol}$) with reaction temperature (*T*) and support standard redox potential (E_{redox}) over Au/TiO_2 (black bars) and Au/CeO_2 (grey bars). *Reaction conditions*: *T* = 413-523 K and *P* = 1 atm.

for the observed lower activity. Gas phase furfural hydrogenation at 413 K over Au/TiO_2 generated the target furfuryl alcohol (step **(a)** in **Fig. 9.4(I)**) as the sole product. Reaction over Au/Al_2O_3 delivered an appreciably higher selective turnover frequency (*TOF* = 206 h^{-1} *vs.* 39 h^{-1}) and Au/CeO_2 was inactive (**Fig. 9.4(II)**). This can be linked to differences in the H_2 chemisorption capacity that decreased in the order: Au/Al_2O_3 (318 μmol g_{Au}^{-1}) > Au/TiO_2 (146 μmol g_{Au}^{-1}) > Au/CeO_2 (87 μmol g_{Au}^{-1}). Moreover, our result is consistent with literature that has identified H_2 dissociation as the rate-determining step in the chemoselective hydrogenation of aldehydes over supported Au [9.43]. Nonetheless, a contribution due to furfural adsorption at surface oxygen vacancies should not be ruled out. These oxygen vacancies can act as sites for strong binding of oxygenated reactants [9.3,9.6]. The higher relative density of oxygen vacancies on Au/CeO_2 (**Table 9.1**) can act to stabilise surface adsorbed furfural, resulting in the observed lower reaction rates. The action of oxygen vacancies to inhibit –C=O reduction is in line with the lower activity recorded for the cinnamaldehyde hydrogenation (to cinnamyl alcohol) over Au/CeO_2 relative to $Au/MgO\text{-}Al_2O_3$ [9.19] though this possibility was not identified by the authors. An increase in temperature (to ≥473 K) (i) elevated *TOF* where Au/CeO_2 consistently delivered lower rates and (ii) resulted in a switch in selectivity from furfuryl alcohol to –C=O hydrogenolysis to 2-methylfuran (step **(b)** in **Fig. 9.4(I)**). Reaction over Au/TiO_2 and Au/Al_2O_3 at 523 K

generated 2-methylfuran as principal product ($S_{2\text{-methylfuran}}$ > 91%). In the case of Au/CeO_2, a higher reaction temperature (473 K) resulted in the selective transformation of furfural to furfuryl alcohol while a further increase (to 523 K) generated 2-methylfuran as by-product. These results suggest that elevated temperatures favour activation of –C=O for hydrogenolytic cleavage, which finds agreement in results reported for Cu/MgO [9.44].

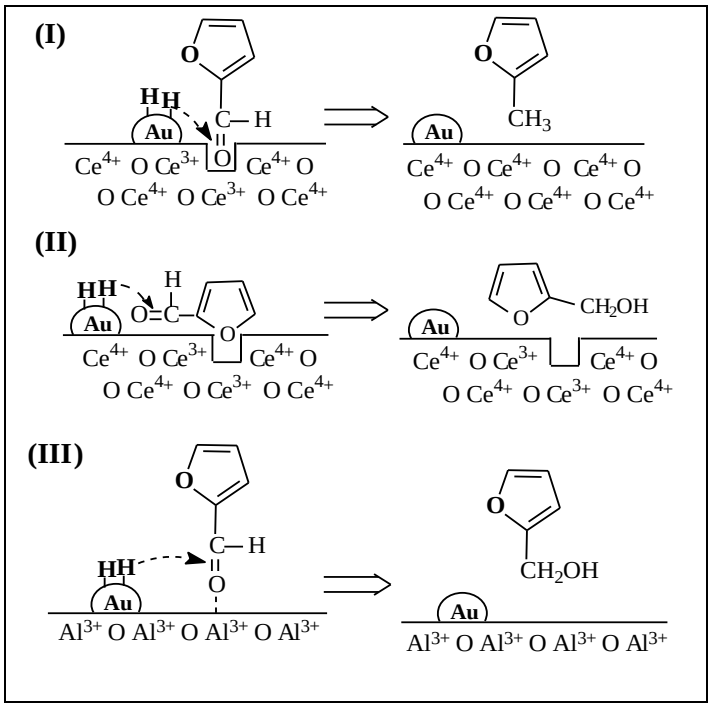

Fig. 9.5: Proposed adsorption/activation mechanisms on (I, II) reducible (with oxygen vacancies) and (III) non-reducible support surfaces *via* carbonyl (I, III) and furan ring (II) oxygen.

Ceria supported Au with a greater oxygen vacancy density exhibited a quite distinct catalytic response when compared with Au/TiO_2 and Au/Al_2O_3. We propose a mechanism that involves direct participation of surface vacancies where the carbonyl group of furfural can be ‘‘anchored’’ to a vacancy (Ce^{3+}) site (see **Fig. 9.5(I)**), forming a covalent Ce–O bond with a high energy of interaction [9.45] that stabilises the surface reactant and lowers reactivity. The (stabilised) carbonyl group can be activated for reaction at higher temperature (523 K) where hydrogenolysis to 2-methylfuran results from hydrogen (supplied by dissociative H_2 adsorption at Au sites) scission of –C=O. The surface Ce^{3+} sites are oxidised by the abstracted oxygen from the carbonyl group. Another possible adsorption mode is through the furan ring oxygen atom that interacts with the electron-rich oxygen vacancy [9.46] (see **Fig. 9.5(II)**). The energy barrier for reaction is lower relative to the covalent –C=O ‘‘anchoring’’ at vacancies. In this case,

the carbonyl group is attacked by reactive hydrogen to form the target furfuryl alcohol with subsequent desorption. Oxygen defects are also present on Au/TiO_2, but at a lower density with a consequent higher overall conversion and enhanced furfuryl alcohol selectivity at lower reaction temperature. Interaction of –C=O with Lewis acid sites (Al^{3+}) on non-reducible Al_2O_3 (see **Fig. 9.5(III)**) facilitates –C=O activation [9.25] and results in greater reactivity and higher *TOF*.

9.4 Conclusion

We have established structure sensitivity in the gas phase hydrogenation of furfural over (0.7-0.8 mol%) Au/TiO_2 and Au/CeO_2 (mean Au particle size = 2.8-3.2 nm). A surface reaction mechanism has been proposed to explain the role of surface oxygen vacancies in determining hydrogenation activity and selectivity. Reaction over Au/CeO_2 delivered a lower furfural *TOF* which can be linked to inhibited H_2 chemisorption capacity. Moreover, the greater oxygen vacancy density on CeO_2 (with higher redox potential) post-TPR served to stabilise the –C=O function, lowering reactivity. Full selectivity was achieved to furfuryl alcohol over Au/TiO_2 (at 413 K) and Au/CeO_2 (at 473 K) where hydrogenolysis to 2-methylfuran was promoted at 523 K. Reaction over Au on non-reducible Al_2O_3 delivered a higher selective furfural (to furfuryl alcohol) *TOF* (at 413 K) with 2-methylfuran formation at $T \geq 473$ K.

9.5 References

[9.1] M. Setvín, U. Aschauer, P. Scheiber, Y.F. Li, W.Y. Hou, M. Schmid, A. Selloni, U. Diebold, *Reaction of O_2 with subsurface oxygen vacancies on TiO_2 anatase (101)*. Science 341 (2013) 988-991.

[9.2] J. Su, X.X. Zou, J.S. Chen, *Self-modification of titanium dioxide materials by Ti^{3+} and/or oxygen vacancies: New insights into defect chemistry of metal oxides*. RSC Adv. 4 (2014) 13979-13988.

[9.3] J. Paier, C. Penschke, J. Sauer, *Oxygen defects and surface chemistry of ceria: Quantum chemical studies compared to experiment*. Chem. Rev. 113 (2013) 3949-3985.

[9.4] M.V. Ganduglia-Pirovano, A. Hofmann, J. Sauer, *Oxygen vacancies in transition metal and rare earth oxides: Current state of understanding and remaining challenges*. Surf. Sci. Rep. 62 (2007) 219-270.

[9.5] X.Y. Pan, M.Q. Yang, X.Z. Fu, N. Zhang, Y.J. Xu, *Defective TiO_2 with oxygen vacancies: Synthesis, properties and photocatalytic applications*. Nanoscale 5 (2013) 3601-3614.

[9.6] C.T. Campbell, C.H.F. Peden, *Oxygen vacancies and catalysis on ceria surfaces*. Science 309 (2005) 713-714.

[9.7] J. Vecchietti, A. Bonivardi, W.Q. Xu, D. Stacchiola, J.J. Delgado, M. Calatayud, S.E. Collins, *Understanding the role of oxygen vacancies in the water gas shift reaction on ceria-supported platinum catalysts*. ACS Catal. 4 (2014) 2088-2096.

[9.8] G.A. Deluga, J.R. Salge, L.D. Schmidt, X.E. Verykios, *Renewable hydrogen from ethanol by autothermal reforming*. Science 303 (2004) 993-997.

[9.9] H.Y. Kim, H.M. Lee, G. Henkelman, *CO oxidation mechanism on CeO_2 supported Au nanoparticles*. J. Am. Chem. Soc. 134 (2012) 1560-1570.

[9.10] T.J. Thibodeau, A.S. Canney, W.J. De-Sisto, M.C. Wheeler, F.G. Amar, B.G. Frederick, *Composition of tungsten oxide bronzes active for hydrodeoxygenation*. Appl. Catal. A: Gen. 388 (2010) 86-95.

[9.11] S.J. Chang, M. Li, Q. Hua, L.J. Zhang, Y.S. Ma, B.J. Ye, W.X. Huang, *Shape-dependent interplay between oxygen vacancies and Ag-CeO_2 interaction in Ag/CeO_2 catalysts and their influence on the catalytic activity*. J. Catal. 293 (2012) 195-204.

[9.12] N. Ta, J. Liu, S. Chenna, P.A. Crozier, Y. Li, A. Chen, W. Shen, *Stabilized gold nanoparticles on ceria nanorods by strong interfacial anchoring*. J. Am. Chem. Soc. 134 (2012) 20585-20588.

[9.13] Y. Maeda, Y. Iizuka, M. Kohyama, *Generation of oxygen vacancies at a Au/TiO_2 perimeter interface during CO oxidation detected by in situ electrical conductance measurement*. J. Am. Chem. Soc. 135 (2013) 906-909.

[9.14] J.W. Ge, Z.Y. Zeng, F.L. Liao, W.R. Zheng, X.L. Hong, S.C.E. Tsang, *Palladium on iron oxide nanoparticles: The morphological effect of the support in glycerol hydrogenolysis*. Green Chem. 15 (2013) 2064-2069.

[9.15] M. Irfan, T.N. Glasnov, C.O. Kappe, *Heterogeneous catalytic hydrogenation reactions in continuous-flow reactors*. ChemSusChem 4 (2011) 300-316.

[9.16] A. Sepúlveda-Escribano, E. Coloma, F. Rodríguez-Reinoso, *Promoting effect of ceria on the gas phase hydrogenation of crotonaldehyde over platinum catalysts*. J. Catal. 178 (1998) 649-657.

[9.17] C. Milone, R. Ingoglia, L. Schipilliti, C. Crisafulli, G. Neri, S. Galvagno, *Selective hydrogenation of α, β-unsaturated ketone to α, β-unsaturated alcohol on gold-supported iron oxide catalysts: Role of the support*. J. Catal. 236 (2005) 80-90.

[9.18] B. Bachiller-Baeza, I. Rodríguez-Ramos, A. Guerrero-Ruiz, *Influence of Mg and Ce addition to ruthenium based catalysts used in the selective hydrogenation of α,β-unsaturated aldehydes*. Appl. Catal. A: Gen. 205 (2001) 227-237.

[9.19] Z.M. Tian, X. Xiang, L.S. Xie, F. Li, *Liquid-phase hydrogenation of cinnamaldehyde: Enhancing selectivity of supported gold catalysts by incorporation of cerium into the support*. Ind. Eng. Chem. Res. 52 (2013) 288-296.

[9.20] X. Wang, N. Perret, J.J. Delgado, G. Blanco, X. Chen, C.M. Olmos, S. Bernal, M.A. Keane, *Reducible support effects in the gas phase hydrogenation of p-chloronitrobenzene over gold*. J. Phys. Chem. C 117 (2013) 994-1005.

[9.21] X. Wang, N. Perret, M.A. Keane, *The role of hydrogen partial pressure in the gas phase hydrogenation of p-chloronitrobenzene over alumina supported Au and Pd: A consideration of reaction thermodynamics and kinetics*. Chem. Eng. J. 210 (2012) 103-113.

[9.22] M. Li, X. Wang, N. Perret, M.A. Keane, *Enhanced production of benzyl alcohol in the gas phase continuous hydrogenation of benzaldehyde over* Au/Al_2O_3. Catal. Commun. 46 (2014) 187-191.

[9.23] G.C. Bond, C. Louis, D.T. Thompson, *Catalysis by gold*, G.J. Hutchings (Ed.), Imperial College Press, London, 2006.

[9.24] V. Jovic, W.-T. Chen, D. Sun-Waterhouse, M.G. Blackford, H. Idriss, G.I.N. Waterhouse, *Effect of gold loading and* TiO_2 *support composition on the activity of* Au/TiO_2 *photocatalysts for* H_2 *production from ethanol-water mixtures*. J. Catal. 305 (2013) 307-317.

[9.25] N. Perret, X. Wang, T. Onfroy, C. Calers, M.A. Keane, *Selectivity in the gas-phase hydrogenation of 4-nitrobenzaldehyde over supported Au catalysts*. J. Catal. 309 (2014) 333-342.

[9.26] M. Ousmane, L.F. Liotta, G. Di-Carlo, G. Pantaleo, A.M. Venezia, G. Deganello, L. Retailleau, A. Boreave, A. Giroir-Fendler, *Supported Au catalysts for low-temperature abatement of propene and toluene, as model VOCs: Support effect*. Appl. Catal. B: Environ. 101 (2011) 629-637.

[9.27] S.Y. Liu, S.M. Yang, *Complete oxidation of 2-propanol over gold-based catalysts supported on metal oxides*. Appl. Catal. A: Gen. 334 (2008) 92-99.

[9.28] S. Salasc, V. Perrichon, M. Primet, M. Chevrier, N. Mouaddib-Moral, *Oxygen titration of spill-over hydrogen in ceria and ceria-alumina supported platinum-rhodium catalysts: Application to the determination of the ceria surface in contact with metal*. J. Catal. 189 (2000) 401-409.

[9.29] S. Salasc, V. Perrichon, M. Primet, N. Mouaddib-Moral, *Titration by oxygen of the spill-over hydrogen adsorbed on ceria-zirconia supported palladium-rhodium catalysts*. J. Catal. 206 (2002) 82-90.

[9.30] X. Wang, N. Perret, M.A. Keane, *Gas phase hydrogenation of nitrocyclohexane over supported gold catalysts*. Appl. Catal. A: Gen. 467 (2013) 575-584.

[9.31] H. Liu, H.T. Ma, X.Z. Li, W.Z. Li, M. Wu, X.H. Bao, *The enhancement of TiO_2 photocatalytic activity by hydrogen thermal treatment*. Chemosphere 50 (2003) 39-46.

[9.32] F. Boccuzzi, A. Chiorino, M. Manzoli, D. Andreeva, T. Tabakova, *FTIR study of the low-temperature water-gas shift reaction on Au/Fe_2O_3 and Au/TiO_2 catalysts*. J. Catal. 188 (1999) 176-185.

[9.33] C. Popa, M.V. Ganduglia-Pirovano, J. Sauer, *Periodic density functional theory study of VO_n species supported on the $CeO_2(111)$ surface*. J. Phys. Chem. C 115 (2011) 7399-7410.

[9.34] Q. Fu, H. Saltsburg, M. Flytzani-Stephanopoulos, *Active nonmetallic Au and Pt species on ceria-based water-gas shift catalysts*. Science 301 (2003) 935-938.

[9.35] F. Cárdenas-Lizana, S. Gómez-Quero, N. Perret, M.A. Keane, *Gold catalysis at the gas-solid interface: Role of the support in determining activity and selectivity in the hydrogenation of m-dinitrobenzene*. Catal. Sci. Technol. 1 (2011) 652-661.

[9.36] M. Manzoli, A. Chiorino, F. Vindigni, F. Boccuzzi, *Hydrogen interaction with gold nanoparticles and clusters supported on different oxides: A FTIR study*. Catal. Today 181 (2012) 62-67.

[9.37] I. Nakamura, H. Mantoku, T. Furukawa, T. Fujitani, *Active sites for hydrogen dissociation over $TiO_x/Au(111)$ surfaces*. J. Phys. Chem. C 115 (2011) 16074-16080.

[9.38] I. Nakamura, H. Mantoku, T. Furukawa, A. Takahashi, T. Fujitani, *Influence of Au and TiO_2 structures on hydrogen dissociation over $TiO_2/Au(100)$*. Surf. Sci. 606 (2012) 1581-1585.

[9.39] T. Fujitani, I. Nakamura, T. Akita, M. Okumura, M. Haruta, *Hydrogen dissociation by gold clusters*. Angew. Chem. Int. Edit. 48 (2009) 9515-9518.

[9.40] T. Akita, M. Okumura, K. Tanaka, M. Kohyama, M. Haruta, *TEM observation of gold nanoparticles deposited on cerium oxide*. J. Mater. Sci. 40 (2005) 3101-3106.

[9.41] B. Campo, M. Volpe, S. Ivanova, R. Touroude, *Selective hydrogenation of crotonaldehyde on Au/HSA-CeO_2 catalysts*. J. Catal. 242 (2006) 162-171.

[9.42] J. Ohyama, A. Esaki, Y. Yamamoto, S. Arai, A. Satsuma, *Selective hydrogenation of 2-hydroxymethyl-5-furfural to 2,5-bis(hydroxymethyl)furan over gold sub-nano clusters*. RSC Adv. 3 (2013) 1033-1036.

[9.43] R. Zanella, C. Louis, S. Giorgio, R. Touroude, *Crotonaldehyde hydrogenation by gold supported on TiO_2: Structure sensitivity and mechanism*. J. Catal. 223 (2004) 328-339.

[9.44] B.M. Nagaraja, A.H. Padmasri, B.D. Raju, K.S.R. Rama, *Vapor phase selective hydrogenation of furfural to furfuryl alcohol over Cu-MgO coprecipitated catalysts*. J. Mol. Catal. A: Chem. 265 (2007) 90-97.

[9.45] G. Kennedy, L.R. Baker, G.A. Somorjai, *Selective amplification of C=O bond hydrogenation on Pt/TiO_2: Catalytic reaction and sum-frequency generation vibrational spectroscopy studies of crotonaldehyde hydrogenation*. Angew. Chem. Int. Edit. 53 (2014) 3405-3408.

[9.46] M. Badawi, S. Cristol, J.F. Paul, E. Payen, *DFT study of furan adsorption over stable molybdenum sulfide catalyst under HDO conditions*. C. R. Chim. 12 (2009) 754-761.

Chapter 10

Overcoming Limitations of Gold Catalysts in Hydrogenation Applications: Enhanced Activity, Reaction Exclusivity and Full Hydrogen Utilisation

Application of nano-scale supported Au in catalytic hydrogenation has been driven by high chemoselectivity but limited by low activity due to restricted capacity for H_2 activation/dissociation. This has resulted in fundamental inefficiency as reactions are conducted with (pressurised) H_2 far in excess of the stoichiometry. This chapter tackles the issues of low reaction rate and hydrogen utilisation in a series of approaches directed at enhancing surface availability of reactive hydrogen.

10.1 Introduction

To date the application of supported Au catalysts has largely focused on selective oxidation and environmental remediation in the conversion of volatile organics [10.1-10.3]. By comparison, use in hydrogenation, a key process in the food, petrochemical, pharmaceutical and agricultural industrial sectors [10.4], is far more limited as has been noted in recent reviews [10.5,10.6]. Interest in Au catalysts for hydrogenation has been driven by the high chemoselectivity achieved in the reduction of targeted functional groups while preserving other, often more reactive, functionalities [10.7,10.8]. There are a number of instances where supported Au has generated enhanced selectivity relative to conventional transition metal (*e.g.* Pd, Pt and Ni) catalysts, notably in batch liquid phase operation[10.9,10.10]. Gold catalysts, however, deliver significantly lower hydrogenation rates, which can be attributed to a lesser capacity for hydrogen activation/dissociation [10.11,10.12]. We set out in this study to exploit the unique selectivity of Au catalysts in hydrogenation and overcome this crucial limitation with a systematic evaluation of potential alternative hydrogen sources. We also evaluate the feasibility of more effective hydrogen utilisation by transfer of reactive hydrogen *via* reaction coupling.

Commercial hydrogenation processes are typically operated in excess (pressurised) gaseous H_2 in order to maximise product yield. Hydrogen is not a naturally occurring feedstock and production, storage and transport represent serious constraints. Over 95% of global H_2 production is fossil fuel based [10.13], notably by methane steam reforming [10.14] and coal gasification [10.14] and issues of sustainability now demand alternative sources and enhanced efficiencies. A step change in catalytic hydrogenation over Au catalyst must tackle H_2 utilisation with a completely new approach. A move away from processing with compressed H_2 is an important driver in achieving safer operations for large scale production. The use of a hydrogen carrier in transfer hydrogenation reactions represents one promising alternative that has been explored in organic synthesis using homogeneous catalysis [10.15-10.17]. However, difficulties in terms of multiple separation and purification steps to isolate the product and facilitate catalyst reuse must be addressed. These drawbacks can be circumvented by a switch to heterogeneous catalysis. In this regard, work to date has employed supported metal (Pd [10.18], Ru [10.19] and Pt [10.20]) catalysts using alcohols as H_2 donors in batch liquid phase transfer hydrogenation. Here we evaluate four approaches to increase the available surface reactive hydrogen and enhance utilisation and reaction rate: (i) modification to external H_2 partial pressure; (ii) role of spillover hydrogen (by incorporation of an oxide to increase the available spillover); (iii) hydrogen donation (*via* catalytic water dissociation); (iv) coupling dehydrogenation (over supported Cu [10.21]) with hydrogenation. With the overarching goal of process sustainability, we have examined carbonyl group reduction as the model reaction using a renewable resource as reactant. Furfural is a biomass (corncob and sugar cane bagasse) derived heterocyclic aldehyde that is attracting attention as a non-petroleum based feedstock [10.22]. Selective hydrogenation generates furfuryl alcohol, a high value chemical (130,000 tons per year world production) used in the manufacture of resins/rubbers/ adhesives and as a chemical building block for drug synthesis [10.23]. We demonstrate here catalytic synergy between Au and Cu in a coupled catalytic system with full H_2 utilisation and significantly increased selective hydrogenation rate.

10.2 Experimental

10.2.1 Catalyst Preparation

Ceria supported Au (0.7 mol%), Pd (0.8 mol%), Ni (0.5 mol%) and Cu (15.2 mol%) on silica used in this work were prepared by deposition-precipitation. Au/CeO_2

(0.7 mol %) was synthesised by combining an aqueous solution of urea (100-fold excess) and $HAuCl_4$ (1.5×10^{-3} mol dm^{-3}, 400 cm^3) with the ceria support (10 g, Sigma-Aldrich). The suspension was stirred and heated (2 K min^{-1}) to 353 K, where the pH progressively increased (to *ca.* 7) after 3 h as a result of urea decomposition. The solid suspension was separated by filtration and washed with distilled water until Cl free (based on the $AgNO_3$ test). Pd/CeO_2 (0.8 mol %) and Ni/CeO_2 (0.5 mol %) were synthesised using $Pd(NO_3)_2$ and $Ni(NO_3)_2$, respectively, as metal precursors. An aqueous (2×10^{-3} mol dm^{-3}, 300 cm^3) solution of the precursor was added to (10 g) the CeO_2 support. Aqueous Na_2CO_3 (2 mol dm^{-3}) was slowly added to the resultant suspension until pH > 10 to ensure complete metal deposition, heating (2 K min^{-1}) to 353 K for 4 h. The solids were separated by filtration, washed with distilled water and dried in a vacuum oven at 333 K for 12 h. A (15 mol %) Cu/SiO_2 was prepared with NaOH as precipitation agent. 20 g (fumed) silica powder (Sigma-Aldrich) were dispersed in a solution of $Cu(NO_3)_2$ (0.25 mol dm^{-3}, 200 cm^3). The suspension was stirred (600 rpm) at room temperature for 1 h, followed by addition of aqueous NaOH (2 M) until pH > 10 with subsequent heating to 353 K, maintained for 4 h to ensure homogeneous $Cu(OH)_2$ deposition. The catalyst precursor was separated by filtration, washed with distilled water until pH = 7 and dried at 393 K overnight. The dried sample was calcined (in air) at 10 K min^{-1} to 723 K for 4 h to generate copper oxide (CuO). All the samples were sieved (ATM fine test sieves) to a mean particle diameter = 75 μm. Before reaction, the samples were activated in 60 cm^3 min^{-1} H_2 to 523-723 K (at 2-10 K min^{-1}) with a final isothermal hold for 1-2 h and passivated at ambient temperature in 1% v/v O_2/He for *ex situ* characterisation.

10.2.2 Catalyst Characterisation

Metal content was measured by atomic absorption spectroscopy using a Shimadzu AA-6650 spectrometer with an air-acetylene flame from the diluted extract in aqua regia (25% v/v HNO_3/HCl). Temperature programmed reduction (TPR), hydrogen chemisorption at reaction temperature (498 K) and subsequent temperature programmed desorption (TPD) were conducted on the CHEM-BET 3000 (Quantachrome) unit with data acquisition/manipulation using TPR Win™ software. The effluent gas passed through a liquid N_2 trap where H_2 uptake/release was monitored by a thermal conductivity detector (TCD). Samples were loaded into a U-shaped Pyrex glass cell (3.76 mm i.d.) and reduced in 17 cm^3 min^{-1} 5% v/v H_2/N_2 to

523-723 K (at 2-10 K min^{-1}) with a final isothermal hold for 1-2 h to ensure full reduction of the metal precursor. The activated samples were swept with 65 cm^3 min^{-1} N_2 for 1.5 h, cooled to 498 K and subjected to H_2 (10 or 50 μl) chemisorption by pulse titration. The samples were subsequently cooled to ambient temperature with TPD in N_2 at 50 K min^{-1} to 973 K. In blank test there was no measurable H_2 uptake over the supports. Scanning transmission electron microscopy (STEM) was performed using a JEOL 2200FS field emission gun-equipped transmission electron microscope unit, employing Gatan Digital Micrograph 1.82 for data acquisition/manipulation. Samples for analysis were prepared by dispersion in acetone and deposited on a holey carbon/Cu grid (300 Mesh). Surface area weighted mean metal particle size (*d*) and size distribution were determined according to

$$d = \frac{\sum_i n_i d_i^3}{\sum_i n_i d_i^2} \qquad \textbf{(10.1)}$$

where n_i is the number of particles of diameter d_i.

10.2.3 Catalytic Procedure

Reactions (independent hydrogenation of furfural (in H_2), coupled dehydrogenation/ hydrogenation of 2-butanol/furfural and formic acid decomposition (in N_2)) were carried out at atmospheric pressure and 498 K *in situ* after activation in a continuous flow fixed-bed tubular reactor (i.d. = 15 mm). Reaction conditions ensured negligible internal/external mass and heat transfer limitations. A layer of borosilicate glass beads served as preheating zone where the reactant was vaporised and reached reaction temperature before contacting the catalyst bed. Isothermal conditions (±1 K) were maintained by diluting the catalyst with ground glass (75 μm); reaction temperature was continuously monitored by a thermocouple inserted in a thermowell within the catalyst bed. The reactant(s) was(were) delivered to the reactor *via* a glass/teflon air-tight syringe and teflon line using a microprocessor controlled infusion pump (Model 100 kd Scientific). The independent hydrogenation of furfural was tested in a co-current flow of H_2 with furfural ($GHSV = 5 \times 10^3$ h^{-1} and molar metal to furfural feed rate (n/F) = 5×10^{-3} h). Coupled dehydrogenation/hydrogenation was conducted in N_2 ($GHSV = 2.5 \times 10^3$ h^{-1}, $n_{Au}/F = 5 \times 10^{-3} - 11 \times 10^{-3}$ h, mole Cu/Au = 65-150). Formic acid decomposition was evaluated in N_2 ($GHSV = 5 \times 10^3$ h^{-1}, $n_{Au}/F = 2 \times 10^{-4}$ h). The reactor effluent was analysed by capillary GC (Perkin-Elmer Auto System XL gas chromatograph equipped

with a programmed split/splitless injector and a flame ionisation detector, employing a DB-1 (50 m × 0.33 mm i.d., 0.20 μm film thickness) capillary column (J&W Scientific)). In a series of control experiments, passage of each reactant in a stream of H_2 or N_2 through the empty reactor or over the support (ceria or silica) alone did not result in any detectable conversion. Reactant (i) fractional conversion (X) is defined by

$$X_{\mathrm{i}}\ (\%) = \frac{[reactant]_{\mathrm{i,\ in}} - [reactant]_{\mathrm{i,\ out}}}{[reactant]_{\mathrm{i,\ in}}} \times 100 \qquad \textbf{(10.2)}$$

and selectivity (S) to product (j) is given by

$$S_{\mathrm{j}}(\%) = \frac{[product]_{\mathrm{j,out}}}{[reactant]_{\mathrm{i,in}} - [reactant]_{\mathrm{i,out}}} \times 100 \qquad \textbf{(10.3)}$$

where the subscripts "in" and "out" refer to the inlet and outlet gas streams, respectively. Repeated reactions using different samples from the same batch of catalyst delivered raw data reproducibility within ±5%. Turnover frequency (*TOF*, rate per active site) was obtained from

$$TOF\ (\mathrm{h}^{-1}) = \frac{R}{D} \qquad \textbf{(10.4)}$$

where D is the metal dispersion (surface metal per total metal atoms) and R (h^{-1}) represents the reactant consumption rate. Metal dispersion was obtained from

$$D = \frac{S_{surface} \times M_{metal}}{A_{metal} \times N_{Avogadro}} = \frac{(6/d \times \rho_{metal}) \times M_{metal}}{A_{metal} \times N_{Avogadro}} \qquad \textbf{(10.5)}$$

where d resulted from STEM measurements, $S_{surface}$ is the metal atom surface area, ρ_{metal} metal density, M_{metal} metal atomic mass, A_{metal} metal atom surface area and $N_{Avogadro}$ the Avogadro number. Reactant consumption rate (R) was obtained from

$$R\ (\mathrm{h}^{-1}) = \frac{X_0 \times F}{n} \qquad \textbf{(10.6)}$$

where initial fractional conversion (X_0) was extracted from time on-stream measurement.

10.3 Results and Discussion

10.3.1 Catalyst (Au/CeO_2) Characterisation

Scanning transmission electron microscopy (STEM) analysis (**Fig. 10.1**) for gold on ceria revealed pseudo-spherical metal particles at the nano-scale (1-5 nm) with an

associated surface area weighted mean of 2.8 nm. It has been noted elsewhere [10.24] Au particle size <5 nm is critical for significant hydrogenation activity. Gold has restricted

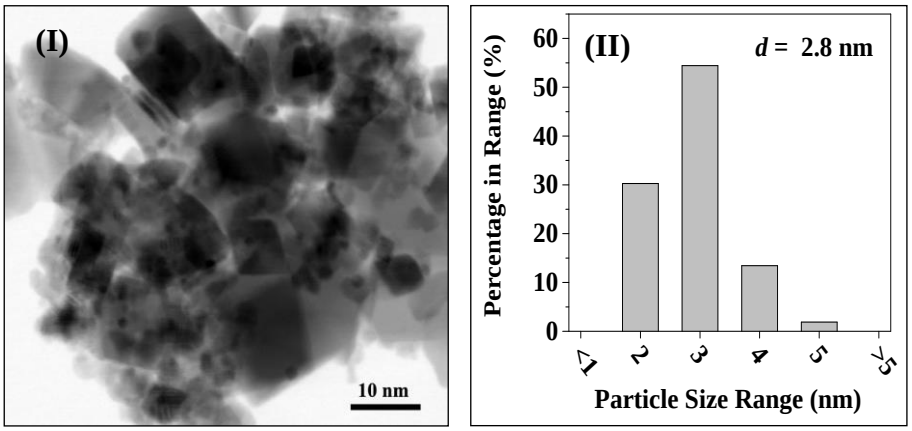

Fig. 10.1: (I) Representative STEM image with (II) associated Au particle size distribution histogram for Au/CeO_2.

capacity for H_2 adsorption/dissociation (2 μmol g^{-1} at reaction temperature), significantly lower than that for Pd/CeO_2 and Ni/CeO_2 (**Table 10.1**) used here as a reference. This is due to the filled 3*d* band in Au that results in a high energy barrier for dissociative adsorption and low binding strength of hydrogen atoms on Au [10.8,10.25]. TPR analysis (**Fig. 10.2**) demonstrates hydrogen consumed was (8 times) greater than that required for the $Au^{3+} \rightarrow Au^0$ reduction step, indicative of partial support reduction resulting in the formation of surface oxygen vacancies, as shown in the schematic in **Fig. 10.3(A)** [10.26].

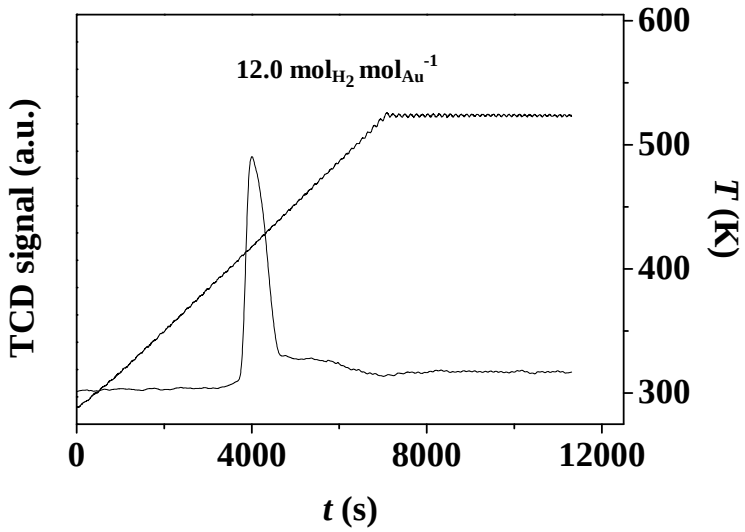

Fig. 10.2: TPR profile of Au/CeO_2 with associated hydrogen consumption.

Table 10.1: Physicochemical properties of CeO_2 supported Au, Pd and Ni.

Supported Metal	Meal loading (mol%)	Mean metal size (nm)	H_2 uptake at 498 K (μmol g^{-1})
Au	0.7	2.8	2
Pd	0.8	3.7	62
Ni	0.5	2.0	22

10.3.2 Catalytic Response

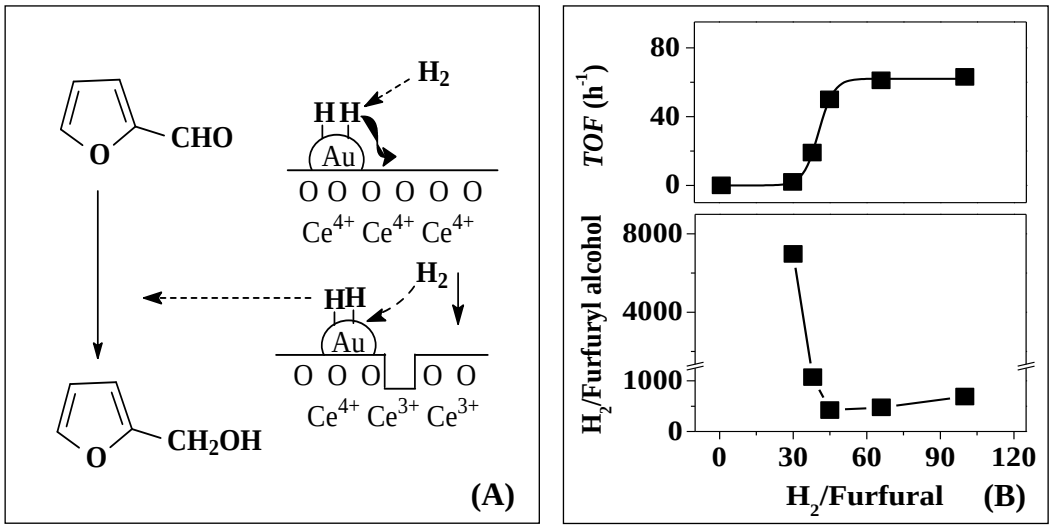

Fig. 10.3: Effect of inlet H_2/Furfural: Partial support reduction and hydrogenation of furfural to furfuryl alcohol over Au/CeO_2. (A) Schematic illustrating spillover hydrogen generation and consumption in partial support reduction and furfural hydrogenation (to furfuryl alcohol). (B) Turnover frequency (*TOF*) and H_2 utilisation with respect to furfuryl alcohol produced (H_2/Furfuryl alcohol) as a function of inlet H_2/Furfural molar ratio over Au/CeO_2. *Reaction conditions*: T = 498 K, P = 1 atm, $n_{Au}/F = 5 \times 10^{-3}$ h.

Given that H_2 activation is a limiting factor, we have explored the effect of H_2 partial pressure (*i.e.* inlet H_2/Furfural ratio) as a possible route to elevate surface hydrogen concentration and increase hydrogenation rate; the results are presented in (**Fig. 10.3(B)**). In every case reaction over Au/CeO_2 resulted in full selectivity to the target furfuryl alcohol, *i.e.* exclusive reduction of carbonyl group (**Fig. 10.3(A)**). We could find only one published study [10.27] on the use of (SiO_2) supported Au in furfural hydrogenation where even at high H_2 pressure (1.0 MPa) conversions were negligible. We observed no detectable catalytic activity at the reaction stoichiometry

(H_2/Furfural = 1) but *TOF* increased to reach an upper value (61 h^{-1}) at H_2/Furfural > 60 (**Fig. 10.3(B)**). Hydrogen utilisation, expressed here in terms of mol H_2 required to produce 1 mol of furfuryl alcohol (H_2/Furfuryl alcohol) was enhanced with increasing inlet H_2/Furfural to 45 (**Fig. 10.3(B)**). The restricted capacity of Au for H_2 adsorption/ dissociation resulted in measurably lower efficiencies at higher H_2/Furfural. Hydrogen utilisation is a critical consideration in terms of process sustainability where the best result (H_2/Furfuryl alcohol = 420) is far removed from the target stoichiometry (= 1).

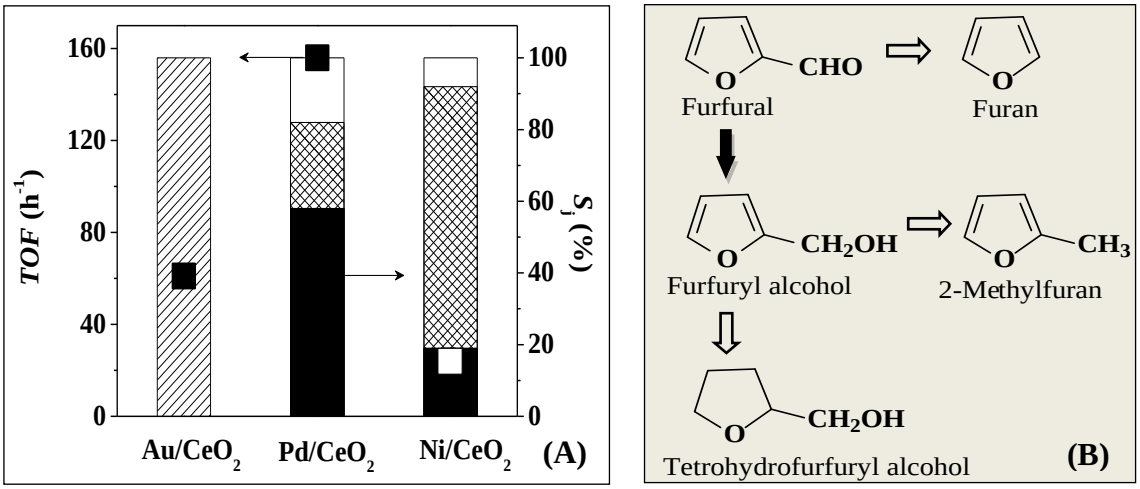

Fig. 10.4: Effect of supported metal: Hydrogenation of furfural over CeO_2 supported Au, Pd and Ni. (A) Turnover frequency (*TOF*; ■, □) and selectivity (S_j) to furfuryl alcohol (hatched bar), 2-methylfuran (solid bar), tetrahydrofurfuryl alcohol (open bar) and furan (cross hatched bar) over Au/CeO_2, Pd/CeO_2 and Ni/CeO_2. (B) Reaction pathway for the hydrogenation of furfural over CeO_2 supported Au (solid arrow), Pd and Ni (open arrows). *Reaction conditions*: T = 498 K, P_{H_2} = 1 atm, n/F = 5 × 10^{-3} h.

Supported transition metals (Pd, Ni and Pt) are effective in dissociative H_2 chemisorption with consequent high hydrogenation activity [10.28]. In order to enhance furfural hydrogenation efficiency, we considered the use of Pd/CeO_2 and Ni/CeO_2 as an index to measure the performance of Au/CeO_2. The activity/selectivity response at the same inlet H_2/Furfural ratio (= 66) for the three catalysts is presented in **Fig. 10.4(A)** where Pd/CeO_2 with the highest H_2 uptake capacity (**Table 10.1**) delivered the greatest *TOF*. In contrast to Au/CeO_2, Pd/CeO_2 promoted hydrogenolysis of furfuryl alcohol to 2-methylfuran, secondary decarbonylation to furan and ring reduction to tetrahydrofurfuryl alcohol (**Fig. 10.4(B)**). Furan was the main product formed over Ni/CeO_2 with no detectable furfuryl alcohol. Our results demonstrate a dependency of product distribution on the catalytic metal where Au facilitates exclusive reduction of the carbonyl group. Hydrogen chemisorption/activation by Au is the limiting step that

controls rate of the alcohol production. Increased furfural conversion must tackle the availability of reactive hydrogen while retaining full selectivity to the target furfuryl alcohol.

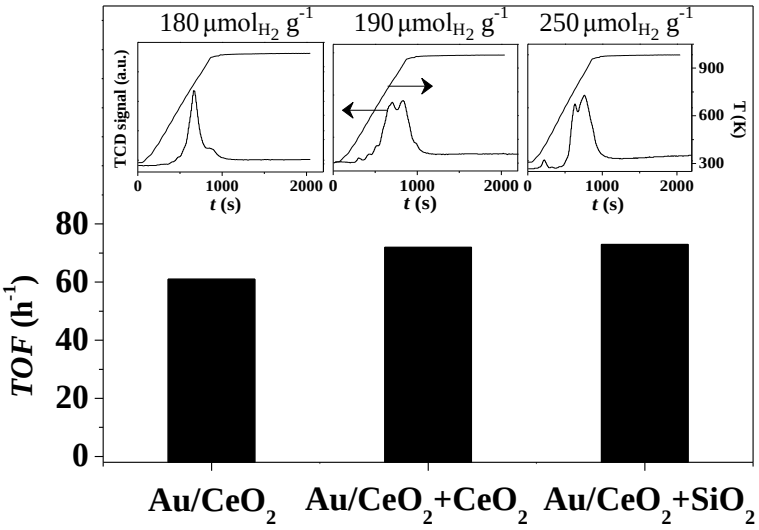

Fig. 10.5: Effect of spillover hydrogen: Hydrogenation of furfural over oxide supported Au. Turnover frequency (*TOF*) and H_2 TPD profiles (as *insets*) for Au/CeO_2 and physical mixtures with CeO_2 and SiO_2. *Reaction conditions*: T = 498 K, P = 1 atm, $n_{Au}/F = 5 \times 10^{-3}$ h, H_2/Furfural = 66.

Spillover hydrogen species, *i.e.* atomic hydrogen generated by dissociative adsorption on metal sites that "spills" across the metal/support interface and onto the support surface can serve as a reactive hydrogen reservoir that contributes to hydrogenation. The spillover phenomenon can take place across solid/solid grain boundaries [10.29] and we have demonstrated that catalyst+support physical mixtures bear greater quantities of hydrogen compared with the catalyst alone [10.30]. Spillover hydrogen can be effectively quantified by temperature programmed desorption (TPD) [10.29]. The TPD profile for Au/CeO_2 (**Fig. 10.5**) is characterised by H_2 desorption (180 μmol g^{-1}) with a temperature maximum (T_{max}) at 788 K that far exceeded H_2 chemisorption (2 μmol g^{-1}) and can be attributed to release of spillover species [10.30]. The incorporation of CeO_2 or SiO_2 with Au/CeO_2 resulted in an additional peak at a higher temperature due to release from the added oxides with a measurably greater H_2 desorption (**Fig. 10.5**). A resultant increase in furfural *TOF* (from 61 h^{-1} to 72 h^{-1}) was obtained while retaining full selectivity to the target alcohol. The lower H_2 desorption from $Au/CeO_2 + CeO_2$ (relative to the physical mixture with non-reducible SiO_2) can be accounted for in terms of hydrogen consumption due to partial ceria reduction as

established in the TPR measurements. The results confirm a contribution from spillover hydrogen that elevates selective hydrogenation rate.

Water is an environmentally benign solvent that has been shown to act as hydrogen donor in water gas shift and steam reforming over (CeO_2 and Fe_2O_3) supported Au [10.31,10.32]. The effect of incorporating water in the furfural feed was tested and the *TOF* delivered by Au/CeO_2 as a function of water content is shown in **Fig. 10.6(A)**. A three-fold higher rate was achieved at H_2O/Furfural = 0.2-1. We envision a surface mechanism (**Fig. 10.6(B)**) where H_2 is dissociatively adsorbed on Au and spills over onto the support (step **I**) with the creation of oxygen vacancies (step **II**). Dissociative interaction of H_2O generates OH that is consumed in a re-oxidation of the support (step **III**) with the generation of two reactive protons (step **IV**) that attack the furfural carbonyl group to produce the target alcohol. At H_2O/Furfural =1/5 a switch from H_2 to N_2 in the feed did not result in any detectable conversion (**Fig. 10.6(A)**). This response suggests that the promoting effect of water is an activated process that involves continuous creation, consumption and regeneration of oxygen vacancies, requiring a co-current H_2/H_2O inlet with hydroxyl consumption and release of reactive hydrogen for –C=O reduction.

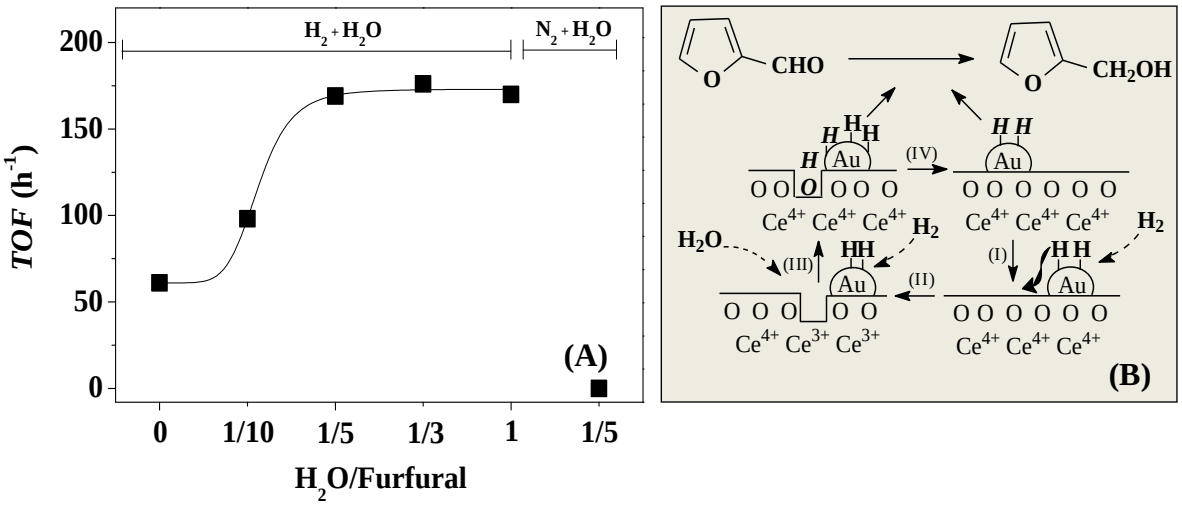

Fig. 10.6: Effect of water addition: Hydrogenation of furfural to furfuryl alcohol over Au/CeO_2. (A) Turnover frequency (*TOF*) as a function of H_2O/Furfural molar ratio (B) Proposed reaction mechanism (steps (I)-(IV)) illustrating effect of water addition on furfural hydrogenation (to furfuryl alcohol). *Reaction conditions*: T = 498 K, P_{H_2} = 1 atm, $n_{Au}/F = 5 \times 10^{-3}$ h, H_2/Furfural = 66.

Results to this point have established reaction exclusivity to furfuryl alcohol over

Au/CeO_2 in continuous operation. Viable commercial application requires more efficient hydrogen utilisation where the use of hydrogen donors (rather than an external gaseous H_2) as a means of transfer hydrogenation represents one possible process option. Catalytic decomposition of formic acid (generated from biorefineries [10.33]) releases hydrogen that can serve as reductant [10.34]. Formic acid decomposition rate (5220 h^{-1} at 498 K) over Au/CeO_2 was significantly greater than the furfural hydrogenation and should ensure sufficient hydrogen supply for the reaction. However, Au/CeO_2 exhibited no activity in coupled formic acid decomposition and furfural hydrogenation. This can be attributed to inhibited hydrogen production due to competitive furfural and formic acid adsorption at Au sites. Catalytic dehydrogenation of alcohols can also serve as an *in situ* source of reactive hydrogen [10.35]. Nagaraja *et al*. [10.36] demonstrated the viability of coupling cyclohexanol dehydrogenation and furfural hydrogenation on Cr_2O_3 promoted Cu-MgO, but similarity (10 K difference) in boiling points of the products necessitated difficult separation/purification and the hydrogen utilisation was inefficient (<10%). 2-Butanone (used as solvent and in the production of plastics, coatings and films [10.37]) can be obtained from 2-butanol dehydrogenation with hydrogen release. Coupling 2-butanol dehydrogenation with furfural hydrogenation generates two high value products (2-butanone and furfuryl alcohol) that can be readily separated (100 K difference in boiling points at 1 atm) by standard distillation [10.38]. Au/CeO_2 exhibited negligible activity in the dehydrogenation of 2-butanol to H_2 generation and there is a requirement for an alternative (dehydrogenation) catalytic metal. Supported copper (on hydrotalcite [10.39], Al_2O_3 [10.40] and SiO_2 [10.41]) is effective in dehydrogenation and was chosen as a suitable candidate to work in tandem with Au/CeO_2. Silica supported Cu was prepared by deposition-precipitation and activated in H_2. STEM analysis (**Fig. 10.7**) revealed Cu particles in the 1-15 nm size range

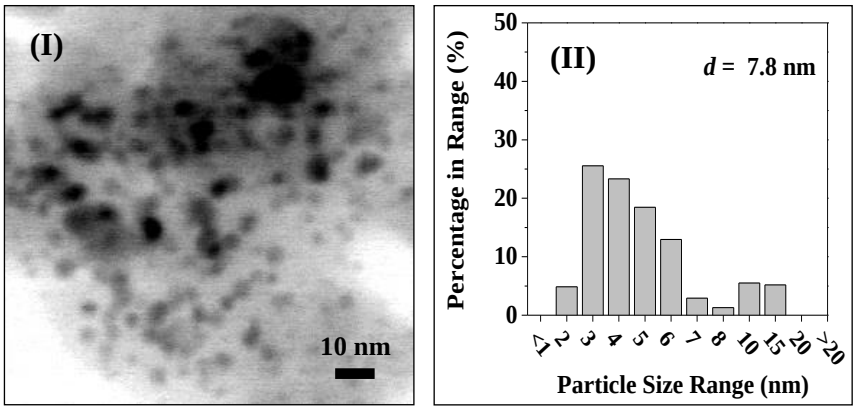

Fig. 10.7: (I) Representative STEM image with (II) associated Cu particle size distribution histogram for Cu/SiO_2.

to give a surface area weighted mean of 7.8 nm where larger Cu size (2-8 nm) has been shown to facilitate 2-butanol dehydrogenation [10.42]. Under our reaction conditions, Cu/SiO_2 delivered low activity ($TOF \leq 13$ h^{-1}) in furfural conversion and so does not contribute significantly to the hydrogenation step in the coupled reaction. Dehydrogenation of 2-butanol over Cu/SiO_2 generated 2-butanone as sole product at a rate that was five times greater than the furfural hydrogenation rate over Au/CeO_2, guaranteeing sufficient hydrogen supply in the coupled reaction. We evaluated catalytic coupling (in N_2) over a physical mixture of Au/CeO_2 with Cu/SiO_2 (with varying Cu/Au) given Cu content determines hydrogen production *via* dehydrogenation and the results are presented in **Fig. 10.8**. In every case 2-butanone and furfuryl alcohol were the only

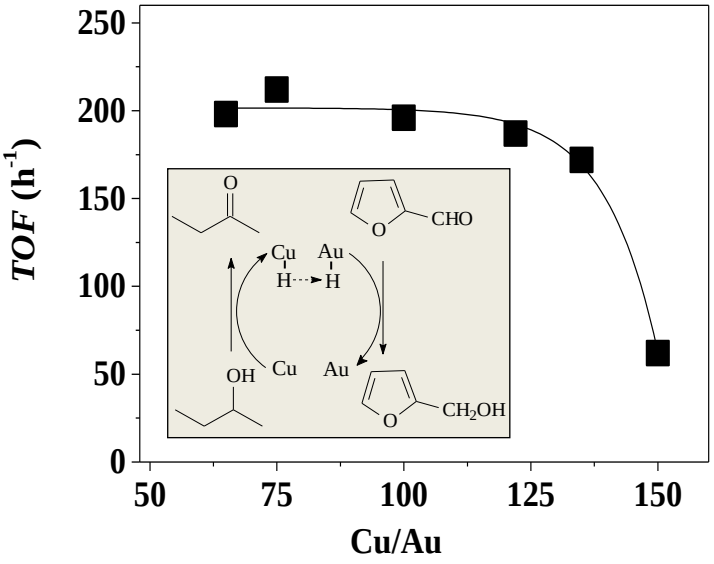

Fig. 10.8: Coupled dehydrogenation-hydrogenation. Turnover frequency (*TOF*) as a function of Cu/Au molar ratio in coupled 2-butanol dehydrogenation with furfural hydrogenation. *Inset*: schematic representation of mechanism involved in coupling of 2-butanol dehydrogenation over Cu with furfural hydrogenation over Au. *Reaction conditions*: T = 498 K, P_{N_2} = 1 atm, 2-BuOH/Furfural = 15.

products obtained. The *TOF* increased (from 62 to 200 h^{-1}) with decreasing Cu/Au (from 150 to 65). This demonstrates Au/CeO_2 successfully "borrowed" the hydrogen (Cu-H) generated *in situ* by dehydrogenation that Fridman *et al.* have demonstrated to proceed *via* a two-step H abstraction mechanism [10.43]; see schematic representation in the inset to **Fig. 10.8**. This supply of reactive hydrogen circumvents the limitations associated with hydrogen activation/dissociation by Au and contributes to enhanced furfural *TOF*. The plateau for furfural *TOF* over Cu/Au = 120-65 can be due to limited capacity of Au to accommodate reactive hydrogen (Au-H). Given that water addition

increased the rate of stand-alone furfural hydrogenation, we evaluated the effect of water incorporation in the coupled reaction system (in N_2). This did not result in any increase in activity and can be attributed to insufficient hydrogen availability for ceria reduction to form the oxygen vacancies necessary for water dissociation and release of reactive hydrogen (see **Fig. 10.6**).

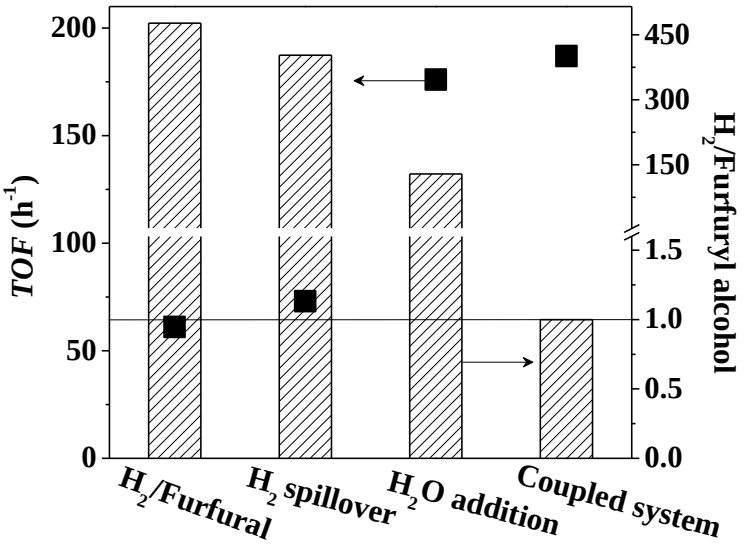

Fig. 10.9: Comparison of the catalytic response for different hydrogen supply strategies. Furfural turnover frequency (*TOF*; ■) and H_2 utilisation with respect to furfuryl alcohol produced (H_2/Furfuryl alcohol, bars) over Au/CeO_2 as a result of variation in inlet H_2/Furfural, participation of spillover H_2, promotion by water dissociation and coupling with dehydrogenation. *Inset line*: reaction stoichiometry. *Reaction conditions*: *T* = 498 K, *P* = 1 atm.

The different approaches that we have considered in this work to address hydrogen utilisation and enhance selective furfural hydrogenation rate are summarised in **Fig. 10.9**. Reaction exclusivity to the target alcohol has been achieved over Au/CeO_2 using conventional external compressed H_2 source but this was accompanied by low hydrogen utilisation efficiency (H_2/Furfuryl alcohol = 420) where the reaction must be conducted with H_2 far in excess. Incorporation (as a physical mixture) of an oxide support (CeO_2 or SiO_2) with Au/CeO_2 served to increase spillover hydrogen with a measurable increase in *TOF* and a marginal decrease in H_2/Furfuryl alcohol. The inclusion of water in the feed resulted in significantly (three-fold) higher chemoselective rates due to the generation of reactive hydrogen *via* water dissociation (on surface oxygen vacancies) but hydrogen utilisation was still far above stoichiometric requirements. The dehydrogenation/hydrogenation coupling strategy enabled full utilisation of (*in situ* generated) hydrogen *via* dehydrogenation where H_2/Furfuryl alcohol converged at

reaction stoichiometry. The latter exhibited the greatest process efficiency in terms of *TOF* and hydrogen utilisation. This approach offers clear advantages over conventional hydrogenation applications and closes a sustainability gap that will allow greater exploitation of the chemoselectivity exhibited by supported Au catalysts.

10.4 Conclusion

We have demonstrated that nano-scale (2.8 nm) Au supported on ceria promotes the exclusive continuous gas phase hydrogenation of (biomass-derived) furfural to furfuryl alcohol. Under the same reaction conditions Pd and Ni on CeO_2 delivered higher rates but promoted decarbonylation, hydrogenolysis and furan ring reduction with no detectable furfuryl alcohol formation. An increase in H_2 content in the feed enhanced activity over Au/CeO_2 but with low hydrogen utilisation efficiency. Greater available surface hydrogen *via* (i) spillover (physical mixture with CeO_2 and SiO_2) and (ii) water dissociation (on surface oxygen vacancies) resulted in up to a three-fold higher selective hydrogenation rate but reaction still required excess H_2. Full hydrogen utilisation (H_2/Furfuryl alcohol = 1) and increased alcohol production rate was achieved by coupling catalytic dehydrogenation (of 2-butanol to 2-butanone) over Cu/SiO_2 with furfural hydrogenation over Au/CeO_2. This addresses the issue of unreacted hydrogen, circumventing the requirement for an external supply of pressurised H_2 with the production of two high value products that are readily separated by standard distillation. Our results demonstrate a feasible solution to the limitations of Au in reductive processes and open new directions in "hydrogen free" hydrogenation.

10.5 References

[10.1] L. Kesavan, R. Tiruvalam, M.H. Ab-Rahim, M.I. bin Saiman, D.I. Enache, R.L. Jenkins, N. Dimitratos, J.A. Lopez-Sanchez, S.H. Taylor, D.W. Knight, C.J. Kiely, G.J. Hutchings, *Solvent-free oxidation of primary carbon-hydrogen bonds in toluene using Au-Pd alloy nanoparticles*. Science 331 (2011) 195-199.

[10.2] M. Stratakis, H. Garcia, *Catalysis by supported gold nanoparticles: Beyond aerobic oxidative processes*. Chem. Rev. 112 (2012) 4469-4506.

[10.3] A. Corma, P. Concepción, M. Boronat, M.J. Sabater, J. Navas, M.J. Yacaman, E. Larios, A. Posadas, M.A. Lopez-Quintela, D. Buceta, E. Mendoza, G. Guilera, A. Mayoral, *Exceptional oxidation activity with size-controlled supported gold clusters of low atomicity*. Nature Chem. 5 (2013) 775-781.

[10.4] M. Irfan, T.N. Glasnov, C.O. Kappe, *Heterogeneous catalytic hydrogenation reactions in continuous-flow reactors*. ChemSusChem 4 (2011) 300-316.

[10.5] L. McEwan, M. Julius, S. Roberts, J.C.Q. Fletcher, *A review of the use of gold catalysts in selective hydrogenation reactions*. Gold Bull. 43 (2010) 298-306.

[10.6] F. Cárdenas-Lizana, M.A. Keane, *The development of gold catalysts for use in hydrogenation reactions*. J. Mater. Sci. 48 (2013) 543-564.

[10.7] A. Corma, P. Serna, H. Garcia, *Gold catalysts open a new general chemoselective route to synthesize oximes by hydrogenation of α, β-unsaturated nitrocompounds with H_2*. J. Am. Chem. Soc. 129 (2007) 6358-6359.

[10.8] M. Pan, A.J. Brush, Z.D. Pozun, H.C. Ham, W.Y. Yu, G. Henkelman, G.S. Hwang, C.B. Mullins, *Model studies of heterogeneous catalytic hydrogenation reactions with gold*. Chem. Soc. Rev. 42 (2013) 5002-5013.

[10.9] A. Corma, P. Serna, *Chemoselective hydrogenation of nitro compounds with supported gold catalysts*. Science 313 (2006) 332-334.

[10.10] T. Mitsudome, K. Kaneda, *Gold nanoparticle catalysts for selective hydrogenations*. Green Chem. 15 (2013) 2636-2654.

[10.11] C. Kartusch, J.A. van Bokhoven, *Hydrogenation over gold catalysts: The interaction of gold with hydrogen*. Gold Bull. 42 (2009) 343-347.

[10.12] G.C. Bond, *Chemisorption and reactions of small molecules on small gold particles*. Molecules 17 (2012) 1716-1743.

[10.13] R.M. Navarro, M.A. Pena, J.L.G. Fierro, *Hydrogen production reactions from carbon feedstocks: Fossils fuels and biomass*. Chem. Rev. 107 (2007) 3952-3991.

[10.14] R. Kothari, D. Buddhi, R.L. Sawhney, *Comparison of environmental and economic aspects of various hydrogen production methods*. Renew. Sust. Energ. Rev. 12 (2008) 553-563.

[10.15] C. Zheng, S.L. You, *Transfer hydrogenation with Hantzsch esters and related organic hydride donors*. Chem. Soc. Rev. 41 (2012) 2498-2518.

[10.16] T. Ikariya, A.J. Blacker, *Asymmetric transfer hydrogenation of ketones with bifunctional transition metal-based molecular catalysts*. Acc. Chem. Res. 40 (2007) 1300-1308.

[10.17] M. Rueping, A.R. Antonchick, T. Theissmann, *A highly enantioselective Brønsted acid catalyzed cascade reaction: Organocatalytic transfer hydrogenation of quinolines and their application in the synthesis of alkaloids*. Angew. Chem. Int. Edit. 45 (2006) 3683-3686.

[10.18] Y. Xiang, X. Li, C. Lu, L. Ma, Q. Zhang, *Water-improved heterogeneous transfer hydrogenation using methanol as hydrogen donor over Pd-based catalyst*. Appl. Catal. A: Gen. 375 (2010) 289-294.

[10.19] K. Yamaguchi, J. He, T. Oishi, N. Mizuno, *The "borrowing hydrogen strategy" by supported ruthenium hydroxide catalysts: Synthetic scope of symmetrically and unsymmetrically substituted amines*. Chem. Eur. J. 16 (2010) 7199-7207.

[10.20] Y.Y. Huang, W.M.H. Sachtler, *Intermolecular hydrogen transfer in nitrile hydrogenation over transition metal catalysts*. J. Catal. 190 (2000) 69-74.

[10.21] B.M. Nagaraja, A.H. Padmasri, P. Seetharamulu, K.H.P. Reddy, B.D. Raju, K.S.R. Rao, *A highly active Cu-MgO-Cr_2O_3 catalyst for simultaneous synthesis of furfuryl alcohol and cyclohexanone by a novel coupling route: Combination of furfural hydrogenation and cyclohexanol dehydrogenation*. J. Mol. Catal. A: Chem. 278 (2007) 29-37.

[10.22] J.-P. Lange, E. van der Heide, J. van Buijtenen, R. Price, *Furfural: A promising platform for lignocellulosic biofuels*. ChemSusChem 5 (2012) 150-166.

[10.23] R.V. Sharma, U. Das, R. Sammynaiken, A.K. Dalai, *Liquid phase chemo-selective catalytic hydrogenation of furfural to furfuryl alcohol*. Appl. Catal. A: Gen. 454 (2013) 127-136.

[10.24] E. Bus, J.T. Miller, J.A. van Bokhoven, *Hydrogen chemisorption on Al_2O_3-supported gold catalysts*. J. Phys. Chem. B 109 (2005) 14581-14587.

[10.25] T. Fujitani, I. Nakamura, T. Akita, M. Okumura, M. Haruta, *Hydrogen dissociation by gold clusters*. Angew. Chem. Int. Edit. 48 (2009) 9515-9518.

[10.26] D. Andreeva, V. Idakiev, T. Tabakova, L. Ilieva, P. Falaras, A. Bourlinos, A. Travlos, *Low-temperature water-gas shift reaction over Au/CeO_2 catalysts*. Catal. Today 72 (2002) 51-57.

[10.27] Y.-C. Hong, K.-Q. Sun, G.-R. Zhang, R.-Y. Zhong, Q. Xu, *Fully dispersed Pt entities on nano-Au dramatically enhance the activity of gold for chemoselective hydrogenation catalysis*. Chem. Commun. 47 (2011) 1300-1302.

[10.28] P. Mäki-Arvela, J. Hájek, T. Salmi, D.Y. Murzin, *Chemoselective hydrogenation of carbonyl compounds over heterogeneous catalysts*. Appl. Catal. A: Gen. 292 (2005) 1-49.

[10.29] R. Prins, *Hydrogen spillover: Facts and fiction*. Chem. Rev. 112 (2012) 2714-2738.

[10.30] C. Amorim, M.A. Keane, *Catalytic hydrodechlorination of chloroaromatic gas streams promoted by Pd and Ni: The role of hydrogen spillover*. J. Hazard. Mater. 211 (2012) 208-217.

[10.31] D.R. Palo, R.A. Dagle, J.D. Holladay, *Methanol steam reforming for hydrogen production*. Chem. Rev. 107 (2007) 3992-4021.

[10.32] D. Andreeva, *Low temperature water gas shift over gold catalysts*. Gold Bull. 35 (2002) 82-88.

[10.33] D.A. Bulushev, S. Beloshapkin, J.R.H. Ross, *Hydrogen from formic acid decomposition over Pd and Au catalysts*. Catal. Today 154 (2010) 7-12.

[10.34] J.F. Hull, Y. Himeda, W.-H. Wang, B. Hashiguchi, R. Periana, D.J. Szalda, J.T. Muckerman, E. Fujita, *Reversible hydrogen storage using CO_2 and a proton-switchable iridium catalyst in aqueous media under mild temperatures and pressures*. Nature Chem. 4 (2012) 383-388.

[10.35] M. Trincado, D. Banerjee, H. Grutzmacher, *Molecular catalysts for hydrogen production from alcohols*. Energ. Environ. Sci. 7 (2014) 2464-2503.

[10.36] B.M. Nagaraja, A.H. Padmasri, B.D. Raju, K.S.R. Rao, *Production of hydrogen through the coupling of dehydrogenation and hydrogenation for the synthesis of cyclohexanone and furfuryl alcohol over different promoters supported on Cu-MgO catalysts*. Int. J. Hydrogen Energ. 36 (2011) 3417-3425.

[10.37] W.G. Zhang, D.H. Yu, X.J. Ji, H. Huang, *Efficient dehydration of bio-based 2,3-butanediol to butanone over boric acid modified HZSM-5 zeolites*. Green Chem. 14 (2012) 3441-3450.

[10.38] A. Javaid, C.S. Bildea, *Design and control of an integrated 1,4-butanediol dehydrogenation and furfural hydrogenation plant*. Chem. Eng. Technol. 37 (2014) 1515-1524.

[10.39] T. Mitsudome, Y. Mikami, K. Ebata, T. Mizugaki, K. Jitsukawa, K. Kaneda, *Copper nanoparticles on hydrotalcite as a heterogeneous catalyst for oxidant-free dehydrogenation of alcohols*. Chem. Commun. 39 (2008) 4804-4806.

[10.40] N.P. Tangale, P.S. Niphadkar, S.S. Deshpande, P.N. Joshi, *Dehydrogenation of cyclohexanol over Cu/Al_2O_3 catalysts prepared with different precipitating agents*. Appl. Catal. A: Gen. 467 (2013) 421-429.

[10.41] P.A. Torresi, V.K. Diez, P.J. Luggren, J.I. Di-Cosimo, *Conversion of diols by dehydrogenation and dehydration reactions on silica-supported copper catalysts*. Appl. Catal. A: Gen. 458 (2013) 119-129.

[10.42] M. Li, Y. Hao, H.H.P. Yiu, F. Cárdenas-Lizana, M.A. Keane, *"Hydrogen-free" production of 2-butanone and aniline over Cu/SiO_2 via reaction coupling*. Top. Catal. 58 (2015) 149-158.

[10.43] V.Z. Fridman, A.A. Davydov, K. Titievsky, *Dehydrogenation of cyclohexanol on copper-containing catalysts: II. The pathways of the cyclohexanol dehydrogenation reaction to cyclohexanone on copper-active sites in oxidation state Cu^0 and Cu^+*. J. Catal. 222 (2004) 545-557.

Chapter 11

Sustainable Production of γ-Butyrolactone from Succinic Acid and Formic Acid over Cu/SiO_2

Previous chapter has established conversion of biomass-derived furfural to furfuryl alcohol by coupling with 2-butanol dehydrogenation. This chapter studies the feasibility of coupling two renewable feedstocks, succinic acid and formic acid, for sustainable production of γ-butyrolactone.

11.1 Introduction

Global energy security and the environmental impacts of fuel and chemical production have provided the impetus for the use of biomass as a renewable feedstock [11.1]. Carboxylic (*e.g.* lactic [11.2], succinic [11.3], itaconic [11.4] and levulinic [11.5]) acids derived from lignocellulose biomass have been identified as a priority building blocks for the production of commodity chemicals [11.6]. Succinic acid, generated *via* fermentation or enzymatic hydrolysis of lignocellulose [11.3], can serve as a replacement for conventional petroleum-based maleic acid (produced from butane oxidation [11.7]) used in the synthesis of γ-butyrolactone. The latter is a high value chemical employed as solvent, flavouring and feedstock in the manufacture of pyrrolidones [11.8]. Hydrogenation of succinic acid has been predominantly conducted over supported metals (Pd, Ru and Re) in liquid phase at elevated pressure (60-150 bar) [11.9-11.13]. There have been no reported continuous gas phase operation, which can present immediate benefits in terms of higher throughout [11.14]. Supported Pd (on TiO_2 [11.9] and Al_2O_3 [11.10]) has delivered the highest (up to 95%) selectivity to γ-butyrolactone from the reduction-esterification of succinic acid (**Fig. 11.1**, step **(I)**). Butyric acid (*via* hydrogenolysis, step **(II)**) and/or propanoic acid (*via* hydrodecarbonylation or decarboxylation, steps **(III)** and **(IV)**) are formed as by-products. Palladium on SiO_2 has been reported to deliver higher catalytic activity than Pd/C and Pd/TiO_2 in the gas phase hydrogenation of propanoic acid [11.15]. But there are no published reports relating to succinic acid hydrogenation. Reaction over Ru-C composite [11.11] and Re/C [11.12] promoted further hydrogenloysis of γ-butyrolactone to tetrahydrofuran (step **(V)**) as principal product (selectivity = 40-50%). Bimetallic catalysts ($Pd-Re/TiO_2$ [11.13] and Ru-Re/C [11.16]) facilitated reduction of

both carboxyl groups (selectivity = 62-83%) to give 1,4-butanediol (step **(VI)**). Although high selectivity to γ-butyrolactone has been achieved over supported Pd, reaction exclusivity remains a challenge.

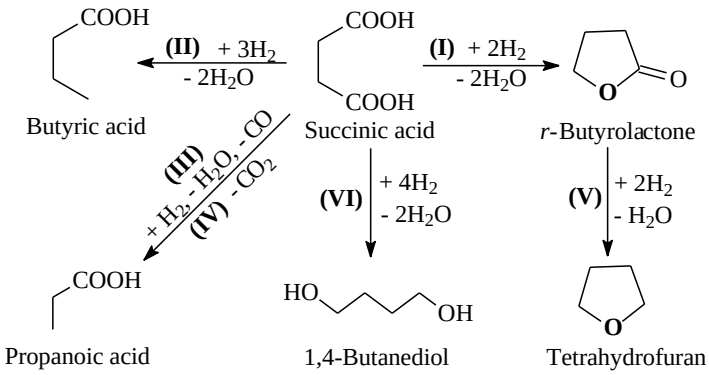

Fig. 11.1: Reaction pathway for the hydrogenation of succinic acid to γ-butyrolactone, butyric acid, propanoic acid, tetrahydrofuran and 1,4-butanediol.

The work to date on succinic acid hydrogenation has employed pressurised hydrogen (up to 150 bar) under conditions far in excess to the stoichiometric requirements. Issues associated with process safety and sustainability call for alternative sources of hydrogen. One possible solution is the use of hydrogen donors in transfer hydrogenation reactions which has been explored in organic synthesis by homogeneous catalysis [11.17-11.19]. This alternative has clear benefits in terms of transportation, storage and handling [11.20] although separation/purification steps to isolate the final target product and facilitate catalyst reuse are decided drawbacks. Recourse to heterogeneous catalysis can circumvent this limitation and we consider here a continuous system that combines a catalytic step to release hydrogen that is utilised in the selective conversion of succinic acid to γ-butyrolactone. Continuous gas phase operation have predominantly focused on coupling (alcohols) dehydrogenation with (olefins and carbonyl compound) hydrogenation [11.21,11.22]. This option is not feasible in this instance due to the facile esterification of alcohols with carboxyl acids [11.23]. Decomposition of formic acid, a by-product of biorefinery processes [11.24], can be used as a source of hydrogen [11.25]. Coupling of formic acid decomposition and hydrogenation has not been studied to any significant extent and a search through literature has served to identify studies on formic acid coupling with phenol [11.26] and ethylene/propylene [11.20] hydrogenation. We have investigated the gas phase hydrogenation of succinic acid to γ-butyrolactone over Pd/SiO_2, comparing the catalytic response with that of silica supported Ni and Cu that have exhibited high activity in gas

phase selective reduction of carboxylic acids [11.27,11.28]. The feasibility of coupling formic acid decomposition with selective hydrogenation (in N_2) is also addressed with an assessment of hydrogen utilisation efficiency relative to conventional operation using pressurised hydrogen.

11.2 Experimental

11.2.1 Catalyst Preparation

Silica supported Cu was prepared by deposition-precipitation with NaOH (Riedel-de Haën, 99%). Fumed SiO_2 and $Cu(NO_3)_2$ were supplied by Sigma Aldrich and used as received. The silica powder (20 g) was dispersed in an aqueous solution of $Cu(NO_3)_2$ (200 cm^3, 0.25 M). The suspension was stirred (600 rpm) at ambient temperature for 1 h, followed by addition of aqueous NaOH (2 M) until pH >10 to ensure copper deposition (as $Cu(OH)_2$), heated to 353 K in air and aged under vigorous stirring for 4 h [11.29]. The solid was separated by filtration, washed with distilled water (until pH = 7) and dried at 393 K overnight. The anhydrous sample was calcined in air (at 10 K min^{-1} to 723 K for 4 h) to generate supported copper oxide (CuO) [11.29]. Silica supported Pd and Ni were prepared by impregnation following the procedure described in detail elsewhere [11.30,11.31]. The catalyst precursors were sieved (ATM fine test sieves) to mean particle diameter = 75 μm and activated in 60 cm^3 min^{-1} H_2 at 4-10 K min^{-1} to 543-720 K, which was maintained for 1-2 h. Samples were passivated at ambient temperature in 1% v/v O_2/He for *ex situ* characterisation.

11.2.2 Catalyst Characterisation

Metal loading was determined by atomic absorption spectroscopy using a Shimadzu AA-6650 spectrometer with an air-acetylene flame from the diluted extract in aqua regia (25% v/v HNO_3/HCl). Temperature programmed reduction (TPR), H_2 (>99.98%, BOC) chemisorption and specific surface area (SSA) measurements were conducted on the CHEM-BET 3000 (Quantachrome Instrument) unit with data acquisition/ manipulation using the TPR Win^{TM} software. Samples were loaded into a U-shaped Pyrex glass cell (3.76 mm i.d.) and heated in 17 cm^3 min^{-1} (Brooks mass flow controlled) 5% v/v H_2/N_2 at 4-10 K min^{-1} to 543-720 K, swept with 65 cm^3 min^{-1} N_2 (>99.98%, BOC) for 1.5 h, cooled to reaction temperature (543 K) and subjected to H_2 chemisorption by pulse (10 μl) titration. There was no measurable H_2 uptake on the

SiO_2 support alone. The effluent gas passed through a liquid N_2 trap and H_2 consumption was monitored by a thermal conductivity detector (TCD). SSA (reproducible to ±8%) was recorded in 30% v/v N_2/He using N_2 as internal standard. At least three cycles of N_2 adsorption-desorption were employed using the standard single point BET method. Powder X-ray diffractograms (XRD) were recorded on a Bruker/Siemens D500 incident X-ray diffractometer using Cu Kα radiation. Samples were scanned at 0.01º $step^{-1}$ over the range $30º \leq 2\theta \leq 85º$ and the diffractograms identified against the JCPDS-ICDD reference (Pd (05-0681), Ni (04-0850) and Cu (04-0836)). Metal crystallite size was estimated from the Scherer equation assuming negligible contribution of strain and instrumental broadening to reflection width

$$d_{XRD} = \frac{K \times \lambda}{\beta \times \cos\theta} \qquad \textbf{(11.1)}$$

where $K = 0.9$, λ is the incident irradiation wavelength (1.54056 Å), β is the peak width at half the maximum intensity and θ represents the diffraction angle corresponding to the (111) plane. Metal particle morphology (size and shape) post-TPR was examined by electron microscopy (TEM/STEM, JEOL JEM-ARM200cF), employing Gatan Digital Micrograph 3.4 for data acquisition/manipulation. Samples for analysis were prepared by dispersion in acetone and deposited on a holey carbon/Cu grid (300 Mesh). Surface area weighted mean metal size ($d_{(S)TEM}$) [11.32] was based on a count of up to 300 particles.

11.2.3 Catalytic Procedure

Succinic acid (Sigma Aldrich, 99%) hydrogenation and formic acid (Sigma Aldrich, ≥98%) decomposition were conducted at atmospheric pressure *in situ* after catalyst activation in a continuous flow fixed bed vertical tubular glass reactor (i.d. = 15 mm) at 513-543 K. A layer of borosilicate glass beads served as preheating zone where the reactant(s) was (were) vaporised and reached reaction temperature before contacting the catalyst bed. Isothermal conditions (±1 K) were maintained by diluting the catalyst bed with ground glass (75 μm); the ground glass was mixed thoroughly with the catalyst before insertion into the reactor. Reaction temperature was continuously monitored by a thermocouple inserted in a thermowell within the catalyst bed. The reactant(s) as aqueous solution was (were) delivered to the reactor *via* a glass/teflon air-tight syringe and teflon line using a microprocessor controlled infusion pump (Model 100 kd Scientific). Succinic acid hydrogenation was conducted in a co-current flow of H_2 (*GHSV*

= 5 × 10^3 h^{-1}, molar metal to reactant (succinic acid, formic acid or mixed succinic acid + formic acid) feed rate (n_{metal}/F) = 5.9 × 10^{-3} – 9.8 × 10^{-1} h) or in N_2 with formic acid (*GHSV* = 1.2 × 10^3 h^{-1}, n_{Cu}/F = 1.5 × 10^{-1} h). Formic acid decomposition was carried out in N_2 (*GHSV* = 1.0 × 10^4 h^{-1}, n_{Cu}/F = 1.0 × 10^{-3} – 6.0 × 10^{-3} h). In blank tests, passage of succinic acid in H_2 through the empty reactor or over the (SiO_2) support alone did not result in any detectable conversion. Conversion <7% of formic acid in N_2 through the empty reactor was observed due to thermal decomposition [11.33]. The reactor effluent was condensed in a liquid nitrogen trap. Products (γ-butyrolactone, 1,4-butanediol, tetrahydrofuran, butyric acid and propanoic acid, Sigma Aldrich, ≥99%) were analysed by gas chromatography (Perkin-Elmer Auto System XL) employing a flame ionisation detector (FID) and a Stabilwax (50 m × 0.32 mm i.d., 0.25 μm film thickness) capillary column. Analysis of succinic and formic acid was performed by high performance liquid chromatography (HP-1100) with UV detection (λ_{max} = 204 nm) and a C18 column (250 mm × 4.6 mm i.d.) with methanol (25%) and water (75%) as mobile phase at a flow rate of 1 cm^3 min^{-1}. Data acquisition and manipulation were performed using the TotalChrom Workstation 2 and Agilent ChemStation. Reactant (i) conversion (*X*) is defined by

$$X_i\,(\%) = \frac{[reactant]_{i,\,in} - [reactant]_{i,\,out}}{[reactant]_{i,\,in}} \times 100 \qquad \textbf{(11.2)}$$

and selectivity (*S*) to product (j) is given by

$$S_j(\%) = \frac{[product]_{j,\,out}}{[reactant]_{i,\,in} - [reactant]_{i,\,out}} \times 100 \qquad \textbf{(11.3)}$$

where the subscripts "in" and "out" refer to the inlet and outlet gas streams, respectively. Initial conversion and turnover frequency (*TOF*) were obtained from time on-stream measurement described in detail elsewhere [11.34]. The applicability of a pseudo-first order kinetic treatment has been established for carboxyl (benzoic) acid hydrogenation [11.35] and formic acid decomposition [11.20] and was used in this study to extract rate constants (*k*, h^{-1}). Repeated reactions with different samples from the same batch of catalyst delivered raw data reproducibility to within ±5 %.

11.3 Results and Discussion

11.3.1 Pd/SiO_2: Characterisation and Application in Succinic Acid Hydrogenation

TPR of Pd/SiO_2 (**Fig. 11.2(A)**) generated a negative signal with a peak maximum (T_{max}) at 362 K. This can be attributed to H_2 release in the decomposition of Pd hydride,

in accordance with that (343-377 K) reported for supported Pd [11.36]. Hydride composition in terms of H/Pd ratio (= 0.45 mol mol^{-1}) falls within the range (0.35-0.50) reported for silica supported Pd [11.37]. The absence of (a positive) H_2 consumption peak

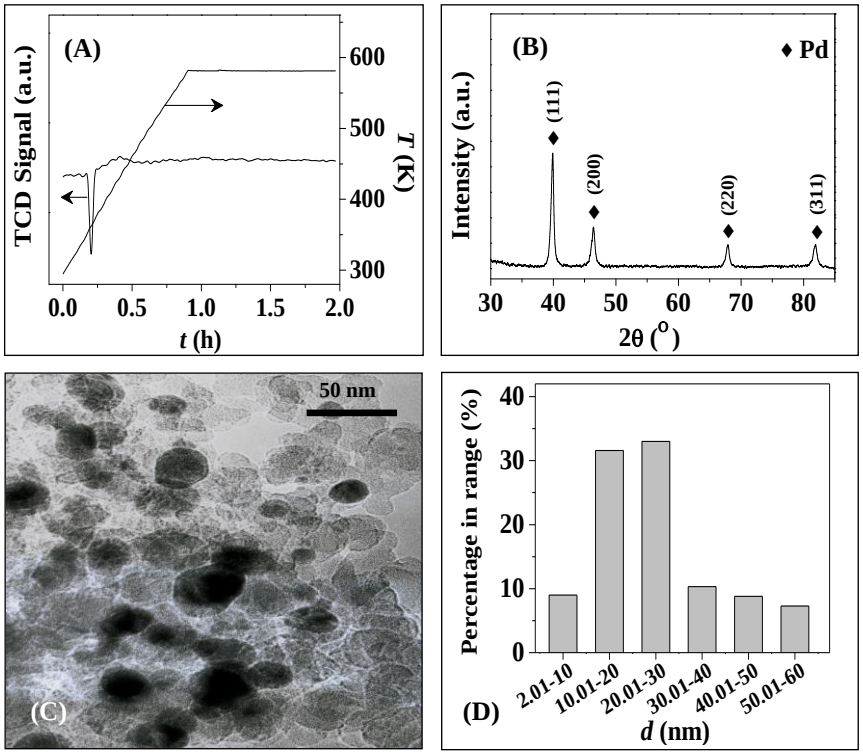

Fig. 11.2: (A) TPR profile, (B) XRD pattern, (C) representative TEM image and (D) associated Pd particle size distribution histogram for Pd/SiO_2.

Table 11.1: Metal loading, specific surface area (SSA), temperature maxima (T_{max}) and associated H_2 consumption during TPR, mean metal size from electron microscopy ($d_{(S)TEM}$) and XRD (d_{XRD}) analysis and H_2 chemisorption at 543 K for SiO_2 supported Pd, Ni and Cu.

Catalyst	Loading (w/w %)	SSA (m^2 g^{-1})	TPR T_{max} (K)	TPR H_2 consumption (mmol g^{-1})	$d_{(S)TEM}$ (nm)	d_{XRD} (nm)	H_2 uptake (μmol g^{-1})
Pd/SiO_2	5	191	362[a]	-	36	33	35
Ni/SiO_2	20	198	616	3.2/3.4[b]	13	12	8
Cu/SiO_2	20	185	543	3.0/3.1[b]	9	8	2

[a] T_{max} associated Pd hydride decomposition; [b]theoretical value for $Ni^{2+} \rightarrow Ni^0$ and $Cu^{2+} \rightarrow Cu^0$.

suggests the presence of a metallic Pd phase prior to the thermal ramp [11.36]. The SSA of activated silica supported Pd (**Table 11.1**) is lower than the support (200 m^2 g^{-1}) and can be attributed to a partial pore filling during catalyst preparation [11.38]. XRD

analysis was employed to probe bulk structural characteristics and the diffractogram in **Fig. 11.2(B)** presents signals at 2θ = 39.9°, 46.4°, 67.9° and 81.9° assigned to Pd (111), (200), (220) and (311) planes where the corresponding *d* spacings (2.26, 1.96, 1.38 and 1.18) are consistent with an exclusive cubic Pd symmetry [11.38]. Standard line broadening analysis using the Scherrer formula yields a Pd particle size of 33 nm (**Table 11.1**). This is confirmed by TEM analysis where the supported metal phase exhibits pseudo-spherical morphology (**Fig. 11.2(C)**) with a broad size range (**Fig. 11.2(D)**) and a surface area weighted mean of 36 nm. Hydrogen chemisorption capacity is an important catalyst property in hydrogenation applications. The uptake over Pd/SiO_2 at reaction conditions (543 K) is shown in **Table 11.1**. We didn't find any hydrogen chemisorption measurement at 543 K over supported Pd. We can note the value was significantly greater than that (6 μmol g^{-1}) recorded previously at ambient temperature [11.38].

Table 11.2: Succinic acid (SA) turnover frequency (TOF_{SA}) and product (γ-butyrolactone (GBL), propanoic acid (PA) and 1,4-butanediol (BDO)) selectivity (S_j, %) for reaction (in H_2) over SiO_2 supported Pd, Ni and Cu; *Reaction conditions*: T = 543 K, P = 1 atm, X_{SA} = 22-28%.

Catalyst	TOF_{SA} (h^{-1})	S_{GBL} (%)	S_{PA} (%)	S_{BDO} (%)
Pd/SiO_2	1222	/	95	5
Ni/SiO_2	39	64	36	/
Cu/SiO_2	3	100	/	/

Succinic acid hydrogenation (using an external supply of H_2) rate over Pd/SiO_2 is shown in **Table 11.2**. The turnover frequency (*TOF*) was appreciably larger than that (3-5 h^{-1}) reported in batch liquid phase reaction (523 K, 100 bar) over silica supported Pd [11.39]. Product selectivity (S_j) is presented in **Fig. 11.3(A)** as a function of conversion, where propanoic acid was the principal (98% selectivity) product with trace amounts of 1,4-butanediol. This is indicative of a predominant decarbonylation and/or decarboxylation (**Fig. 11.1**, steps **(III)** and **(IV)**) and secondary reduction of both carboxyl groups (step **(VI)**). Selectivity invariance with conversion suggests reaction pathways to propanoic acid and 1,4-butanediol that proceed in parallel, as shown in **Fig. 11.1**. Supported Pd catalysts have been reported to promote direct decarboxylation (CO_2 release) and/or dehydroxylation-decarbonylation (H_2O and CO release) with loss of the

carboxyl function in the gas phase hydrogenation (T = 473-673 K) of fatty acids [11.40] and octanoic acid [11.41].

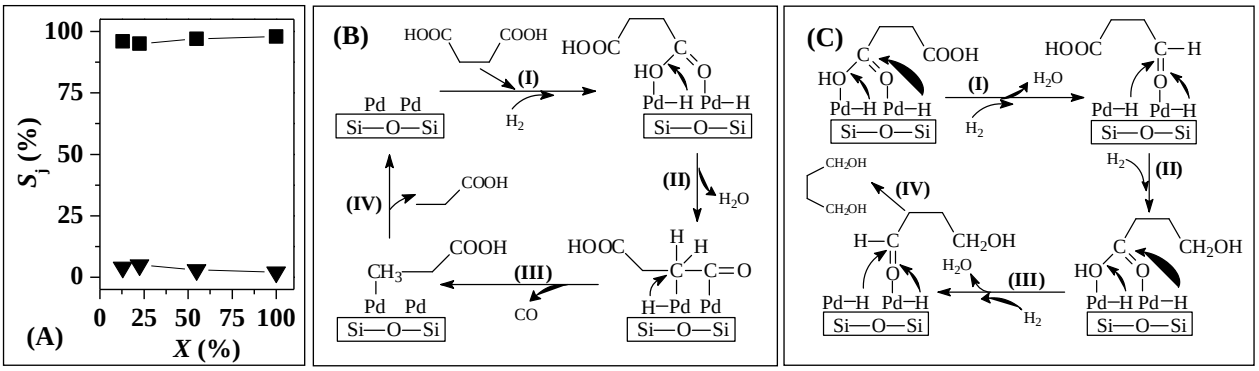

Fig. 11.3: (A) Product selectivity (S_j, ■: propanoic acid, ▼: 1,4-butanediol) as a function of succinic acid conversion (X) for reaction over Pd/SiO_2 and surface reaction mechanism for succinic acid to (B) propanoic acid and (C) 1,4-butanediol. *Reaction conditions*: T = 543 K, P = 1 atm.

In this study, we propose adsorption of the acid at surface Pd sites *via* carboxyl oxygen atoms that results in hydrogenolytic scission of −C−OH bond (dehydroxylation, **Fig. 11.3(B),** steps **(I)** and **(II)**) and subsequent interaction through carbonyl and alkyl carbons with hydrogen scission of the –C–C– bond (decarbonylation, step **(III)**) with desorption of propanoic acid (step **(IV)**). Heyden *et al.* [11.42] using DFT analysis to investigate the transformation of propanoic acid to ethane over Pd (111) established that dehydroxylation-decarbonylation is more favourable than decarboxylation. Reduction of both carboxyl groups to 1,4-butanediol can be explained by the surface reaction mechanism in **Fig. 11.3(C)**. Surface interaction is again through the carboxyl oxygens with partial reduction of carbonyl group to γ-hydroxybutyric acid *via* perpendicular adsorption through –C=O (**Fig. 11.3(C)**, steps **(I)** and **(II)**). Further reduction of the second carboxyl group (step **(III)**) generates 1,4-butanediol which desorbs from the catalyst (step **(IV)**). However, the perpendicular adsorption of –C=O on Pd is less favourable than the parallel configuration due to a facile interaction of the carbonyl π orbital with *d* electrons of Pd [11.43] with a consequent predominant decarbonylation to propanoic acid.

11.3.2 Ni/SiO_2: Characterisation and Application in Succinic Acid Hydrogenation

The TPR profile of Ni/SiO_2 (**Fig. 11.4(A)**) exhibits a reduction peak with T_{max} (= 616 K) within the range (605-643 K) reported for Ni/SiO_2 by Ermakova and Ermakov

which they ascribed to reduction of NiO to Ni [11.44]. Hydrogen consumption matched that required for NiO reduction and total surface area post-TPR was close to Pd/SiO_2 (**Table 11.1**). XRD analysis (**Fig. 11.4(B)**) revealed three diffraction signals at 2θ = 44.6°, 51.9° and 76.6° corresponding to Ni (111), (200) and (220) planes with no evidence of NiO (2θ = 37.1°, 43.1°, 62.6° and 75.1°, JCPDS-ICCD 71-1179) [11.45]. The representative STEM image (**Fig. 11.4(C)**) and associated particle size distribution histogram (**Fig. 11.4(D)**) show Ni particles in the range 4-24 nm with a surface area weighted mean (13 nm) that agrees with the size obtained from XRD (**Table 11.1**). Hydrogen chemisorption on Ni/SiO_2 was (four times) lower than that recorded on Pd/SiO_2 (**Table 11.1**), a result that can be attributed to the higher activation energy barrier for H_2 adsorption/dissociation on Ni [11.46,11.47].

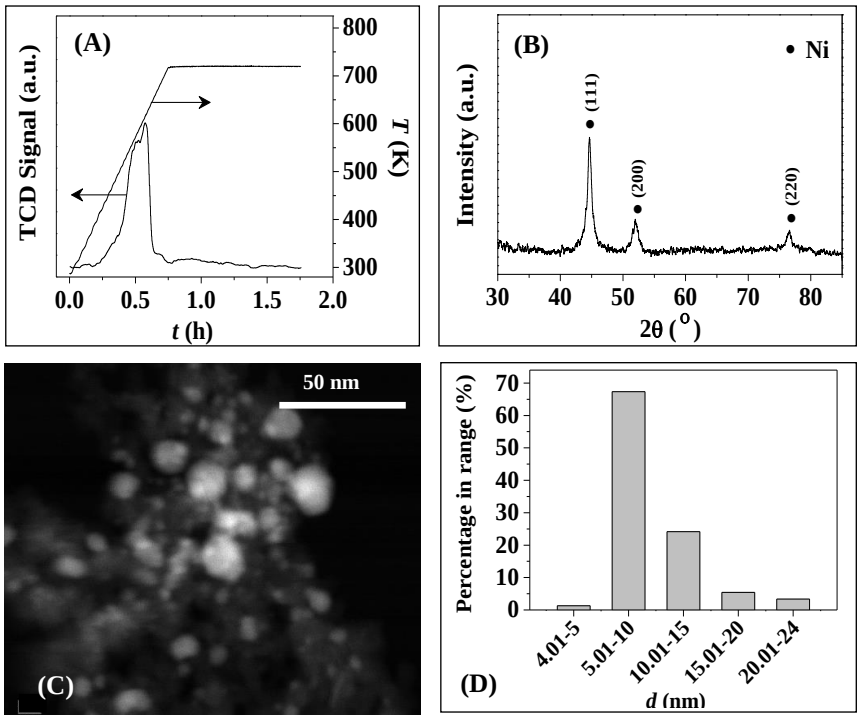

Fig. 11.4: (A) TPR profile, (B) XRD pattern, (C) representative STEM image and (D) associated Ni particle size distribution histogram for Ni/SiO_2.

Succinic acid turnover frequency (*TOF*) on Ni/SiO_2 (**Table 11.2**) was thirty times lower than Pd/SiO_2, which can be linked to the lower H_2 uptake capacity. In contrast to Pd/SiO_2, Ni/SiO_2 (**Fig. 11.5(A)**) promoted preferential formation of γ-butyrolactone (66% selectivity) with propanoic acid (34% selectivity) as secondary product. Product distribution was constant with conversion, demonstrating mutually exclusive routes to γ-butyrolactone and propanoic acid. In the case of propanoic acid, a similar mechanism (to that shown in **Fig. 11.3(B)**) can also apply here. The formation of γ-butyrolactone can

proceed by surface interaction with Ni sites *via* the hydroxyl function with the formation of γ-hydroxybutyric acid as a reactive intermediate (**Fig. 11.5(B)**, steps **(I)-(III)**) and that undergoes cyclisation-esterification to generate the lactone (step **(IV)**). Esterification can be promoted at Brønsted sites on the support [11.48]. No detectable 1,4-butanediol can be linked to lower surface reactive hydrogen over Ni/SiO_2 could inhibit reduction of γ-hydroxybutyric acid.

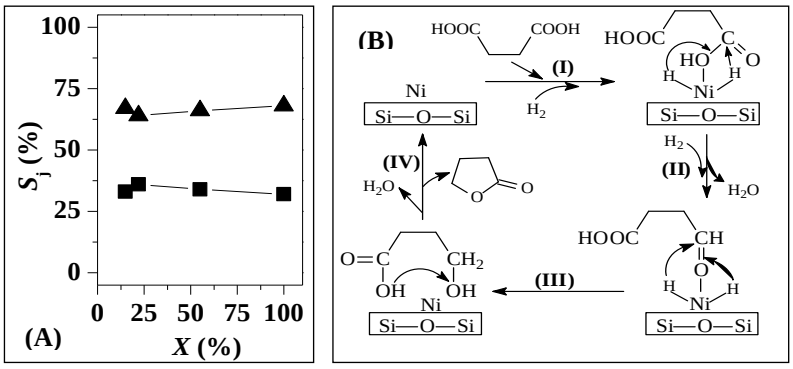

Fig. 11.5: (A) Product selectivity (S_j, ■: propanoic acid, ▲: γ-butyrolactone) as a function of succinic acid conversion (X) for reaction over Ni/SiO_2 and (B) surface reaction mechanism for succinic acid to γ-butyrolactone. *Reaction conditions*: T = 543 K, P = 1 atm.

11.3.3 Cu/SiO_2: Characterisation and Application in Succinic Acid Hydrogenation

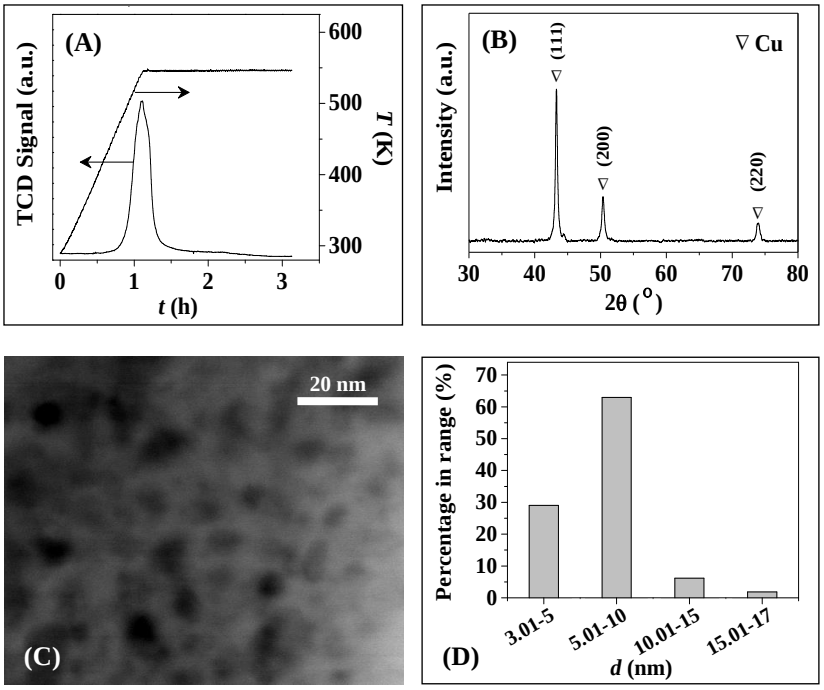

Fig. 11.6: (A) TPR profile, (B) XRD pattern, (C) representative TEM image and (D) associated Cu particle size distribution histogram for Cu/SiO_2.

TPR of Cu/SiO_2 (**Fig. 11.6(A)**) generated a single peak with T_{max} at the final isothermal hold (543 K) where H_2 consumed is consistent with the reduction of CuO to Cu (**Table 11.1**). Smith and co-workers [11.49] applied *in situ* XRD to study the reduction of Cu/SiO_2 and proposed a stepwise $Cu^{2+} \rightarrow Cu^{+} \rightarrow Cu^{0}$ where metallic copper prevailed at $T > 523$ K. Cu/SiO_2 post-TPR showed a total surface area close to Pd/SiO_2 and Ni/SiO_2 (**Table 11.1**). The XRD pattern (**Fig. 11.6(B)**) exhibits diffraction peaks at $2\theta = 43.1°$, 50.2° and 73.8° that match the Cu (111), (200) and (220) planes. There were no signals due to bulk copper oxides (tenorite (CuO), $2\theta = 35.5°$, 38.7° and 48.7° JCPDS-ICCD (05-0661) or cuprite (Cu_2O), $2\theta = 36.6°$ (05-0667)). The representative TEM image (**Fig. 11.6(C)**) illustrates Cu dispersion with particles in the 3-17 nm (**Fig. 11.6(D)**) and a mean that matches the XRD measurement (**Table 11.1**). Hydrogen uptake on Cu/SiO_2 was measurably lower than that recorded for Pd/SiO_2 and Ni/SiO_2 (**Table 11.1**). Borgschulte *et al.* reported the same sequence of decreasing H_2 chemisorption (Pd > Ni > Cu) with an order of magnitude difference in uptake [11.46]. Hydrogen adsorption/dissociation on metals depends on the filling of *d*-orbital and bandwidth [11.50]. The lower adsorption capacity of Cu/SiO_2 can be attributed to the filled *d* band that limits H_2 chemisorption with a low binding strength of dissociated hydrogen atoms on Cu [11.51,11.52].

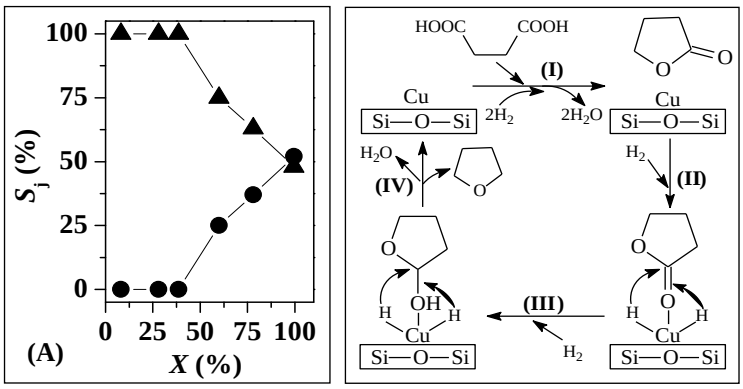

Fig. 11.7: (A) Product selectivity (S_j, ▲: γ-butyrolactone, ●: tetrahydrofuran) as a function of succinic acid conversion (X) for reaction over Cu/SiO_2 and (B) surface reaction mechanism for succinic acid to tetrahydrofuran. *Reaction conditions*: T = 543 K, P = 1 atm.

Reaction over Cu/SiO_2 (**Table 11.2**) delivered an appreciably lower reaction rate than Pd/SiO_2 and Ni/SiO_2. In contrast to supported Pd and Ni, full selectivity to γ-butyrolactone was achieved over Cu/SiO_2 at conversions <40% (**Fig. 11.7(A)**), *i.e.* exclusive reduction-esterification (succinic acid → γ-hydroxybutyric acid → γ-butyrolactone). This is the first report of 100% selectivity to γ-butyrolactone in the

hydrogenation of succinic acid. This can be attributed to the critical selective activation/reduction of carbonyl group to γ-hydroxybutyric acid *via* perpendicular interaction through the carbonyl oxygen atom, which has been demonstrated as the preferential adsorption mode of carbonyl compounds on Cu/SiO_2 [11.53]. The low availability of surface reactive hydrogen on Cu/SiO_2 may suppress reduction of γ-hydroxybutyric acid to 1,4-butanediol. A decrease in γ-butyrolactone selectivity at higher conversions was accompanied by the generation of tetrahydrofuran with a near equimolar product mixture at full conversion. This is consistent with a sequential reaction pathway with γ-butyrolactone as reactive intermediate (**Fig. 11.1**, steps **(I)** and **(V)**). Followed by succinic acid conversion to γ-butyrolactone (**Fig. 11.7(B)**, step **(I)**) where surface reaction mechanism is similar to that shown in **Fig. 11.5(B)**, γ-butyrolactone is adsorbed on Cu sites *via* perpendicular interaction of the carbonyl oxygen atom (step **(II)**) with hydrogenolysis to tetrahydrofuran (steps **(III)** and **(IV)**).

11.3.4 Cu/SiO_2: Coupled Formic Acid Decomposition with Succinic Acid Hydrogenation

Reaction exclusivity to γ-butyrolactone over Cu/SiO_2 was maintained in the 513-543 K temperature range to give an apparent activation energy of 99 kJ mol^{-1} from the Arrhenius plot in **Fig. 11.8**. This is similar to that (108 kJ mol^{-1}) reported for reaction over Ru-Re/C in batch liquid phase operation [11.54]. Hydrogenation was conducted in

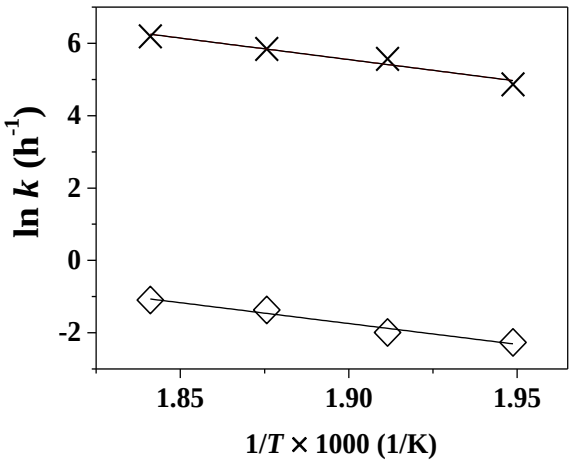

Fig. 11.8: Arrhenius plots for the stand-alone hydrogenation of succinic acid (◇) and catalytic decomposition of formic acid (×) over Cu/SiO_2. *Reaction conditions*: T = 513-543 K, P = 1 atm.

excess H_2 and the utilisation efficiency, expressed in terms of the mol ratio of H_2 supply

to the lactone generated (= 1200), was appreciably greater than the stoichiometric requirement for lactone production (= 2). Hydrogen utilisation is a crucial sustainability consideration in this hydrogenation process. The catalytic decomposition of formic acid can serve as an alternative hydrogen source where the Arrhenius plot for reaction over Cu/SiO_2 included in **Fig. 11.8** exhibits an activation energy of 97 kJ mol^{-1} that is equivalent to the value (100 kJ mol^{-1}) reported elsewhere [11.55] for reaction over (SiO_2 and Al_2O_3) supported Cu. A prerequisite for effective coupling of formic acid decomposition with succinic acid hydrogenation is that the former proceeds at a greater rate to ensure a sufficient supply of hydrogen. As demonstrated in **Fig. 11.8**, this requirement is met with four orders of magnitude higher H_2 production (from formic acid) relative to H_2 consumption in "stand-alone" γ-butyrolactone production.

Table 11.3: Formic acid (FA) (TOF_{FA}) and succinic acid (SA) (TOF_{SA}) turnover frequency and H_2 utilisation (mol ratio of H_2 generated to γ-butyrolactone (GBL) formed) in coupled formic acid decomposition and succinic acid hydrogenation over Cu/SiO_2; *Reaction conditions*: P = 1 atm, inlet FA/SA = 50.

T (K)	TOF_{FA} (h^{-1})	TOF_{SA} (h^{-1})	H_2 /GBL
513	170	0.03	1530
543	196	0.2	340

Coupling formic acid decomposition with succinic acid hydrogenation (in N_2) over Cu/SiO_2 generated the *TOFs* presented in **Table 11.3** at two representative temperatures (513 and 543 K). The coupled reaction generated γ-butyrolactone as the sole product, demonstrating successful "borrowing" of hydrogen released in formic acid decomposition with an "auto-transfer" in the selective lactone production. Formic acid decomposition over (carbon) supported Pd has been proposed to generate transitory Pd-H that can promote gas phase hydrogenation of ethylene/propylene (358-473 K) [11.20]. A similar effect may apply here where formic acid decomposition over Cu supplies reactive hydrogen (Cu-H) for succinic acid hydrogenation. Moreover, Gao *et al*. [11.56] studied the hydrogenation of maleic anhydride to γ-butyrolactone over (Al_2O_3, ZrO_2 and ZnO) supported Cu (513-573 K) using ethanol as hydrogen source and obtained ethyl acetate, *n*-butanol (from hydrogenolysis and ring-opening of maleic anhydride) and diethyl succinate (from cross reaction of ethanol and maleic anhydride) as major products. Our results demonstrate formic acid serves as effective hydrogen

source for selective hydrogenation of succinic acid (to γ-butyrolactone) and circumvents cross reaction, which is advancement over the existing study using alcohol as hydrogen donor. The exclusive production of γ-butyrolactone achieved in our work employing formic acid circumvents downstream separation/purification unit operations as the target lactone is readily extracted as liquid product. Higher reaction temperature (513 K → 543 K) resulted in increased γ-butyrolactone production rate (**Table 11.3**) due to facilitated formic acid decomposition with greater hydrogen generation. Although γ-butyrolactone formation rate (at 543 K) in the coupled system was lower relative to the conventional stand-alone hydrogenation using external pressurised hydrogen (**Table 11.2**), H_2 utilisation was improved significantly (by a factor of three).

11.4 Conclusion

The results presented establish the viability of *in situ* hydrogen generation *via* the catalytic decomposition of formic acid and direct utilisation in selective succinic acid hydrogenation for the production of γ-butyrolactone. Silica supported Cu favoured exclusive lactone formation in both stand-alone hydrogenation (using external H_2) and reaction coupling with formic acid decomposition (in N_2). Tetrahydrofuran was detected at higher conversion (>40%) over Cu/SiO_2 due to hydrogenolysis of γ-butyrolactone. Reaction over Pd/SiO_2 and Ni/SiO_2 promoted dehydoxylation-decarbonylation to propanoic acid at higher reaction rates that can be linked to carboxyl/carbonyl adsorption mode and greater H_2 chemisorption capacity. 1,4-butanediol was a secondary product over Pd/SiO_2 with γ-butyrolactone as principal product on Ni/SiO_2. Coupled reaction over Cu/SiO_2 exhibited improved H_2 utilisation efficiency relative to conventional hydrogenation. This opens new possibilities for sustainable "hydrogen free" hydrogenation processes to deliver commercially important chemicals using renewable feedstock.

11.5 References

[11.1] B. Gabrielle, L. Bamière, N. Caldes, S. De-Cara, G. Decocq, F. Ferchaud, C. Loyce, E. Pelzer, Y. Pérez, J. Wohlfahrt, G. Richard, *Paving the way for sustainable bioenergy in Europe: Technological options and research avenues for large-scale biomass feedstock supply*. Renew. Sust. Energ. Rev. 33 (2014) 11-25.

[11.2] M.A. Abdel-Rahman, Y. Tashiro, K. Sonomoto, *Lactic acid production from lignocellulose-derived sugars using lactic acid bacteria: Overview and limits*. J. Biotechnol. 156 (2011) 286-301.

[11.3] J. Akhtar, A. Idris, R.A. Aziz, *Recent advances in production of succinic acid from lignocellulosic biomass*. Appl. Microbiol. Biotechnol. 98 (2014) 987-1000.

[11.4] T. Klement, J. Buchs, *Itaconic acid: A biotechnological process in change*. Bioresour. Technol. 135 (2013) 422-431.

[11.5] D.W. Rackemann, W.O.S. Doherty, *The conversion of lignocellulosics to levulinic acid*. Biofuel. Bioprod. Biorefin. 5 (2011) 198-214.

[11.6] R.A. Sheldon, J.P.M. Sanders, *Toward concise metrics for the production of chemicals from renewable biomass*. Catal. Today 239 (2015) 3-6.

[11.7] B. Chen, E.J. Munson, *Investigation of the mechanism of n-butane oxidation on vanadium phosphorus oxide catalysts: Evidence from isotopic labeling studies*. J. Am. Chem. Soc. 124 (2002) 1638-1652.

[11.8] C. Delhomme, D. Weuster-Botz, F.E. Kuehn, *Succinic acid from renewable resources as a C_4 building-block chemical: A review of the catalytic possibilities in aqueous media*. Green Chem. 11 (2009) 13-26.

[11.9] B. Tapin, F. Epron, C. Especel, B.K. Ly, C. Pinel, M. Besson, *Study of monometallic Pd/TiO_2 catalysts for the hydrogenation of succinic acid in aqueous phase*. ACS Catal. 3 (2013) 2327-2335.

[11.10] U.G. Hong, S. Hwang, J.G. Seo, J. Lee, I.K. Song, *Hydrogenation of succinic acid to gamma-butyrolactone (GBL) over palladium catalyst supported on alumina xerogel: Effect of acid density of the catalyst*. J. Ind. Eng. Chem. 17 (2011) 316-320.

[11.11] U.G. Hong, J.K. Kim, J. Lee, J.K. Lee, J.H. Song, J. Yi, I.K. Song, *Hydrogenation of succinic acid to tetrahydrofuran (THF) over ruthenium-carbon composite (Ru-C) catalyst*. Appl. Catal. A: Gen. 469 (2014) 466-471.

[11.12] U.G. Hong, H.W. Park, J. Lee, S. Hwang, J. Yi, I.K. Song, *Hydrogenation of succinic acid to tetrahydrofuran (THF) over rhenium catalyst supported on H_2SO_4-treated mesoporous carbon*. Appl. Catal. A: Gen. 415 (2012) 141-148.

[11.13] B.K. Ly, D.P. Minh, C. Pinel, M. Besson, B. Tapin, F. Epron, C. Especel, *Effect of addition mode of Re in bimetallic Pd-Re/TiO_2 catalysts upon the selective aqueous-phase hydrogenation of succinic acid to 1,4-butanediol*. Top. Catal. 55 (2012) 466-473.

[11.14] R.J. Giraud, P.A. Williams, A. Sehgal, E. Ponnusamy, A.K. Phillips, J.B. Manley, *Implementing green chemistry in chemical manufacturing: A survey report*. ACS Sustain. Chem. Eng. 2 (2014) 2237-2242.

[11.15] Y.K. Lugo-José, J.R. Monnier, C.T. Williams, *Gas-phase, catalytic hydrodeoxygenation of propanoic acid, over supported group VIII noble metals: Metal and support effects*. Appl. Catal. A: Gen. 469 (2014) 410-418.

[11.16] D.P. Minh, M. Besson, C. Pinel, P. Fuertes, C. Petitjean, *Aqueous-phase hydrogenation of biomass-based succinic acid to 1,4-butanediol over supported bimetallic catalysts*. Top. Catal. 53 (2010) 1270-1273.

[11.17] C. Zheng, S.L. You, *Transfer hydrogenation with Hantzsch esters and related organic hydride donors*. Chem. Soc. Rev. 41 (2012) 2498-2518.

[11.18] T. Ikariya, A.J. Blacker, *Asymmetric transfer hydrogenation of ketones with bifunctional transition metal-based molecular catalysts*. Acc. Chem. Res. 40 (2007) 1300-1308.

[11.19] M. Rueping, A.R. Antonchick, T. Theissmann, *A highly enantioselective Brønsted acid catalyzed cascade reaction: Organocatalytic transfer hydrogenation of quinolines and their application in the synthesis of alkaloids*. Angew. Chem. Int. Edit. 45 (2006) 3683-3686.

[11.20] D.A. Bulushev, J.R.H. Ross, *Vapour phase hydrogenation of olefins by formic acid over a Pd/C catalyst*. Catal. Today 163 (2011) 42-46.

[11.21] F. Alonso, P. Riente, M. Yus, *Nickel nanoparticles in hydrogen transfer reactions*. Acc. Chem. Res. 44 (2011) 379-391.

[11.22] B.M. Nagaraja, A.H. Padmasri, B.D. Raju, K.S.R. Rao, *Production of hydrogen through the coupling of dehydrogenation and hydrogenation for the synthesis of cyclohexanone and furfuryl alcohol over different promoters supported on Cu-MgO catalysts*. Int. J. Hydrogen Energ. 36 (2011) 3417-3425.

[11.23] S.R. Kirumakki, N. Nagaraju, K.V. Chary, *Esterification of alcohols with acetic acid over zeolites Hβ, HY and HZSM-5*. Appl. Catal. A: Gen. 299 (2006) 185-192.

[11.24] J.Z. Zhang, M. Sun, X. Liu, Y. Han, *Catalytic oxidative conversion of cellulosic biomass to formic acid and acetic acid with exceptionally high yields*. Catal. Today 233 (2014) 77-82.

[11.25] B. Loges, A. Boddien, F. Gartner, H. Junge, M. Beller, *Catalytic generation of hydrogen from formic acid and its derivatives: Useful hydrogen storage materials*. Top. Catal. 53 (2010) 902-914.

[11.26] D.M. Zhang, F.Y. Ye, T. Xue, Y.J. Guan, Y.M. Wang, *Transfer hydrogenation of phenol on supported Pd catalysts using formic acid as an alternative hydrogen source*. Catal. Today 234 (2014) 133-138.

[11.27] D. Lee, S.I. Cho, G.J. Kim, H. Kim, I.M. Lee, *Efficient and selective hydrogenation of carboxylic acid catalyzed by Ni or Pd on ZSM-5*. J. Ind. Eng. Chem. 13 (2007) 1067-1075.

[11.28] Y. Kitayama, M. Muraoka, M. Takahashi, T. Kodama, H. Itoh, E. Takahashi, M. Okamura, *Catalytic hydrogenation of linoleic acid on nickel, copper, and palladium*. J. Am. Oil Chem. Soc. 73 (1996) 1311-1316.

[11.29] Z. Huang, F. Cui, J. Xue, J. Zuo, J. Chen, C. Xia, *Cu/SiO_2 catalysts prepared by hom- and heterogeneous deposition-precipitation methods: Texture, structure, and catalytic performance in the hydrogenolysis of glycerol to 1,2-propanediol*. Catal. Today 183 (2012) 42-51.

[11.30] G. Pina, C. Louis, M.A. Keane, *Nickel particle size effects in catalytic hydrogenation and hydrodechlorination: Phenolic transformations over nickel/silica*. Phys. Chem. Chem. Phys. 5 (2003) 1924-1931.

[11.31] S.G. Shore, E.R. Ding, C. Park, M.A. Keane, *Vapor phase hydrogenation of phenol over silica supported Pd and Pd-Yb catalysts*. Catal. Commun. 3 (2002) 77-84.

[11.32] M. Li, Y. Hao, H.H.P. Yiu, F. Cárdenas-Lizana, M.A. Keane, *"Hydrogen-free" production of 2-butanone and aniline over Cu/SiO_2 via reaction coupling*. Top. Catal. 58 (2015) 149-158.

[11.33] S. Inaba, *Theoretical study of water cluster catalyzed decomposition of formic acid*. J. Phys. Chem. A 118 (2014) 3026-3038.

[11.34] M. Li, X. Wang, N. Perret, M.A. Keane, *Enhanced production of benzyl alcohol in the gas phase continuous hydrogenation of benzaldehyde over Au/Al_2O_3*. Catal. Commun. 46 (2014) 187-191.

[11.35] N. Perret, X. Wang, J.J. Delgado, G. Blanco, X. Chen, C.M. Olmos, S. Bernal, M.A. Keane, *Selective hydrogenation of benzoic acid over Au supported on CeO_2 and $Ce_{0.62}Zr_{0.38}O_2$: Formation of benzyl alcohol*. J. Catal. 317 (2014) 114-125.

[11.36] F. Cárdenas-Lizana, Y. Hao, M. Crespo-Quesada, I. Yuranov, X. Wang, M.A. Keane, L. Kiwi-Minsker, *Selective gas phase hydrogenation of p-chloronitrobenzene over Pd catalysts: Role of the support*. ACS Catal. 3 (2013) 1386-1396.

[11.37] M. Bonarowska, J. Pielaszek, W. Juszczyk, Z. Karpiński, *Characterization of Pd-Au/SiO_2 catalysts by X-ray diffraction, temperature-programmed hydride decomposition, and catalytic probes*. J. Catal. 195 (2000) 304-315.

[11.38] S. Jujjuri, E. Ding, S.G. Shore, M.A. Keane, *A characterization of Ln-Pd/SiO_2 (Ln=La, Ce, Sm, Eu, Gd and Yb): Correlation of surface chemistry with hydrogenolysis activity*. J. Mol. Catal. A: Chem. 272 (2007) 96-107.

[11.39] S.H. Chung, Y.M. Park, M.S. Kim, K.Y. Lee, *The effect of textural properties on the hydrogenation of succinic acid using palladium incorporated mesoporous supports*. Catal. Today 185 (2012) 205-210.

[11.40] E. Santillan-Jimenez, M. Crocker, *Catalytic deoxygenation of fatty acids and their derivatives to hydrocarbon fuels via decarboxylation/decarbonylation*. J. Chem. Technol. Biotechnol. 87 (2012) 1041-1050.

[11.41] K.Y. Sun, A.R. Wilson, S.T. Thompson, H.H. Lamb, *Catalytic deoxygenation of octanoic acid over supported palladium: Effects of particle size and alloying with gold*. ACS Catal. 5 (2015) 1939-1948.

[11.42] J. Lu, S. Behtash, A. Heyden, *Theoretical investigation of the reaction mechanism of the decarboxylation and decarbonylation of propanoic acid on Pd(111) model surfaces*. J. Phys. Chem. C 116 (2012) 14328-14341.

[11.43] S. Sitthisa, P. Trung, T. Prasomsri, T. Sooknoi, R.G. Mallinson, D.E. Resasco, *Conversion of furfural and 2-methylpentanal on Pd/SiO_2 and Pd-Cu/SiO_2 catalysts*. J. Catal. 280 (2011) 17-27.

[11.44] M.A. Ermakova, D.Y. Ermakov, *Ni/SiO_2 and Fe/SiO_2 catalysts for production of hydrogen and filamentous carbon via methane decomposition*. Catal. Today 77 (2002) 225-235.

[11.45] M.A. Keane, G. Jacobs, P.M. Patterson, *Ni/SiO_2 promoted growth of carbon nanofibers from chlorobenzene: Characterization of the active metal sites*. J. Colloid Interf. Sci. 302 (2006) 576-588.

[11.46] A. Borgschulte, R.J. Westerwaal, J.H. Rector, H. Schreuders, B. Dam, R. Griessen, *Catalytic activity of noble metals promoting hydrogen uptake*. J. Catal. 239 (2006) 263-271.

[11.47] C.G. Zhou, S.J. Yao, J.P. Wu, R.C. Forrey, L. Chen, A. Tachibana, H.S. Cheng, *Hydrogen dissociative chemisorption and desorption on saturated subnano palladium clusters ($Pd_{(n)}$, n=2-9)*. Phys. Chem. Chem. Phys. 10 (2008) 5445-5451.

[11.48] W. Daniell, U. Schubert, R. Glockler, A. Meyer, K. Noweck, H. Knozinger, *Enhanced surface acidity in mixed alumina-silicas: A low-temperature FTIR study*. Appl. Catal. A: Gen. 196 (2000) 247-260.

[11.49] M.L. Smith, A. Campos, J.J. Spivey, *Reduction processes in Cu/SiO_2, Co/SiO_2, and CuCo/SiO_2 catalysts*. Catal. Today 182 (2012) 60-66.

[11.50] I. Cabria, M.J. López, S. Fraile, J.A. Alonso, *Adsorption and dissociation of molecular hydrogen on palladium clusters supported on graphene*. J. Phys. Chem. C 116 (2012) 21179-21189.

[11.51] C.Y. Lee, A.E. Depristo, *Dissociative chemisorption dynamics of H_2 on Ni and Cu surfaces: Morphology and surface temperature effects*. J. Chem. Phys. 85 (1986) 4161-4171.

[11.52] J. Batista, A. Pintar, J.P. Gomilsek, A. Kodre, F. Bornette, *On the structural characteristics of γ-alumina-supported Pd-Cu bimetallic catalysts*. Appl. Catal. A: Gen. 217 (2001) 55-68.

[11.53] S. Sitthisa, T. Sooknoi, Y. Ma, P.B. Balbuena, D.E. Resasco, *Kinetics and mechanism of hydrogenation of furfural on Cu/SiO_2 catalysts*. J. Catal. 277 (2011) 1-13.

[11.54] R.V. Chaudhari, C.V. Rode, R.M. Deshpande, R. Jaganathan, T.M. Leib, P.L. Mills, *Kinetics of hydrogenation of maleic acid in a batch slurry reactor using a bimetallic Ru-Re/C catalyst*. Chem. Eng. Sci. 58 (2003) 627-632.

[11.55] E. Iglesia, M. Boudart, *Decomposition of formic acid on copper, nickel and copper-nickel alloys: II. Catalytic and temperature-programmed decomposition of formic acid on Cu/SiO_2, Cu/Al_2O_3, and Cu powder*. J. Catal. 81 (1983) 214-223.

[11.56] D.Z. Gao, Y.H. Feng, H.B. Yin, A.L. Wang, T.S. Jiang, *Coupling reaction between ethanol dehydrogenation and maleic anhydride hydrogenation catalyzed by Cu/Al_2O_3, Cu/ZrO_2, and Cu/ZnO catalysts*. Chem. Eng. J. 233 (2013) 349-359.

Chapter 12

Summary and Future Work

The ultimate objective of this PhD thesis was the improvement of catalytic process (in terms of activity, selectivity and sustainability) through modification of catalyst structure, process coupling, utilisation of hydrogen and renewable resources and optimisation of operation conditions. The results presented demonstrate the viability of tuning Au particle size and support to control the catalytic response in the hydrogenation of aldehydes (benzaldehyde and furfural). A series of approaches have been proposed to enhance the hydrogenation activity of supported Au catalysts. The work has established *in situ* hydrogen generation *via* catalytic dehydrogenation (of alcohols) and formic acid decomposition with viable utilisation in the production of target fine chemicals. All the catalyst testing was conducted under mild reaction condition (P = 1 atm, 393 K $\leq T \leq$ 573 K) in the continuous gas phase operation.

12.1 General Conclusions

The results have established selective hydrogenation of –C=O compounds (benzaldehyde and biomass-derived furfural) to the target alcohol over oxide supported nano-scale Au (mean = 2-8 nm) catalysts. The role of support, Au particle size and electronic character in determining catalytic activity and selectivity has been demonstrated. The presence of Lewis acid/basic sites (on Au/Al_2O_3) facilitates –C=O activation resulting in enhanced turnover frequency (*TOF*). Reducible supports (TiO_2, CeO_2, Fe_2O_3 and Fe_3O_4) post-activation exhibit oxygen vacancies that act to stabilise surface reactant with a consequent lower reaction rate. Hydrogenation *TOF* increases with decreasing Au size (from 8 to 4 nm) with measurably lower *TOF* over Au < 3 nm. Application of nano-scale supported Au in catalytic hydrogenation is limited by low activity due to the restricted capacity for H_2 activation/dissociation. A series of approaches, (i) promotional effect of water *via* catalytic dissociation; (ii) increased spillover hydrogen with addition of oxide support and (iii) coupling dehydrogenation (2-butanol to 2-butanone over Cu/SiO_2) and resultant hydrogen release with hydrogenation (over Au/CeO_2), have been developed to enhance available surface hydrogen to promote selective (benzaldehyde and furfural) hydrogenation rate.

Two catalytic routes for imine (*N*-benzylideneimine) synthesis in continuous gas phase operation have been established. The reductive coupling of benzaldehyde with nitrobenzene (using an external source of hydrogen) over supported Au resulted in preferential hydrogenation of nitrobenzene to aniline that underwent condensation with benzaldehyde to deliver up to 99% selectivity to the target imine. Under the same reaction conditions, Pd/TiO_2 exhibited higher reaction rate but promoted benzaldehyde hydrogenolysis to toluene leading to lower imine selectivity (83%). Coupling benzyl alcohol dehydrogenation with nitrobenzene hydrogenation (in nitrogen) over Au/TiO_2 + Cu/SiO_2 mixtures generated the imine with full hydrogen utilisation. The inclusion of Au/TiO_2 in the mixture enhanced nitrobenzene hydrogenation and suppressed catalyst deactivation.

In the coupling of 2-butanol dehydrogenation with nitrobenzene hydrogenation, full yields to target products (2-butanone and aniline) were achieved. Hydrogen utilisation efficiency was appreciably greater (by a factor of up to 50) in the coupled system relative to conventional stand-alone hydrogenation using pressurised hydrogen. This response is attributed to the generation of reactive hydrogen associated with the Cu sites (Cu-H) that is effectively transferred for $–NO_2$ reduction. This circumvents the limitations associated with H_2 activation/dissociation by Cu.

Continuous gas phase synthesis of benzylamine from benzyl alcohol by tandem dehydrogenation/amination/reduction has been studied over Cu/SiO_2 and Au/TiO_2. A synergy between Cu/SiO_2 and Au/TiO_2 serves to promote benzylamine generation through an optimization of process parameters, notably hydrogen partial pressure and reaction temperature.

Selective continuous production of γ-butyrolactone from succinic acid has been achieved in both stand-alone hydrogenation (using external H_2) and reaction coupling with formic acid decomposition (as a source of H_2) over Cu/SiO_2. Pd/SiO_2 and Ni/SiO_2 exhibited higher reaction rates but promoted propanoic acid formation as by-product. Coupled reaction over Cu/SiO_2 delivered three-fold higher H_2 utilisation efficiency than conventional hydrogenation.

12.2 Future Directions

12.2.1 Application of *in situ* IR Spectroscopy for Benzaldehyde Hydrogenation over Oxides Supported Au

Reaction mechanisms for the hydrogenation of benzaldehyde and furfural have been proposed in **Chapters 3** and **9** to account for the effect of support surface sites (non-reducible sites and oxygen vacancies) to modify –C=O adsorption/activation and consequent activity/selectivity. Validation of the mechanism requires further characterisation by *in situ* IR spectroscopy. This should be directed at an analysis of the mode of adsorption on Al_2O_3 and CeO_2 pre- and post- Au introduction. Analysis (in a reaction cell) of surface interactions in H_2 and under reaction conditions can serve to pinpoint differences due to the redox character of the support. Theoretical (DFT) calculations can provide molecular level mechanistic information in terms of reactant/surface dynamics and the nature of the transition-state.

12.2.2 Succinic Acid Hydrogenation

The work presented in **Chapter 11** has established selective hydrogenation of biomass-derived succinic acid to γ-butyrolactone over Cu/SiO_2 but at low conversions (<40%). Copper delivered a lower hydrogenation rate than that obtained for Pd and Ni due to the lower H_2 chemisorption capacity of Cu. Further work is required to raise the activity with the target of 100% conversion and full selectivity to γ-butyrolactone. Support acidity (surface Brønsted acid sites) has been shown to facilitate cyclisation-esterification of γ-hydroxy-butyric acid and enhance activity and selectivity to γ-butyrolactone [12.1]. Benzoic acid hydrogenation rates over $Au/Ce_{0.62}Zr_{0.38}O_2$ have been correlated to support reducibility and the formation of the reactive benzoate intermediate [12.2]. Moreover, metal nitride/carbide support serves to activate/ dissociate hydrogen and enhance hydrogenation [12.3]. The influence of support nature in terms of acidity-basicity, redox character, and hydrogen uptake capability should be investigated in the gas phase hydrogenation of succinic acid over supported Cu catalysts. Hydrogen uptake is sensitive to metal particle size which impacts on hydrogenation rate [12.4]. A decrease in supported Au and Cu size resulted in enhanced hydrogenation activity in the conversion of benzaldehyde and nitrobenzene (**Chapters 3** and **6**). Variations in Cu size should be tested in succinic acid hydrogenation to probe possible structure sensitivity. Gold belongs to the same group as copper and has common physicochemical properties. It has been established in **Chapters 2**, **3**, **8** and **9**

that supported Au catalysts exhibit unique chemoselectivity for reduction of multiple saturated functionalities (–C=O and $–NO_2$). This could be exploited in carboxyl group hydrogenation, *i.e.* succinic acid.

12.2.3 Enhance Coupling Performance of Formic Acid Decomposition with Succinic Acid Hydrogenation

The work presented in **Chapter 11** has established the viability of formic acid as an efficient hydrogen donor for succinic acid hydrogenation with enhanced reaction rate and hydrogen utilisation relative to conventional hydrogenation using external gaseous hydrogen. However, hydrogen utilisation efficiency was far lower than stoichiometry. Future work should focus on enhancing succinic acid hydrogenation to γ-butyrolactone in the coupled reaction. Incorporation of a second metal in either physical mixture or as a supported bimetallic system is an avenue of research that should be explored. As hydrogen supply governs overall rate a range of donor compounds warrant examination where cross-reactions that generate unwanted by-products must be avoided. Dehydrogenation of alcohols derived from biomass (polyols) in a coupled system may form the basis for sustainable "hydrogen free" hydrogenations.

12.3 References

[12.1] U.G. Hong, S. Hwang, J.G. Seo, J. Lee, I.K. Song, *Hydrogenation of succinic acid to γ-butyrolactone (GBL) over palladium catalyst supported on alumina xerogel: Effect of acid density of the catalyst*, J. Ind. Eng. Chem. 17 (2011) 316-320.

[12.2] N. Perret, X. Wang, J.J. Delgado, G. Blanco, X.W. Chen, C.M. Olmos, S. Bernal, M.A. Keane, *Selective hydrogenation of benzoic acid over Au supported on CeO_2 and $Ce_{0.62}Zr_{0.38}O_2$: Formation of benzyl alcohol*, J. Catal. 317 (2014) 114-125.

[12.3] N. Perret, X. Wang, L. Delannoy, C. Potvin, C. Louis, M.A. Keane, *Enhanced selective nitroarene hydrogenation over Au supported on β-Mo_2C and β-MO_2C/Al_2O_3*, J. Catal. 286 (2012) 172-183.

[12.4] D. Uzio, G. Berhault, *Factors governing the catalytic reactivity of metallic nanoparticles*, Catal. Rev. 52 (2010) 106-131.